Hadron Production in 90 GeV/c Proton-Carbon Interactions

by

Kyle K Allison

B.A., Pomona College, 2018

M.S., University of Colorado Boulder, 2021

A thesis submitted to the
Faculty of the Graduate School of the
University of Colorado in partial fulfillment
of the requirements for the degree of
Doctor of Philosophy
Department of Physics
2024

Committee Members:
Alysia Marino, Chair
Jeremy Darling
Jamie Nagle
Kevin Stenson
Eric Zimmerman

Allison, Kyle K (Ph.D., High Energy Physics)

Hadron Production in 90 GeV/c Proton-Carbon Interactions

Thesis directed by Professor Alysia Marino

The neutrino flux for accelerator-based neutrino experiments originates from the decay of mesons, which are produced via hadron-nucleus interactions in extended targets. Since the cross sections of primary and secondary hadronic processes are difficult to model or calculate, neutrino flux uncertainties are typically a leading uncertainty in present day measurements of neutrino oscillation parameters with accelerator-based neutrino experiments. These uncertainties can be significantly constrained with precise measurements of the hadronic production processes occurring in the production of neutrino beams. The NA61/SHINE experiment at the CERN SPS has a dedicated program to precisely measure these processes; the T2K experiment has already incorporated previous NA61/SHINE measurements for a substantial flux uncertainty reduction. This thesis will present multiplicity measurements of $\pi^{\pm}$, $K^{\pm}$, $p/\bar{p}$, K^0_S, Λ, and $\bar{\Lambda}$ produced in the interaction of 90 GeV/c protons with a carbon target.

Dedication

To Tessa.

Acknowledgements

There are many people who contributed greatly to the completion of this thesis, both directly and indirectly. Of course, the first person to thank is my advisor Alysia Marino, who provided excellent guidance and support along my entire graduate school career. Along with the rest of the Neutrino Group at CU, I would also like to thank Eric Zimmerman, who acted as a second advisor, providing additional help whenever I needed it.

When I first joined the Neutrino Group, I knew only the bare minimum of coding, and I had never worked on a particle physics experiment before. This journey would have been immeasurably rougher without the help of Brant Rumberger, who patiently answered any questions I had.

As is often the case in experimental particle physics, there are too many people inside the NA61/SHINE Collaboration who helped me to list. Suffice it to say they introduced me to the world of particle physics, provided an international group of friends, gave helpful advice, and guided me throughout this process.

Lastly, I would like to thank my parents, family, and friends for always supporting my journey and making my life at Boulder fun.

Contents

Chapter

Appendix

Tables

Table

Figures

Figure

65;6800;1c

Chapter 1

Introduction

This thesis aims to measure the multiplicity of hadrons produced in proton-carbon interactions with a 90 GeV/c proton beam on a graphite target, where the interactions are occurring between a proton and a single carbon nucleus. These interactions are difficult to model or calculate, so the only way to truly probe them is through experiment [1–3]. While there is existing data on proton-nucleus collisions, before NA61/SHINE (North Area 61/Super-proton-synchrotron Heavy Ion Neutrino Experiment), the experiment which took the dataset analyzed in this thesis, there was a lack of data in the momentum range typically used by long-baseline neutrino oscillation experiments. (Section 3.3 will discuss this in more detail.) While the lack of existing data for hadron production in 90 GeV/c proton-carbon collisions makes this interaction interesting enough to study on its own merits, the underlying reason for the analysis performed in this thesis is to aid long-baseline neutrino oscillation experiments.

Chapter 2 will first introduce the theory of the Standard Model of Particle Physics and neutrino oscillations, then Chapter 3 will introduce a subset of the experiments probing the neutrino oscillation parameters. These long-baseline neutrino oscillation experiments measure beams of neutrinos at near and far detectors to study neutrino oscillations and the parameters that define these oscillations.

In the current phase of neutrino study, uncertainties are making it difficult to accurately measure all of the desired quantities. One of the largest uncertainties results from the difficulty in modeling the hadron production that is an integral part of the creation of neutrino beams; Figure

1.1 shows a depiction of a hadronic interaction inside a target.

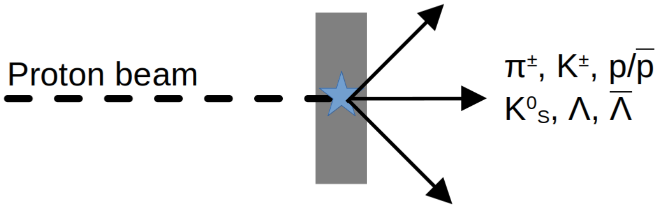

Figure 1.1: A depiction of particle beam interacting inside a target and producing a shower of neutral and charged hadrons.

Several experiments, including NA61/SHINE , have dedicated programs to study hadron production for long-baseline neutrino oscillation experiments. Chapter 4 will introduce the NA61/SHINE experiment, which took the proton-carbon dataset being analyzed for this thesis back in 2017, and Chapter 5 will describe the software framework used by NA61/SHINE to analyze its data. Chapter 6 will discuss the calibration procedure necessary before a physics analysis can be performed.

When analyzing physics data, the NA61/SHINE experiment is capable of measuring the production of both neutral and charged hadrons. Measuring the differential multiplicities of hadrons requires total cross section measurements to normalize the results, which will be described in Chapter 7, and then Chapter 8 will explain the analysis procedure and show differential multiplicity results for the neutral K^0_S, Λ, and $\bar{\Lambda}$ hadrons. After this, Chapter 9 will present the charged analysis procedure and results for measuring the charged $\pi^{\pm}$, $K^{\pm}$, $p/\bar{p}$ hadrons before a brief, final discussion in Chapter 10.

Chapter 2

The Standard Model of Particle Physics and Neutrinos

2.1 Standard Model of Particle Physics

The Standard Model of Particle Physics is a celebrated theoretical and experimental success, correctly predicting the existence of the $W^{\pm}$ and Z bosons, the top quark, and the Higgs boson [4–6]. At its base, the Standard Model is a quantum field theory obeying $SU(3)_c \otimes SU(2)_L \otimes U(1)$ gauge symmetry. Each symmetry corresponds to one of the three forces present in the Standard Model: the strong, the weak, and the electromagnetic forces, respectively. Gravity, the fourth known force, is currently excluded from the Standard Model. This section will only briefly introduce the Standard Model, adapting the formulation in Griffiths [7] and Schwartz [8]. Table 2.1 shows the elementary particles in the Standard Model with some of their fundamental properties; these consist of the spin-$\frac{1}{2}$ fermion matter particles, the spin-1 gauge bosons that act as force carriers, and the spin-0 Higgs boson.

2.1.1 The Strong Force

The strong force mediators, the gluons, are represented by the $SU(3)_c$ group and act on color charge, denoted by the subscript c. Only the quarks and gluons carry color charge, and so only they participate in the strong interaction. Each quark can be either red, green, or blue. From the group structure of $SU(3)_c$, there are nine possible color states for the gluons, though the ninth, the color singlet state, is forbidden experimentally. (There are also anti-color states.)

The Lagrangian defining the dynamics of the strong interaction can be constructed by starting

Particle	Mass [$/c^2$]	Spin	Charge
up quark	~ 2.2 MeV	1/2	2/3
charm quark	~ 1.28 GeV	1/2	2/3
top quark	~ 173.1 GeV	1/2	2/3
down quark	~ 4.7 MeV	1/2	$-1/3$
srange quark	~ 96 MeV	1/2	$-1/3$
bottom quark	~ 4.18 GeV	1/2	$-1/3$
electron	0.511 MeV	1/2	-1
muon	105.66 MeV	1/2	-1
tau	1.7768 GeV	1/2	-1
electron neutrino	NA	1/2	0
muon neutrino	NA	1/2	0
tau neutrino	NA	1/2	0
gluon	0	1	0
photon	0	1	0
W boson	91.19 GeV	1	± 1
Z boson	80.360 GeV	1	0
Higgs boson	125.11 GeV	0	0

Table 2.1: All of the elementary particles in the Standard Model and some of their basic properties [9]. Each particle listed has an associated anti-particle with the same mass and spin, but opposite charge.

with the free fermion Lagrangian for a spin-$\frac{1}{2}$, massive quark field:

$$\mathcal{L} = \bar{\psi}_{\alpha,i}(i\partial\!\!\!/ - m)\psi_{\alpha,i}. \tag{2.1}$$

Here $\psi_{\alpha,i}$ is a Dirac spinor transforming under the fundamental representation of $SU(3)_c$, $i = 1, 2, 3$ (red, green, blue), and $\alpha = 1, 2, 3, 4$ is the spinor index. (The Dirac spinors are solutions to the Dirac equation; two of the indices are needed to describe the chirality of particles, and two more are needed to describe the chirality of anti-particles.) Dropping the indices for simplicity, $\bar{\psi}$ represents the anti-quark field, the adjoint spinor. Finally, $\partial\!\!\!/ = \gamma^\mu \partial_\mu$, where γ^μ are the Dirac matrices, and m is the mass. This is essentially just a classical Lagrangian, where $\bar{\psi} i \partial\!\!\!/ \psi$ is the kinetic term and $\bar{\psi} m \psi$ is the potential term.

Equation 2.1 already holds Poincaré invariance and local color invariance, and it is also invariant under global $SU(3)_c$ transformations, all by construction. The next step is to impose local $SU(3)_c$ gauge symmetry, requiring the Lagrangian to be invariant under transformations of the form $\psi'(x) = U(x)\psi(x)$, where

$$U(x) = e^{\frac{i}{2}\epsilon(x)_a\lambda^a}, \tag{2.2}$$

and $\epsilon(x)$ is some arbitrary, well-defined function dependent on position, which is why this is called a local symmetry. λ_a are the Gell-Mann matrices, and are 3×3 generators of the $SU(3)_c$ group. Imposing this condition requires the introduction of the eight gluon fields mentioned earlier, $A^\mu = \frac{1}{2}A^\mu_a\lambda^a$. These are used to define the covariant derivative

$$D_\mu = \partial_\mu - igA_\mu. \tag{2.3}$$

Here g is the coupling strength of the gluon fields to the quark fields, and A_μ is the gluon field. Now that eight gluon fields have been added, the Lagrangian needs the addition of a kinetic term for each field. (They are massless, so they do not get a potential term; a mass term of the form $mA_\mu A^\mu$ would violate gauge invariance.) The free gluon Lagrangian is given by

$$\mathcal{L}_{gluons} = -\frac{1}{4}F^{\mu\nu}F_{\mu\nu}, \tag{2.4}$$

where the gluon field strength tensor is defined by

$$F^{\mu\nu} \equiv \partial^\mu A^\nu - \partial^\nu A^\mu - ig[A^\mu, A^\nu]. \tag{2.5}$$

Putting it all together, the Lagrangian describing the strong force is

$$\mathcal{L} = \bar{\psi}(i\not{D} - m)\psi - \frac{1}{4}F^{\mu\nu}F_{\mu\nu}. \tag{2.6}$$

With the Lagrangian in Equation 2.6, the three basic interactions allowed by the strong force can be read off: a quark emitting or absorbing a gluon, a gluon emitting or absorbing another gluon, or two gluons directly interacting. All other interactions can be built up from these three interaction shown in the Feynman diagrams in Figure 2.1.

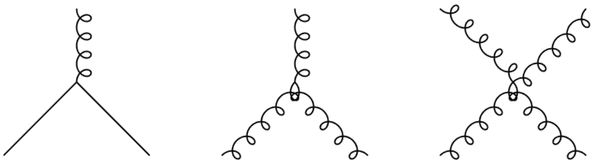

Figure 2.1: Feynman diagrams of the three basic interactions of the strong force. A straight line is used for quarks, and a curly line is used for gluons. Time is left to right.

2.1.2 Electroweak and the Higgs Mechanism

Before electroweak symmetry breaking, the electromagnetic and weak forces can be unified into the electroweak sector, which interacts with the symmetry group $SU(2)_L \otimes U(1)$. The L subscript specifies coupling to only left-chiral fermions (and right-chiral anti-fermions), an experimental observation. In an analagous manner to the strong force — before the inclusion of Higgs and Yukawa terms — the electroweak Lagrangian for leptons can be written

$$\mathcal{L} = \bar{\psi}_{i,L} i \not{D} \psi_{i,L} + \bar{\psi}_{i,R} i \not{D} \psi_{i,R} - \frac{1}{4} W_a^{\mu\nu} W_{\mu\nu}^a - \frac{1}{4} B^{\mu\nu} B_{\mu\nu}. \tag{2.7}$$

Now $\psi_{i,L}$ represents a left-handed doublet fermion field, the index $i = 1, 2, 3$ differentiates between the three particle generations, and $\psi_{i,R}$ is the right-handed singlet fermion field. The covariant derivative is again defined with the gauge fields

$$D_\mu \equiv \partial_\mu - i \frac{g_w'}{2} Y_W B_\mu - i \frac{g_w}{2} \tau_i W_\mu^i. \tag{2.8}$$

For the $U(1)$ symmetry group Y_W represents the weak hypercharge, the generator of $U(1)$, B_μ is the gauge field, and g_w' is the coupling strength of the hypercharge current to the gauge field.

Meanwhile, for the $SU(2)_L$ symmetry group, the τ matrices are the generators of $SU(2)_L$, W_μ is the gauge field, and g_w is the coupling strength. Currently, all of the fermions in Equation 2.7 do not have mass terms, and any $m\bar{\psi}\psi$ term would violate local $SU(2)_L$ gauge invariance. Similarly, and just like the gluons, the four gauge fields also have to be massless to not violate gauge symmetry. However, experimentally fermions and the mediators of the weak force have mass. The solution to this problem is the Higgs mechanism, which introduces the Higgs field, a complex scalar field in $SU(2)_L$:

$$\phi = \frac{1}{\sqrt{2}} \begin{pmatrix} \phi^+ \\ \phi^0 \end{pmatrix}. \tag{2.9}$$

With the addition of a new field, the electroweak Lagrangian picks up the following terms for the interactions between the new field, itself, and the gauge bosons:

$$\mathcal{L}_{Higgs} = |D_\mu \phi|^2 + \mu^2 \phi^\dagger \phi - \lambda (\phi^\dagger \phi)^2. \tag{2.10}$$

Equation 2.10 comes from quantum field theory treating fields as fluctuations above the ground (vacuum) state. Before Equation 2.10 the ground state was always the trivial one of $\phi = 0$. Now, only considering terms up to the renormalizeable order ϕ^4, Equation 2.10 allows for a non-zero ground state. Separating the μ and λ terms as the potential energy of this Lagrangian and restricting $\lambda > 0$ and $\mu^2 < 0$, the minima of the potential energy then lie in a circle where $(\phi^+)^2 + (\phi^0)^2 = \mu^2/\lambda$. To expand around a particular vacuum, set $\phi^+ = 0$. With this gauge choice, $\phi^0_{min} = \mu/\sqrt{\lambda} = v$, where v is the vacuum expectation value of the Higgs field. Expanding around the vacuum in this gauge and taking the lower component to only be real (fields can always be freely redefined up to a phase), the Higgs field can be written as

$$\phi = \frac{1}{\sqrt{2}} \begin{pmatrix} 0 \\ v + h \end{pmatrix}, \tag{2.11}$$

where h is a real scalar field. Substituting the gauged, symmetry broken Equation 2.11 into Equation

2.10 is the foundation of the Higgs mechanism, and breaks the electroweak force into its constituent weak and electromagnetic parts. Starting with just the terms containing v,

$$|D_\mu\phi|^2 = g_w\frac{v^2}{8}\left[(W_\mu^1)^2 + (W_\mu^2)^2 + \left(\frac{g_w'}{g_w}B_\mu - W_\mu^3\right)^2\right]^2. \tag{2.12}$$

To diagonlize the masses, define

$$\begin{aligned} Z_\mu &\equiv \cos\theta_w W_\mu^3 - \sin\theta_w B_\mu, \\ A_\mu &\equiv \sin\theta_w W_\mu^3 + \cos\theta_w B_\mu, \\ \tan\theta_w &= \frac{g_w'}{g_w}. \end{aligned} \tag{2.13}$$

This leads to the expected form for the kinetic part of the photon Lagrangian, where the A boson can now be recognized as the massless photon, along with a clear mass term for the Z boson:

$$\begin{aligned} \mathcal{L}_{Z,A} &= -\frac{1}{4}F^{\mu\nu}F_{\mu\nu} - \frac{1}{4}Z^{\mu\nu}Z_{\mu\nu} + \frac{1}{2}m_Z^2 Z^\mu Z_\mu, \\ m_z &= \frac{g_w v}{2\cos\theta_w}. \end{aligned} \tag{2.14}$$

The interaction terms are more complicated, and the lengthy algebra will be skipped. Collecting terms in factors of $e = g_w \sin\theta_w$ and $W_\mu^\pm = \frac{1}{\sqrt{2}}(W_\mu^1 \mp W_\mu^2)^2$, the rest of the Lagrangian can be written

$$\begin{aligned}
\mathcal{L}_v = {} & m^2{}_W W^+_\mu W^{\mu,-} - \frac{1}{2}(\partial_\mu W^+_\nu - \partial_\nu W^+_\mu)(\partial^\nu W^{\mu,-} - \partial^\mu W^{\nu,-}) \\
& - ie \cot\theta_w [\partial_\mu Z_\nu (W^{\mu,+} W^{\nu,-} - W^{\nu,+} W^{\mu,-}) \\
& + Z_\nu (W^{\mu,-} \partial^\nu W^+_\mu - W^{\mu,+} \partial^\nu W^-_\mu + W^{\mu,+} \partial_\mu W^{\nu,-} - W^{\mu,-} \partial_\mu W^{\nu,+})] \\
& - ie[\partial_\mu A_\nu (W^{\mu,+} W^{\nu,-} - W^{\nu,+} W^{\mu,-}) \\
& + A_\nu (W^{\mu,-} \partial^\nu W^+_\mu - W^{\mu,+} \partial^\nu W^-_\mu + W^{\mu,+} \partial_\mu W^{\nu,-} - W^{\mu,-} \partial_\mu W^{\nu,+})] \\
& + \frac{1}{2} \frac{e^2}{\sin^2\theta_w} (W^{\mu,+} W^+_\mu W^{\nu,-} W^-_\nu - W^{\mu,+} W^-_\mu W^{\nu,+} W^-_\nu) \\
& - e^2 \cot^2\theta_w (Z^\mu W^+_\mu Z^\nu W^-_\nu - Z^\mu Z_\mu W^{\nu,+} W^-_\nu) \\
& + e^2 (A^\mu W^+_\mu A^\nu W^-_\nu + A^\mu A_\mu W^{\nu,+} W^-_\nu) \\
& + e^2 \cot\theta_w [A^\mu W^+_\mu Z^\nu W^-_\nu + A^\mu W^-_\mu Z^\nu W^+_\nu - A^\mu Z_\mu W^{\nu,+} W^-_\nu].
\end{aligned} \tag{2.15}$$

Equation 2.15 contains every possible basic interaction between the $W^\pm$, Z, and A bosons. In addition, there is clear prediction for the difference between the $W^\pm$ and Z boson masses, explicitly $m_Z = \frac{m_W}{\cos\theta_w}$. Finally, the interactions between the Higgs and the $W^\pm$ and Z bosons are given by the terms with h:

$$\begin{aligned}
\mathcal{L}_{Higgs} = {} & -\frac{1}{2} h(\Box + m_h^2) h - g_w \frac{m_h^2}{4m_W} h^3 - g_w^2 \frac{m_h^2}{32 m_W^2} h^4 \\
& + 2\frac{h}{v}(m_W^2 W^{\mu,+} W^-_\mu + \frac{1}{2} m_Z^2 Z^\mu Z_\mu) + \frac{h^2}{v^2}(m_W^2 W^{\mu,+} W^-_\mu + \frac{1}{2} m_Z^2 Z^\mu Z_\mu).
\end{aligned} \tag{2.16}$$

2.1.3 Fermion Masses and Weak and Electromagnetic Interactions

The final step is to add in the Yukawa couplings, that, along with the Higgs mechanism, gives the fermions in the Standard Model their mass. As stated before, any terms of the form $m\bar{\psi}\psi$ will break the gauge symmetry, and so mass terms of this form are forbidden. At this point in the electroweak sector, there is also no connection between right and left-handed fermions. Currently they are just two separate fields that happen to have the same charge. (In the strong force sector, they are connected by the $m\bar{\psi}\psi$ terms.) The Yukawa coupling is just an assumption of interactions between the fermions and the Higgs field, usually written as generally as possible as an input to the Standard Model:

$$\mathcal{L}_{Yuk} = Y_a^{ij}\bar{\psi}^a_{L,i}(i\sigma_2\phi^*)\psi^a_{R,j} + Y_b^{ij}\bar{\psi}^i_{L,b}\phi\psi^j_{R,j} + h.c. \tag{2.17}$$

The Y_{ij} are the Yukawa couplings, and they are arbitrary complex numbers; with just a single scalar field ϕ, they are proportional to the mass matrices. $a = u, \nu$ (up-type quarks, neutrinos), $b = d, l$ (down-type quarks, charged leptons), and σ_2 is the second Pauli matrix. $h.c.$ is the Hermitian conjugate of all of the previous terms. All of these terms are $SU(2)$ invariant. Starting with the quarks, after electroweak symmetry breaking, the quark mass terms become

$$\mathcal{L}_{quark\ masses} = -\frac{v}{\sqrt{2}}(\bar{d}_L Y_d d_R + \bar{u}_L Y_u u_R) + h.c. \tag{2.18}$$

For clarity, d represents the three down-type quarks (d, s, b), u represents the three up-type quarks (u, c, t), and the Y are 3×3 matrices. Equation 2.18 is currently in the flavor basis. Going back to Equation 2.7 and rotating to the weak flavor basis, the symmetry broken electroweak Lagrangian for the quarks is given by:

$$\begin{aligned}
\mathcal{L}_{quarks} &= \frac{e}{sin\theta_w} Z^\mu J^Z_\mu + eA_\mu J^\mu_{EM} - m_j^\mu(\bar{d}^j_L d_{R,j} + \bar{d}^j_L d_{L,j}) - m_j^\mu(\bar{u}^j_L u_{R,j} + \bar{u}^j_L u_{L,j}) \\
&\quad + \frac{e}{\sqrt{2}\sin\theta_w}(W^+_\mu \bar{u}^i_L \gamma^\mu V_{ij} d^j_L + W^-_\mu \bar{d}^i_L \gamma^\mu V^\dagger_{ij} u^j_L), \\
J^{EM}_\mu &= (T^3 + Y_w)(\bar{\psi}^L_i \gamma^\mu \psi^{L,i} + \bar{\psi}^R_i \gamma_\mu \psi^{R,i}), \\
J^3_\mu &= \bar{\psi}^L_i \gamma_\mu T^3 \psi^{L,i}, \\
J^Z_\mu &= \frac{J^3_\mu - \sin^2\theta_w J^{EM}_\mu}{\cos\theta_w}.
\end{aligned} \tag{2.19}$$

There are many important details in Equation 2.19. First, the right and left-handed fermion fields are now explicitly connected by their mass terms, and they are no longer separate fields. Second, all of the interesting mixing effects from switching to the mass basis from the flavor basis are encoded in a single 3×3 matrix V, known as the Cabibbo–Kobayashi–Maskawa (CKM) matrix. Writing it more explicitly, the CKM matrix relates the strong interaction quark states to their weak interaction states:

$$\begin{pmatrix} d \\ s \\ b \end{pmatrix}_{weak} = \begin{pmatrix} V_{ud} & V_{us} & V_{ub} \\ V_{cd} & V_{cs} & V_{cd} \\ V_{td} & V_{ts} & V_{tb} \end{pmatrix} = \begin{pmatrix} d \\ s \\ b \end{pmatrix}. \tag{2.20}$$

Third, Equation 2.19 gives the explicit form of all of the weak interactions available for the quarks, where the J_μ terms have been left general, as they take the same form for the leptons. T^3 is the third component of weak isospin, and Y_W is the weak hypercharge. The CKM is close to being diagonal, meaning there is not much mixing between the mass and flavor basis for the quarks [10]. Some examples of electroweak interactions are shown in Figure 2.2.

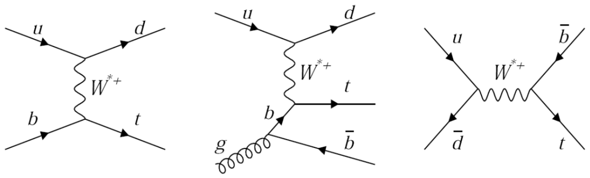

Figure 2.2: Electroweak diagrams for top quark production [11].

Equation 2.19 takes the same form for the charged leptons and the neutrinos, assuming the neutrinos' masses are purely Dirac and right-handed neutrinos exist. (The neutrinos are neutral and do not couple to the photon.) However, neutrinos are a tricky particle, and the intricacies of their mass terms will be addressed in the next section.

2.1.4 Neutrino Mass

So far, all of the calculations were done assuming right-handed neutrinos exist; however, they have not yet been observed, and they do not appear to couple to the W or Z bososn. Neutrinos in the Standard Model are also usually considered massless, though they were included in the same manner as quarks and leptons in the previous section for simplicity. In fact, neutrinos were not even confirmed to have mass until recently [12–15]. If right-handed neutrinos do exist, they are color, weak isospin, and electrically neutral, meaning they do not participate in any of three forces in the Standard Model; hence the difficulty in observing them. Because of all of these ambiguities, the mechanism behind the neutrino masses is not yet known. There are many proposed theories, and this section will briefly describe just a small handful of them.

A good place to start is with the most general renormalizable mass terms:

$$\begin{aligned} \mathcal{L}_{\nu\ mass} &= Y_{ij}\bar{\nu}^i_L \nu^j_R - iM_{ij}(\nu^i_R)^C \nu^j_R + h.c., \\ \nu^C &= \hat{C}\nu = i\gamma^2\gamma^0\nu. \end{aligned} \tag{2.21}$$

The first term is the standard Dirac mass that the rest of the fermions in the Standard Model generate mass from, and the second is the Majorana mass term, which is only allowed for neutrinos; this is forbidden by electroweak symmetry for all other fermions. (A charged fermion cannot turn into/be its own anti-particle; this violates charge conservation.) If neutrinos are Majorana, this couples right-handed and left-handed neutrinos together, and this is being probed by neutrinoless double-β decay experiments, like GERDA [16].

If right-handed neutrinos carry any conserved quantum number at all, say lepton number, then the Majorana mass term is forbidden. Switching to constructing the Dirac spinors out of single Weyl spinors (instead of from independent left and right-handed Weyl spinors), $\psi_R = \begin{pmatrix} i\sigma_2\nu^*_R \\ \nu_R \end{pmatrix}$, and dropping to just a single generation for simplicity, the neutrino mass Lagrangian can be written

$$\mathcal{L}_{\nu\ mass} = -m\bar{\psi}_L\psi_R - \frac{M}{2}\bar{\psi}_R\psi_R. \tag{2.22}$$

The physical masses resulting from Equation 2.22 are $\sqrt{m^2 + \frac{1}{4}M^2} \pm \frac{1}{2}M$. If the limit $M \gg m$ is taken, then a very heavy $m_{heavy} \approx M$ mass and a very light $m_{light} \approx \frac{m^2}{M}$ mass pop out. This is known as the Type-I Seesaw Mechanism, and gives a possible explanation for the very light neutrino masses. It includes not-yet-observed very heavy right-handed neutrinos that cannot be directly detected through Standard Model processes, so confirmation of this particular mechanism would be difficult.

Another possible mechanism for neutrino mass, which does not necessitate the inclusion of right-handed neutrinos, would be the addition of a dimension-5 term to the Lagrangian.

$$\mathcal{L}_{dim-5} = -M_{ij}(\nu_L^i i\sigma_2\phi^*)(i\sigma_2\phi^*\nu_L^j)^\dagger. \tag{2.23}$$

Equation 2.23 implies lepton number violation and is non-renormalizeable, but it is another possibility for the neutrino mass mechanism.

2.1.5 Standard Model Particles

Before going any further, it is useful to take a step back from all of the theory and more generally look at the particle content of the Standard Model. Figure 2.3 shows all the particles present in the Standard Model and their interactions.

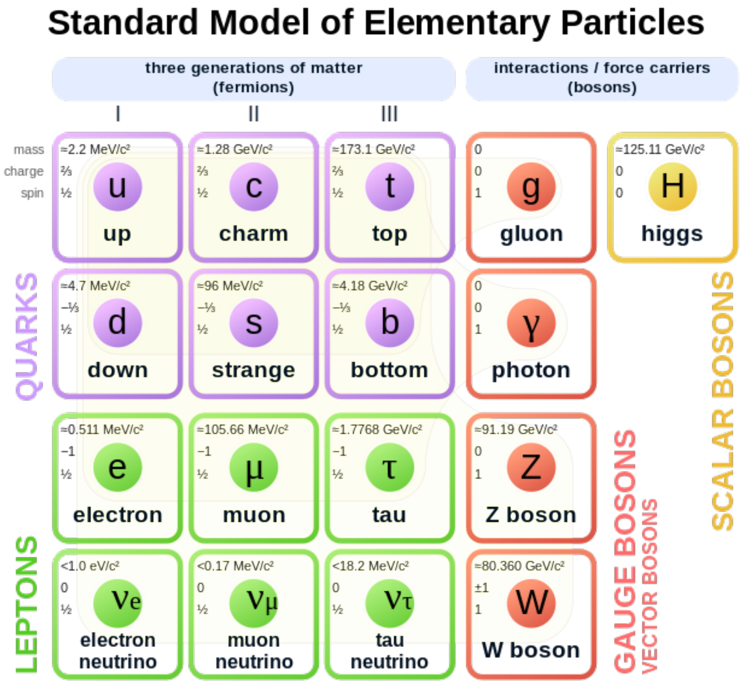

Figure 2.3: The particle content of the Standard Model. If one looks closely at this image, faint groupings can be seen that show boson-fermion couplings [9].

There is the Higgs boson, which is electrically neutral and spin-0; through the Higgs mechanism all of the fermions (except for the neutrinos?) and the weak force bosons acquire mass. Next, there is the gluon, a massless spin-1 boson responsible for mediating the strong force. As only the quarks carry color charge, out of all of the fermions, only the six quarks participate in the strong force. They are separated into the three generations of matter, and each generation is differentiated by its relative mass to the other generations. There are two families of quarks; the up-type quarks have charge $+\frac{2}{3}$, and the down-type quarks have charge $-\frac{1}{3}$. All of the fermions, including the neutrinos, are spin-$\frac{1}{2}$.

In the present electroweak symmetry broken universe, the next boson is the photon, the massless mediator of electromagnetic interactions. The electromagnetic interaction occurs between all charged particles of the Standard Model, so only the neutrinos and the uncharged bosons do not participate in it. Lastly, the weak bosons mediate the weak force, which is the interaction between particles with non-zero weak isospin. All of the fermions participate in the weak force.

This represents all of the elementary particles of the Standard Model, and particles like protons, neutrons, hydrogen, pions, kaons, etc. are all built up from these basic building blocks. In addition to this list, every particle has an anti-particle. Each anti-particle has the same quantum numbers as its particle partner, but with opposite charge. All of the bosons are their own anti-particles (W^+ is the anti-particle of W^-), and it is an open question in physics if this is also applies to neutrinos.

2.2 Neutrinos

Experimentally there are several holes in the Standard Model; theoretically, it could be improved upon as well. To name just a few issues with it, the Standard Model doesn't have a definitive mechanism for neutrino mass, and it also doesn't provide an explanation for neutrinos being roughly a million times lighter than the next lightest particle, the electron. Conspicuously, gravity is also missing from the Standard Model, and there is no definitive way to include it, or explain why gravity is so much weaker than the other three forces. Also, experimentally there are very clearly three generations of matter, but the generations and the Yukawa couplings are an input into the Standard Model Lagrangian. The large number of parameters that have to be determined experimentally is also unsatisfactory; is there some kind of unified theory that reduces the number of parameters? (The particle masses, the CKM matrix elements, the gauge couplings, the vacuum angle, and the Higgs mass and vacuum expectation value all have to be measured. Including the neutrino parameters adds to this list.)

Narrowing down to just neutrino physics, there is still a plethora of open questions. The rest of this chapter will address the open questions in neutrino physics related to this thesis.

2.2.1 Neutrino Mixing Matrix

As shown in Figure 2.3, there are three weak interaction flavor states for the neutrinos, where each state corresponds to one of the three charged leptons. In the exact same manner as for quarks, there is a mixing matrix for rotations between the neutrino flavor basis and the well-defined neutrino mass basis. (Well-defined here means eigenstates of the Hamiltonian.) The typical form of this matrix, known as the Pontecorvo–Maki–Nakagawa–Sakata (PMNS) matrix is

$$\begin{pmatrix} \nu_e \\ \nu_\mu \\ \nu_\tau \end{pmatrix} = \begin{pmatrix} U_{e1} \; U_{e2} \; U_{e3} \\ U_{\mu 1} \; U_{\mu 2} \; U_{\mu 3} \\ U_{\tau 1} \; U_{\tau 2} \; U_{\tau 3} \end{pmatrix} = \begin{pmatrix} \nu_1 \\ \nu_2 \\ \nu_3 \end{pmatrix}, \tag{2.24}$$

where ν_e represents the electron neutrino, and ν_1 represents neutrino mass state 1. The PMNS matrix can be fully defined with three angles $(\theta_{12}, \theta_{13}, \theta_{23})$ and one phase; if there is a Majorana mass term, there are an additional two Majorana phases α_{12} and α_{31}. Letting $s_{12} = \sin\theta_{12},\ c_{12} = \cos\theta_{12}$, a typical parameterization ([7]) is

$$U_{PMNS} = \begin{pmatrix} c_{12}c_{13} & s_{12}c_{13} & s_{13} \\ -s_{12}c_{23} - c_{12}s_{23}S_{13}e^{i\delta} & c_{12}c_{23} - s_{12}s_{23}s_{13}e^{i\delta} & s_{23}c_{13} \\ s_{12}S_{23} - c_{12}c_{23}s_{13}e^{i\delta} & -c_{12}s_{23} - s_{23}s_{13}e^{i\delta} & c_{23}c_{13} \end{pmatrix} \begin{pmatrix} 1 & 0 & 0 \\ 0 & e^{\frac{i}{2}\alpha_{12}} & 0 \\ 0 & 0 & e^{\frac{i}{2}\alpha_{31}} \end{pmatrix}. \tag{2.25}$$

In this parameterization, θ_{12} is known as the solar mixing angle, because it is measured by solar neutrino oscillation experiments. θ_{23} is the atmospheric mixing angle, θ_{13} is measured by accelerator and reactor-based experiments, and δ is the CP-violating phase factor. If $\delta \neq 0, \pi$, then there are clear predictions for how neutrinos and anti-neutrinos will behave differently. (See Equation 2.28 for an example.) The term CP comes from applying the charge and parity operators to particle fields. The charge operator switches particles with their anti-particles, and vice versa, while the parirty operator applies a mirror inversion. If CP is an exact symmetry, the underlying physics would be invariant under these two transformations. Finally, α_{12} and α_{31} are the Majorana phases, which are necessary to include if neutrinos are Majorana particles.

Currently there is ambiguity in the ordering of the neutrino masses, as experiments have only definitively determined $\Delta m^2_{ij} = m^2_i - m^2_j$ for the atmospheric and solar sectors; this means the mass ordering can either be $m_1 < m_2 < m_3$, or $m_3 < m_1 < m_2$. The first possible ordering is known as the normal hierarchy $(1, 2, 3)$, and the second ordering is known as the inverted hierarchy. Figure 2.4 depicts the two allowed hierarchies, along with the predicted flavor content of each mass state.

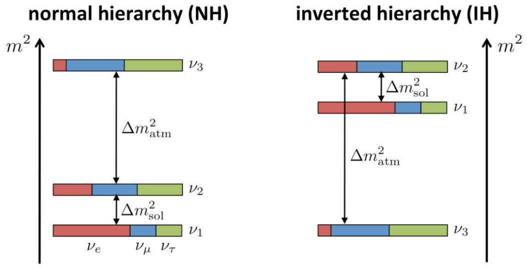

Figure 2.4: The two allowed neutrino mass hierarchies: ν_3 is either the heaviest mass state or the lightest mass state [17].

The neutrino mass hierarchy, the exact values of the PMNS matrix elements, if neutrinos are Majorana or not, and the absolute mass scale of the neutrinos are all open questions in physics. Experimentally, the CKM matrix is mostly diagonal, while the PMNS matrix is not, and this is another open question. Current and planned neutrino experiments hope to definitevely answer many of these questions; long-baseline neutrino oscillation experiments, which will be described in Chapter 3, are expected to determine the mass hierarchy and the value of δ in the near future.

2.2.2 Neutrino Oscillation Theory

As for any state in quantum mechanics, the time evolution of the neutrino flavor states is given by

$$|\nu_\alpha(t)\rangle = e^{-i\hat{H}t}\,|v_\alpha(0)\rangle \,. \tag{2.26}$$

If neutrino flavor states were eigenstates of the Hamiltonian, then $\nu_\alpha(t) = \nu_\alpha(0)$, where $\alpha = e, \mu, \tau$. The flavor states are not eigenstates, however; so the flavor states are changing as a function of time. Rewriting $\nu_\alpha(t)$ in terms of the mass basis gives:

$$|\nu_\alpha(t)\rangle = U_{\alpha i} e^{-i\hat{H}t}\,|v_i(0)\rangle \,. \tag{2.27}$$

Here the subscript $i = 1, 2, 3$ refers to the three mass neutrino states, and $U_{\alpha i}$ is the PMNS matrix element, which rotates neutrinos from the mass to the flavor basis. This is the foundation of neutrino oscillations. Assuming normal hierarchy, if a muon neutrino is produced at time 0, then at time t the probability of measuring an electron neutrino is

$$\begin{aligned}
&P(\nu_\mu \to \nu_e) = |\langle \nu_\alpha(0)|\nu_\beta(t)\rangle|^2 = P1 + P2 + P3 + P4,\\
&P1 = \sin^2(\theta_{23})\sin^2(2\theta_{13})\sin^2(\Delta m^2_{32} L/4E),\\
&P2 = \cos^2(\theta_{23})\sin^2(2\theta_{13})\sin^2(\Delta m^2_{21} L/4E),\\
&P3 = \mp J\sin(\delta)\sin(\Delta m^2_{32} L/4E),\\
&P4 = J\cos(\delta)\cos(\Delta m^2_{32} L/4E),\\
&J = \cos(\theta_{13})\sin(2\theta_{13})\sin(2\theta_{23})\sin(\Delta m^2_{32} L/4E)\sin(\Delta m^2_{21} L/4E).
\end{aligned} \tag{2.28}$$

$P3$ is negative for $\nu_\mu \to \nu_e$, and positive for $\bar{\nu}_\mu \to \bar{\nu}_e$. L is the travel length of the neutrino between production and measurement, and E is the energy of the neutrino. It can be difficult to gain much insight from Equation 2.28, but several things are clear; neutrino flavor oscillation is dependent on the three mixing angles, the CP-violating phase δ, the mass-squared splittings Δm^2_{ij}, and the proper time the neutrino travelled (L/E). The Majorana phases do not factor into neutrino oscillations. There is even a clear prediction for a difference between neutrino and anti-neutrino oscillations from the $P3$ term. (If $\delta = 0, \pi$, however, then $P3 = 0$.)

Using the simpler model of two neutrinos for oscillations can be better for a qualitative understanding of the physics behind Equation 2.28. Limiting neutrinos to just two flavors and two mass states, the oscillation probability becomes

$$P(\nu_\mu \to \nu_e) = \sin(2\theta)\sin^2(\Delta m^2 L/4E). \tag{2.29}$$

A plot of this for three separate variations of θ, m^2, and E is shown in Figure 2.5. The specific algebra and results become much more complicated moving to three flavors, but the basics can be understood from the two-flavor approximation; in two-flavor neutrino oscillations, shifting θ changes the peak heights, and changing Δm^2 moves the peaks.

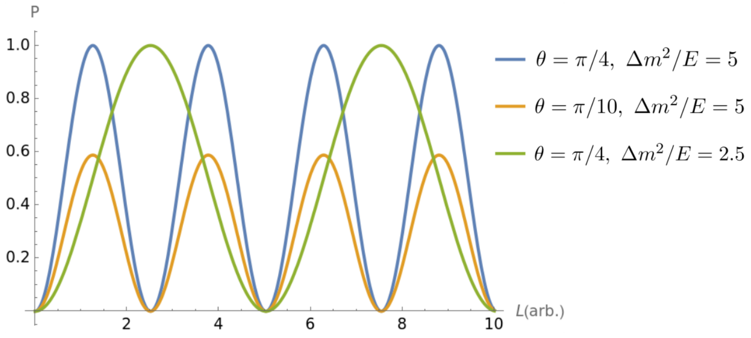

Figure 2.5: Two flavor neutrino oscillations as a function of propagation length L.

2.2.3 Neutrino Oscillation Parameters

After decades of experiments, the PMNS matrix elements and mass-squared splittings have all been reasonably well measured, with a few exceptions. The octant of θ_{23} is currently unknown; $\theta_{23} \approx 45°$, and the current data does not exclude either $\theta_{23} < 45°$ or $\theta_{23} > 45°$. Both the normal and inverted mass ordering are allowed, and the uncertainty on δ is unacceptably large. The next generation of neutrino oscillation experiments are expected to answer all of these questions, and will be discussed in Chapter 3. The implications of definitively determining these parameters is difficult to understate; CP-violation is necessary for baryon asymmetry, or matter being prevalent over anti-matter in the universe [18]. Table 2.2 shows the current best-fit values for the neutrino oscillation parameters [19, 20]. Unfortunately, many questions, such as the neutrino mass mechanism and the absolute scale of neutrino masses, cannot be determined by long-baseline neutrino oscillation experiments, and require neutrino experiments and theory beyond the scope of this thesis.

NuFIT 5.2 (2022)

		Normal Ordering (best fit)		Inverted Ordering ($\Delta\chi^2 = 2.3$)	
		bfp $\pm 1\sigma$	3σ range	bfp $\pm 1\sigma$	3σ range
without SK atmospheric data	$\sin^2\theta_{12}$	$0.303^{+0.012}_{-0.011}$	$0.270 \to 0.341$	$0.303^{+0.012}_{-0.011}$	$0.270 \to 0.341$
	$\theta_{12}/^\circ$	$33.41^{+0.75}_{-0.72}$	$31.31 \to 35.74$	$33.41^{+0.75}_{-0.72}$	$31.31 \to 35.74$
	$\sin^2\theta_{23}$	$0.572^{+0.018}_{-0.023}$	$0.406 \to 0.620$	$0.578^{+0.016}_{-0.021}$	$0.412 \to 0.623$
	$\theta_{23}/^\circ$	$49.1^{+1.0}_{-1.3}$	$39.6 \to 51.9$	$49.5^{+0.9}_{-1.2}$	$39.9 \to 52.1$
	$\sin^2\theta_{13}$	$0.02203^{+0.00056}_{-0.00059}$	$0.02029 \to 0.02391$	$0.02219^{+0.00060}_{-0.00057}$	$0.02047 \to 0.02396$
	$\theta_{13}/^\circ$	$8.54^{+0.11}_{-0.12}$	$8.19 \to 8.89$	$8.57^{+0.12}_{-0.11}$	$8.23 \to 8.90$
	$\delta_{\mathrm{CP}}/^\circ$	197^{+42}_{-25}	$108 \to 404$	286^{+27}_{-32}	$192 \to 360$
	$\frac{\Delta m^2_{21}}{10^{-5}\ \mathrm{eV}^2}$	$7.41^{+0.21}_{-0.20}$	$6.82 \to 8.03$	$7.41^{+0.21}_{-0.20}$	$6.82 \to 8.03$
	$\frac{\Delta m^2_{3\ell}}{10^{-3}\ \mathrm{eV}^2}$	$+2.511^{+0.028}_{-0.027}$	$+2.428 \to +2.597$	$-2.498^{+0.032}_{-0.025}$	$-2.581 \to -2.408$
		Normal Ordering (best fit)		Inverted Ordering ($\Delta\chi^2 = 6.4$)	
		bfp $\pm 1\sigma$	3σ range	bfp $\pm 1\sigma$	3σ range
with SK atmospheric data	$\sin^2\theta_{12}$	$0.303^{+0.012}_{-0.012}$	$0.270 \to 0.341$	$0.303^{+0.012}_{-0.011}$	$0.270 \to 0.341$
	$\theta_{12}/^\circ$	$33.41^{+0.75}_{-0.72}$	$31.31 \to 35.74$	$33.41^{+0.75}_{-0.72}$	$31.31 \to 35.74$
	$\sin^2\theta_{23}$	$0.451^{+0.019}_{-0.016}$	$0.408 \to 0.603$	$0.569^{+0.016}_{-0.021}$	$0.412 \to 0.613$
	$\theta_{23}/^\circ$	$42.2^{+1.1}_{-0.9}$	$39.7 \to 51.0$	$49.0^{+1.0}_{-1.2}$	$39.9 \to 51.5$
	$\sin^2\theta_{13}$	$0.02225^{+0.00056}_{-0.00059}$	$0.02052 \to 0.02398$	$0.02223^{+0.00058}_{-0.00058}$	$0.02048 \to 0.02416$
	$\theta_{13}/^\circ$	$8.58^{+0.11}_{-0.11}$	$8.23 \to 8.91$	$8.57^{+0.11}_{-0.11}$	$8.23 \to 8.94$
	$\delta_{\mathrm{CP}}/^\circ$	232^{+36}_{-26}	$144 \to 350$	276^{+22}_{-29}	$194 \to 344$
	$\frac{\Delta m^2_{21}}{10^{-5}\ \mathrm{eV}^2}$	$7.41^{+0.21}_{-0.20}$	$6.82 \to 8.03$	$7.41^{+0.21}_{-0.20}$	$6.82 \to 8.03$
	$\frac{\Delta m^2_{3\ell}}{10^{-3}\ \mathrm{eV}^2}$	$+2.507^{+0.026}_{-0.027}$	$+2.427 \to +2.590$	$-2.486^{+0.025}_{-0.028}$	$-2.570 \to -2.406$

Table 2.2: Current best-fit values for the neutrino oscillation parameters from the Nu-Fit collaboration [19, 20]. $\Delta m^2_{3l} \equiv \Delta m^2_{31}$ for normal ordering, and $\Delta m^2_{3l} \equiv \Delta m^2_{32}$ for inverted ordering.

Chapter 3

Long-Baseline Neutrino Oscillation Experiments

In order to measure the PMNS matrix parameters, long-baseline neutrino experiments start with the creation of a beam of neutrinos, and then measure the neutrino flux at near and far detectors. By measuring the flux of neutrinos of specific flavors, the oscillation probability $P(\nu_\alpha \rightarrow \nu_\beta)$ can be determined through the difference in event rate at the near and far detectors, as a function of energy. A measurement of the oscillation probability provides a way to calculate the elements of the PMNS matrix. Currently, ongoing long-baseline neutrino experiments such as Tokai to Kamioka (T2K) [21] and NuMI Off-Axis electron neutrino Appearance (NOνA) [22] have set the precision on θ_{23}, Δm^2_{31}, and δ. It is expected that the next generation of neutrino experiments, which includes experiments like the Deep Underground Neutrino Experiment (DUNE) [23] and Hyper-Kamiokande [24], will determine the octant of θ_{23}, the mass hierarchy, and a value for δ. In order to accurately measure these parameters, long-baseline neutrino oscillation experiments are dependent on hadron production measurements, which will be discussed in Section 3.3

3.1 Accelerator-Based Neutrino Beams

3.1.1 Neutrino Beam Lines

The start of any conventional long-baseline neutrino oscillation experiment is the creation of the neutrino beam. Beginning with the extraction of a proton beam from an accelerator, the proton beam is then steered to a nuclear target, where hadronic interactions between the proton beam and the target nuclei produce a wide shower of hadrons, predominantly pions. Figure 3.1 shows the layout of the NuMI (Neutrinos at the Main Injector) beam line, located at Fermilab.

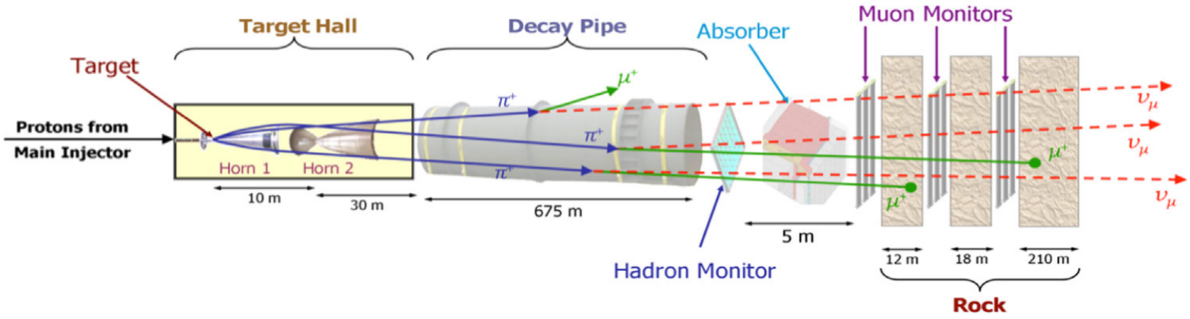

Figure 3.1: The schematic layout of the NuMI beam line [25].

The NuMI beam line uses a 120 GeV/c proton beam incident on an approximately one meter long graphite target; the T2K experiment has a 31 GeV/c proton beam on a 90 cm long graphite target. Graphite is chosen for its ability to withstand great beam intensities without changing shape significantly. Higher-Z materials would produce more hadrons, but they would also absorb too much of the beam energy; graphite still provides a high hadron yield. Other low-Z materials, like beryllium, are also commonly used. The length of the target is chosen so that each proton should inelastically interact roughly once while passing through; the DUNE experiment target will most likely be 150 cm long.

Once the proton beam has passed through the target, there is now a shower of hadrons in the target hall, including $\pi^{\pm}$, $K^{\pm}$, $p/\bar{p}$, K^0_L, Λ, and $\bar{\Lambda}$. (The NA61/SHINE experiment measures K^0_S instead of K^0_L, but a measurement of the K^0_S multiplicity can be used to estimate the K^0_L multiplicity; the physically produced states, K^0 and $\bar{K^0}$, are roughly equal mixtures of K^0_S and K^0_L, so measuring K^0_S multiplicity provides an estimate of K^0_L multiplicity.) Magnetic horns placed after the target then direct charged hadrons towards/away from the near detector. Since positively charged pions almost entirely decay to ν_μ, using the horns to steer positive hadrons towards the near detector will produce a neutrino beam, while focusing negative hadrons will produce an anti-neutrino beam. Typically, the horns are designed with the ability to reverse the current direction, which makes switching between neutrino and anti-neutrino beams fairly easy. After the particles have been focused by the magnetic horns, they enter the decay hall. The decay hall length is chosen so that the majority of the pions in the beam have decayed by the end of it, but the muons present in the beam are mostly undecayed.

At the end of the decay hall abosrbers capture the remaining muons and hadrons, and muon monitors help to indirectly monitor the direction and intensity of the neutrino beam. If the horns were focusing positively charged particles, the neutrino beam being sent to the near and far detectors is mostly ν_μ, with some small contamination of $\bar{\nu}_\mu$, ν_e, and $\bar{\nu}_e$. Table 3.1 shows the branching ratios of particles direclty and significantly contributing to the neutrino flux at long-baseline neutrino experiments.

Decay Product	Branching Ratio [%]
$\pi^+ \rightarrow \mu^+ + \nu_\mu$	> 99.9
$K^+ \rightarrow \mu^+ + \nu_\mu$	63.55
$K^+ \rightarrow \pi^0 + e^+ + \nu_e$	5.07
$K_L^0 \rightarrow \pi^\pm + e^\mp + \nu_e$	40.55
$K_L^0 \rightarrow \mu^\pm + \mu^\mp + \nu_e$	27.04
$\mu^+ \rightarrow e^+ + \nu_e + \bar{\nu}_\mu$	≈ 100

Table 3.1: Branching ratios of neutrino parent particles significantly contributing to the neutrino flux.

One final consideration in the creation of a neutrino beam is whether to have the detectors on- or off-axis. From the kinematics of the decays contributing to the neutrino flux, placing the detectors slightly off-axis from the neutrino beam results in a narrower flux peak as a function of neutrino energy, as shown in Figure 3.2. For the T2K experiment, running off-axis not only allows for selecting the neutrino energy to be near the oscillation maximum, but it also reduces background events from the higher energy tail [2]. DUNE is planned as an on-axis experiment to probe multiple oscillation peaks.

Typically, one of the leading uncertainties on the neutrino beam flux comes from imprecise modeling of proton interactions inside the target and other particle interactions with material in the beam hall. The importance of constraining this uncertainty through hadron production measurements will be discussed in Section 3.3.

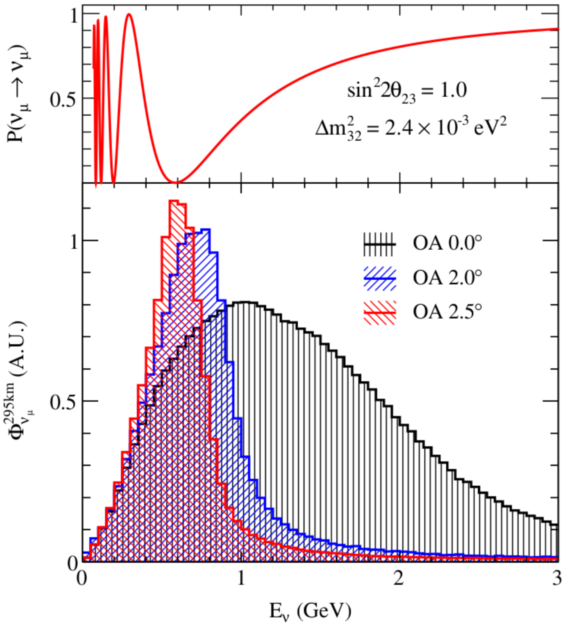

Figure 3.2: The predicted neutrino flux for the T2K experiment as a function of energy for three different off-axis angles [2]. T2K nominally uses 2.5°.

3.1.2 Near and Far Detectors

Once the neutrino beam has been produced, the next step is to measure the difference in the number of neutrinos, of a certain flavor, at the near and far detectors. Using DUNE as an example, the DUNE near detector is being built at Fermilab, while the far detector will be placed 1300 km away at the Sanford Underground Reasearch Facility in Lead, South Dakota; Figure 3.3 shows the DUNE baseline, and Figure 3.4 shows the neutrino distribution at the near detector for the T2K experiment in both neutrino mode and anti-neutrino mode.

For the near detector, the planned Phase II DUNE near-detector complex consists of three main components: a liquid argon detector (ND-LAr), a gaseous argon detector (ND-GAr), and a System for on-Axis Neutrino Detection (SAND) [27]. As the DUNE far detector is planned as a liquid-argon time-projection-chamber (TPC), ND-LAr will serve to measure neutrino interactions on the same target nuclei as the far detector. (As discussed later this section, it is difficult to

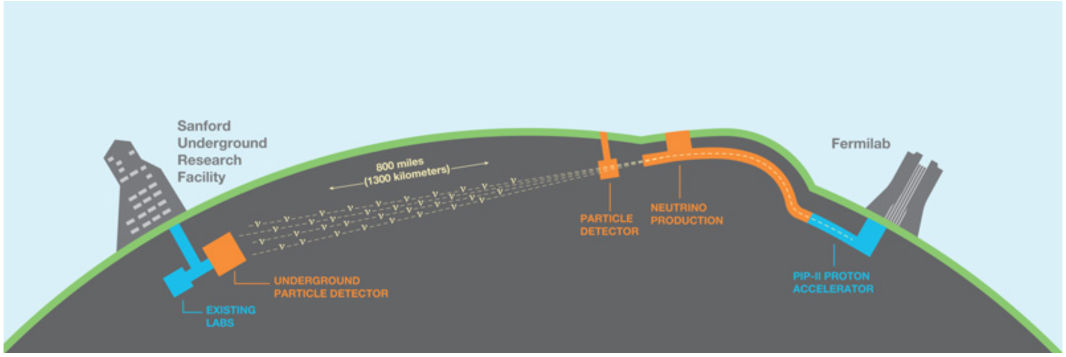

Figure 3.3: The DUNE baseline starts with the creation of the neutrino beam at Fermilab, where it passes through the near detector shortly after creation. After traversing through 1300 km of earth, the neutrino reaches the far detector, located in an underground mine in South Dakota [17].

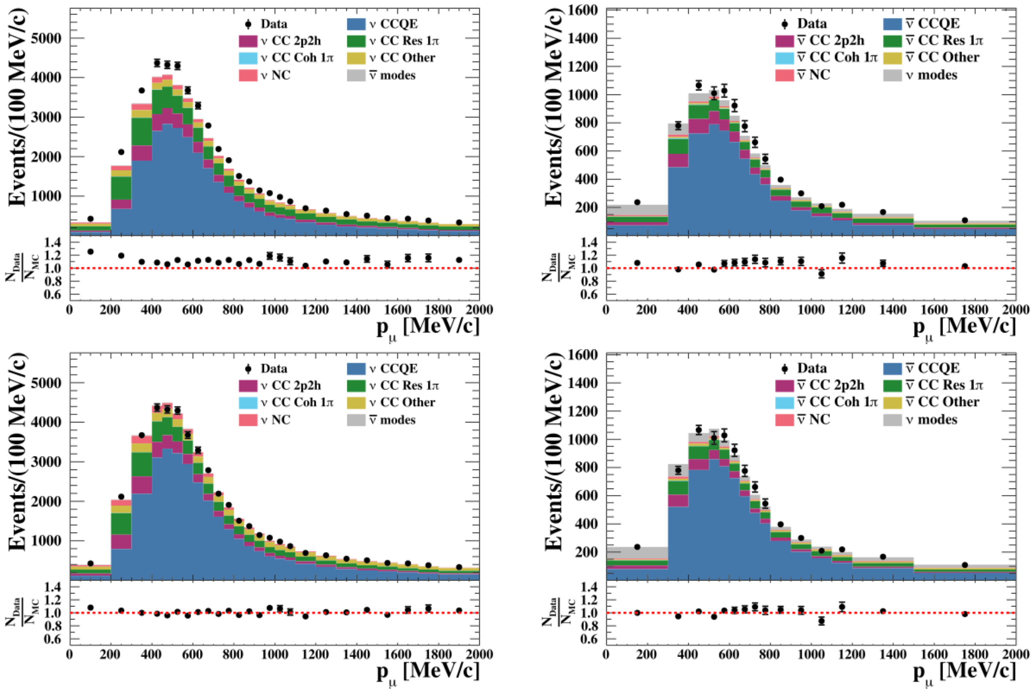

(a) FGD1 ν-mode ν_μ CC0π

(b) FGD2 $\overline{\nu}$-mode $\overline{\nu}_\mu$ CC0π

Figure 3.4: Comparisons of the predicted and measured event distributions for part of the T2K near detector as a function of the reconstructed muon candidate momentum [26]. Top Left: Neutrino mode before fitting the MC to the data. Bottom Left: Neutrino mode after fitting the MC to the data. Top Right: Anti-neutrino mode before fitting the MC to the data. Bottom Right: Anti-neutrino mode after fitting the MC to the data.

reconstruct neutrino interactions on nuclei. Using the same target material in the near and far detectors helps simplify this.) ND-GAr, a high-pressure, gaseous argon TPC surrounded by an electromagnetic calorimeter, will provide excellent tracking resolution and nearly uniform angle coverage for muons leaving ND-LAr. In addition, the expected neutrino beam intensity is so high pile-up in ND-LAr is expected, which means separate neutrino interactions occurring near the same time can look like one event; ND-GAr will help distinguish pile-up events. Finally, SAND will provide magnetized on-axis beam monitoring.

In addition to these three detectors, ND-LAr and ND-GAr will be able to move on and off-axis; this capability is known as DUNE Precision Reaction-Independent Spectrum Measurement (DUNE-PRISM). Taking data at a variety of off-axis angles will help deconvolve the neutrino flux and interaction cross section, as well as the reconstructed versus true energy response of the detector.

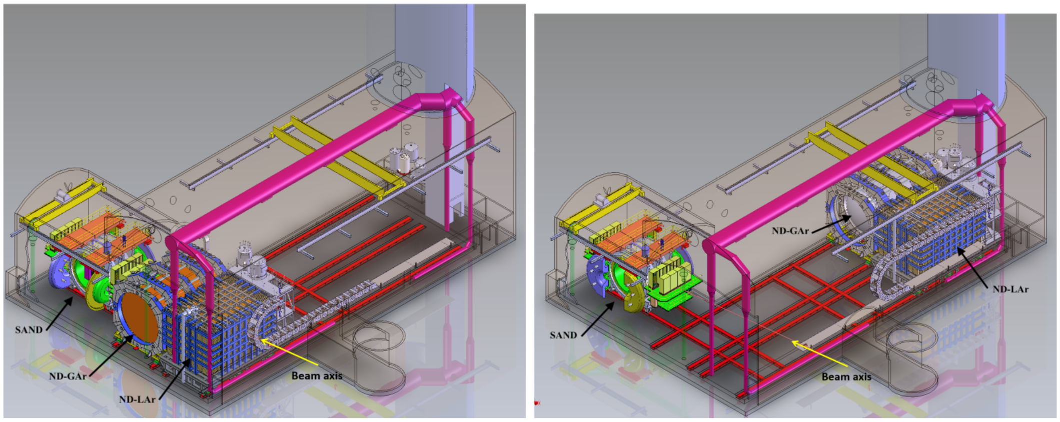

Figure 3.5: The planned DUNE near-detector complex [27].

The DUNE far detector is planned as four 10 kiloton liquid argon TPCs [28]. Typically neutrino detectors are built as large as possible, since the neutrino interaction rate is so small. (More than 99.99% of 1 GeV/c muon neutrinos will pass through the 1300 km of earth between the DUNE near and far detectors without interacting inelastically.)

Once the near and far detectors are in place and taking data, the next step is to measure the number of neutrinos N_{ν_α} of flavor α at each detector. In principle, this can be done with a measurement of the neutrino flux:

$$N_{\nu_\alpha}(E_{\nu_\alpha}) = \sigma(E_{\nu_\alpha})\Phi(E_{\nu_\alpha})\epsilon(E_{\nu_\alpha})P(E_{\nu_\alpha}). \tag{3.1}$$

All dependent on the energy of the neutrino, σ is the cross section, ϵ accounts for detector inefficiencies or other effects, and Φ is the measured flux, and P is the probability the neutrino has stayed as the flavor it started in. With the spectrum of measured neutrinos at the near and far detectors, $P(\nu_\alpha \rightarrow \nu_\beta)$ is known, and from that the PMNS matrix elements can be extracted. Figure 3.6 shows the neutrino event count at the far detector for the T2K experiment, comparing the measured number of neutrinos to the number expected, if there were no oscillations.

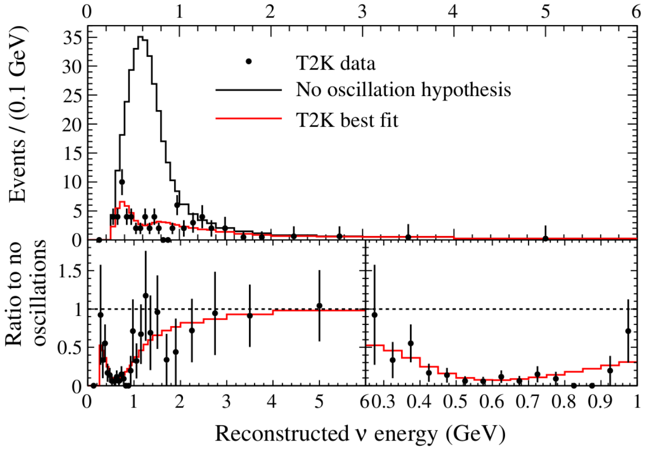

Figure 3.6: The number of measured ν_μ events at the T2K far detector, compared to the number expected [14].

Of course, the actual process of calculating neutrino events is not as simple as Equation 3.1 makes it seem. To begin with, tagging a neutrino interaction as ν_μ or ν_e for Equation 3.1 usually requires an outgoing lepton. A ν_μ interacting with a proton might use the channel $\nu_\mu + p \rightarrow \mu^- + p + \pi^+$; if the outgoing muon is identified correctly and the sign is known, then the event can be tagged as a ν_μ. However, neutrino detectors are quite large, and having a powerful enough magnetic field to measure the momentum and sign of the muon over the full detector fiducial volume is difficult. If a magnetic field cannot be used, then the capture or decay of the outgoing lepton can also be used for particle sign identification, but it requires good final state reconstruction.

$\nu_\mu + p \rightarrow \mu^- + p + \pi^+$ is known as charged-current interaction (CC), as there is an exchange of a W boson. Neutral current (NC) interactions are also possible, such as $\nu_e + e^- \rightarrow \nu_e + e^-$, and these are usually part of the background in long-baseline oscillation experiments.

Even with proper outgoing lepton tagging and reconstruction, when actually measuring neutrinos passing through a detector volume, the incident neutrino energy is still very difficult to reconstruct. In general there is a smearing applied that translates the true neutrino energy to the reconstructed neutrino energy.

$$N_{\nu,\ E_{meas}} = \int U(E_{\nu,\ true},\ E_{\nu,\ meas}) \frac{d\sigma(E_{\nu,\ meas}, E_{\nu,\ true})}{dE_{\nu,\ true}} \Phi(E_{\nu,\ true}) \epsilon(E_{\nu,\ true}) P(E_{\nu,\ true}) dE_{\nu,\ true}. \tag{3.2}$$

This smearing, represented by U, results from a variety of factors. The Fermi motion of the nucleons and the nuclear binding energy complicates reconstructing the neutrino energy; in addition, tracking and reconstructing produced neutrons is a difficult task, and many detectors do not have this capability. As the hadrons exit the nucleus, they do not exit cleanly, and there are final state interactions that distort the kinematics and change the final state topology.

If this was not problematic enough, the neutrino cross sections are another complicating factor in Equation 3.2. Typically, the types of neutrino interactions occurring are classified into three broad types of interactions: quasi-elastic scattering from a neutrino-nucleon interaction, resonant pion production from the neutrino exciting a nucleon, and deep inelastic scattering from a neutrino interacting with a quark. Figure 3.7 shows diagrams of these interactions [29].

Even the simplest of these interactions, the quasi-elastic scattering of a neutrino off of a nucleon, is difficult to calculate exactly. Skipping over the exact details, calculating this cross section requires the introduction of hadronic current form factors, which have to be informed through experiment. Resonant pion production is more complicated, as there are multiple resonances that can lead to pion production, and each possible contribution has interference terms. For deep-inelastic scattering, where the neutrino is resolving the internal structure of a nucleon, the high-

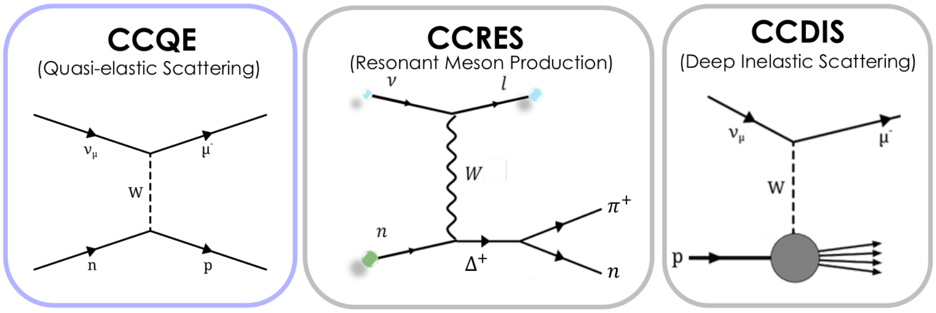

Figure 3.7: Examples of possible neutrino interactions occuring at the near and far detectors [29].

energy, inclusive cross section is reasonably well understood. However, at low-energy transfer, QCD becomes non-perturbative and the cross section becomes very difficult to calculate.

Another complication is that the near detector sees an extended line source for the neutrino beam, while the far detector sees a point source; this reults in the fluxes and energy spectra being different betweeen the near and far detectors.

As a result of all of these complications, long-baseline neutrino oscillation experiments rely on accurate neutrino flux predictions to aid in their event reconstruction. As the hadronic processes between protons and the target nucleons are not well modeled, there is a large amount of uncertainty in the predicted neutrino flux. Experiments like NA61/SHINE are capable of taking hadron production measurements using the same beam and target material as the long-baseline oscillation experiments. The oscillation experiments can then tune their flux predictions based on NA61/SHINE's measurements, and this significantly reduces their uncertainties. (Section 3.3 will discuss this in more detail.)

3.2 Neutrino Beam Flux Simulation

In the prediction of neutrino flux at long-baseline oscillation experiments, there are four main steps. The first step is the accurate modeling of all of the components in the beam line, including the target and its supports, the magnetic horns, and any other material present that particles can interact with. Once the components are in place, the second step is to propagate the proton beam through the target. Dedicated hadronic cascade simulation models, such as those included in the FLUKA and GEANT4 particle transport packages, are typically used to model the initial hadronic interaction [30, 31]. (More details on the specific simulation packages used by long-baseline neutrino oscillation experiments will be described later in this section.) In the third step, any produced particles, and the beam proton if it still exists, are propagated through the rest of the target hall. The produced particles and the beam proton can reinteract inside the target, as well as with any of the material inside the beam hall; these are known as secondary and tertiary interactions. All of the particles are then propagated until they either decay or are captured by absorbers, and now there is a simulated neutrino beam with some predicted flux.

As will be shown in Chapters 8, 9, and 10, models can be quite inaccurate in predicting hadron production in this situation. To account for this, the fourth and final step of the neutrino beam simulation is reweighting the neutrino flux with hadron production measurements taken by experiments like NA61/SHINE. Based on the neutrino's parent particle's momentum and species, a weight of

$$w_s = \frac{m_s(p,\theta)_{data}}{m_s(p,\theta)_{MC}}, \tag{3.3}$$

is applied, where m_s is the multiplicity of hadron species s, in the momentum bin defined by the particle's total momentum p and angle θ. (See Chapter 8 for an explanation of the binning.) Equation 3.3 is known as thin-target reweighting, as the data comes from hadron production measurements with thin targets ($\sim 3\%$ of the interaction length) made from the same material as the oscillation experiment's target. A thin target measurement analyzes the multiplicity of particles produced from the interaction between a proton and a single atomic nucleus; thin target measurements benefit from being a basic physics measurement, and are more generally applicable than replica target measurements, described in the next paragraph.

NA61/SHINE also takes measurements using replica targets where hadron production is measured using a replica of the target from the neutrino beam line. The replica-target reweighting is especially useful as it eliminates the need to simulate reinteractions inside the target; here the hadrons are also binned in terms of their exit point from the target z:

$$w_s = \frac{m_s(p,\theta,z)_{data}}{m_s(p,\theta,z)_{MC}}. \tag{3.4}$$

The dataset being analyzed for this thesis uses a thin carbon target. NA61/SHINE plans to take DUNE replica target data during the summer of 2024.

To expand on the details of the long-baseline neutrino oscillation flux predictions a little more, the NuMI beam line specifically uses the G4NuMI simulation package, which uses GEANT4-FTFP_BERT for their modeling of the neutrino beam line [1]. (GEANT4's physics lists, like FTFP_BERT, will be explained in Section 5.2.2; inside GEANT4 there are a variety of different physics lists available, which can act as independent MC simulations.) The simulation accounts for all particles and propagation in the beam line up to the decay into a neutrino beam. NuMI uses a 120 GeV/c beam incident on carbon, and hadron production measurements by NA61 for 120 GeV/c proton-carbon interactions were not available until recently [32]. To work around this, NuMI uses FLUKA simulations to scale 158 GeV/c NA49 data down to their desired momentum. (Even with data at their beam momentum, secondary and tertiary interactions would necessitate momentum scaling.)

The T2K experiment's simluation package, JNUBEAM, uses FLUKA to simulate the intitial hadronic interactions in the target and baffle [2]. Then, the produced particles from the primary interaction are passed to a GEANT3 simulation for propagation, reinteractions, and decay; later hadronic interactions are modeled by GCALOR. (T2K plans to move to GEANT4 in the near future.) Figure 3.8 shows the difference between the simulation's predicted multiplicity in thin targets at the T2K energy and experimental thin target data from NA61; the differences are quite large, exceeding 50% in certain regions of phase space.

DUNE's simulation package, G4LBNF, currently uses GEANT4-QGSP_BERT for their neutrino flux predictions [33]. (The GEANT4 physics lists will be described in more detail in Section

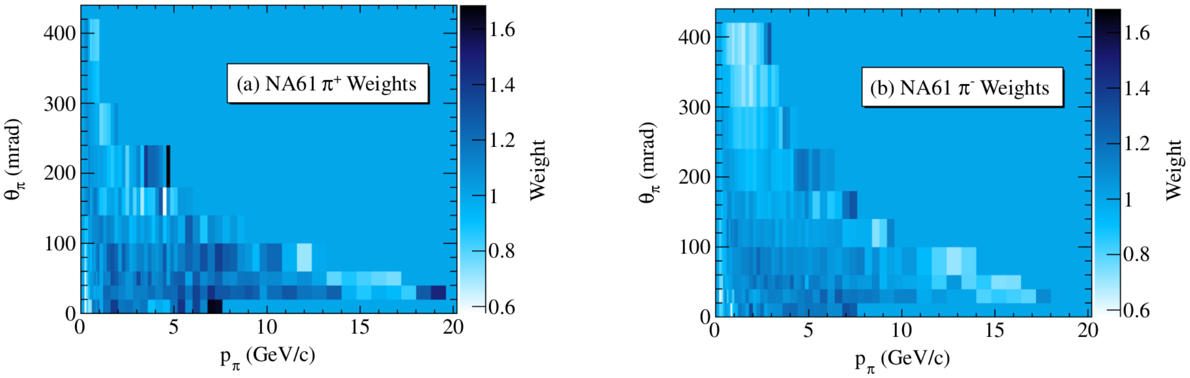

(a)

(b)

Figure 3.8: The differential production weights used by T2K in their neutrino beam flux simulation [2]. Left: π^+. Right: π^-.

5.2.2.) Figure 3.9 shows the predicted neutrino flux for the DUNE far detector.

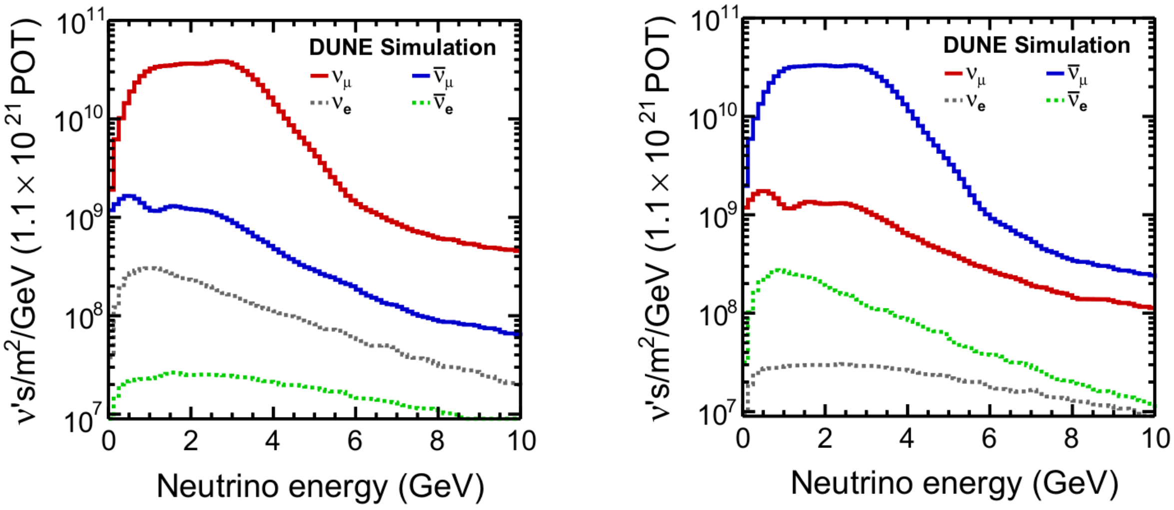

(a)

(b)

Figure 3.9: Left: The predicted neutrino flux for the DUNE far detector, running in neutrino mode. Right: The predicted neutrino flux for the DUNE far detector, running in anti-neutrino mode [34].

In order to align with the methods used by the long-baseline neutrino oscillation experiments, a neutrino analysis in NA61/SHINE uses GEANT4 for all parts of the simulations; see Section 5.2.2 for more details on the MC simulations used by NA61/SHINE.

3.3 Hadron Production Measurements and Their Applications

As mentioned in the previous section, long-baseline neutrino oscillation experiments incorporate hadron production measurements to improve their neutrino beam flux predictions; reweighting their simulations with experimental data significantly reduces the uncertainties in the predicted neutrino beam flux. Figure 3.10 shows the neutrino beam flux uncertainty from the T2K experiment, which has been significantly reduced with thin and replica-target measurements taken by NA61/SHINE.

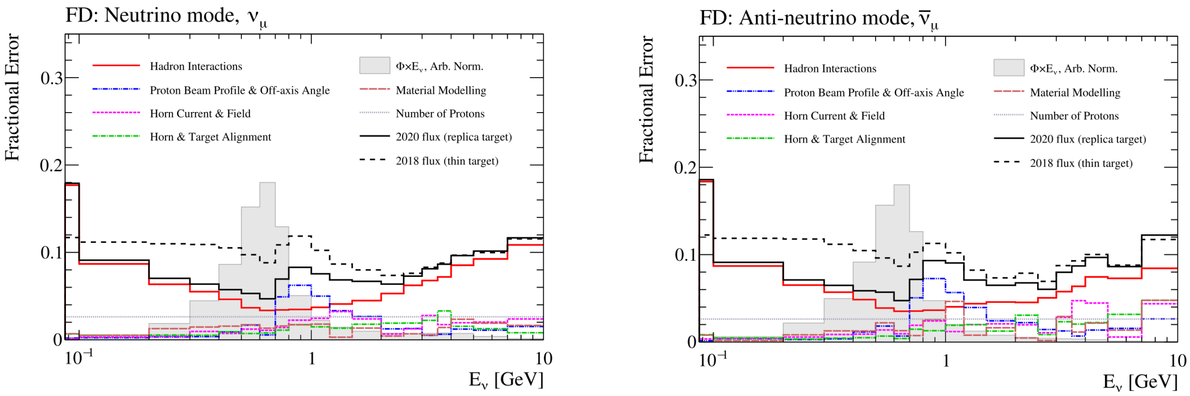

(a) (b)

Figure 3.10: Left: The flux uncertainty for ν_μ at the T2K far detector. Right: $\bar{\nu}_\mu$ [35].

In order for the next generation of neutrino oscillation experiments to reach their desired physics goals, it is absolutely critical for all of the uncertainties to be reduced as significantly as possible. To illustrate this, Figure 3.11 shows the drastic changes in DUNE's expected CP-violating phase sensitivity from small uncertainty changes. Typically one of the leading contributions to the uncertainty comes from modeling hadron production during the prediction of the neutrino beam flux; this can be seen from the red line in Figure 3.10, which represents uncertainty stemming from hadron interactions.

To help lower the neutrino flux uncertainties by providing the necessary hadron production measurements, the NA61/SHINE facility is capable of running with protons, $\pi^{\pm}$, and $K^{\pm}$ in the momentum range of $13 - 350$ GeV/c, on thin and replica targets. Before NA61/SHINE, there was

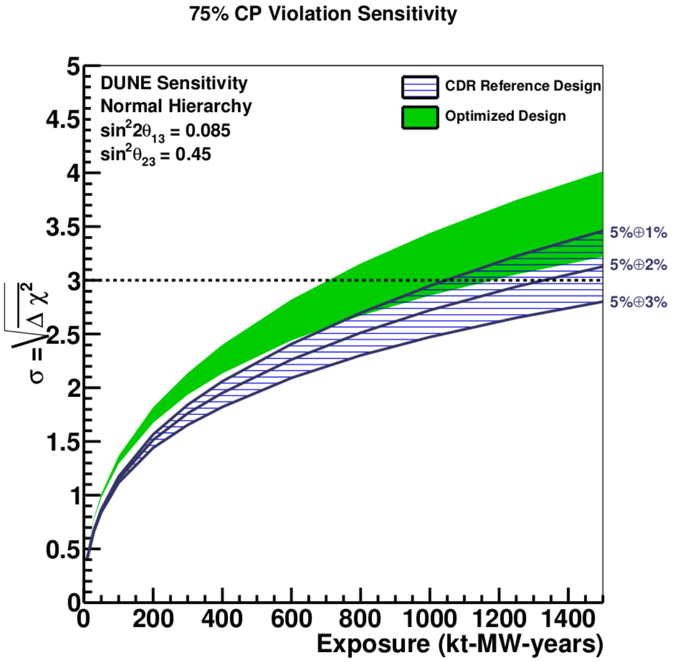

Figure 3.11: DUNE's CP-violating phase sensitivity covering 75% of the possible values for δ [36]. The 5% refers to the absolute ν_μ uncertainty, and each curve then varies the ν_e samples uncertainty.

a wide variety of existing data on hadron production measurements, with many examples given in the following list:

- 8.9 GeV/c proton-beryllium [37]
- 6.4, 12.3, and 17.5 GeV/c proton-beryllium [38]
- 12 GeV/c proton-carbon and pion-carbon [39]
- 12.9 GeV/c proton-aluminum [40]
- 19.2 GeVc proton-proton, proton-beryllium, proton-aluminum, proton-copper, and proton-lead [41]
- 24 GeV/c proton-beryllium, proton-aluminum, proton-copper, and proton-lead [42]
- 158 GeV/c proton-carbon [43]

- 200 GeV/c proton-beryllium [44]
- 300 GeV/c proton-beryllium [45]
- 450 GeV/c proton-beryllium [46]

However, there was a lack of data in momentum region between 24 GeV/c and 158 GeV/c, which is especially crucial for long-baseline neutrino experiments, as these experiments operate in this region. (T2K uses 31 GeV/c protons, NOvA uses 120 GeV/c protons, and DUNE will probably use 120 GeV/c protons). Secondary and tertiary reinteractions occurring in this momentum region also need to be covered by hadron production measurements; Figure 3.12 shows the grandparents of ν_μ and ν_e in the NuMI beam line, and it shows that less than half of the predicted neutrino flux comes from the primary proton interacting inside the target.

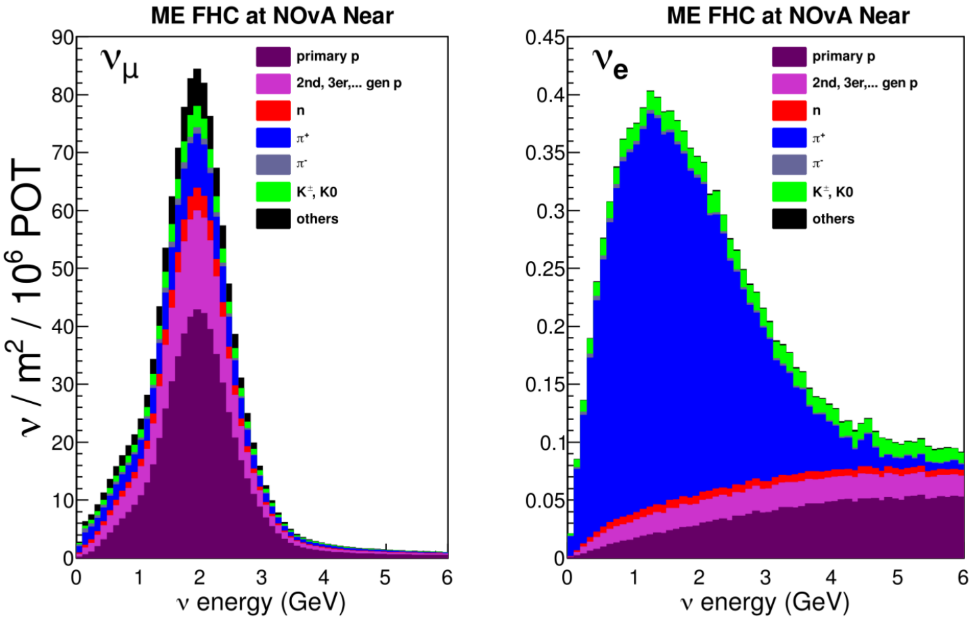

Figure 3.12: NuMI ν_e and ν_μ grandparents [47].

Due to the large gap in momentum coverage in existing hadron production measurements, NA61/SHINE has been systematically measuring interactions in this gap with a variety of beam particles and target materials. Table 3.2 shows the existing NA61/SHINE hadron production datasets and their analysis status. The recent analysis of the p+C@120 GeV/c dataset helps to fill in the large gap in analyzed data [48], and the 90 GeV/c dataset will expand on this coverage.

Dataset	Measurements	Status
p+C@31 GeV/c	$\pi^{\pm}, K^{\pm}, p/\bar{p}, K^0_S, \Lambda, \bar{\Lambda}, \sigma_{\text{prod}}, \sigma_{\text{inel}}$	Finished [49]
p+T2K Replica Target@31 GeV/c	$\pi^{\pm}, K^{\pm}, \sigma_{\text{prod}}, \sigma_{\text{inel}}$	Finished [50]
p+C@60 GeV/c	$\sigma_{\text{prod}}, \sigma_{\text{inel}}$	Finished [51]
p+Be@60 GeV/c	$\sigma_{\text{prod}}, \sigma_{\text{inel}}$	Finished [51]
p+Al@60 GeV/c	$\sigma_{\text{prod}}, \sigma_{\text{inel}}$	Finished [51]
π^++C@60 GeV/c	$\pi^{\pm}, K^{\pm}, p/\bar{p}, K^0_S, \Lambda, \bar{\Lambda}, \sigma_{\text{prod}}, \sigma_{\text{inel}}$	Finished [52]
π^++Be@60 GeV/c	$\pi^{\pm}, K^{\pm}, p/\bar{p}, K^0_S, \Lambda, \bar{\Lambda}, \sigma_{\text{prod}}, \sigma_{\text{inel}}$	Finished [52]
p+Al@60 GeV/c	$\sigma_{\text{prod}}, \sigma_{\text{inel}}$	Finished [52]
p+C@90 GeV/c	$\pi^{\pm}, K^{\pm}, p/\bar{p}, K^0_S, \Lambda, \bar{\Lambda}, \sigma_{\text{prod}}, \sigma_{\text{inel}}$	This thesis
p+Be@120 GeV/c	$\sigma_{\text{prod}}, \sigma_{\text{inel}}$	Finished [51]
p+C@120 GeV/c	$\pi^{\pm}, K^{\pm}, p/\bar{p}, K^0_S, \Lambda, \bar{\Lambda}, \sigma_{\text{prod}}, \sigma_{\text{inel}}$	Finished [32, 53]
p+NuMI Replica Target@120 GeV/c	$\pi^{\pm}, K^{\pm}, p/\bar{p}, K^0_S, \Lambda, \bar{\Lambda}, \sigma_{\text{prod}}, \sigma_{\text{inel}}$	Ongoing
2022 p+T2K Replica Target@31 GeV/c	$\pi^{\pm}, K^{\pm}, p/\bar{p}, K^0_S, \Lambda, \bar{\lambda}, \sigma_{\text{prod}}, \sigma_{\text{inel}}$	Ongoing
2023 K^++C@60 GeV/c	$\pi^{\pm}, K^{\pm}, p/\bar{p}, K^0_S, \Lambda, \bar{\Lambda}, \sigma_{\text{prod}}, \sigma_{\text{inel}}$	Not started
2023 p+Ti@31 GeV/c	$\pi^{\pm}, K^{\pm}, p/\bar{p}, K^0_S, \Lambda, \bar{\Lambda}, \sigma_{\text{prod}}, \sigma_{\text{inel}}$	Not Started
2023 π^++Ti@60 GeV/c	$\sigma_{\text{prod}}, \sigma_{\text{inel}}$	Not Started
2023 K^++Ti@60 GeV/c	$\sigma_{\text{prod}}, \sigma_{\text{inel}}$	Not Started

Table 3.2: Datasets and their analysis status taken by the NA61/SHINE experiment. The datasets labelled 2022 and 2023 come from after the NA61/SHINE hardware upgrade, and they have drastically increased statistics compared to datasets taken before the upgrade. For example, the old T2K replica target data has a total of ~10 million interaction triggers; the more recent 2022 replica target dataset has ~170 million.

It is also important to note the DUNE beam momentum has not yet been finalized. The planned beam momentum could be anywhere from 60 GeV/c to 120 GeV/c, meaning the primary interaction could be 90 GeV/c protons on carbon; even if the 120 GeV/c beam is used, as shown in Figure 3.12, interactions of lower energy protons and other produced hadrons are important to measure due to reinteractions. Hence the relevance of the dataset analyzed for this thesis.

Finally, neutrino flux predictions also typically rely on momentum scaling of hadron production results, as the current data does not cover their full phase space. (For example, proton-carbon interaction at 120 GeV/c results can be scaled down to proton-carbon interactions at 15 GeV/c.)

Momentum scaling relies on simulation packages like GEANT4, or theoretical, empirically informed formulas like in Bonesini *et al.* [3]. Chapter 10 will briefly compare the results of proton-carbon interactions at 120 GeV/c scaled to the results of this thesis, proton-carbon interactions at 90 GeV/c.

Chapter 4

NA61/SHINE Experiment

The NA61/SHINE (61^{st} experiment in the North Area at CERN/Super-Proton-Synchrotron Heavy Ion and Neutrino Experiment) experiment is a fixed-target, large-acceptance hadron spectrometer. Mainly comprising TPCs, the TPCs provide 3-dimensional tracking as particles pass through them; the tracking in conjunction with the vertex magnets enables momentum and charge sign measurements. The TPCs also measure energy loss, which can be used with the momentum measurement to identify particle types. (See Section 5.2.1.5 for a description of the energy loss measurement.) For identifying low-momentum particle species, NA61/SHINE has three time-of-flight walls, the Time-of-Flight-Forward, Left, and Right walls. Before the target, there are a variety of beam-position detectors, Cherenkov detectors, and scintillators; these provide measurements of the incoming beam particle and inform the triggering system. In addition, there is the projectile-spectator-detector (PSD), a forward hadronic calorimeter used by the heavy ion program in nucleus-nucleus interactions. Figure 4.1 shows the 2017 layout of the NA61/SHINE detector [54].

4.1 NA61/SHINE Physics Programs

As the name implies, NA61/SHINE is capable of more than just hadron production measurements for long-baseline neutrino oscillation experiments. The largest component of NA61/SHINE is actually the nuclear/heavy ion program, which has two main goals. First, it studies the properties of the onset of deconfinement, which is the phase transition between hadron gas and quark-gluon plasma. Second, in terms of the baryon chemical potential and temperature, it is a long-standing

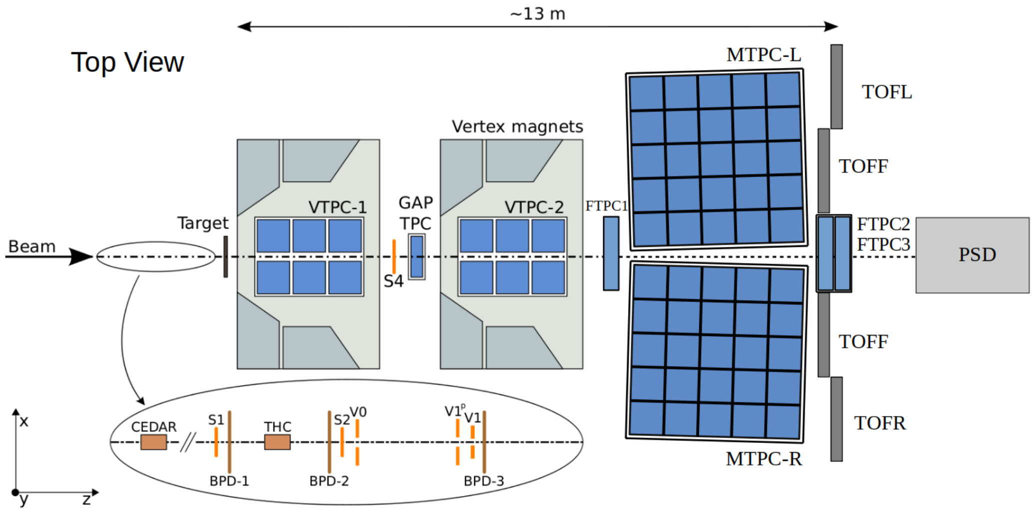

Figure 4.1: Top view of the NA61/SHINE detector layout from 2017 [54]. The origin of the NA61/SHINE coordinate system is near the center of the GTPC, and thin targets are typically placed at $\sim (0, 0, -580)$ cm.

question whether a critical point exists; the heavy ion program at NA61/SHINE aims to provide experimental evidence towards the existence and location of a critical point [55, 56]. To achieve these goals, NA61/SHINE probes various regions of the phase diagram with measurements of varying beam and nuclei (p+p, p+Pb, Be+Be, Ar+Sc, Xe+La, Pb+Pb) in a wide range of beam momenta (13A-158A GeV/c). By varying the energy and system size, it is expected for fluctuations due to the phase transition of strongly interacting manner to occur, and these fluctuations would provide insight into the properties of deconfinement and the existence of a critical point.

NA61/SHINE also has a dedicated cosmic ray physics program. For the cosmic ray program, NA61/SHINE aids simulations of cosmic ray showers for cosmic ray observatories, in a similar manner to how the neutrino program aids long-baseline neutrino oscillation experiments. Already, datasets of π^- incident on thin carbon targets at 158 GeV/c and 350 GeV/c have been taken and analyzed; more recently nuclear fragmentation measurements were taken [57]. The cosmic ray program also studies anti-deuteron production for the AMS and GAPS experiments [58, 59].

Lastly, there is the neutrino physics program, which studies interactions important for long-baseline neutrino oscillation experiments, like NOνA, DUNE, and T2K. The 90 GeV/c proton-carbon dataset taken in 2017 for the neutrino program is the focus of this thesis.

4.2 Beam Line

NA61/SHINE receives its beam from the SPS, where the H2 beam line extracts beams from the SPS and delivers them to the North Area at CERN. Depending on whether a proton or ion beam is desired as the input to the H2, a different path for the pre-injector chain to the Proton-Synchrotron is used. As can be seen in Figure 4.2, the proton beam starts before the LINAC2; generated from hydrogen gas with a duo-plasmatron ion source, the protons are then sent through a quadrupole (Radio-Frequency Quadrupole RFQ2), which bunches and focuses the beam. After the beam is bunched, it enters the LINAC2, an Alvarez drift tube linear accelerator.

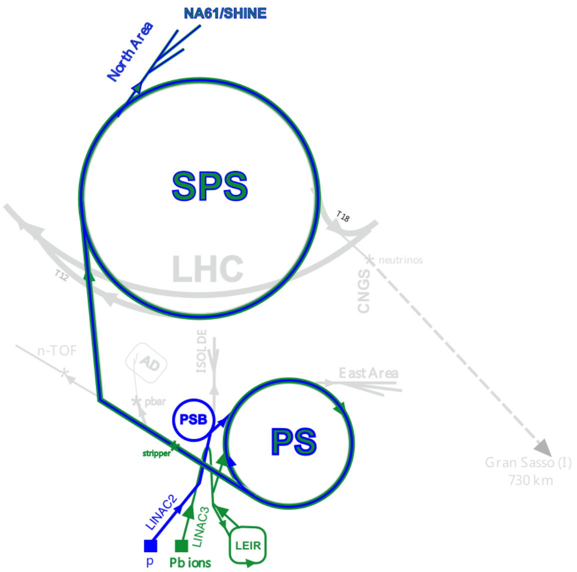

Figure 4.2: The SPS accelerator chain [54]. The location of NA61/SHINE can be seen at the top of the SPS ring.

Once the proton beam has passed through the LINAC2, it is then distributed to the Proton-Synchrotron-Booster (PSB), a system of four rings that accumulate the proton beam and increase its luminosity. After the PSB, the protons enter the PS; the PS has a circumference of 628 meters and accelerates the beam up to 14 GeV/c. The final stage for the proton beam before extraction to the H2 beam line is the SPS, which has a circumference approximately 11 times larger than the PS. The SPS accelerates the beam up to 400 GeV/c, and the beam is then de-bunched and extracted over the course of several seconds.

The production of an ion beam is similar, but follows a different trajectory into the PS. Using a lead beam as an example, ^{208}Pb is inserted into a crucible along with oxygen gas. While the crucible is heated, microwaves accelerate electrons to form an oxygen plasma, which ionizes the heated lead vapor. The ionized lead beam is then extracted, and then a 135° spectrometer specifically selects Pb29+. The lead ions missing 29 electrons then enter LINAC3, which accelerates the beam before sending it through a carbon foil that strips more electrons off of the lead ions. Another spectrometer selects Pb54+, and this beam is then directed to the PS. Before exiting the PS and entering the SPS, the beam goes through a final stripping stage of aluminum foil, which ionizes the beam to Pb82+.

After the SPS comes the H2 beam line, which directs proton and ion beams towards the North Area. The start of the H2 beam line, the T2 target station, consists of a variety of beryllium plates of different lengths. These beryllium plates are used to produce the desired beam particle being sent to the NA61/SHINE experiment; dependent on the desired secondary particle type and energy, the target type is used in conjunction with a set of upstream dipole magnets to optimize the produced particles' momentum and type. After the T2 target station, collimators and dipole magnets allow for momentum (technically rigidity p/q, momentum over charge) selection. Figure 4.3 shows the schematic of the H2 beam line.

4.3 Beam Detectors and Triggering

Once the beam has been produced and sent towards the NA61/SHINE detector, the first step is to measure the beam position before it hits NA61/SHINE's target, along with a positive identification signal of the beam particle. Figure 4.4 shows the triggering layout used for the thin target 90 GeV/c proton-carbon dataset.

The start of the triggering system is the Cherenkov Differential Counter with Achromatic Ring

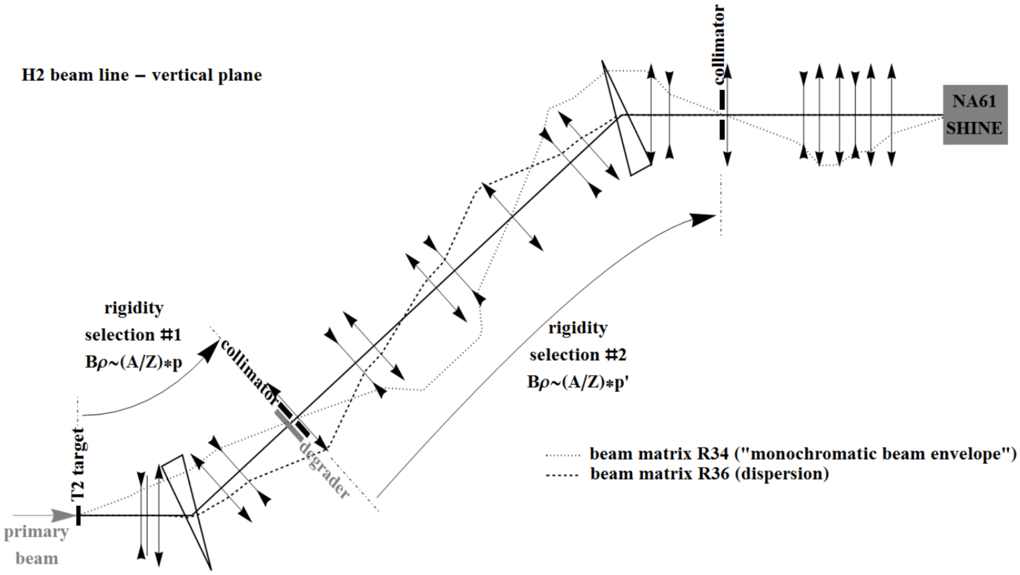

Figure 4.3: The H2 beam line [54]. The lines with arrows represent focusing quadrupole magnets, and the wedges represent the two dipole magnets used for momentum selection.

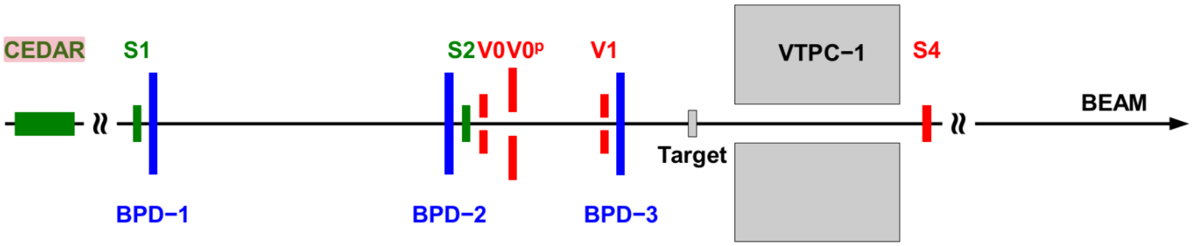

Figure 4.4: Beam-position detector (BPD) and triggering layout for thin targets in 2017 [54]. The positive trigger components are in green, while the negative trigger components are in red.

Focus (CEDAR) [60]. The CEDAR is filled with helium for high beam momenta (> 60 GeV/c) and nitrogen for low momenta. As particles pass through the CEDAR, they emit Cherenkov radiation, and the photons are collected into a diaphragm with eight PMTs inside. By tuning the gas pressure and the diaphragm opening inside the CEDAR, only photons from specific particle species will pass through, which allows for positive tagging of wanted particles.

Once the beam particles have been positively identified, they enter the region with the beam-position detectors (BPDs) and scintillation triggers. Stationed at three known locations in z (from Figure 4.1, z is the beam traversal direction), the BPDs measure the (x, y) coordinates of the beam before it hits the NA61/SHINE target. Constructed in 2009, the BPDs used in 2017 were proportional wire chambers operated with an Ar/CO_2 gas mixture. The schematic of the BPDs along with a sample signal is shown in Figure 4.5. Events without a well measured BPD track or a BPD track that misses the target are discarded from analyses; this will be discussed in more detail in Chapter 8.

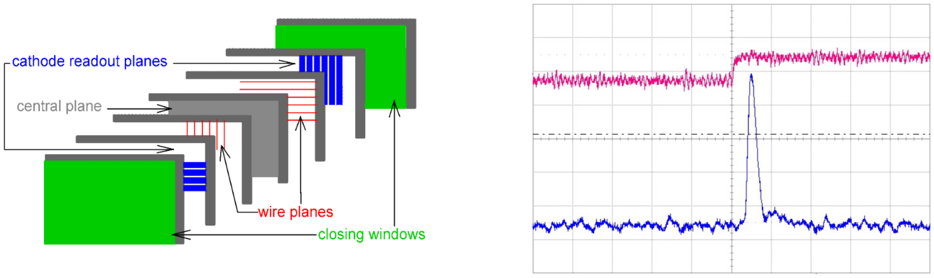

Figure 4.5: The left image shows the schematic layout of one of the BPDs, while the image on the right shows a sample pre-amplifier (upper) and output (lower) signal. Each division on the x-axis corresponds to 500 ns [54].

In coordination with the positive identification signal from the CEDAR, signals from the S1, S2, V0, $V0^{\mathrm{p}}$, V1, and S4 scintillators are used to define the trigger logic of the NA61/SHINE data-acquisition system (DAQ). Since the BPD track reconstruction requires calibration and slow software reconstruction, the scintillators provide a fast triggering signal used during the data taking. The S1 is a 6×6 cm scintillator equipped with four PMTs, and the S2 is a circular scintillator equipped with one PMT with a radius of 1.4 cm. The V0, $\mathrm{V0^p}$, and V1 veto scintillators have holes of 1 cm, 2 cm, and 0.8 cm, respectively, and the S4 scintillator, which has a diameter of 2 cm, is placed about 300 cm downstream of the target. For thin-target data there are four main trigger labels:

- T1 (identified beam particle): $\mathrm{CEDAR} \cdot \mathrm{S1} \cdot \mathrm{S2} \cdot \overline{\mathrm{V0}} \cdot \overline{\mathrm{V0}^{\mathrm{p}}} \cdot \overline{\mathrm{V1}}$
- T2 (identified beam particle interaction): $\mathrm{CEDAR} \cdot \mathrm{S1} \cdot \mathrm{S2} \cdot \overline{\mathrm{V0}} \cdot \overline{\mathrm{V0}^{\mathrm{p}}} \cdot \overline{\mathrm{V1}} \cdot \overline{\mathrm{S4}}$
- T3 (unidentified beam particle): $\mathrm{S1} \cdot \mathrm{S2} \cdot \overline{\mathrm{V0}} \cdot \overline{\mathrm{V0}^{\mathrm{p}}} \cdot \overline{\mathrm{V1}}$
- T4 (unidentified beam particle interaction): $\mathrm{S1} \cdot \mathrm{S2} \cdot \overline{\mathrm{V0}} \cdot \overline{\mathrm{V0}^{\mathrm{p}}} \cdot \overline{\mathrm{V1}} \cdot \overline{\mathrm{S4}}$

As an example, the T2 trigger label means the CEDAR positively identified the beam particle (proton for proton-carbon interactions at 90 GeV/c), followed by a positive signal from the S1 and S2; a positive signal from the S1 means a particle passed through it, and its scintillation light was detected by the attached PMTs and readout electronics. After the S2, the veto scintillators ensure the beam particle is on a trajectory to hit the target, and that there is no attached beam halo. Finally, the S4 is placed where the beam particle would propagate to if there was no significant interaction beteen the beam particle and the target. So, an event with positive signals from the CEDAR, S1, and S2 and negative signals from the V0, $\mathrm{V0^p}$, V1, and S4 most likely means the desired beam particle interacted with the target, and there was no corresponding beam halo attached to the event. Of course, the trigger labelling is not perfect, and corrections need to be made, as will be discussed in Chapter 8.

Only events labelled as either T1, T2, T3, or T4 are saved by the DAQ. All other events are discared. In addition, the primary trigger of interest is the T2 trigger, so the triggers are prescaled; this means that all T2 triggers are kept, while only a small, unbiased portion of the T1, T3, and T4 triggers are saved by the DAQ.

Lastly, there is also a waveform-analyzer (WFA) attached to the S1 scintillator. The WFA analyzes the timing of S1 signals to allow for the selection of a beam particle well separated in time from any other particle coming down the beam line.

4.4 Targets

Mentioned previously in Chapter 3, NA61/SHINE is capable of running with both thin and replica targets. The dataset analyzed for this thesis used a 1.48 cm long carbon target with a measured density of 1.80 ± 0.01 g/cm^3, and it is shown in Figure 4.6. Figure 4.7 shows the NuMI replica target.

Figure 4.6: The thin carbon target used in the 90 GeV/c proton-carbon dataset analyzed for this thesis.

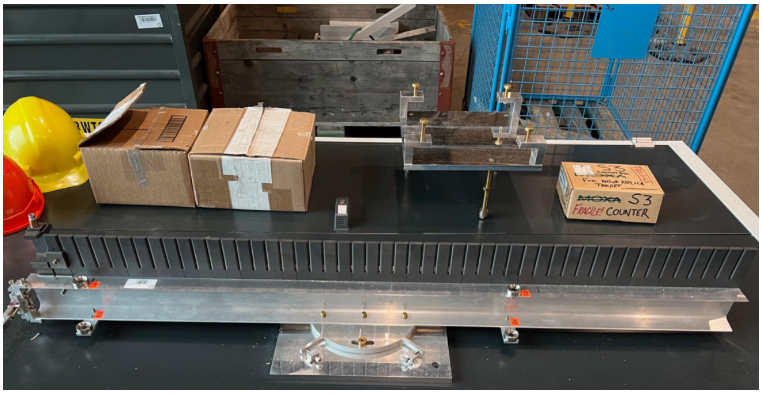

Figure 4.7: The 125 cm long NuMI replica target.

4.5 Time Projection Chambers

As mentioned earlier, the main components of the NA61/SHINE detector are the TPCs. Vertex TPC 1 and 2 and the Gap TPC are placed inside the magnetic field generated from the two vertex magnets in order to provide a momentum and charge sign measurement. After the VTPCs and the GTPC are the Main TPCs, which are the largest TPCs in the experiment. The three

Forward TPCs sit in the beam line, and are only used for the neutrino physics program; they would be overwhelmed during heavy ion collisions.

All of the TPCs consist of a large Ar/CO$_2$ gas volume in which charged particles leave ionization trails (electrons and their ionized partner) as they pass through. Surrounding the gas volume is a field cage made of aluminized Mylar strips connected by a resistor chain. The field cage is supplied with a voltage on the order of 10 kV, which creates a uniform electric field in the body of the TPC. In the presence of the electric field the electrons drift toward the cathode plane, travelling at a drift velocity dependent on the electric field, the gas composition, and the gas pressure. The electrons drift up in each TPC, except for FTPC2, where the drift direction is down. Figure 4.8 shows a basic schematic of the GTPC, and all of the other TPC designs are similar.

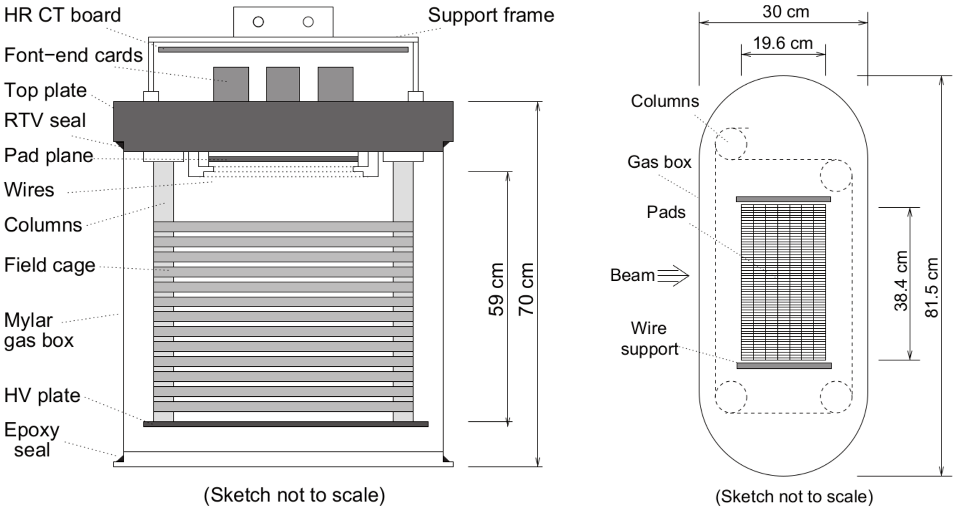

Figure 4.8: Schematic layout of the GTPC [54]. The left view shows the beam view, and the right view is a top view of the detector.

At the top in y (bottom for FTPC2) of the TPCs is the pad plane, a finely segmented metal plane where each pad is connected to one channel of the readout electronics. As the electrons near the pad plane, there are three sets of wires used to create the signal sent through the pad planes to the readout electronics; Figure 4.9 shows the general principle behind the three sets of wires and the pad plane. The first set, the gating grid, screens electrons when the trigger is inactive in order to prevent signal over-amplification and damage to the other wires; the gate is closed by applying a voltage $\pm\Delta V$ to alternating wires, and this collects any charge before it can reach the thinner, more sensitive wires after the gating grid. After the gating grid the cathode grid (or shielding grid) terminates the chamber drift volume and prevents any back flow from the sense wires. Finally, the sense and field wires then collect the electrons, which are amplified via Townsend avalanche as they accelerate towards the wire. This induces an image charge on the pad planes, and the image charge is amplified and readout by the connected electronics. While some TPCs are readout from the sense wires, NA61/SHINE reads out the induced charge on the pad plane. Figure 4.10 shows the FTPC wiring schematic.

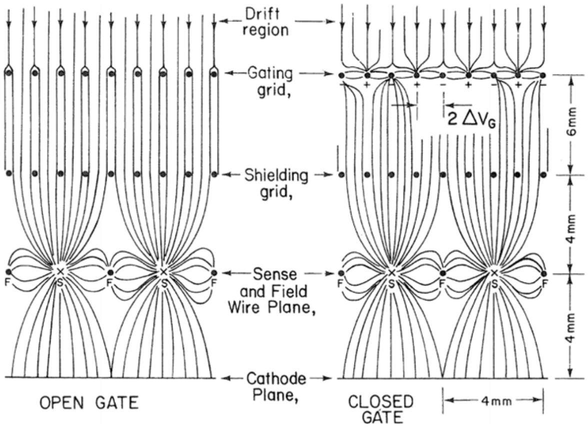

Figure 4.9: The general principle behind the charge collection in the NA61/SHINE TPCs. As electrons near the end of the drift volume, the shielding grid, they are collected by the sense and field wire plane. This collection induces an image charge on the pad planes, which is then amplified and measured by the readout electronics [61].

Each discrete collection of charge by a pad (or several adjacent pads) is defined as a cluster. Since the TPC and pad geometry are fixed, this automatically gives a measurement of the x and z coordinates of the cluster. The y coordinate of the cluster is initially unknown, but the time arrival of the cluster is recorded, and this can be used with the drift velocity to reconstruct the ionization track's y position. In addition to the (t, x, y, z) coordinates of each ionization deposit as charged tracks pass through the gas volume, the total charge is also recorded by the readout electronics; this is then used to measure the energy loss of the track as it passes through the TPCs. The specifics of

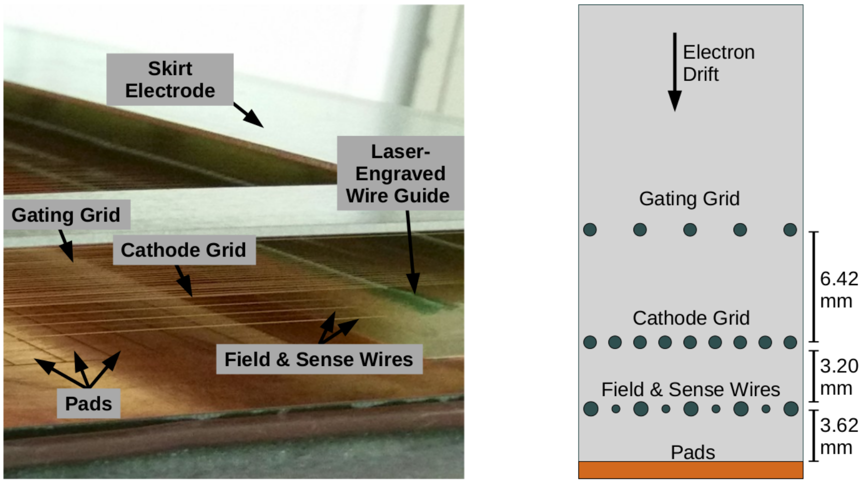

Figure 4.10: The wiring schematic for the FTPCs [48].

track and cluster reconstruction will be discussed in Chaper 5.

4.6 Time-of-Flight Walls

At the end of the NA61/SHINE detector are the three time-of-flight walls, which as one might guess from their name, are used to measure the time-of-flight of particles. Using the TOFF as an example, it is composed of rectangular slabs of scintillating plastic with a PMT at each end. Figure 4.11 shows the schematic layout of the TOFF.

When a charged particle passes through one of the TOFF bars, light is produced and measured by the attached PMTs and readout electronics; this allows the reconstruction of the time of the scintillation event. Then, the difference between the start signal of the triggering, the S1 scintillator, and the measured time at the TOFF gives the time-of-flight of the particle. (The beam travel time from the S1 to the interaction point where the particle was produced has to be subtracted off.) Using the measured time-of-flight along with the reconstructed track length and momentum gives the mass of the particle:

$$m^2 = p^2 \left(\frac{c^2 t^2}{l^2} - 1 \right). \tag{4.1}$$

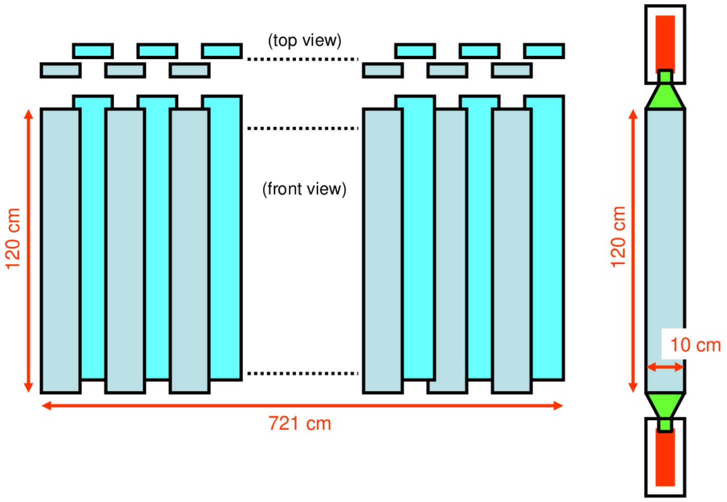

Figure 4.11: The schematic layout of the TOFF [54].

Here m is the mass of the particle, p is the momentum, c is the speed of light, t is the time-of-flight, and l is the track length. Time-of-flight measurements are only useful for low-momentum particles, as illustrated in Figure 4.12.

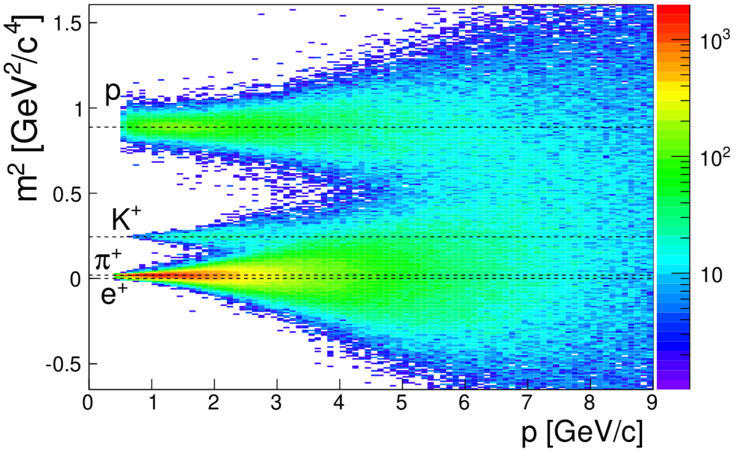

Figure 4.12: Sample mass reconstruction from the TOFF [62].

The other two time-of-flight walls, the TOF-Left and the TOF-Right, function in the same manner as the TOFF. Initially the analysis presented in this thesis was going to include both energy loss and time-of-flight measurements for particle identification, but this plan was abandoned due to the lack of phase space coverage; see Chapter 9 for more details.

4.7 Projectile Spectator

There is one final component of the NA61/SHINE detector that is not generally used by the neutrino program. The PSD is a calorimeter used to measure the energy of forward going nucleons in nucleus-nucleus collisions. Measuring these nucleons, spectators in the heavy ion collision, enables a measurement of the number of interacting nucleons. Shown in Figure 4.13, the PSD consists of 44 calorimetric modules; each module has 120 alternating layers of lead plates and scintillator tiles.

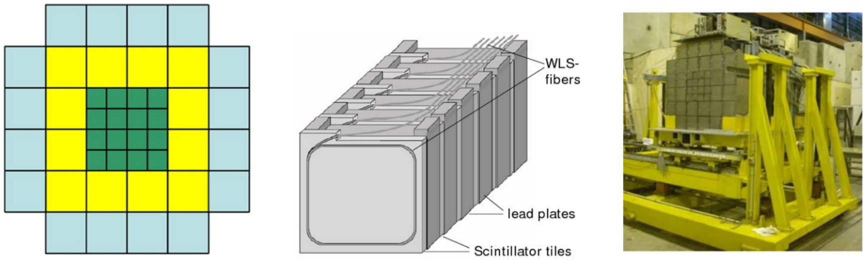

Figure 4.13: The schematic layout of the PSD. The left image shows the front view, the center image shows a single module, and the right image shows the full detector inside the NA61/SHINE detector area [54].

4.8 NA61/SHINE Detector Upgrade

In 2022, NA61/SHINE inherited the front-end-electronics (FEEs) for the TPCs from the ALICE experiment, and replaced the readout electronics of the PSD, beam counters, TOFL, TOFR, and BPDs with domino-ring-sampler DRS boards; the TOFF was used as a test of the DRS boards back in 2017. As the dataset analyzed for this thesis is from 2017, the details of the upgrade will not be elaborated. However, the new FEEs enable data taking at rates up to 10 times faster than before, and they also provide clearer signals with less noise. The DRS boards provide a digitization of the full signal, with single cell time resolution on the order of tenths of picoseconds. To put the upgrade into perspective, the 2017 proton-carbon dataset was taken over the course of a full week. With the new readout electronics, the same statistics could now be gathered in less than a single day.

Chapter 5

NA61/SHINE Software

The NA61/SHINE software suite starts with the raw data acquisition, triggering, and storage into custom binary files. Once the raw data has been stored, the SHINE framework (SHINE is the same of the software suite) includes all of the necessary tools to read, calibrate, and reconstruct any desired quantities from the raw data. Once the data has been fully reconstructed, the next step is to analyze and extract the desired physics measurements. Special attention will be paid to the DRS and TOFF software, as they were developed by the author of this thesis.

5.1 Raw Data and the Trigger

The NA61/SHINE Data Acquisition system (DAQ) is the first part of any physics analysis. It is responsible for the taking, processing, and organizing of raw data during physics runs. The base of the DAQ is the firmware on each subdetector's readout and organization electronics. For example, in 2017 the TOFF's PMTs were readout by domino-ring-sampler (DRS) boards; these boards have 32 readout channels each, and each channel stores a charge readout in 1,024 individual inverters. A single PMT of the TOFF was connected to one DRS channel, and for every event 1,024 charge samples were stored. (The electronics store the data in physical cell order, but the sampling order changes event-by-event.) Before any data could be recorded, the firmware and calibration taking software needed to be loaded into every DRS board. Figure 5.1 shows a simplified inverter schematic next to a sample raw data trace recorded during the 2017 proton-carbon run.

In addition to the base firmware required for every subdetector's readout electronics, the

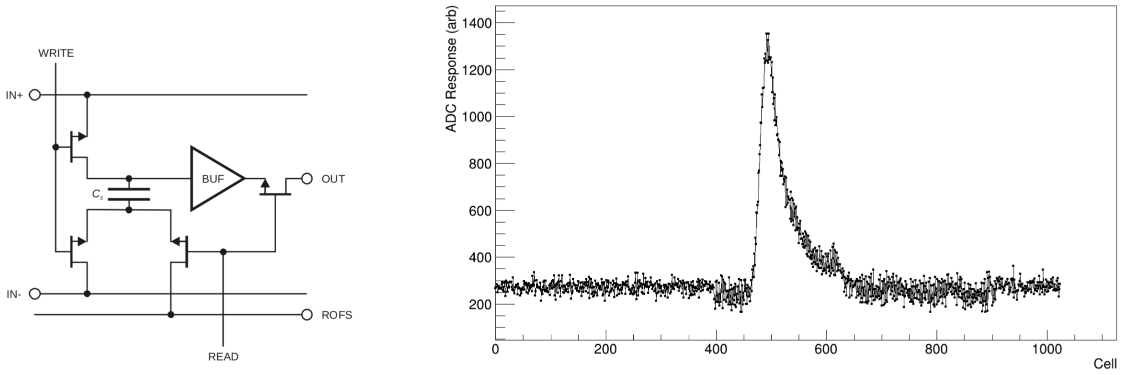

(a)

(b)

Figure 5.1: Left: A simplified schematic of one sampling cell on the DRS boards [63]. Right: A sample raw TOFF trace readout by the DRS boards. Each entry on the x axis represents one individual sample cell, and the y axis is in arbitrary ADC counts. The max ADC count is 65,535.

triggering and busy logic also need to be setup prior to the run starting. Briefly discussed earlier in Section 4.3, the triggering system is responsible for sending the start signal to every subdetector. One of the PMTs attached to the S1 scintillator, known as the S11, is responsible for sending the pre-trigger signal. Once the the pre-trigger signal has been sent, the subdetectors, like the TOFF, enter their normal data taking state; for the TOFF this encompasses only 2.048 ns, as each cell has an average time width of 0.2 ns. (The time cell width is set by the DRS board firmware.) If the triggering system designates the event as T1, T2, T3, or T4 the event is saved. If not, the stored data is cleared and the detector enters the ready state for the next event. Figure 5.2 shows the schematic overview of the triggering system; for a deeper description see [64].

After the trigger system and detector readout firmware is in place, the next step is the actual collection, organization, and storage of the raw data. For the TPCs, there are four logical components that participate in this. The first component, the front-end-electronics (FEE), directly connect one readout channel to each individual pad of the TPCs; the FEEs amplify and shape the image charges from the sense wires, storing them in a switched capacitor array. Each FEE services 32 total pads, and 24 FEEs are sent to one motherboard. The second logical component, the motherboards, are responsible for building the subdetector event structure, subtracting pedestals,

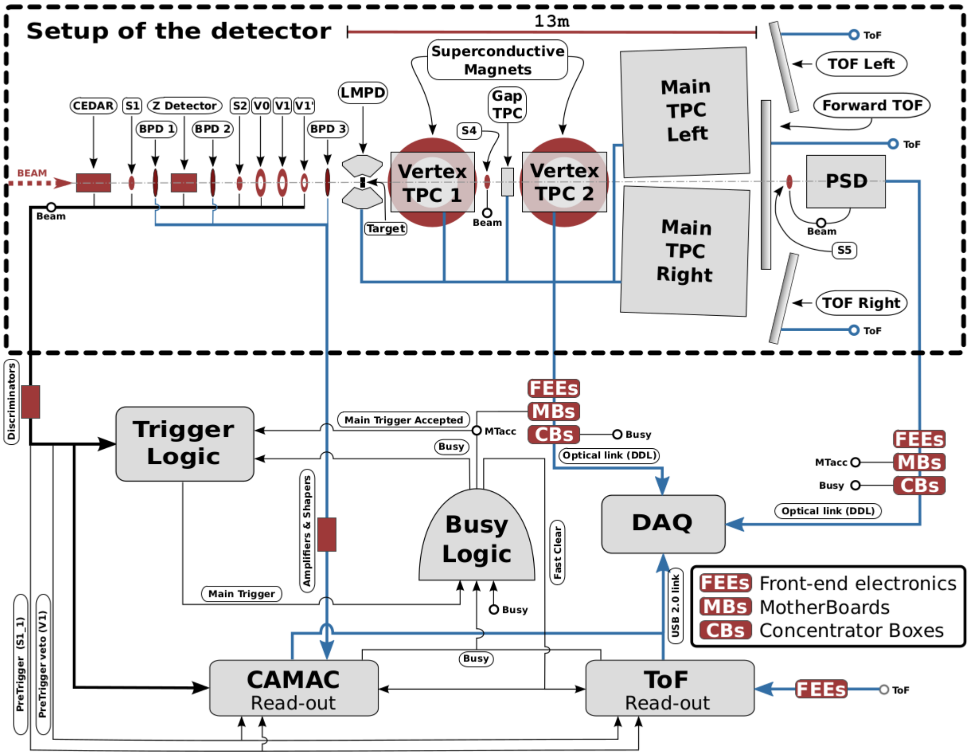

Figure 5.2: The schematic of the NA61/SHINE triggering system [64].

and applying noise and zero suppression.

For the pedestal subtraction, the baseline readout of each FEE chip is calculated (one FEE chip amplifies 16 pads), and each chip's baseline is subtracted off for every event. The zero suppression applies a threshold of 5 ADC counts to every channel, where 5 ADC counts $\approx 2\sigma$ of noise.

Once the FEE data has been collected by the motherboards, concentrator boxes "concentrate" data from up to 32 motherboards, which serializes the data and prepares it for transfer to the central DAQ computer. The fourth and final logical component, the detector data links, are optical links capable of large, fast data transfer; these links send the data from the concentrator boxes to the central DAQ computer. After the data arrives, the central DAQ computer takes each subdetector's data and builds a single event, and the event is now ready for storage on CERN's tape archive.

In the overall event structure, each subdetector's data is packaged together into a single binary structure with a total event header. The event header defines the event and run numbers, along with the total event size, so that the SHINE framework knows the correct number of bytes to read when it loads the raw data. Inside the overall event structure are the subdetector events. Each subdetector event has its own event header that defines the payload type (for example TPC or TOFF) and subdetector event size. When the SHINE framework reads a raw data file, it first parses the event header before reading the subevent data. Based on the payload type set in the subevent header, the subevent is then passed to the appropriate decoder that fills the relevant data structures inside the SHINE framework.

Figure 5.3 shows the subevent structure for events readout by the DRS boards. The header stores a number of necessary variables, including the board ID, the DRS sampling speed, and the stop cell. (The DRS boards are domino-ring-samplers, so the stop cell is not fixed.) After the header, the detector data is stored; for the TOFF this is the scintillation light signal amplified by the PMT and readout by the DRS board. In the SHINE framework, a single TOFF raw data channel is fully represented by the DRS board ID, chip ID (8 data channels are connected to one chip), channel number respective to the other channels connected to the same chip, stop cell, data type (as discussed in Section 6.5 the data type can be either data, voltage calibration, or time calibration), and the raw trace ADC values. This set of variables fully defines any single DRS channel's data, and provides all of the necessary components for reconstruction and later physics analysis.

The rest of the subdetectors follow the same procedure as the TOFF. For the TPCs, the raw data is fully defined by the TPC ID, sector ID, padrow ID, and the 256 time slices of raw ADC data from the pad readout attached to this specific set of Ids. Just like for the DRS detector data, there is a specific decoder inside the SHINE framework that parses the input raw binary data and stores it in the relevant SHINE data structures. Figure 5.4 shows a sample visualization of raw FTPC data for one event. (Figure 5.4a and Figure 5.4b come directly from the SHINE framework's "eventBrowser", which can be used to visualize raw and reconstructed data.)

<table>
<tr><td></td><td></td><td colspan="48">Bit ID</td><td colspan="2">Address</td></tr>
<tr><td></td><td>Word ID</td><td>0</td><td>1</td><td>2</td><td>3</td><td>4</td><td>5</td><td>6</td><td>7</td><td>8</td><td>9</td><td>10</td><td>11</td><td>12</td><td>13</td><td>14</td><td>15</td><td>16</td><td>17</td><td>18</td><td>19</td><td>20</td><td>21</td><td>22</td><td>23</td><td>24</td><td>25</td><td>26</td><td>27</td><td>28</td><td>29</td><td>30</td><td>31</td><td>32</td><td>33</td><td>34</td><td>35</td><td>36</td><td>37</td><td>38</td><td>39</td><td>40</td><td>41</td><td>42</td><td>43</td><td>44</td><td>45</td><td>46</td><td>47</td><td>Byte</td><td>Hex</td></tr>
<tr><td rowspan="25">HEADER</td><td>0</td><td colspan="32">length - number of bytes = 6*(number of 48-bit words)</td><td colspan="16">magic number (0x1001)</td><td>6</td><td>0x6</td></tr>
<tr><td>1</td><td colspan="8">buf ID</td><td colspan="12">board ID (rotary switches)</td><td colspan="8">*</td><td colspan="8">calib config bits **</td><td colspan="4">X</td><td colspan="4">trg type</td><td colspan="4">AFE array</td><td>12</td><td>0xC</td></tr>
<tr><td>2</td><td colspan="8">WSR 0</td><td colspan="8">WSR 1</td><td colspan="8">WSR 2</td><td colspan="8">WSR 3</td><td colspan="16">ADC buffer counter (low 16 bits)</td><td>18</td><td>0x12</td></tr>
<tr><td>3</td><td colspan="48">ADC buffer counter (high 48 bits)</td><td>24</td><td>0x18</td></tr>
<tr><td>4</td><td colspan="10">DRS0 stop cell</td><td colspan="10">DRS1 stop cell</td><td colspan="10">DRS2 stop cell</td><td colspan="10">DRS3 stop cell</td><td colspan="8">Channel (0)</td><td>30</td><td>0x1E</td></tr>
<tr><td>5</td><td colspan="10">DRS0 stop cell</td><td colspan="10">DRS1 stop cell</td><td colspan="10">DRS2 stop cell</td><td colspan="10">DRS3 stop cell</td><td colspan="8">Channel (1)</td><td>36</td><td>0x24</td></tr>
<tr><td>6</td><td colspan="10">DRS0 stop cell</td><td colspan="10">DRS1 stop cell</td><td colspan="10">DRS2 stop cell</td><td colspan="10">DRS3 stop cell</td><td colspan="8">Channel (2)</td><td>42</td><td>0x2A</td></tr>
<tr><td>7</td><td colspan="10">DRS0 stop cell</td><td colspan="10">DRS1 stop cell</td><td colspan="10">DRS2 stop cell</td><td colspan="10">DRS3 stop cell</td><td colspan="8">Channel (3)</td><td>48</td><td>0x30</td></tr>
<tr><td>8</td><td colspan="10">DRS0 stop cell</td><td colspan="10">DRS1 stop cell</td><td colspan="10">DRS2 stop cell</td><td colspan="10">DRS3 stop cell</td><td colspan="8">Channel (4)</td><td>54</td><td>0x36</td></tr>
<tr><td>9</td><td colspan="10">DRS0 stop cell</td><td colspan="10">DRS1 stop cell</td><td colspan="10">DRS2 stop cell</td><td colspan="10">DRS3 stop cell</td><td colspan="8">Channel (5)</td><td>60</td><td>0x3C</td></tr>
<tr><td>10</td><td colspan="10">DRS0 stop cell</td><td colspan="10">DRS1 stop cell</td><td colspan="10">DRS2 stop cell</td><td colspan="10">DRS3 stop cell</td><td colspan="8">Channel (6)</td><td>66</td><td>0x42</td></tr>
<tr><td>11</td><td colspan="10">DRS0 stop cell</td><td colspan="10">DRS1 stop cell</td><td colspan="10">DRS2 stop cell</td><td colspan="10">DRS3 stop cell</td><td colspan="8">Channel (7)</td><td>72</td><td>0x48</td></tr>
<tr><td>12</td><td colspan="10">DRS0 stop cell</td><td colspan="10">DRS1 stop cell</td><td colspan="10">DRS2 stop cell</td><td colspan="10">DRS3 stop cell</td><td colspan="8">Channel (8)</td><td>78</td><td>0x4E</td></tr>
<tr><td>13</td><td>X</td><td colspan="3">***</td><td colspan="2">X</td><td colspan="10">DRS hsample</td><td colspan="8">X</td><td colspan="4">DRS PLL LCK</td><td colspan="8">ADC clock pattern</td><td colspan="12">X</td><td>84</td><td>0x54</td></tr>
<tr><td>14</td><td colspan="48">alive time (low 48 bits)</td><td>90</td><td>0x5A</td></tr>
<tr><td>15</td><td colspan="16">alive time (high 16 bits)</td><td colspan="32">trg time (low 32 bits)</td><td>96</td><td>0x60</td></tr>
<tr><td>16</td><td colspan="32">trg time (high 32 bits)</td><td colspan="16">X</td><td>102</td><td>0x66</td></tr>
<tr><td>17</td><td colspan="32">delay readout</td><td colspan="16">trg delay alive (low 16 bits)</td><td>108</td><td>0x6C</td></tr>
<tr><td>18</td><td colspan="16">trg delay alive (high 16 bits)</td><td colspan="32">delay readout</td><td>114</td><td>0x72</td></tr>
<tr><td>19</td><td colspan="48">trig number (low 48 bits)</td><td>120</td><td>0x78</td></tr>
<tr><td>20</td><td colspan="15">trig number (high 16 bits)</td><td colspan="33">discard (CLEAR) number (low 32 bits)</td><td>126</td><td>0x7E</td></tr>
<tr><td>21</td><td colspan="33">discard (CLEAR) number (high 32 bits)</td><td colspan="15">eventID (low 16 bits)</td><td>132</td><td>0x84</td></tr>
<tr><td>22</td><td colspan="15">eventID (high 16 bits)</td><td colspan="26">X</td><td colspan="2">stat</td><td colspan="5">err flags</td><td>138</td><td>0x8A</td></tr>
<tr><td>23</td><td colspan="16">DRS0 temperature</td><td colspan="16">DRS1 temperature</td><td colspan="16">X</td><td>144</td><td>0x90</td></tr>
<tr><td>24</td><td colspan="16">DRS2 temperature</td><td colspan="16">DRS3 temperature</td><td colspan="16">X</td><td>150</td><td>0x96</td></tr>
<tr><td rowspan="14">DATA</td><td>25</td><td colspan="24"># words (48-bit words, exclusive)</td><td colspan="12">Channel #</td><td colspan="12">DRS #</td><td>156</td><td>0x9C</td></tr>
<tr><td>26</td><td colspan="12">seqLen</td><td colspan="12">seqStart</td><td colspan="12">V0</td><td colspan="12">V1</td><td>162</td><td>0xA2</td></tr>
<tr><td>27</td><td colspan="12">V2</td><td colspan="12">V3</td><td colspan="12">...</td><td colspan="12">...</td><td>...</td><td></td></tr>
<tr><td>...</td><td colspan="12">Vn-1</td><td colspan="12">seqLen</td><td colspan="12">seqStart</td><td colspan="12">V0</td><td></td><td></td></tr>
<tr><td>...</td><td colspan="12">V1</td><td colspan="12">...</td><td colspan="12">Vn-1</td><td colspan="12">X</td><td></td><td></td></tr>
<tr><td>...</td><td colspan="48">...</td><td></td><td></td></tr>
<tr><td>...</td><td colspan="24"># words (48-bit words, exclusive)</td><td colspan="12">Channel #</td><td colspan="12">DRS #</td><td></td><td></td></tr>
<tr><td>...</td><td colspan="12">seqLen</td><td colspan="12">seqStart</td><td colspan="12">V0</td><td colspan="12">V1</td><td></td><td></td></tr>
<tr><td>...</td><td colspan="12">V2</td><td colspan="12">V3</td><td colspan="12">...</td><td colspan="12">...</td><td></td><td></td></tr>
<tr><td>...</td><td colspan="12">Vn-1</td><td colspan="12">seqLen</td><td colspan="12">seqStart</td><td colspan="12">V0</td><td></td><td></td></tr>
<tr><td>...</td><td colspan="12">V1</td><td colspan="12">...</td><td colspan="12">Vn-1</td><td colspan="12">X</td><td></td><td></td></tr>
</table>

Figure 5.3: The DRS event structure for detectors using the DRS readout electronics.

5.2 SHINE Framework

With the DAQ's job done, the physics data has been recorded and is sitting in the CERN tape archive waiting to be analyzed; this is where the SHINE framework comes in. The SHINE framework is a modular C++ calibration, reconstruction, and analysis software framework. It provides an abstract detector interface allowing users to easily obtain detector calibration parameters like TPC drift velocity, detector positions, and the light-propagation speed in each of the TOFF scintillators. (Just a few examples among many detector properties.) On top of the detector structures, the SHINE framework has GEANT4 based Monte-Carlo (MC) simulation and reconstruction capabilities.

After reading in raw data or continuing the chain during the MC simulation, the framework can then output a custom SHINE Offline Event (SHOE) data file, which contains any higher-level raw and reconstructed data desired by the user; the framework is also capable of running on produced SHOE files. Inside the SHOE file the data is stored through C++ classes and namespaces. For

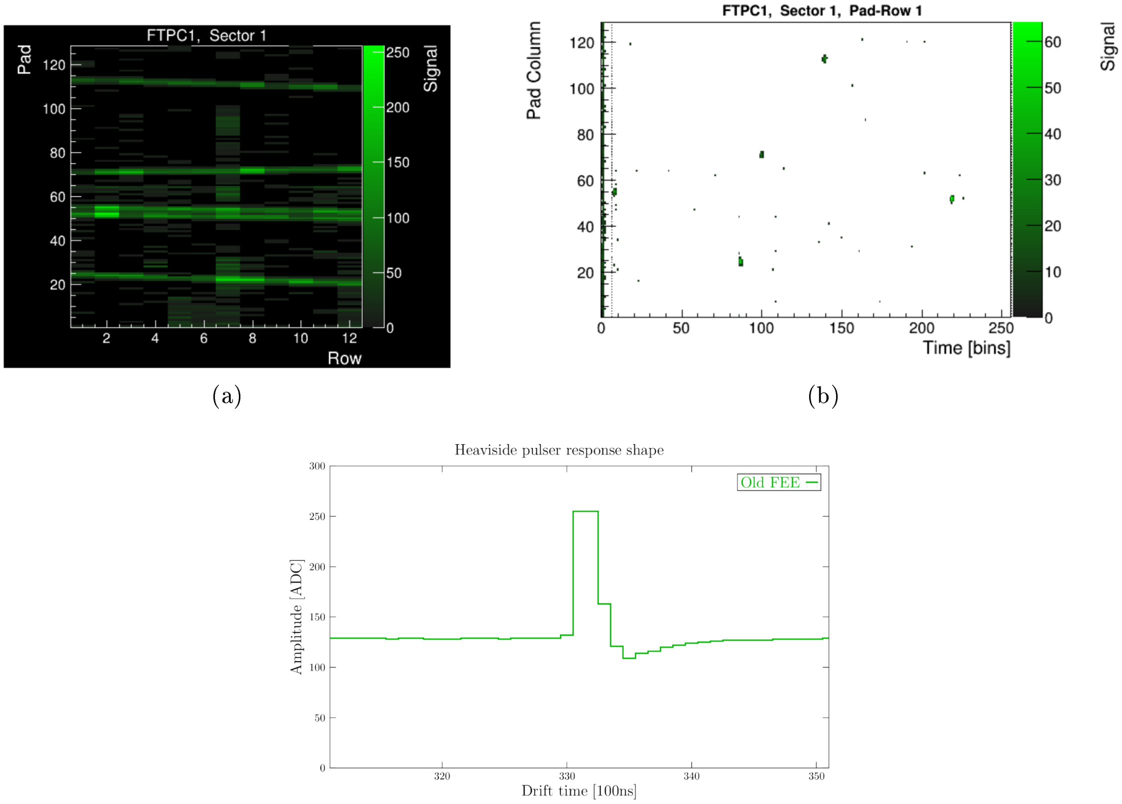

(a)

(b)

(c)

Figure 5.4: Visualization of one event's worth of raw data for FTPC1, sector 1. Top Left: The $x - z$ projection of the raw data; every bin contains 256 time slices worth of raw ADC values, and the plot is showing the max value. In the SHINE coordinate system, the rows are the z coordinate and the pads are the x coordinate [48]. Top Right: Essentially the $x - y$ projection for pad-row 1. This plot shows the charge collection for every pad in row 1 as a function of time [48]. Bottom: A sample trace for a single pad, without a baseline correction or any filtering applied. "Old FEE" means the data is from before the SHINE hardware upgrade in 2022, as discussed in Section 4.8 [65].

example, a reconstructed track will have all of its information stored in an indexed "rec::Track" object, where the index is used to uniquely identify the track from other reconstructed tracks in the same event. All of the tracks for a single event are then attached to a "RecEvent" object, which uses custom Root dictionaries to store the data in a SHOE file. The SHOE file format allows for any version of the framework to read in a SHOE file produced from past and future versions of the framework. Of course, new information from future SHOE files cannot be used by older versions. This section will walk through all of the steps necessary to go from raw data to reconstructed data ready for a physics analysis.

5.2.1 Reconstruction

5.2.1.1 Clusterizing

The first step in track reconstruction is clusterization, which transforms the islands of charge from Figure 5.4b into an (x, y, z) measurement of the track's position as it progresses through the TPCs. Each cluster also includes a charge measurement, which is the foundation of measuring the energy loss of tracks as they progress through the detector, as described in Section 5.2.1.5. Inside the SHINE framework, the cluster finder searches every single pixel on the padplane for pixels above the threshold. For this analysis the threshold was set to 9 ADC. Once these pixels have been identified, they are grouped into islands of charge. For each pixel passing the initial threshold, directly neighboring pixels are added to the island if they pass a slightly lower threshold. (6 ADC counts in this analysis.) Figure 5.5 shows an example of this for FTPC1.

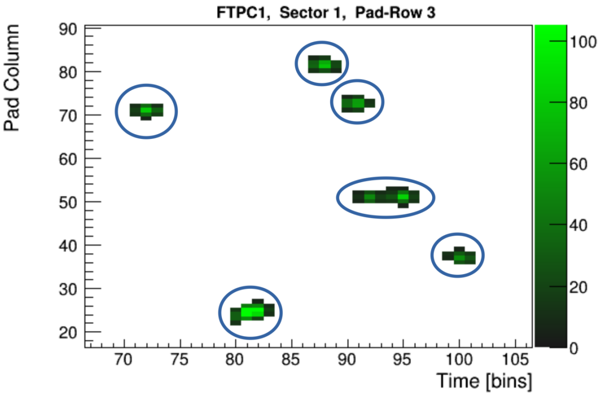

Figure 5.5: An example of the cluster finding algorithm grouping islands of charge into a single possible cluster [48].

Once the possible clusters have been identified, a weighted mean is used to calculate the (x, y) positions:

$$x = \frac{\sum_i (ADC)_i x_i}{\sum_i (ADC)_i}, \quad y = \frac{\sum_i (ADC)_i y_i}{\sum_i (ADC)_i}. \tag{5.1}$$

The index i runs over all pixels in the island, x is the pad's x-coordinate, and y is the timebin's y-coordinate. The z position comes from the padrow's z-coordinate. After the initial (x, y) positions have been calculated, a small correction is applied for clusters in the GTPC, VTPC1, and VTPC2, known as the $E \times B$ correction; this comes from the magnetic field not being perfectly parallel to the cluster drift direction. In addition, the y position comes from the time arrival of the charge cloud on the plane, which requires knowing the drift velocity in the TPC chamber at the time of ionization and the individual pad's T0, a calibration correction to the pad's timing offset in relation to all other pads in the experiment. This will be discussed in more detail in Section 6.1. Experimentally, the cluster point position uncertainties are $\sim$ 200 µm.

5.2.1.2 Tracking

With the clusters identified and measured, the next step passes all of the clusters to the tracking algorithm. The tracking algorithm can be broken down into three distinct parts: local tracking, global tracking, and vertex finding.

Starting with the local tracking, it groups clusters into track candidates in each individual TPC. The first stage of the local tracking is tracklet (potential track segments) seeding. The tracklet seeding is a cellular-automaton-based seeding algorithm that uses a pattern recognition alogirthm to initially group adjacent (in z) clusters together [66]. Clusters on the same padrow cannot be linked together, as all measurable particles produced in the target are forward going. Once directly adjacent clusters have been linked, each triplet is applied a sorting metric

$$m_{\text{cluster}} = \sqrt{\Delta\theta_{xz}^2 + \Delta\theta_{yz}^2}. \tag{5.2}$$

$\Delta\theta_{xz}$ and $\Delta\theta_{yz}$ are the differences in the angles between the first and middle cluster and the middle and last cluster in the cluster triplet. Once the metric has been calculated for all triplets, filtering is applied, which keeps only the best connections for every cluster. Figure 5.6 illustrates this process.

The tracklets in Figure 5.6b are then passed to either a simple least squares straight line fit

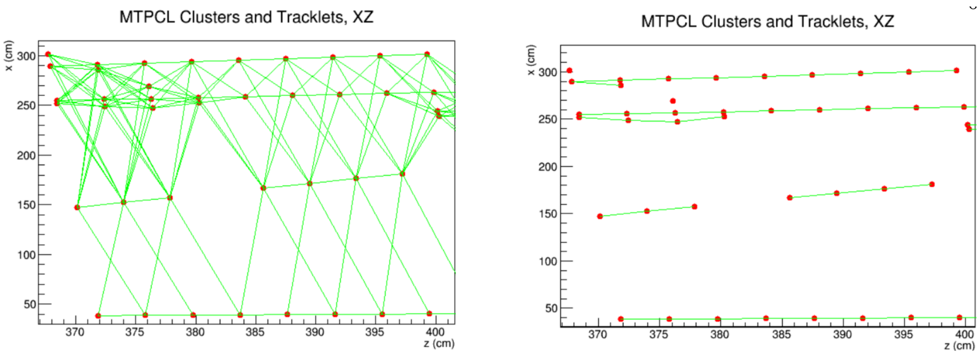

(a) (b)

Figure 5.6: The tracklet seeding algorithm in the MTPCL. Left: All potential cluster triplets. Right: The remaining tracklets after filtering [48].

or the Kalman filter; if the tracklet is inside a magnetic field is is passed to the NA61/SHINE's Kalman filter. These fitters provide measurements of the tracklet's slope and intercept in the $x - z$ and $y - z$ planes near the tracklet's most upstream cluster. (Most upstream refers to the smallest z position of the clusters. So this is the cluster closest to the target.)

The final stage of local tracking is track extension, where tracklets in individual TPCs are joined together. A list of all possible merging candidates is formed and measured with the metric

$$m_{\text{track}} = \sqrt{w_x \Delta x^2 + w_y \Delta y^2 + w_A \Delta A^2 + w_B \Delta B^2 + w_{q/p} (\Delta q/p)^2}, \tag{5.3}$$

where w_x refers to the weight applied to the track mismatch in their x coordinates, A represents θ_{XZ}, B represents θ_{YZ}, and q/p is the charge over momentum. These five parameters are one possible set of variables that fully define the behavior of a particle in a magnetic field, provided the field is known. This means that knowing these five parameters at one point in z allows extrapolation to any other point in z.

After the metric in Equation 5.2 is calculated for every single possible track extention candidate, the best candidates are linked together into a single local track spanning one full TPC. These local tracks are then passed to the global tracking algorithm, which connects local tracks from disparate TPCs together.

The global tracking algorithm uses the same weighting metric as the track extension, Equation 5.3, to link local TPC tracks together. Since extrapolating tracks over distances on the order of meters greatly magnifies any uncertainties or possible mis-reconstruction effects, it starts by linking tracks in nearby (in z) TPCs together. Then it searches for track matching candidates between farther apart TPCs. So, a global track might start with the merging of a FTPC3 and a FTPC2 track together, and then this merged track is then connected to a GTPC track; Figure 5.7 shows an example of this process for a low-mulitplicity neutrino event.

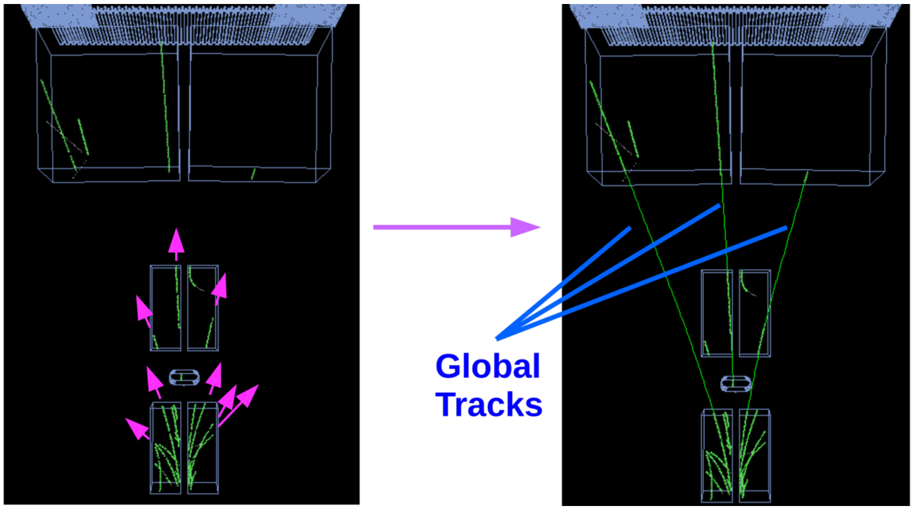

Figure 5.7: An sample illustration of global track merging. Once the local TPC tracks have been formed, they are then merged into global TPC tracks [48].

Once global tracks have been formed, the final step is vertex finding, which attaches a vertex, a production point, to global tracks. There are two types of vertices used in the SHINE framework. The first one, a main vertex, estimates the production point inside the target based on extrapolating all tracks to the target's z position. The second one, a V^0 vertex, labels possible neutral particles that have decayed inside the detector; the neutral particle will come from the main vertex, but the decay products come from some production point outside the target at the point of decay.

For the main vertex, the reconstructed beam track's position at the target is used as a constraint on the (x, y) position of the vertex. The z position is found by minimizing the function

$$f(z) = \sum_i \ln\left(1 + \frac{(x_i(z_v) - x_v)^2}{2\sigma_{x,i}^2(z_v)}\right) + \ln\left(1 + \frac{(y_i(z_v) - y_v)^2}{2\sigma_{y,i}^2(z_v)}\right). \tag{5.4}$$

In this minimization function, i sums over all tracks, $x_i(z_v)$ is the track's position at the current step in z_v, x_v is the seed position from the beam track, and σ is the uncertainty in the track's extrpolated position.

For the V^0 vertex, a brute-force method takes every possible pair of positive and negative tracks and extrapolates them towards each other. If the two tracks come close enough, they are designated as potential V^0 decay particles. A V^0 vertex is assigned at their point of closest approach (PCA), and a new neutral track is created; the kinematics of the neutral particle are fully described by the two decay particles. In this analysis a very loose minimum PCA of 10 cm is required. Many spurious V^0 tracks will be created even with a stricter, more realistic constraint, but the cuts applied in the neutral analysis as well as the invariant mass fit, as discussed in Chapter 8, will cut any fake V^0s from the analysis. It is also worth noting this method will only find V^0s with two charged decay particles. To accomadate for this, the neutral analysis corrects for the missing pathways from the known branching ratios.

5.2.1.3 Beam Track Reconstruction

Briefly mentioned in the previous section, reconstructing the beam track is a critical component of every event, as it is used in the main vertex fit as well as an event-level cut; events where the beam track is not well reconstructed or the beam track misses the target are not considered in the physics analysis of data. As can be seen in Figure 4.1, the BPDs provide three (x, y, z) measurements of the beam track before it reaches the NA61/SHINE target.

Each BPD measures a charge on two orthognal strips of wires. Typically the beam track induces a charge distribution covering five strips in either direction. Then, the (x, y) position is found by taking a weighted mean of the induced charge with each strip's position. Adding in the known z position of the detectors, the beam track's x-z and y-z slopes are then used to get the beam position at the target.

5.2.1.4 TOFF Reconstruction

Located at the end of the experiment in z, the TOFF provides time-of-flight measurements used to indentify the species of low-momentum particles. The start signal for the TOFF walls comes from the S11 scintillator, which triggers the wall to enter its data taking state. Each scintillator bar is $120 \times 10 \times 2.5$ cm^3 of Bicron BC-408 plastic, and they are staggered with one cm overlaps to ensure full coverage, as can be seen in Figure 4.11. When a charged particle traverses one of the bars, it creates scintillation light; with the bars wrapped in aluminum foil underneath heavy layers of light-blocking black foils and tape, the scintillation light is contained and sent to the PMTs on the top and bottom of the scintillator bar. Each PMT is set to a specific voltage to maximize its average response while keeping the number of overflow events to a minimum, as can be seen in Figure 5.8. The average supplied PMT voltage during the 2017 data taking runs was -1650 V.

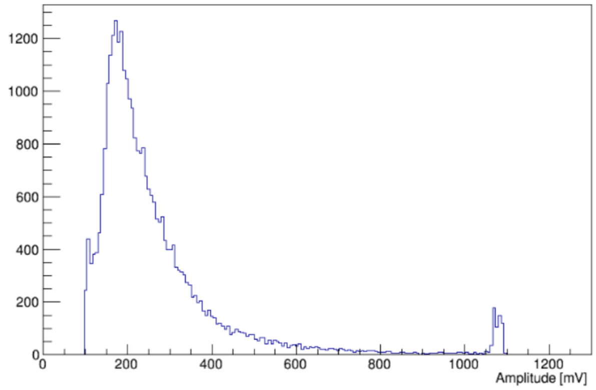

Figure 5.8: The voltage-calibrated signal amplitude from the top PMT for scintillator 0. Each PMT is set to a voltage to maximize the average signal response while keeping the overflow tail, which occurs from maxing out the readout of the DRS boards, at a minimum. For this plot a cut of 100 mV is applied, but during an analysis a much smaller cut is used, as requiring a matched track will remove the majority of the noise responses.

Once the response signal has been recorded, the first step in reconstruction converts the raw ADC trace to a calibrated voltage response in time. This process will be described in Section 6.5, and it applies a time width to every cell, as well as converts from ADC to voltage. Figure 5.9a shows the uncalibrated response next to the calibrated response in Figure 5.9b. The pedestal has already been removed in the calibrated trace, which places the baseline of the response at zero; even with the voltage calibration, some channels have a baseline of $\sim \pm 2$ mV, and removing this baseline improves the timing resolution of the TOFF wall. For the TOFF, the baseline correction is found by taking the average of cells 1 to 31. Cell 0 is skipped as the first and last cell of the response can spike.

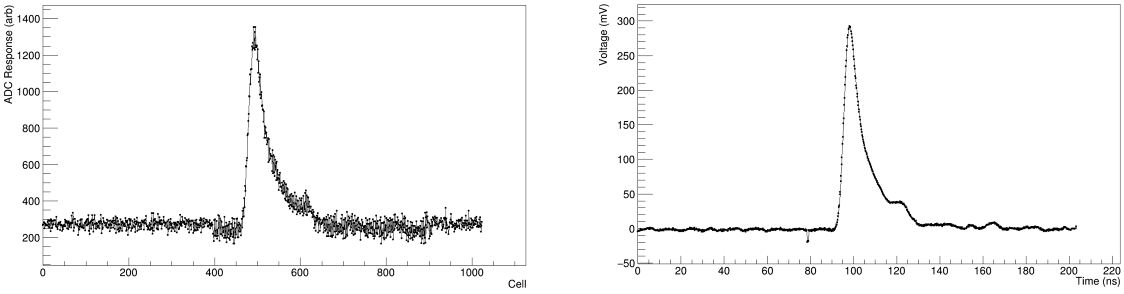

(a)

(b)

Figure 5.9: Left: An uncalibrated response from the TOFF wall. Right: Calibrated. This image shows the bunching that is an intrinsic property of the DRS boards; the time cell widths are on average 0.2 ns, but the actual grouping alternates between short and long cell widths.

With a calibrated signal response, the TOFF reconstruction then needs to extract a time measurement from the signal. All extraction methods will use some point on the rising curve of the response, but there is no definitive way to extract a timing measurement from Figure 5.9b. A variety of differing threshold voltages in combination with fits were tested (along with just threshold voltages), and a third-degree polynomial fit to the rising curve with a fractional threshold of 10% was found to maximize the TOFF timing resolution.

With this algorithm, the measured hit time of a single TOFF PMT can be extracted from the baseline-corrected, calibrated response trace. The extracted time, however, is actually the combination of many timing delays that have to subtracted off to get the time-of-flight for the particle. Writing the measured time as a function of all possible timing delays,

$$t_{\text{Meas}} = t_{\text{Hit}}(p, l, m) + t_{\text{Light}} + t_0 + t_{\text{S1}} + t_{\text{Ref}} + t_C. \tag{5.5}$$

In Equation 5.5, the difference between the time at the point of production and t_{Hit} is the actual time-of-flight used in Equation 4.1; it is only a function of the particle's momentum, path length, and mass. Eight DRS channels are connected to a single chip on the DRS readout electronics, and t_{Ref} is the reference signal time of the chip relative to the start signal of the experiment. (Section 6.5 will describe this in more detail.) t_{Light}, t_0, and t_{S1} are the light travel time from the scintillation point to the PMT, the individual PMT's T0, and the jitter at the S1 scintillator, respectively. All of these require calibration, and they will be described in Section 6.6. Finally, t_C represents any additional, unnaccounted for effects, such as amplitude dependence of the timing. t_C was found to be negligible, except for traces maxing out the response of the DRS boards.

With the TOFF wall fully calibrated, the particle hit timing can be properly reconstructed, and the time-of-flight is the difference between the start signal timing and the hit timing. (The beam travel time from the S1 to the main vertex of the event has to be subtracted off.) Each hit at the TOFF wall will have two timing measurements, one from the top PMT and one from the bottom the PMT. The average of these two measurements is taken, and this is combined with the TPC's reconstruction of the track's momentum and travel length to calculate a mass.

It is worth noting that even the maxed out responses can be properly reconstructed with some additional work. Figure 5.10 shows two sample maxed out responses on top of a collection of non-maxed responses. Each trace has been normalized, baseline corrected, and shifted in time for the purpose of the plot. While any amplitude dependence was found to be negligible for non-maxed out responses, a clear shape difference can be seen in the rising curve of the two blue curves in Figure 5.10.

To correct for this effect (and test for voltage dependence in all responses), the responses of every PMT were grouped together into bins spanning 25 mV with the S1 jitter and the reference channel time subtracted off. From Equation 5.5, subtracting the average measured time gives

$$t_{\text{Meas}} - \bar{t}_{\text{Meas}} = (t_{\text{Hit}} - \bar{t}_{\text{Hit}}) + (t_{\text{Light}} - \bar{t}_{\text{Light}}) + (t_0 - \bar{t}_0) + (t_C - \bar{t}_C). \tag{5.6}$$

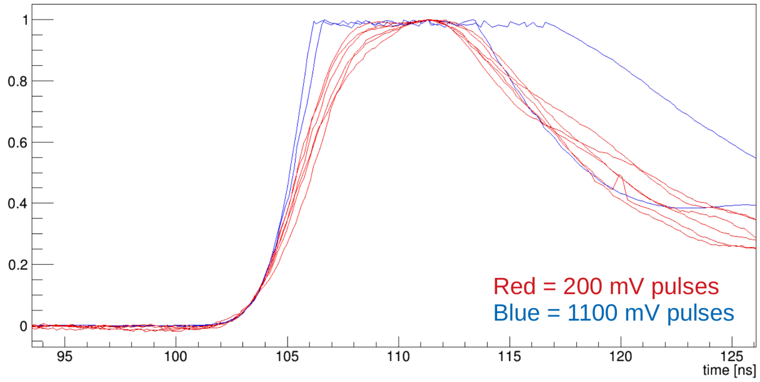

Figure 5.10: Two sample responses where the readout of the DRS electronics was maxed out, resulting in clipping of the trace (blue) with sample traces (red). A clear shape difference can be seen between the two sets of traces. The traces have all been normalized to one for this plot.

$t_0 - \bar{t}_0 = 0$, as t_0 is a constant and does not change event-by-event. Then, Equation 5.6 can be simplified further by combining the top and bottom PMTs for each scintillator and using

$$(t_{\text{t, Light}} - \bar{t}_{\text{t, Light}}) = \frac{\bar{y} - y}{v}, \quad (t_{\text{b, Light}} - \bar{t}_{\text{b, Light}}) = \frac{y - \bar{y}}{v}, \tag{5.7}$$

where y is the position of the hit, and v is the propagation speed of light inside the scintillator, and $t_{\text{t, Light}}$ is the light travel time for the top PMT. Putting Equations 5.6 and 5.7 together gives

$$\frac{1}{2}(t_{\text{t, Meas}} - \bar{t}_{\text{t, Meas}} + t_{\text{b, Meas}} - \bar{t}_{\text{b, Meas}}) = (t_{\text{Hit}} - \bar{t}_{Hit}) + (t_C - \bar{t}_C). \tag{5.8}$$

This assumes t_C is the same for all PMTs. Figure 5.11 shows the results of using Equation 5.8 to combine all of the PMT's responses together to discern any voltage-dependent effects. The timing resolution of the TOFF wall is $\sim$ 110 ps, and all of the bins below 1000 mV are centered near zero well within this range; the first couple of bins are not centered at zero, but this comes from noise responses. Applying a voltage-dependent time correction to the low voltage responses did not improve the reconstruction or timing resolution of the TOFF wall. However, as can be seen for traces above 1000 mV, there is a definitive time shift. Applying an additional time correction of 590 ps to traces above 1000 mV, the mean from a Gaussian fit to the distribution in Figure 5.11, resulted in the reconstructed mass peak for pions in this region shifting from -0.2 GeV/c^2 to the proper value of 0.139 GeV/c^2.

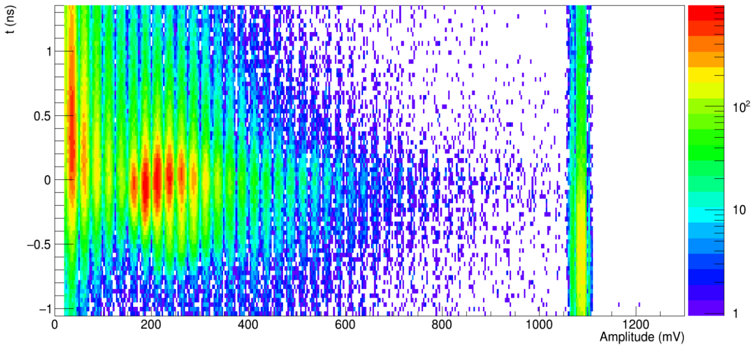

Figure 5.11: The voltage-dependent timing response of the TOFF wall. For responses below 100 mV, the offset from zero is not physical and arises from the noise responses shifting the means. However, the offset from zero for responses above 1000 mV is physical, and needs to be corrected.

There is one final caveat to the TOFF reconstruction that needs to be mentioned. The TOFF was used as a test of the DRS readout electronics in 2017 before they were used in the other detectors starting in 2022 and onwards. As a result of this, the firmware on the boards was not yet perfected and the DAQ of the boards was not synchronized with the rest of the experiment; not only were the TOFF events stored in completely separate files, there were dropped events, meaning the DAQ failed to store the occasional TOFF event. There were no clear indicators when events were dropped, so the TOFF events and the central DAQ events could not be easily matched. To work around this, the beam timing structure from the SPS was used to match the groups of TOFF and central DAQ events corresponding to the same beam spill. Once this higher level matching was in place, the number of events recorded in the two disparate event files for the same beam spill were counted. If they recorded the same number of events, then a one-to-one matching correspondance could be constructed between the TOFF event numbers and the central DAQ event numbers. If the beam spill had a dropped TOFF event, then there was no hope of correctly matching the events, and all events from the beam spill were cut. This information was then stored in matching tables, and the SHINE framework can load the matching tables in addition to the TOFF and central DAQ event files, which allows for the raw TOFF data to be properly reconstructed for the 2017 datasets. In total, only 37 out of $\sim$ 7400 beam spills for the full proton-carbon 90 GeV/c dataset had a missing TOFF event. 5 of these 37 beam spills had more than one missing TOFF event.

5.2.1.5 Energy Loss Reconstruction

On top of the tracking inside the TPCs, reconstuction of the energy loss of charged particles as they propagate through the gas volumes provides crucial information necessary to identify particle species. As a charged particle progresses through the gas volume, it stochastically deposits charge via interactions with the medium, with the main contributions coming from ionization and atomic excitation of the gas. The energy deposition depends on the mass of the particle, the particle's speed, and various properties of the medium being traversed. NA61/SHINE's phase space covers the region near the minimum ionization region in Figure 5.12, which shows the specific energy loss ($-dE/dx$) for muons in copper, known as the Bethe-Bloch curve.

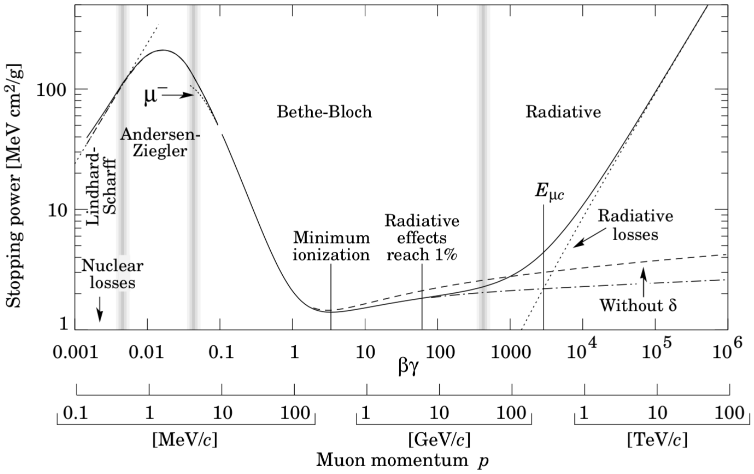

Figure 5.12: The specific energy loss for muons in copper. NA61/SHINE covers the region near the minimum ionization point. Near this point, there are two distinct trends the energy loss can follow. Below, the curve approximately increases as $1/\beta^2$, where β is the particle's velocity relative to c. Above the minimum ionization point, the curve roughly follows $\ln(\beta\gamma)$, where $\gamma^{-1} = \sqrt{1-\beta^2}$ [10].

During reconstruction, the SHINE framework gets the associated charge from every cluster on a track, and then calculates the $[0, 50]\%$ truncated mean of this collection, meaning the lowest

50% of the clusters are kept for the energy loss distribution. The energy loss for particles follows a probability distribtion known as a straggling function, where the tail is infinite; various parameterizations of this distribution exist, such as the Landau distribution, as shown in Figure 5.13. Taking the truncated mean of this distribution tempers the long tail, and allows an approximation of the distribution as an asymmetric Gaussian. This approximation makes fitting energy loss distributions much less computationally intensive, a requirement for performing the thousands of fits in the charged analysis; it also makes the measurements less sensitive to fluctuations from the long tail, which greatly improves the energy loss particle ID resolution.

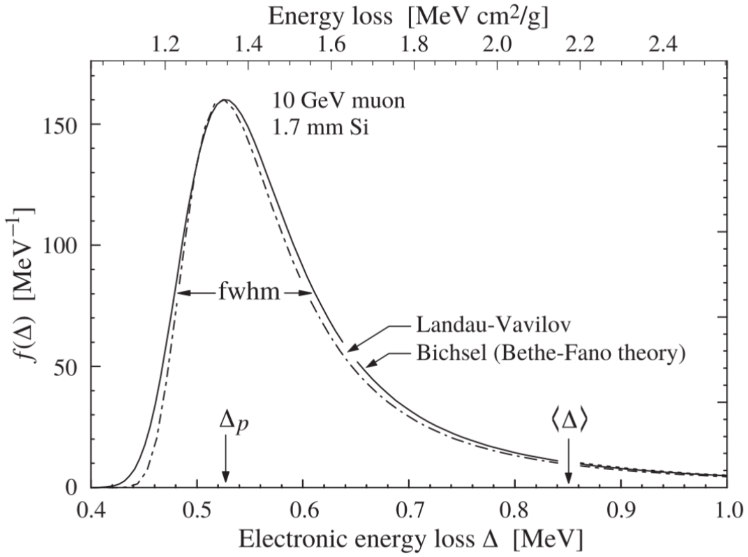

Figure 5.13: Two sample straggling functions for muons on silicon. The most probably energy loss is denoted by the p near 0.5 MeV, while the mean energy loss is indicated by the Δ near 0.9 MeV. This graph highlights the importance of truncating the long tails of the energy loss distribution [10].

Parameterizations of the exact energy loss for particles can be used to approximate the curve shown in Figure 5.12, which take into account the atomic number and mass of the medium, the ionization potential of the medium, and density corrections, among other variables. However, due to impurities, experimentally it can be easier to parameterize the energy loss by setting the minimum ionization for pions to unity and then fitting for the parameters with data. NA61/SHINE uses the "ALEPH parameterization" [67]:

$$-\frac{\langle dE/dx\rangle}{\langle dE/dx\rangle_{\mathrm{MIP}}} = \frac{p_0}{\beta^{p_3}}\left[p_1 - \beta^{p_3} - \ln(p_2 + \frac{1}{(\beta\gamma)^{p_4}})\right]. \tag{5.9}$$

The p_i parameters are found by fitting to the experimental dE/dx data, which will be described in more detail in Section 6.4.

5.2.2 Simulation

Inside the SHINE framework, GEANT4 is the particle tracking package and basis of the detector simulation used for neutrino analyses. Every subdetector inside the NA61/SHINE experiment is modeled as a GEANT4 object, and the SHINE framework stores every simulated track's true position, momentum, production point, and ID, along with a collection of "hits", which are the simulated analog of clusters. Inside the TPCs, electron drift and the TPC response are simulated, and the response is digitized and converted to the raw data format. From this point on, the simulated raw data is passed to the exact same reconstruction as for real raw data. The simulation is a critical component of any physics analysis, as it is the basis for simulating the detector acceptance corrections (among others), as will be discussed in Chapters 8 and 9.

For this thesis, GEANT4 version 10.7 and four different physics lists were used. The first physics list, FTFP_BERT, is recommended by the GEANT4 developers for use in high energy physics simulations and is used for calculation of the central multiplicities' MC corrections [68]. The other physics lists, QBBC, QGSP_BERT, and FTF_BIC, are used for comparisons between MC predictions and experimental data, like FTFP_BERT, as well as to estimate any uncertainties arising from the use of MC corrections. Each physics list represents differing ways of simulating hadronic interactions, specified by their names. "QGS" stands for quark gluon string (model), "FTF" is Fritiof string, "BIC" is Binary cascade, "BERT" is Bertini cascade, and "P" means the standard GEANT4 G4Precompound model is used for de-excitation. So for FTFP_BERT, the Fritiof string model is used for higher energy interactions between 3 GeV and 100 TeV, the Bertini cascade model is used for lower energy interactions between 0 GeV and 6 GeV, and the G4Precompound model is used for de-excitation. Where there is overlap in the energy range coverage between the FTF and Bertini models, Bertini is invoked with a linearly decreasing probability between 1.0 and 0.0, and FTF is complentarily invoked with an increasing probability. (See Allison *et al.* for a deeper discussion of GEANT4 and its physics lists [68]; the GEANT4 online user guide also provides additional details [69].)

As mentioned in Section 3.3, this use of MC simulations and models is chosen to align with the methods used by long-baseline neutrino oscillation experiments. It is worth mentioning that while a specific MC model is necessary for the MC corrections of the neutral and charged analysis (see Section 8.3 for more details), NA61/SHINE's results are not strongly dependent on the specific MC model; any dependence is a result of the finite bins used in the hadron analysis. (This is accounted for with the MC model uncertainty. See Sections 8.7 and 9.5 for more details.)

Chapter 6

Calibration

This chapter will walk through all of the calibration steps necessary to prepare the 90 GeV/c proton-carbon dataset for analysis. Special attention will be paid to the TOFF and DRS calibration, as they were developed by the author of this thesis.

6.1 TPCs

For the TPCs, excluding the energy loss calibration, there are six discrete calibration stages. The first, the pad-by-pad T0s, calibrates the timing shift of every pad in each chamber relative to an arbitrary reference pad. (The whole chamber will get a T0 later.) As the y position of clusters comes the time response of the pad, this stage is necessary to correctly reconstruct cluster positions. For this calibration stage, a special pulser run is taken, where the same signal is sent to every cathode wire in a chamber, with several thousand iterations performed. Figure 6.1 shows a sample signal used in this calibration stage.

After the pulser calibration run is finished, the timing response of the signal for every pad is collected, and a T0 is calculated with a weighted mean. Figure 6.2 shows the T0s calculated for FTPC1 sector 1, which are typically on the order of 30 ns.

The second stage is the calibration of the delay between the S11 trigger and the start of the TPC readout with respect to the S11 trigger. This is referred to as the TPC phase shift. From the hardware construction, the TPC primary clock width was set to 40 ns. With this known clock width and a plot of the TPC phase shift for a representative sample of events the phase shift as

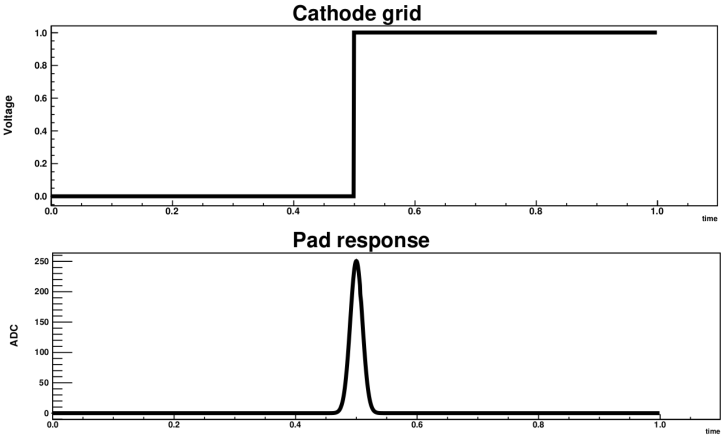

Figure 6.1: A sample signal sent to the cathode wires and an individual pad's response. All units in this plot are arbitrary [70].

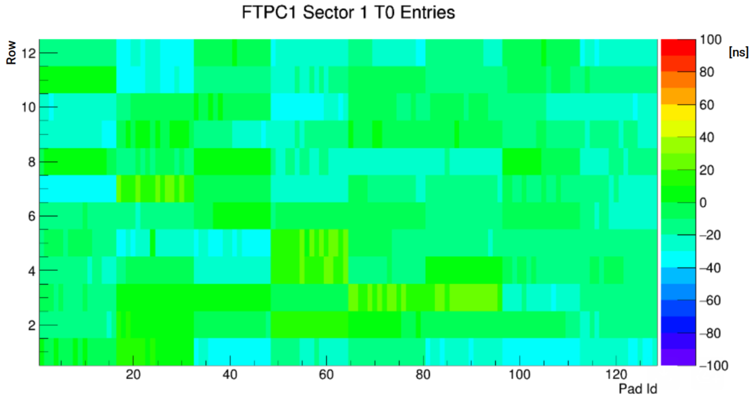

Figure 6.2: FTPC1 sector 1 T0s. The y axis represents the padrow, and the z scale is in ns.

well as the TDC to time conversion factor can be calculated. Figure 6.3 shows the results of the calibration for this dataset.

The next three stages, drift velocity, chamber and global T0s, and chamber alignment, are often the trickiest part of the calibration process; they are dependent on each other and require multiple runnings for the results of each stage to converge. When calculating a cluster's y position, the exact formula used by SHINE is

$$y_c = y_{wp} - v_d(t_{0,\text{ global}} + t_{0,\text{ chamber}} + t_{0,\text{ pad}} + w_t(t_{\text{center}} - 0.5)). \tag{6.1}$$

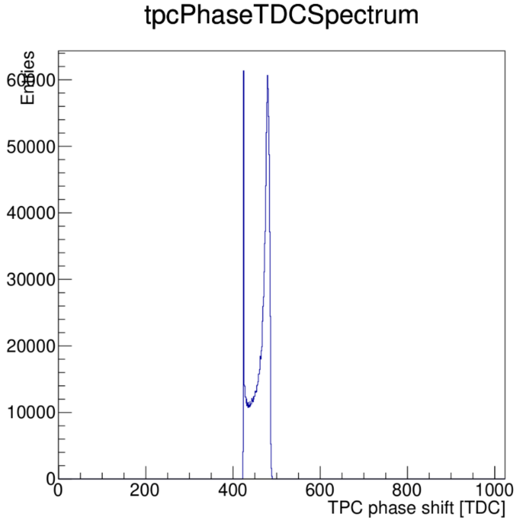

Figure 6.3: The overall phase shift comes from the beginning of this distribution, and the TDC to time conversion factor comes from the width of the distibution and the TPC clock width being set 40 ns.

There are three T0s here. The first, the pad-by-pad T0, was discussed previously. The second, the global T0, is conventionally set so that VTPC1's chamber T0 is exactly -94.6 ns. The third and final, the chamber T0, is the delay between the DAQ's acceptance of the main trigger signal and execution of the signal by each TPC. Each T0 needs to be precisely calibrated (on the order of 1 ns) in order to accurately reconstruct cluster positions. In addition to the T0s, y_{wp} is the position of the sense wireplane, v_d is the electron drift velocity, and t_{center} is the weighted central timebin from the cluster reconstruction. The factor of 0.5 is used to center the measurement in the middle of the time bin.

The first stage in this sequence of three stages calibrates the drift velocity of each TPC, where the exact value is dependent on the gas composition and atmospheric conditions. In the SHINE framework the drift velocity is recorded every 20 seconds, and the initial measurement of the drift velocity comes from monitoring the composition of the TPC exhaust gas. With the initial measurement in hand, the SHINE framework performs track reconstruction, and then looks at the mismatch in extrapolating tracks inbetween adjacent TPC chambers. Using the TOFL as a reference, tracks in MTPCL are matched to TOFL hits. This provides an initial calibration of the drift velocity in MTPCL, and then the other chambers are calibrated starting from MTPCL. Figure 6.4 shows an example of this for VTPC2 and MTPCL. In the drawing, the drift velocty in VTPC2 is too small, resulting in the VTPC2 tracks reconstructing with too large of a y position; this can then be seen by the VTPC2 tracks' displacement above the MTPCL tracks.

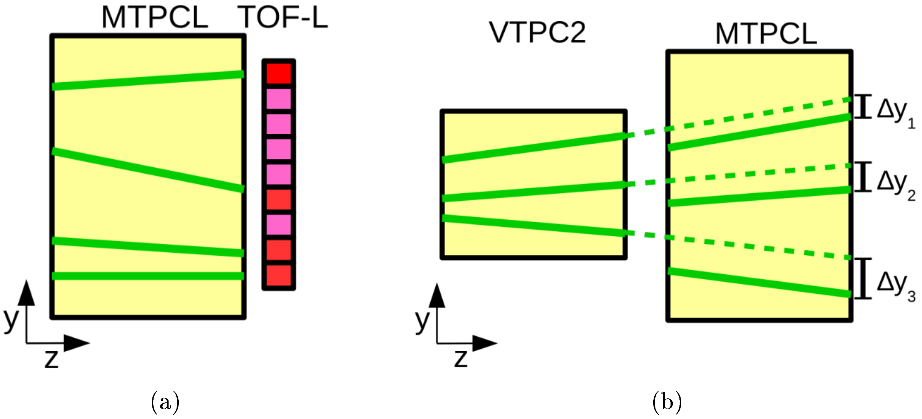

(a) (b)

Figure 6.4: Left: Matching of MTPCL tracks to TOFL hits. The TOFL is used as an absolute reference for the drift velocity calibration. Right: Once MTPCL has been calibrated, it can be used as the reference to calibrate other chambers, like VTPC2. In this schematic, the drift velocity of VTPC2 is too low, resulting in the tracks being reconstructed too close to the pad plane [48].

Figure 6.5 shows the ordering of the drift velocity and which chambers are used as a reference for other chambers. It also highlights part of the difficulty with this stage. At a minimum, the drift velocity procedure needs to be repeated at least three times, as first MTPCL needs to be calibrated, then VTPC2, then GTPC. A miscalibration of any of the earlier reference chambers will result in a miscalibration of later TPCs.

When actually calculating the drift velocity shifts from the calibration, plots of the track mismatch at a common z plane are plotted against one of the track's y positions. This is done for discrete segments of time, where the time windows are made as small as possible while still having reasonable statistics in each window. Then, a simple linear fit is performed in each window. Any slope to the line comes from drift velocity miscalibration, as track mismatch will change linearly moving away from the readout plane. The slope of the line is then used to shift the drift velocity values.

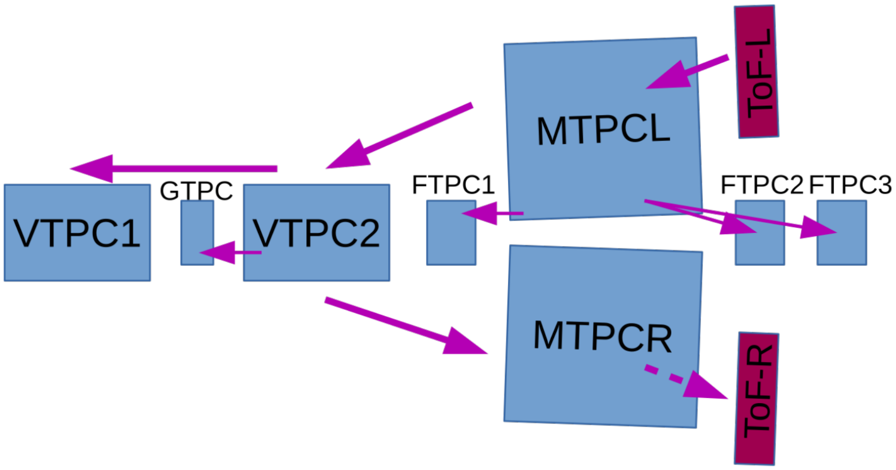

Figure 6.5: The calibration procedure for the drift velocity. MTPCR matching to TOFR is used as a check of the calibration [48].

Once the drift velocity has been properly calibrated (along with the T0s), these same plots can be used to calibrate the chamber positions; the intercept of the line gives the chamber offsets. Figure 6.6a shows an example of a track mismatch plot where the drift velocities and chamber positions are well calibrated, as can be seen from the distribution's slope and intercept. Figure 6.6b shows a poor drift velocity calibration. This (in addition to a small x displacement) resulted in the beam momentum for this dataset reconstructing at 98 GeV/c instead 90 GeV/c before being fixed. The drift velocity calibration is considered done when the slope in every time window for every chamber is less than 0.001.

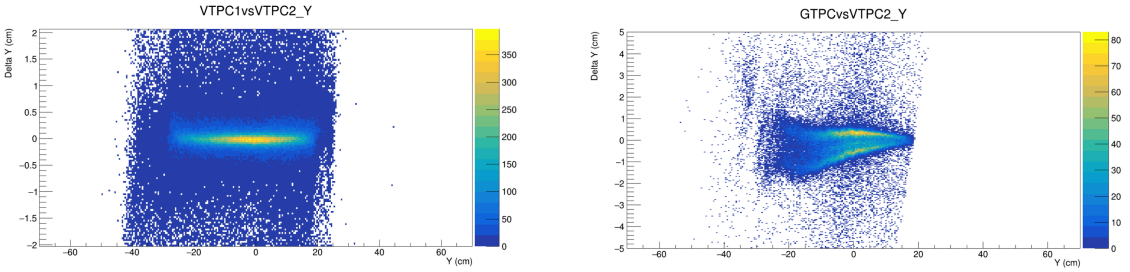

(a)

(b)

Figure 6.6: Left: Track mismatch plot with good drift velocity calibration and no chamber offsets. Right: Track mismatch plot with poor drift velocity calibration, as can be seen by the slopes of the distributions. The multiple distributions results from different time windows having varying degrees of miscalibration.

While this track mismatch procedure can be used to calibrate the chamber drift velocity and alignment, a separate procedure is needed for the global and chamber T0s. For the T0s, tracks that exit the bottom point (cathode end) of the TPC are selected. Then, the final cluster on each of these tracks is taken and its raw drift time is collected. A plot of all of the raw drift times will have a peak that is equal to the total drift time in the chamber, plus the global and chamber T0. Subtracting off the total drift time then gives the T0s. As mentioned earlier, the global T0 is defined by setting VTPC2's chamber T0 to -94.6 ns; all other chambers can then be calibrated with the global T0 defined. Figure 6.7 shows the results of this calibration stage for VTPC1. For the GTPC and the FTPCs, there can be additional difficulties to this stage as very few tracks pass through the bottom of these TPCs. To work around this, additional cuts are required, such as restricting the padrows or adding in loose cuts around an estimated total drift time.

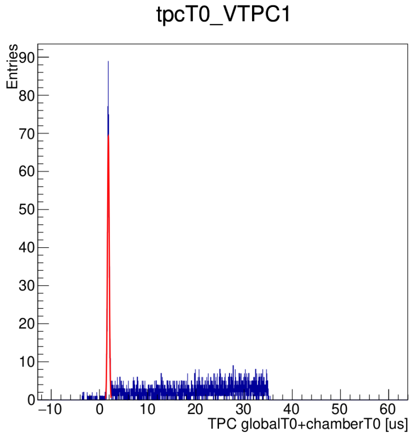

Figure 6.7: The results of the T0 calibration for VTPC1. The line is the data, and the red line is a Gaussian fit to the T0 peak.

The drift velocity, the T0s, and the chamber alignment are all dependent on each other, which increases the difficulty of properly calibrating these three detector parameters. Without a well-measured drift velocity, the raw drift time of clusters cannot be properly calculated, which means the T0s cannot be extracted. Without the T0s, the drift velocity cannot be calibrated, as the track y position is dependent on the T0s. (The same applies for the chamber y position.) To work around this, the three stages are run iteratively multiple times, until the results of every stage converges.

The final TPC calibration stage, besides the energy loss calibration, is the TPC residuals correction. The residuals correction applies local position distortions inside each TPC, and is designed to remove any distortions resulting from electric field inhomogeneities, mechanical component sag, or other, unaccounted for effects. (It is possible for the residuals correction to accidentally correct for uncalibrated chamber angle and position shifts, but any evidence of this would necessitate recalibration of the chamber alignment.)

To calculate the residuals correction, the TPCs are finely binned into $1 \times 1 \times 1$ cm cubes. For a representative sample of the dataset, track reconstruction is performed and a residual is calculated between every cluster on a track and the track's extrapolated position at that cluster. All of the (x, y) residuals are gathered, and if a bin has at least ten total entries, the residual correction for that bin is the average of all of the track-cluster residuals. Bins with too few entries do not get a correction. Figure 6.8 shows the results of the residuals correction; the effects of electric field distortions can be seen in the repeating spikes near sector edges.

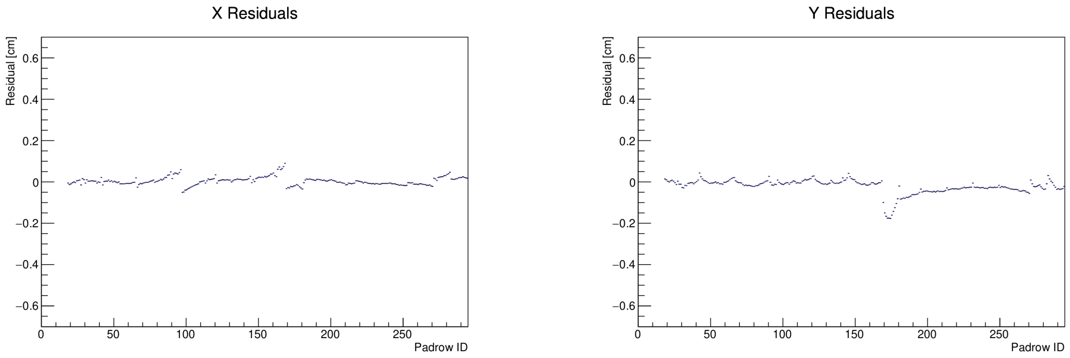

(a)

(b)

Figure 6.8: Left: The average x local residual correction for each padrow. Right: The average y correction. The repeating spikes are due to electric field distortions, and correcting for this is one of the primary reasons for applying the residuals correction.

6.2 BPDs

As the extrapolated beam track is used for both event cuts and as the (x, y) position of the main vertex, the position of each BPD needs to be well calibrated. To calibrate their positions, VTPC1 tracks are extrapolated to the target's center in z, and the impact parameters, the difference between the beam track's (x, y) and the VTPC1 track's (x, y), is plotted. Any overall displacement represents a shift in the BPDs' positions. This stage was performed for the dataset in this thesis, but no shift was required, as the calibration from a dataset taken directly before the 90 GeV/c dataset was still applicable. Figure 6.9 shows the results of the calibration.

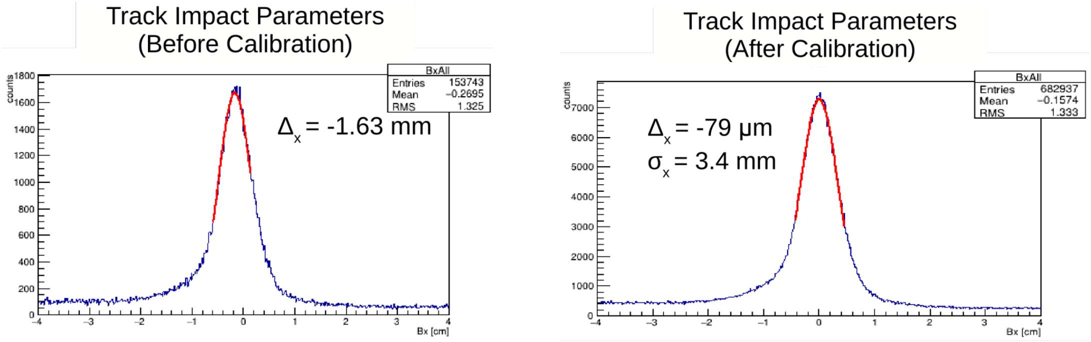

(a) (b)

Figure 6.9: Left: The x impact parameter before BPD-TPC alignment. Right: After alignment [48].

6.3 Target Calibration

Once the BPDs and TPCs are calibrated, the position of the target can be calibrated as well. Having an accurate production point greatly improves the momentum reconstruction of vertex tracks, hence the target position calibration. The target's z position is calibrated by using a least-squares three-dimensional fit for the vertex position in every event. The center of the resulting distribution over a representative sample of events gives the center of the target position; the result of this stage is shown in Figure 6.10.

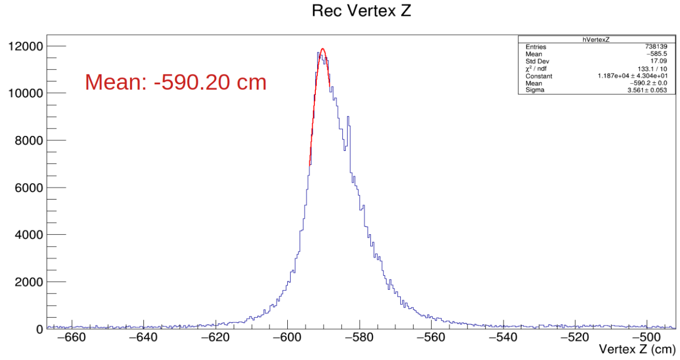

Figure 6.10: The results of calibrating the target z position by allowing the vertex position to float event-by-event. The bump at -583 cm is the seed position of the target before calibration.

6.4 Energy Loss

Once the BPDs, target, and TPCs have been calibrated, the final stage for the TPCs can be started; this is the energy loss calibration. The energy loss calibration is broken into 5 different stages: Kr^{83} gain calibration, time correction, y dependence, sector constants, and chip gain.

The first stage, the krypton gain calibration, corrects for gain fluctuations mainly resulting from the FEE pre-amplifier response. Kr^{83} gas is introduced in each TPC via a Rb^{83} source (Rb^{83} decays predominantly via electron capture to Kr^{83}), and then the krypton decays over the course of hours through several well-defined (in energy) pathways. These decays deposit electrons inside the TPCs at specific expected energies, with the most prominent peak occuring at 41.6 keV. Figure 6.11 shows the expected energy spectrum from the Kr^{83} decay.

To actually calculate the corrections, the data needs to be taken with enough decays for each pad to receive a sufficient number of decays, ~ 1000. Once each pad has recorded adequate statistics, the peak position corresponding to the 41.6 keV decay is used to calculate the gain for each pad. This calibration stage drastically increases the charge resolution of the TPCs, as can be seen in Figure 6.12.

The next stage, the time dependence calibration, calculates the time-dependent, charge-amplification gains for each TPC sector. The time dependence of the gain results from a variety of factors, including atmospheric conditions and high-voltage supply drift; the time dependence needs

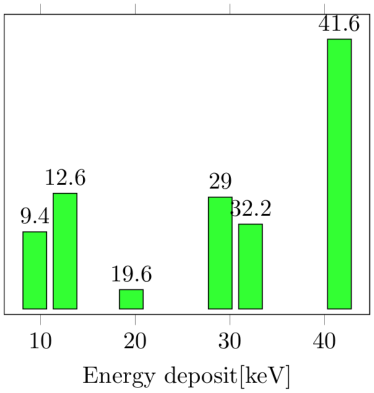

Figure 6.11: The electron energy output of the most prominent decay channels of Kr^{83} [71].

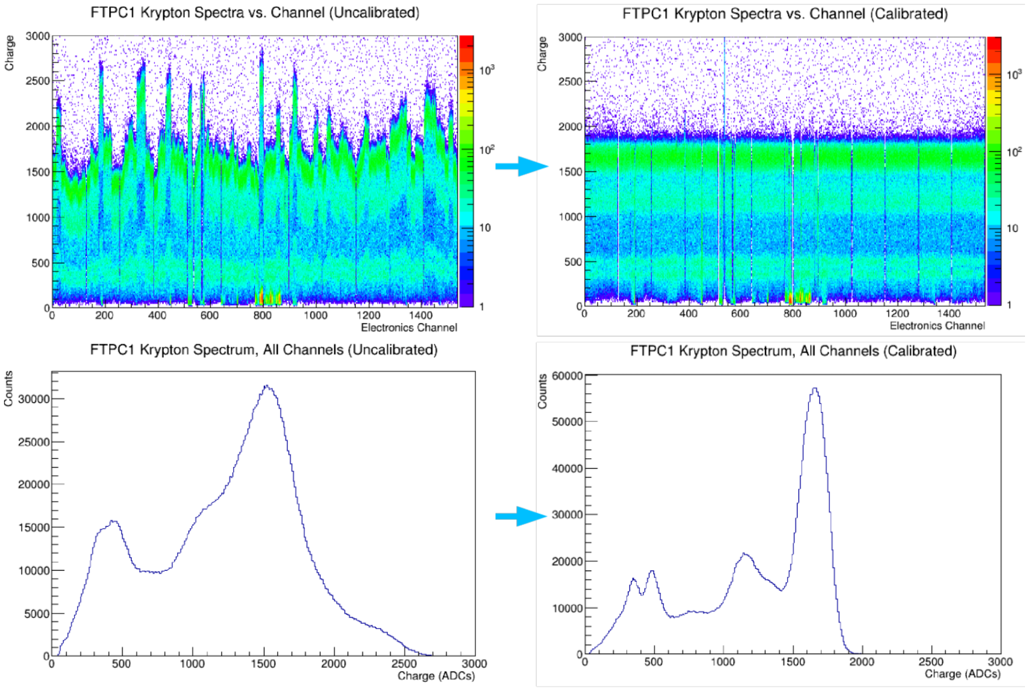

(a) (b)

Figure 6.12: Left: The collected charge spectrum from Kr^{83} before calibration for all FTPC1 channels. The bottom image shows a one-dimensional projection of the top image. Right: After calibration. All six expected decay peaks are visible after performing this calibration stage [48].

to be corrected for to allow the grouping of the energy loss across the whole dataset. To correct for the gain fluctuations, a Gaussian smoother corrects for statistical flucuations while calculating the gain in each time window (by default set to 5 minutes)

$$g(t) = \frac{\sum_i w_i q_i}{\sum_i w_i}, \;\; w_i = e^{-\frac{(t_i - t)^2}{2\sigma_s}}. \tag{6.2}$$

Here $g(t)$ is the gain measurement, t is the center of the time bin, t_i is the time of the individual charge i, and σ_s is the smoothing width, which has a default value of 15 minutes.

With the gain calculated in each time window, the gains are then normalized to the overall average gain measurement for the sector, and each time window now has a correction factor. Figure 6.13 shows the results of this calibration stage, which lowers the post-calibration, time-dependent fluctuations to less than 1%.

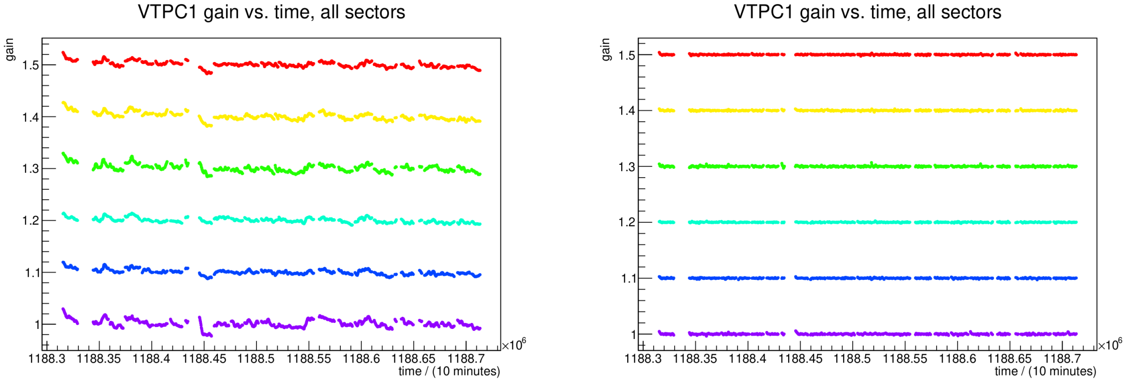

(a) (b)

Figure 6.13: Left: The calculated gain for the six VTPC1 sectors in five minute time windows. Each line corresponds to one sector in VTPC1, and is centered at $1+0.1(sectorId-1)$. (The purple line is sector 1, and the red line is sector 6.) Right: The gain after applying the time-dependent gain corrections.

Following the time-dependent gain corrections is the y-dependence correction. As the electrons drift from the point of ionization inside the TPC, they systematically lose charge, mainly due to attachment to oxygen and water contaminants inside the gas volume. The charge loss is modeled as an exponential process, which is then approximated to first order.

$$q(y) = q_i e^{-cy} \approx q_i(1 - cy), \tag{6.3}$$

where q_i is the initial charge at the point of ionization, c is a constant describing the charge loss, and $q(y)$ is the y-dependent measured charge. (As shown in Figure 6.14, a linear approximation is reasonable.) With this approximation for the charge loss, the asymmetry factor $a(y)$ is then defined by

$$a(y) = \frac{q(y) - q(-y)}{q(y) + q(-y)} \approx \frac{(1 + cy) - (1 - cy)}{(1 + cy) + (1 + cy)} = -cy. \tag{6.4}$$

In the first-order approximation, the asymmetry factor is easily calculated from data, and the y-dependent correction applied to each cluster is $(1 - cy_c)$, where y_c is the production position of the cluster. Figure 6.14 shows the calculation of c from fitting to experimental data for VTPC1, sector 2.

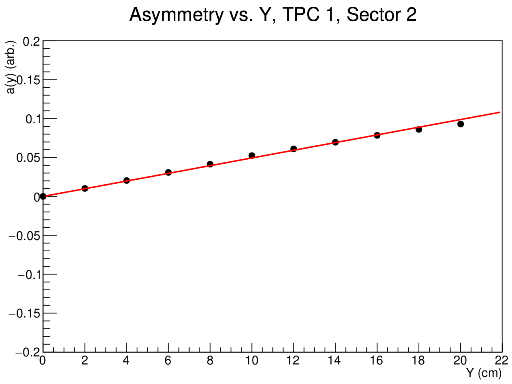

Figure 6.14: Y-dependent charge asymmetry. The constant describing the charge loss, c, is the slope of the best-fit line.

The most difficult part of the energy loss calibration comes next, the sector constant calibration; the sector constant calibration calculates the sector ampflication factor for each sector inside the TPCs. This amplification factor converts the raw cluster ADC to a value on the Bethe-Bloch curve, normalized to the minimum ionization point for pions.

To run the sector constants calibration, tracks are first split into segments spanning a single sector, and each segment's truncated mean energy loss is collected and added to finely-grained momentum bins. A multi-species dE/dx fit (see Chapter 9 for more details on the fit) is performed in each bin, and the average of the pion means, for one sector, are used to calculate the sector constant.

Figure 6.15 shows a sample fit in one momentum bin for VTPC1 sector 2. Only momentum bins with high enough pion purity are considered, as shown in Figure 6.16. The pion purity is a measure of the overlap between the pion distribution and other particle's distributions. A large overlap could lead to an unreasonable estimate for the pion mean.

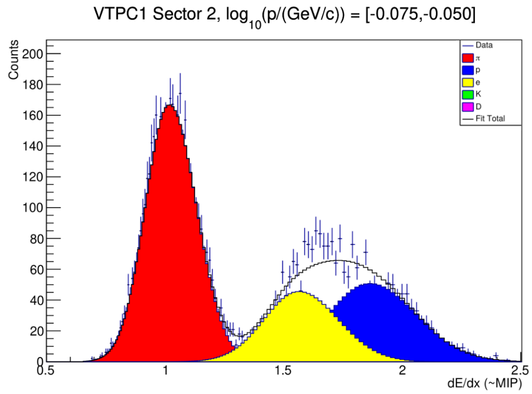

Figure 6.15: A sample fit for the pion mean during the sector constants calibration. The center of the fit pion distribution is used to calculate each sector's amplification.

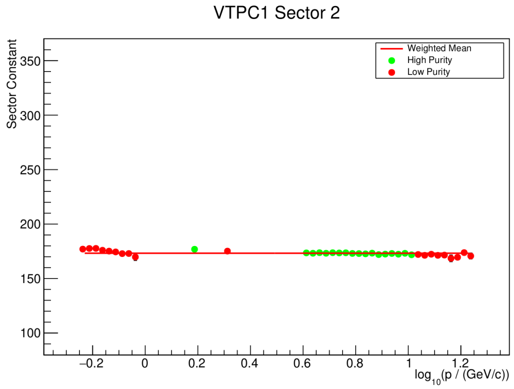

Figure 6.16: The calculation of the sector constant from averaging all of the high-purity momentum bins. The bins entering the calculation are shown in green.

The final step in the energy loss calibration calculates the gain for each pre-amplifier chip on the FEEs, as each chip can vary in gain. For this stage, the track's charges are binned by chip ID and normalized to each track's mean dE/dx. In order to decouple this stage from the previous stage, the gain factors for one sector are normalized to the mean gain factor in the sector, and the chip gain calibration comes after the sector constants calibration.

Once all of the energy loss calibration stages have finished, deviations from the expected Bethe-Bloch value for tracks quantifies the accuracy of the calibration and the energy loss measurements. Figure 6.17 shows the measured pion Bethe-Bloch deviations, and the average deviation being well under 1% indicates excellent energy loss calibration.

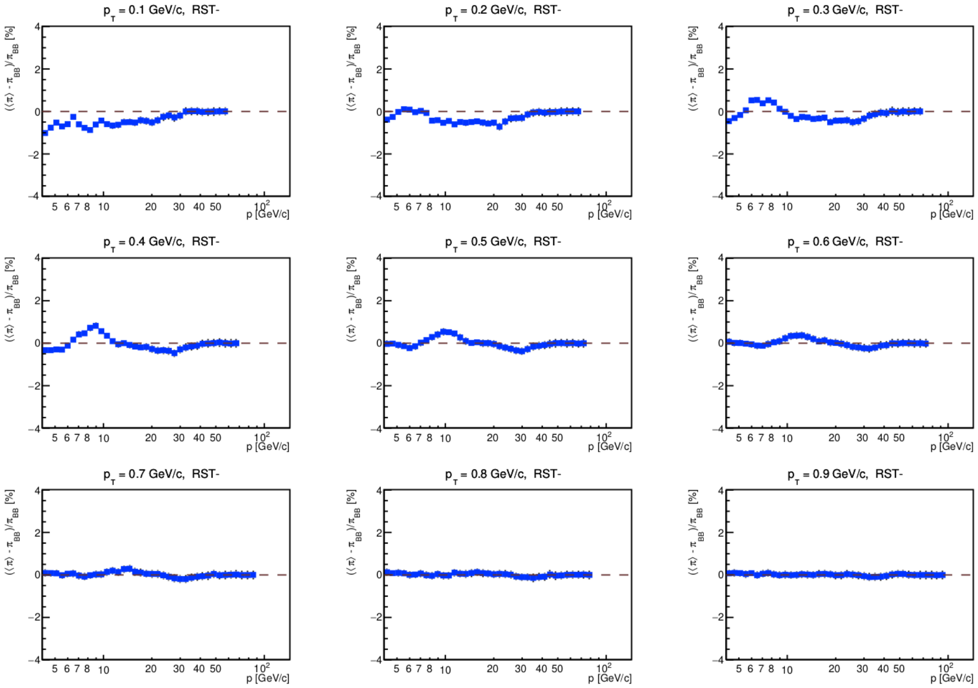

Figure 6.17: Average deviations from the expected Bethe-Bloch values for π^- tracks after calibration. “RST” means Right Side Track, which will be explained in Chapter 9.

6.5 DRS

The readout electronics for the TOFF were replaced with DRS boards in 2017, and many other subdetectors moved to DRS readout after 2022. These boards allow for full quantization of the detector signals, but they require prior calibration of both the cell widths in time and each individual cell’s ADC to voltage conversion factors. In the SHINE framework, this is based on the procedure developed by Stricker-Shaver *et. al* [72], and requires special calibration runs. The calibration coefficients are expected to be stable in time (but not temperature), but during NA61/SHINE data taking runs the calibration runs are performed every couple of days to be safe.

The form of the readout for one DRS channel is 1,024 samples of charge at discrete times, initially defined by cell number and recorded ADC by that cell. Calibrating the DRS boards provides a conversion from ADC to voltage (referred to as voltage calibration) and also gives each cell a time width (referred to as time calibration); this was shown earlier in Figure 5.9. Time calibration of the DRS boards requires the voltage calibration, so the voltage calibration comes first.

During the voltage calibration, every channel on each DRS board is provided a sequence of step voltages. Inside NA61/SHINE, 100 events are recorded at 0.0 V, 0.1 V, and so on up to 0.9 V. Then, each cell's recorded ADC response is averaged at the voltage steps, and a straight-line fit provides the gain and offset coefficients for each cell; the gain converts from ADC to voltage, while the offset places the baseline of the cell at 0 V. Figure 6.18 shows an example of this for one cell of the TOFF DRS boards. Although the process is simple, every DRS board has 32 channels and four synchronization channels, which means one board requires $73,728$ floats just for the voltage calibration. With almost 200 total boards in the NA61/SHINE experiment, the storage and handling of the calibration becomes arduous, a major drawback of the DRS readout electronics.

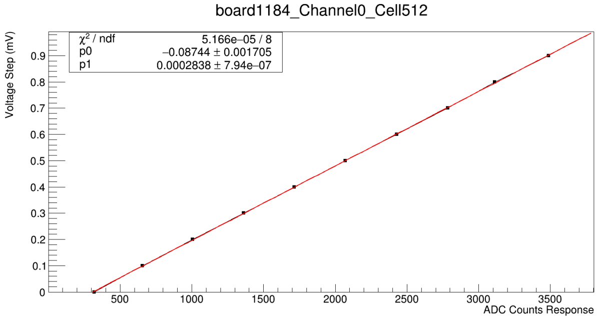

Figure 6.18: A sample fit to calculate the gain and offset coefficents for one cell of one of the TOFF DRS boards. Each point is the average of 100 events collected at that step's voltage.

After the voltage calibration is finished, the time widths of each cell can be calculated. To perform the time calibration, a large number (1000) of sine waves of known frequency and random phase are sent to each channel; Figure 6.19 shows a sample calibration signal. Once the software has utilized the voltage calibration and converted the calibration signal from ADC to voltage, the signal is then normalized to an amplitude of 1.0. The normalization is accomplished by measuring the voltage at each ± peak of the signal, and then averaging all of the peaks to place them at 1.0. For a very small number of signals some of the peaks may differ by more than 5% from the other peaks, and these are excluded in the normalization calculation.

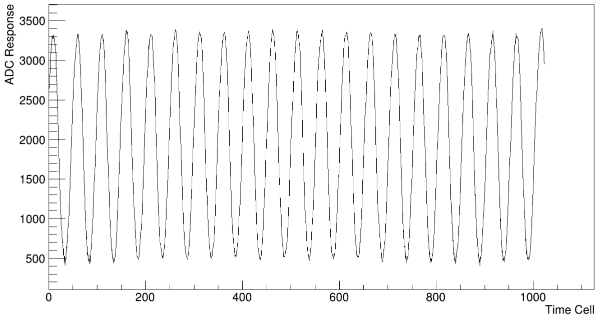

Figure 6.19: A sample uncalibrated signal used in the DRS time calibration.

With the input signal oscillating around zero with an amplitude of 1.0, the next steps of the DRS time calibration are performed in two separate parts. The first part, the local time calibration, initially estimates cell widths approximating the zero crossings as straight lines:

$$\frac{\Delta t_i}{\Delta U_i} = \frac{\sum_i \Delta t_i}{\sum_i \Delta U_i}. \tag{6.5}$$

The ratio of the time difference between two cells, Δt_i, over the voltage difference, ΔU_i, is proportional to the total ratio; this is valid as long as the signal is a straight line. For the total time difference, the default time cell width (0.2 ns for the TOFF DRS boards) is used. Figure 6.20 shows a sample of this, with the boundary voltage set at 0.4 V. In practice, this calibration procedure is robustly independent of the boundary voltage. There were no changes to the calibration results in the range of 0.2 to 0.8 V.

The local time calibration only provides a rough estimate of each cell width, and then the global time calibration refines these estimates. As the frequency of the input calibration signal is known, the global time calibration adds all of the cell widths between two zero crossings, and compares the summed value to the expected value. Any difference is used as a correction factor

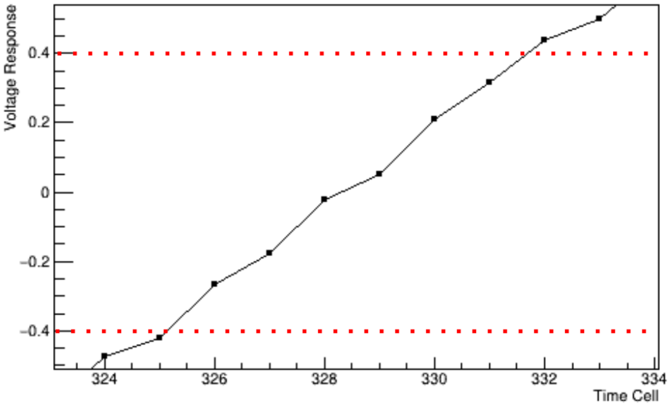

Figure 6.20: In the local time calibration of the DRS boards, the signal is approximated as a straight line around zero crossings. An initial estimate for each individual cell's time width comes from the voltage difference between adjacent cells. The red lines are indicating a possible boundary voltage of 0.4 V.

for the cells in the sum. To elaborate, if the expected period was 10 ns, and the measured period was 10.1 ns, then a correction factor of 10/10.1 is applied; the cells widths were too long, and they needed to be shortened.

As the cell measurements are discrete, Figure 6.21 shows an additional important step in calculating the measured period. To correct for the individual measurements not occuring at 0 V, the offset of the cell width from zero (in time) is added into the measurement of the signal's period.

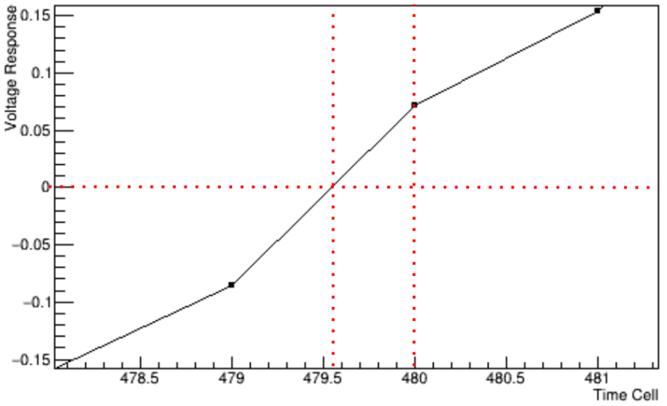

Figure 6.21: When measuring the period between two zero crossings in the global time calibration, the voltage measurements do not occur at exactly 0 V. In this plot, the time between the actual zero crossing and the measurement at cell 480 needs to be added to the measured period.

From either the signal generator or the DRS response, there are differences in the recorded voltage shape between the falling and rising edges of the input calibration signal. (The falling edges' slopes were found to be up to 20% steeper than the rising edges' slopes.) To mitigate these effects, the local time calibration averages the initial estimates over all of the input signals for rising and falling edges separately, and then combines the two averages at the end. In the global time calibration, only zero crossings on the same type of slope (rising or falling) are used. So in practice, if there were eight zero crossings in one signal, the procedure is: correction factor for cells between zero crossings 0 and 2, followed by 2 and 4, 4 and 6, 6 and 8, 1 and 3, 3 and 5, 5 and 7, 0 and 4, 4 and 8, and so on. Including not directly adjacent zero crossings slightly improves the overall calibration results, but greatly improves the computational intensity.

After the voltage and time calibration are finished, their results are tested by once again looking at the expected versus measured period between zero crossings. If the boards are well calibrated, they should accurately measure the period of the input sine wave. Figure 6.22 shows the results of this before the local time calibration, after the local time calibration, and after the global time calibration. The local time calibration leaves "global" structures that are removed by the global calibration, hence the naming scheme. In practice the width of the distribution in 6.22c was found to be two to four times larger than expected. After some investigation, the most likely cause found was small deviations of the input signal's frequency; each channel was found to have $\sim 0.2\%$ frequency deviations, which corresponds to the period of the wave changing by ±20 ps. This was mitigated by tempering the global correction factor and only applying 10% of it for each zero crossing pair. Figure 6.23 shows the fit input signal frequency over 1000 calibration events, after voltage calibration and assuming a cell time width of one.

The final part of the DRS calibration is event-by-event timing synchronization. On the DRS boards, eight channels are readout by one chip; each chip has a timing offset from the start signal relative to all other chips in the event. In order to synchronize the chips together, the chips have a synchronization channel, where the same synchronization signal is sent to every chip. In the 2017 data the synchronization signal was the S11 signal, while for data after 2022 it was a sine wave.

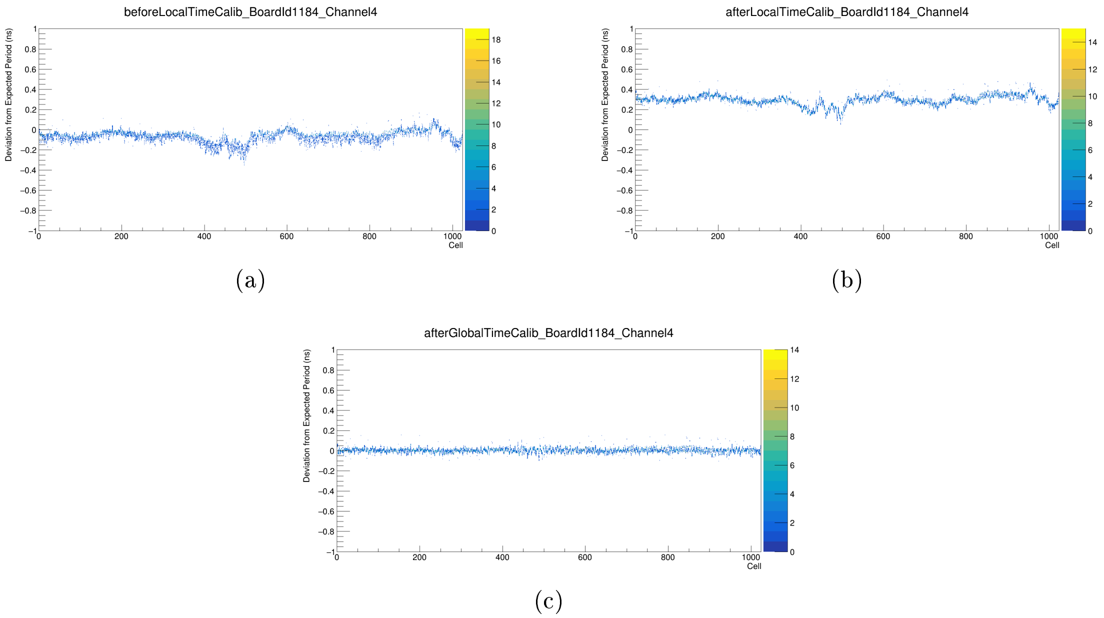

beforeLocalTimeCalib_BoardId1184_Channel4

afterLocalTimeCalib_BoardId1184_Channel4

afterGlobalTimeCalib_BoardId1184_Channel4

(a) (b)

(c)

Figure 6.22: The deviation from the expected period during the three stages of the time calibration. Top Left: Before the local time calibration, assuming cell widths of 0.2 ns. Top Right: After the local time calibration. Bottom: After the global time calibration.

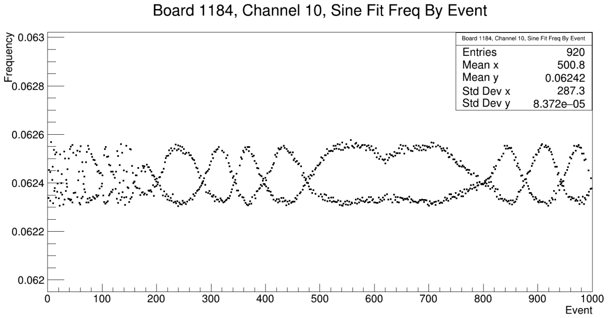

Board 1184, Channel 10, Sine Fit Freq By Event

Figure 6.23: The fit frequency to all of the input time calibration signals after applying the voltage calibration and assuming a cell time width of one. The deviations around the expected frequency of 0.0624 are the most likely cause for the distribution in Figure 6.22c being larger than expected.

The timing of the signal at each chip is used to calculate each chip's T0 for the event.

6.6 TOFF

Coming last are the four stages of the TOFF calibration, as the TOFF calibration relies on the energy loss and DRS calibrations. There are four separate stages: scintillator bar position, light propagation speed, T0, and S1 jitter correction.

For the first stage, for each scintillator bar, a plot of all track positions at the TOFF wall is made, where only events in which the scintillator had a response above a minimum voltage (25 mV) are considered. Performed over a representative sample of events, this builds up a clear outline of each scintillator bar over the background. This stage is only performed in the x direction, as the bars extend past the MTPCs in y. (Any offsets in y or z will be corrected for during the T0 calibration.) Once the distribution is made, a fit of the form

$$f(x) = \frac{A}{2}[\tanh(\mu(x - x_0 + \Delta)) - \tanh(\mu(x - x_0 - \Delta))] + C, \tag{6.6}$$

is used to calculate the each scintillator's x position. x_0 is the center of the scintillator, μ corresponds to the slope of the sides of the fit, Δ is the half-width, A is the peak height, and c is the background. Figure 6.24 shows the results of one of these fits.

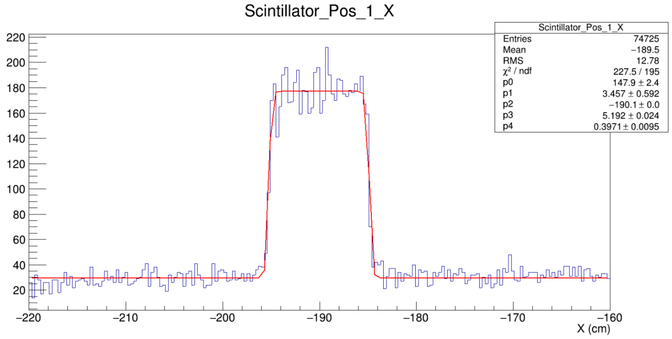

Figure 6.24: Calibration of one of the scintillator bars of the TOFF wall. Each entry is the position of a track extrapolated to the z plane of the TOFF wall, for an event where the scintillator had a response above the minimum required voltage. The red line is the result of fitting the data to Equation 6.6.

When the particle passes through a scintillator bar, the light takes time to travel from the scintillation point to the PMTs. Reconstruction of the actual hit time from the recorded time at the PMT requires knowing the light propagation speed inside each scintillator. To calculate these speeds, the second TOFF calibration stage plots the arrival time of each hit as a function of the hit's y position (this requires matching tracks to TOFF hits). The inverse slope of the distribution gives the light speed, and the results from the top and bottom PMTs are then averaged. Figure 6.25a shows the results of this for one PMT next to Figure 6.25b, which shows the overall results for the entire TOFF wall; there are deviations between scintillators up to 5%, which is why this stage is necessary for proper TOFF reconstruction.

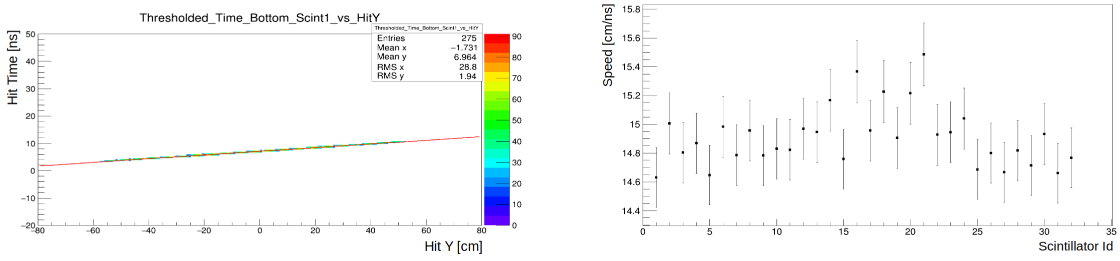

(a) (b)

Figure 6.25: Left: A plot of the hit time versus the matched track's y position. The inverse slope of the best-fit line gives the light propagation speed. Right: All calibrated light speeds in the TOFF wall.

The next stage, the PMT T0s, requires the energy loss calibration and calculates the timing offsets for all of the PMTs. To start, this stage selects low-momentum (< 10 GeV/c) pion tracks by selecting tracks within 3σ of the expected pion Bethe-Bloch value. Then, for each track, the measured and predicted time-of-flight is calculated, and the average difference gives the PMTs T0. This stage is performed twice. After running once, an additional cut on the reconstructed track mass is added to enhance the pion selection. Figure 6.26 shows the Gaussian fit to calculate one PMT's T0.

The final of the many calibration stages is the S1 jitter correction, a small event-by-event timing correction. In the NA61/SHINE experiment, there are four PMTs attached to the S1 scintillator, but the start signal timing, which is used to calculate particles' time-of-flight, comes from just the S11 PMT. (S11 means the first of the four PMTs attached to the S1 scintillator.) If the beam position was stationary for the entire dataset, there would be no need to apply any correction. However, as the beam position shifts, the distance between the beam at the S1 scintillator and the S11 PMT changes. This causes the light travel time between the actual arrival of the beam at the

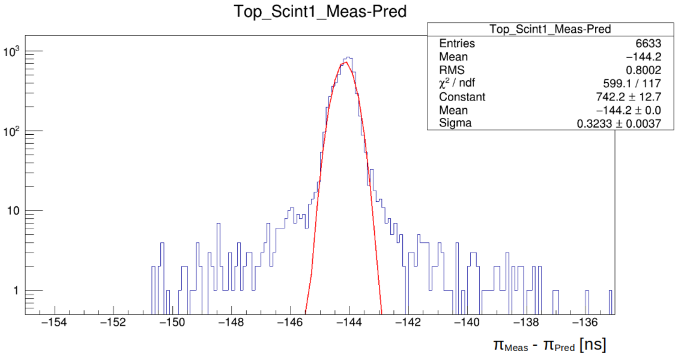

Figure 6.26: The mean of the measured minus predicted time-of-flight for low momentum pions gives the PMT's T0.

S1 and the output of the S11 trigger signal to change event-by-event. While the jitter is a very small effect, it smears the time-of-flight and can be corrected. As the PMT T0 calibration removes the light travel time in the S1 from the average beam position, only shifts from the average position need to be corrected for. The average timing response of the S11, S12, S13, and S14 PMTs are collected, and then the jitter correction for each event is

$$t_{\mathrm{Jitter}} = \frac{1}{4}(\Delta \mathrm{S11} + \Delta \mathrm{S12} + \Delta \mathrm{S13} + \Delta \mathrm{S14}). \tag{6.7}$$

ΔS11 is the difference in the time recorded for the current event and the average time recorded by the S11 for the whole dataset. If the jitter is correctly removed, then the distribution of the predicted minus measured time-of-flight for pions should be flat as a function of the S12, S13, and S14 timing. Figure 6.27 shows this disttribution before and after applying the jitter correction.

With the calibration done, the mass of particles can finally be determined, as seen in Figure 6.28. To test the resolution of the TOFF wall, low-momentum pion tracks that traverse two scintillators are selected. The difference in the measured timing gives the resolution of the TOFF wall, as shown in Figure 6.29; the resolution of the TOFF wall was measured at 120.4 ps.

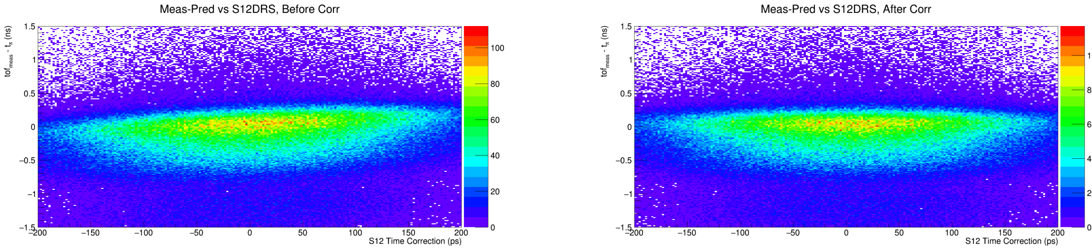

(a) (b)

Figure 6.27: The effects of the S1 jitter correction can be seen by looking at the measured minus predicted time-of-flight for pions as a function of the S12, S13, and S14 timing. Left: Before applying the jitter correction for the S12. Right: After. The flat distribution indicates the time-of-flight has no dependence on the timing of the S12 PMT signal, as desired.

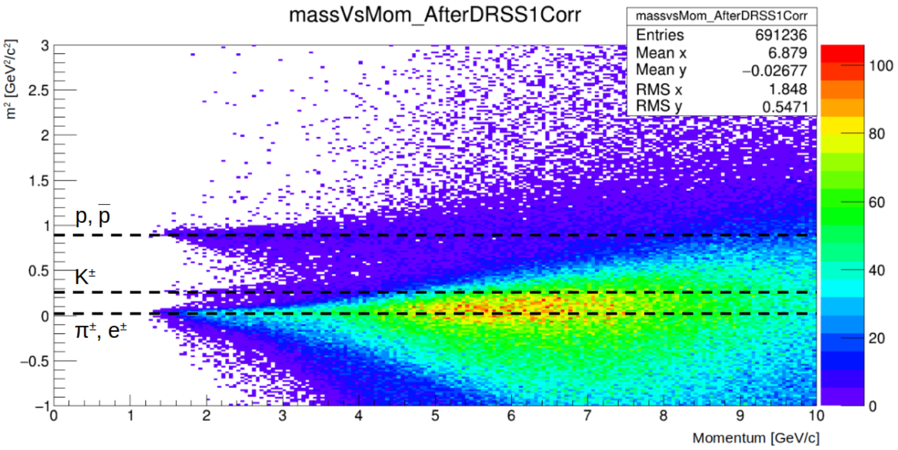

Figure 6.28: Reconstructed mass squared plot from the TOFF wall after applying all calibration stages.

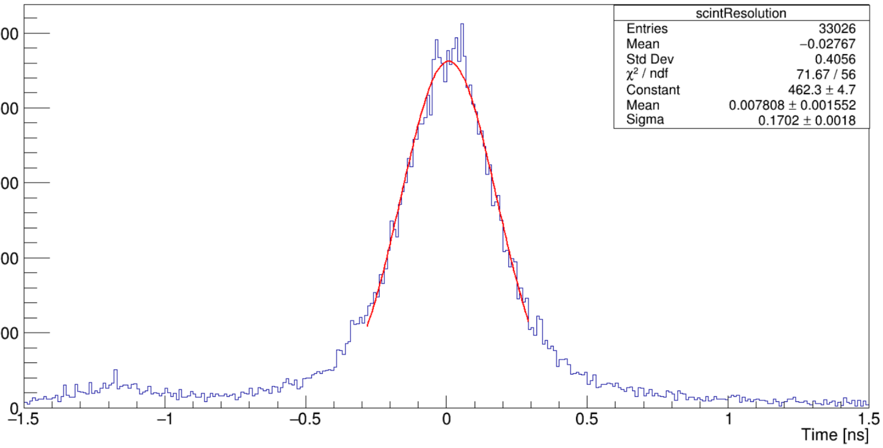

Figure 6.29: The TOFF resolution is measured by taking the timing difference of pion tracks passing through two scintillators.

Chapter 7

Total Cross Section Measurements

The total production cross-section measurement between a proton and single carbon nucleus is necessary to normalize the hadron multiplicity measurements. During data taking periods, NA61/SHINE takes data with the target both "in" and "out", where target in means the target is placed in-line with the beam line, and target out means the target is removed from the beam line. This allows for the subtraction of interactions occurring outside the target volume, which removes a small, but significant, number of interactions. The 2017 proton-carbon 90 GeV/c dataset being analyzed for this thesis was taken during the first week of September, and the extra 2023 cross-section data (analyzed in this chapter) was taken in one 24 hour period starting on July 24th.

For the purpose of this thesis, the inelastic cross section is defined as any interaction that is not elastic, meaning the carbon nucleus is not left intact. With this definition, the inelastic cross section can then be divided into two parts, the quasi-elastic cross section σ_{qe} and the production cross section σ_{prod}.

$$\sigma_{\mathrm{inel}} = \sigma_{\mathrm{prod}} + \sigma_{\mathrm{qe}}. \tag{7.1}$$

Quasi-elastic interactions do not involve the production of new hadrons, like $\pi^{\pm}$ or Λ, but they can involve fragmentation of the carbon nucleus, where protons or neutrons splinter off. Elastic interactions have no produced new hadrons, and no outgoing protons or neutrons besides the incoming beam particle.

The measurement of the inelastic and production cross sections in NA61/SHINE begins with the measurement of the trigger cross section, as this is the quantity the experiment actually measures. To start, the trigger probability is the ratio of the number of T1 triggers (identified beam particle, S4 hit) over the number of T2 triggers (identified beam particle, no S4 hit).

$$P_{\mathrm{In/Out}} = \frac{N(T1)_{\mathrm{In/Out}}}{N(T2)_{\mathrm{In/Out}}}. \tag{7.2}$$

P_{In} is the trigger probability with the target in, and P_{Out} is the trigger probability with the target out.

To perform the target-out subtraction, a measurement of the trigger probability is made for both target-in and target-out configurations. Target-out measurements are taken during the same run period as the target-in data and with the same detector configuration. As mentioned earlier, performing target-out subtraction corrects for the small number of interaction triggers occurring due to effects outside of target-proton interactions, such as interactions in beam line detectors. To remove the target-out contribution, the trigger probability is calculated as

$$P_{\mathrm{trig}} = \frac{P_{\mathrm{In}} - P_{\mathrm{Out}}}{1 - P_{\mathrm{Out}}}. \tag{7.3}$$

For thin targets, P_{trig} is proportional to the length of the target L, the density of the target nuclei n, and the trigger cross section:

$$P_{\mathrm{trig}} = nL\sigma_{\mathrm{trig}}. \tag{7.4}$$

To account for beam attenuation inside the target, the target length L needs to be replaced with L_{eff}, where

$$L_{\mathrm{eff}} = \lambda_{\mathrm{abs}}(1 - e^{-L/\lambda_{\mathrm{abs}}}), \tag{7.5}$$

and $\lambda_{\mathrm{abs}} = A/(\rho N_A \sigma_{\mathrm{trig}})$ is the absorption length. (The absorption length is the distance of material traversed when the probability of the beam particle not being absorbed has dropped to $1/e$. It is

~ 50 cm for a 90 GeV/c proton in carbon, and the target length is 1.48 cm.) With this correction in place, and rewriting the number density in terms of Avogadro's number N_A, the material density ρ, and the target's atomic number A, Equation 7.4 can be rearranged to give

$$\sigma_{\text{trig}} = \frac{AP_{\text{trig}}}{\rho L_{\text{eff}} N_A}. \tag{7.6}$$

In the limit $L \ll \lambda_{\text{abs}}$, Equation 7.6 can be simplified to

$$\sigma_{\text{trig}} = -\frac{A \ln(1 - P_{trig})}{\rho N_A L}. \tag{7.7}$$

After obtaining a measurement of the trigger cross section, NA61/SHINE has to use MC correction factors to obtain the individual contributions of elastic, quasi-elastic, and production events that scatter out of the S4. (Unfortunately, NA61/SHINE cannot experimentally measure these quantities, as is does not have perfect 4π coverage.) Writing out each contribution explicitly,

$$\sigma_{\text{trig}} = f_{\text{prod}}\sigma_{\text{prod}} + f_{\text{qe}}\sigma_{\text{qe}} + f_{\text{el}}\sigma_{\text{el}}. \tag{7.8}$$

Here f_{prod} is the fraction of simulated production events that scatter out of the S4 scintillator (likewise for f_{qe} and f_{el}); if the triggering and detector coverage was perfect, f_{prod} would be one, and f_{el} would be zero. From Equations 7.1 and 7.8, the inelastic and production cross sections can be written as

$$\begin{aligned} \sigma_{\text{inel}} &= \frac{1}{f_{\text{inel}}}(\sigma_{\text{trig}} - f_{\text{el}}\sigma_{\text{el}}), \\ \sigma_{\text{prod}} &= \frac{1}{f_{\text{prod}}}(\sigma_{\text{trig}} - f_{\text{qe}}\sigma_{\text{qe}} - f_{\text{el}} - \sigma_{\text{el}}). \end{aligned} \tag{7.9}$$

7.1 Measurements

With all of the definitions in place, it is now possible to experimentally measure σ_{trig} and use MC correction factors to extract σ_{prod} and σ_{inel}.

The dataset being analyzed for this thesis was taken in 2017, and there was an issue with the triggering prescaling wiring during the dataset. Resulting from an improperly connected wire, the total number of T1 triggers was lost. The T1 and T2 labels were applied correctly, which is all that is necessary for the multiplicity analysis, but as shown in this section, the cross section analysis relies on knowing the exact ratio of T1 to T2 triggers. All of the T2 interaction triggers were kept, but the T1s were prescaled, meaning only a fraction of their total number was kept. Due to the wiring problem, the prescaling was essentially applied randomly, meaning there is no way to recover the actual number of T1 triggers recorded in 2017.

There are two methods of working around this. First, the detector-control-system (DCS) records the raw counts corresponding to each trigger count per beam spill. However, using the DCS eliminates any possibility of event-by-event counts, such as requiring the beam track to hit the target. It is only a crude way to measure the trigger probability. Second, during the summer of 2023, there was an opportunity to take more proton-carbon data at 90 GeV/c. This opportunity arose during a several day (unplanned) shutdown of the TPCs; even without the TPCs, NA61/SHINE can still record BPD and trigger data, which is all that is necessary for the cross section measurements. In the 2023 dataset, 8.7 million target-in events were recorded, along with 6.5 million target-out events. (The author of this thesis acted as a run coordinator during the beginning of the 2023 run, and they also setup, monitored, and developed the quality assessment software used to monitor the data quality during the 2023 and future runs.) This section will now present the results of both of these analyses.

Starting with the scalers data from 2017, Figure 7.1 shows the DCS recorded trigger probabilies for each beam spill in the dataset.

Taking the average and standard deviation of the two distributions in Figure 7.1b gives a target-in trigger probability of 3.60 ± 0.10, a target-out trigger probability of 0.49 ± 0.03, and an interaction probability of 3.1 ± 0.2. Converting this interaction probability into cross-section measurements requires the MC correction factors.

The calculation of these factors is based off the procedure presented in Aduszkiewicz *et.*

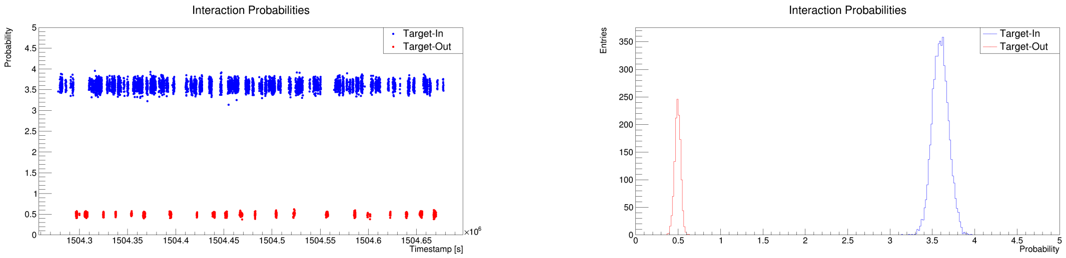

(a)

(b)

Figure 7.1: Left: The trigger probability for each beam spill recorded in the 2017 dataset. Right: A projection of the left plot.

al [51]. 1,000,000 events are simulated with GEANT4 inside the SHINE framework with four different physics lists. Then, after each physics list's simulation, the correction factors and σ_{el} and σ_{qe} can be calculated exactly. FTFP_BERT, one of the four available physics lists, is used for the central values. The other three physics lists, QBBC, QGSP_BERT, and FTF_BIC, are only used to calculate the model uncertainties. Table 7.1 lists the four physics lists samples and their MC-predicted cross sections and correction factors for the 2023 dataset. These MC factors were generated with GEANT4 version 10.7, and the last column shows the nominal FTFP_BERT factors with GEANT version 10.4.p03.

	FTFP_BERT	QBBC	QGSP_BERT	FTF_BIC	FTFP_BERT, GEANT 10.4.p03
σ_{el} [mb]	65.8	65.7	61.3	65.9	73.3
f_{el}	0.108	0.108	0.102	0.106	0.119
σ_{qe} [mb]	18.8	19.0	26.0	15.3	25.1
f_{qe}	0.601	0.612	0.801	0.820	0.595
f_{inel}	0.944	0.943	0.950	0.966	0.912
f_{prod}	0.972	0.971	0.968	0.976	0.947

Table 7.1: The MC cross sections and correction factors for each physics list. Except for the last column, all of these MC samples were generated with GEANT 10.7.

In addition to the different physics lists, six additional MC samples are generated to calculate the uncertainties associated with the S4 size and position. Previously, the diameter of the S4 was found to have an uncertainty of ±0.40 mm, and a conservative ±1.0 mm (x, y) position uncertainty is assumed as well. FTFP_BERT is used to generate the two additional samples for the diameter uncertainty, along with the four additional samples for the position uncertainty. Like with the model uncertainties, any differences between the nominal sample and the uncertainty samples are propagated through to uncertainties on the cross-section measurements. Table 7.2 shows the six S4 samples.

	S4 Diameter +	S4 Diameter −	S4 $(+,+)$	S4 $(-,-)$	S4 $(+,-)$	S4 $(-,+)$
σ_{el} [mb]	67.9	66.1	67.0	65.6	67.1	66.3
f_{el}	0.094	0.118	0.131	0.101	0.105	0.129
σ_{qe} [mb]	18.1	19.0	18.1	18.7	18.9	19.1
f_{qe}	0.602	0.623	0.607	0.610	0.624	0.611
f_{inel}	0.941	0.944	0.945	0.942	0.941	0.941
f_{prod}	0.968	0.971	0.972	0.970	0.967	0.969

Table 7.2: The MC cross sections and correction factors for the two S4 diameter uncertainty samples and the four S4 position uncertainty samples.

Outside of the uncertainties calculated from simulation, there is also a 0.69% uncertainty on the target density (central value of 1.80 g/cm^3), and for the 2023 measurement, there is an additional uncertainty related to the DRS readout of the S4 scintillator. For the S4 to register a particle, the response has to pass a threshold voltage. The noise at the one sigma level for the S4 readout is ~ 2 mV, so the S4 threshold was changed by this amount and the difference in the calculated cross sections was taken as an uncertainty. Any uncertainty associated to the beam purity is negligible. The two different versions of GEANT4, 10.4 and 10.7, were found to give significantly different results for the inelastic cross section; this difference is taken as an uncertainty, and is negligible for the production cross section.

7.2 Cuts

Mentioned earlier, the scalers analysis is unable to make event-by-event cuts, while the 2023 measurement can. The first cut used in the 2023 cross-section analysis is an off-time beam particle cut. If a second proton comes closely after/before the triggering beam proton, it can falsely trigger the S4. To accomodate for this, a conservative ±2 µs cut is applied around the triggering beam particle. Any event with a second beam particle within this window is discarded. In addition to the off-time beam particle cut, this analysis requires a well-reconstructed BPD track (a cluster in the most downstream BPD and a successful fit to the BPD data), and for the beam track to extrapolate within 0.75 cm of the S4 center. The S4 has a radius of 1.0 cm, so this is also a conservative cut. Figure 7.2 shows the extrapolated beam position at the S4 scintillator for the 2023 dataset, with the outline of the S4 superimposed, and Table 7.3 shows the target-in and target-out cut flow.

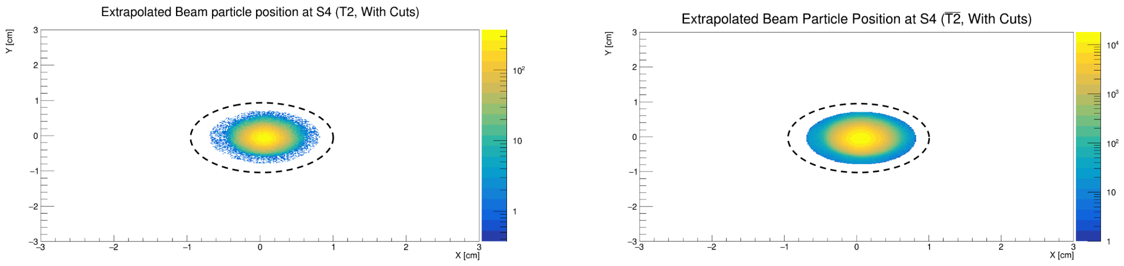

(a) (b)

Figure 7.2: Left: The extrapolated beam position at the S4 scintillator for the 2023 cross-section dataset for T2 triggers. The outline of the S4 is shown with the black outline. Right: Not T2 triggers.

Cut	Target-In	Target-Out
No Cuts	8.74M	6.54M
BPD Cuts	8.30M	6.21M
Off-Time Particle Cut	8.02M	6.00M
S4 Radial Cut	7.97M	5.97M

Table 7.3: The cut flow in the cross section analysis for the 2023 dataset.

7.3 Results

Putting it all together, the final measured inelastic and production cross sections for the 2023 analysis are summarized in Table 7.4. From the 2017 scalers measurement, $\sigma_{\text{trig}} = 236 \pm 19$ mb, $\sigma_{\text{prod}} = 224\ ^{+19}_{-21}$ mb, and $\sigma_{\text{inel}} = 242\ ^{+20}_{-21}$ mb, which is in good agreement with the 2023 measurements. Figures 7.3 and 7.4 show the cross-section results from this analysis along with results from proton-carbon interactions at various beam momenta from previous NA61/SHINE measurements, and in addition to results from other experiments. They also show the results of this same analysis applied to the 2023 120 GeV/c proton-carbon dataset, which was used as an additional cross-check for this analysis, as there are previous NA61/SHINE measurements at 120 GeV/c. All of the results agree well within their uncertainties.

	Value	Δ_{model}	Δ_{S4}	Δ_{target}	Δ_{GEANT}	Δ_{DRS}	Δ_{stat}	Δ_{total}
σ_{trig} [mb]	234.5	NA	NA	NA	NA	NA	± 1.2	± 1.2
σ_{prod} [mb]	222.2	$+0.2 - 8.0$	± 1.4	± 1.7	NA	± 2.5	± 1.2	$+3.6 - 8.8$
σ_{inel} [mb]	240.8	$+6.6 - 5.4$	$+1.5 - 2.0$	± 1.7	± 7.6	± 2.5	± 1.2	$+10.7 - 10.1$

Table 7.4: The measured trigger, production, and inelastic cross sections and the contributions from each uncertainty for the 2023 cross-section measurement.

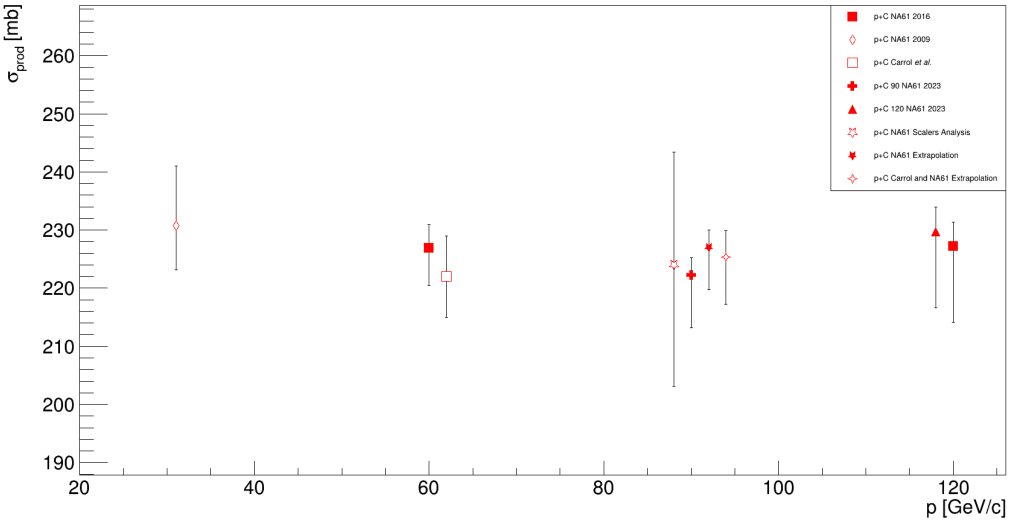

Figure 7.3: Production cross-section results. In addition to results from Carrol *et. al*, both plots show predicted cross sections from extrapolating existing data to 90 GeV/c via a straight-line fit [73]. All measurements are at either 31, 60, 90, or 120 GeV/c, but measurements at the same momentum are offset in x to better show the results.

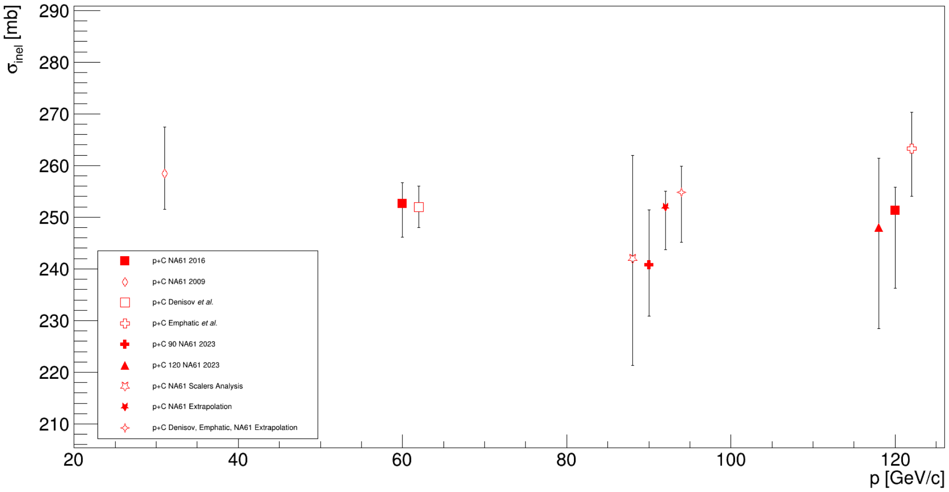

Figure 7.4: Inelastic cross-section results. In addition to results from Denisov *et. al* and the Emphatic collaboration, both plots show predicted cross sections from extrapolating existing data to 90 GeV/c via a straight-line fit. [74, 75]. All measurements are at either 31, 60, 90, or 120 GeV/c, but measurements at the same momentum are offset in x to better show the results.

Chapter 8

Neutral Hadron Analysis

The NA61/SHINE experiment is able to identify the weakly decaying K^0_S, Λ, and $\bar{\Lambda}$ hadrons by tracking their charged decay products. Measurements of the multiplicities of these particles can be used to both inform the neutrino flux predictions for long-baseline oscillation experiments as well as improve the uncertainties on the predictions of the number of charged hadrons produced by weak decays in NA61/SHINE's reactions. Constraining these predictions through reweighting feed-down corrections, which are corrections for particles produced outside the target via weak decays, will be discussed in Chapter 9.

While NA61/SHINE can only measure K^0_S, Λ, and $\bar{\Lambda}$, since neutral kaons are produced almost entirely through strong interactions, there should be an approximately equal number of K^0_S and K^0_L produced. Table 8.1 shows the dominant decay modes of K^0_S, K^0_L, Λ, and $\bar{\Lambda}$. As can be seen in the table, the neutral kaon decays directly contribute to the neutrino flux, while the other hadrons produce particles that can decay to neutrinos and contribute to the flux. In addition, the decay products may interact with material in the beamline, which will indirectly contribute.

8.1 Cut flow

In order to measure the neutral hadrons, NA61/SHINE matches every possible negative track with each positive track as a possible V^0 candidate for T2 events. Then, 14 cuts are applied to remove as much of the background as possible and select candidates from the dominant decay mode. Once all of the cuts are applied, an invariant mass fit is performed to measure the number of neutral

Decay Product	Branching Ratio [%]
$K_S^0 \to \pi^+ + \pi^-$	69.2
$K_S^0 \to \pi^0 + \pi^0$	31.7
$K_L^0 \to \pi^\pm + e^\mp + \nu_e$	40.5
$K_L^0 \to \pi^\pm + \mu^\mp + \nu_e$	27.0
$\Lambda \to p + \pi^-$	63.9
$\Lambda \to n + \pi^0$	35.8
$\bar{\Lambda} \to \bar{p} + \pi^+$	63.9
$\bar{\Lambda} \to \bar{n} + \pi^0$	35.8

Table 8.1: Branching ratios of neutrino neutral ancestor particles significantly contributing to the neutrino flux.

particles in each kinematic bin. The kinematic bins are finite blocks in total momentum $|p|$ and angle θ. When the bins were originally created for an analysis performed by S. Johnson, they were created to bin the phase space as finely as possible while still having adequate statistics for the mass fits after applying all of the cuts [76]. For consistancy and compatibility, the subsequent analysis by B. Rumberger and this analysis use the same binning scheme [48]; the only changes were the removal or addition of a small number of bins dependent on the reaction's phase space. (A reaction with a 120 GeV/c proton will produce hadrons with a higher total possible momentum than a reaction with a 90 GeV/c proton.) Figure 8.1 shows the binned and unbinned phase space for the K_S^0 analysis before applying any cuts.

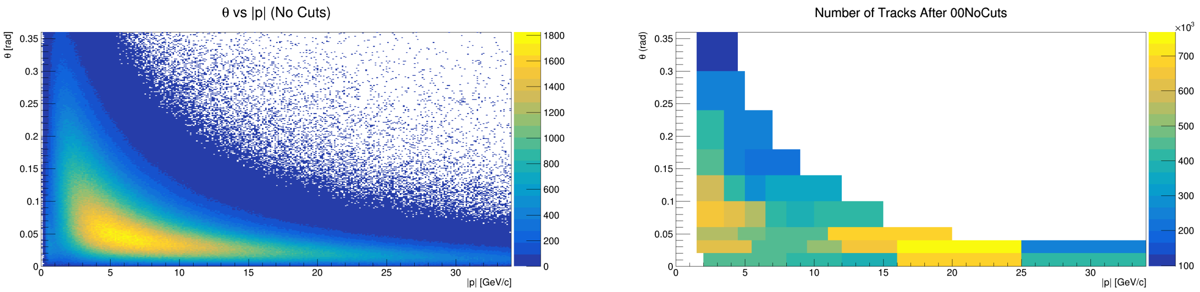

(a)

(b)

Figure 8.1: Left: The phase space of neutral tracks in the K_S^0 analysis before applying any cuts. Right: The binned phase space before applying any cuts.

Each kinematic bin in Figure 8.1 is subject to 14 cuts. Like the binning scheme, these cuts are unchanged from the analysis by B. Rumberger. This section will now briefly walk through each cut.

The first three cuts are event-level cuts. Cut 1 requires the beam particle to extrapolate within 0.95 cm of the center of the S4, which removes any T2 events resulting from the beam particle missing the S4 trigger. The second cut removes offtime beam particles to ensure any measured hadrons were produced by the triggering beam particle; this is applied by requiring a 2.5 µs window around the beam particle. The last event cut requires a reconstructed BPD track with a cluster in the most downstream BPD, as a BPD track is necessary to reconstruct the event's vertex position. Table 8.2 shows the cut for the event-level cuts in the neutral analysis. The event-level cuts are the same for the three particle species, but a few of the track-level cuts differ between the three species.

Cut	Target In	Target Out
00 No Cuts	2,189,177	161,679
01 S4	2,160,666	148,101
02 Offtime Beam Particle	1,670,592	114,257
03 BPD Track	1,542,835	82,591

Table 8.2: The number of T2 events after applying each event-level cut for the neutral analysis.

The next five cuts are track-level cuts that are the same for the three neutral species. The first track-level cut, cut 4, requires the reconstructed V^0 vertex to be after the main vertex for the event. Cuts 5 and 6 are cluster topology cuts for the minimum number of clusters to properly reconstruct tracks; cut 5 selects tracks with at least 12 total clusters, and cut 6 requires at least 12 VTPC clusters. (These are redundant, but the cut flow is following previous analyses. In addition, future analyses may desire to change these cut values, which could make the two cuts not redundant.) After cut 6, cut 7 removes tracks with an impact parameter greater than $(4.0, 2.0)$ cm. The impact parameter is the (x, y) difference in the V^0's extrapolated position at the main vertex and the main vertex. If the positions are too different, the V^0 was probably not produced inside the target; Figure 8.2 shows a schematic of this cut. Following cut 7, cut 8 defines the area in which neutral particles can be reconstructed. This cut requires tracks to come between 3.5 cm and 300 cm after the main vertex. Allowing V^0 vertices too close to the target would greatly increase the background from false V^{0}s, and the other end of the cut is the boundary in which the track's momentum can be reconstructed.

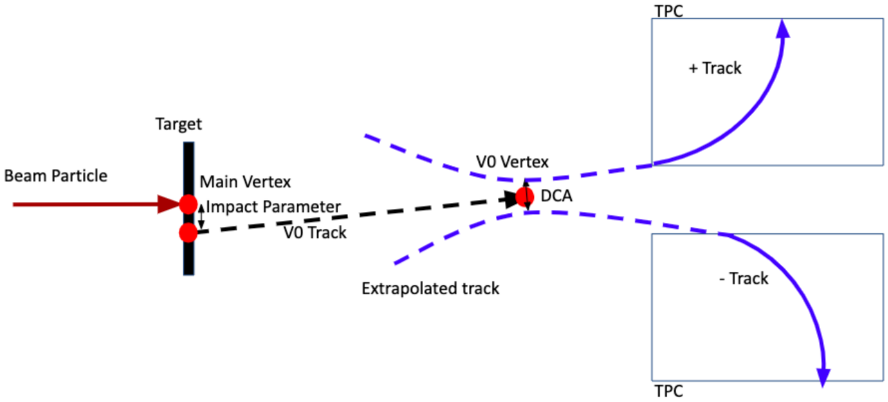

Figure 8.2: The reconstructed impact parameter for a V^0 candidate is the difference between the main vertex and the track's position at the main vertex [76].

Besides cut 13, the proper lifetime cut, the rest of the cuts are specific to each particle species. Cut 9 is the low transverse momentum cut, which removes photons undergoing pair production. For K^0_S $p_T > 0.05$ GeV/c, and for Λ and $\bar{\Lambda}$ $p_T > 0.03$ GeV/c. Before introducing cut 10, the concept of the Armenteros-Podlanski plot must be introduced [77]. The asymmetry of the longitudinal momenta of the decay products is defined as

$$\alpha = \frac{p_L^{+,*} - p_L^{-,*}}{p_L^{+,*} + p_L^{-,*}}. \tag{8.1}$$

Here $p_L^{+,*}$ is the longitudinal momentum of the positively decay product in a comoving frame with the V0, and $p_L^{-,*}$ is for the negatively charged particle. The total transverse momentum is

$$p_T = p_T^{+,*} + p_T^{-,*}, \tag{8.2}$$

where $p_T^{+,*}$ is the transverse momentum of the positive track. Figure 8.3 shows the Armenteros-

Podlanski plot before applying any cuts.

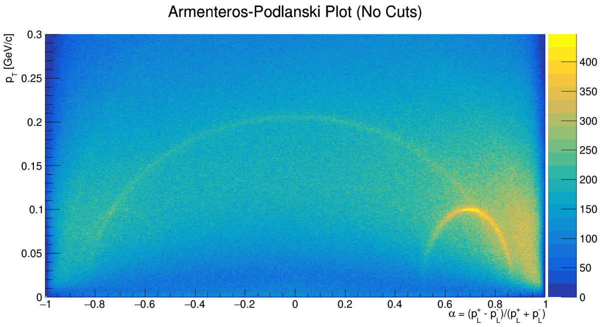

Figure 8.3: Armenteros-Podlanski distribution before applying any cuts. The large arc in the center corresponds to K^0_S, while the small arc in the bottom right corner is Λ. Before applying cuts, the $\bar{\Lambda}$ distribution is barely visible in the bottom left corner.

As can be seen in Figure 8.3, there is contamination between the legs of the K^0_S distribution and the Λ and $\bar{\Lambda}$ distributions. To remove this contamination, cut 10 applies a cut on the angles between the decay products and their parent particle. The angle, θ^*, is calculated between the momentum vector of the decay product in the rest frame of the parent particle and the momentum vector of the V^0 in the lab frame. For K^0_S the cuts are $-0.9 < \cos(\theta^{+*}) < 0.7$ and $-0.7 < \cos(\theta^{-*}) < 0.9$. Applying a similar cut for Λ and $\bar{\Lambda}$ also helps to remove false V^{0}s. For Λ the allowed ranges are $-0.7 < \cos(\theta^{+*}) < 0.9$ and $-0.9 < \cos(\theta^{-*}) < 0.7$; the ranges for $\bar{\Lambda}$ are $-0.9 < \cos(\theta^{+*}) < 0.7$ and $-0.7 < \cos(\theta^{-*}) < 0.9$.

The eleventh cut, a cut on the max p_T, was found to result in a non-uniform background and is excluded from this analysis. Cut 12 places a range on the reconstructed mass of the neutral particle, which for a two-body decay is

$$M = \sqrt{m_+^2 + m_-^2 + 2E_+^* E_-^* - 2\vec{p}_+^{\,*} \cdot \vec{p}_-^{\,*}}. \tag{8.3}$$

m_+ is the mass of the postively charged particle, and $\vec{p}_+^{\,*}, E_+^*$ are the momentum and energy in the decay frame. For K^0_S the allowed range is $0.40 < M < 0.65$ GeV/c^2, while the range for Λ and $\bar{\Lambda}$ is $1.09 < M < 1.215$ GeV/c^2.

The second to last cut, the thirteenth cut, requires the proper lifetime of the V^0 to be at least

0.25 of the mean proper lifetime; the sample of reconstructed neutral particles with too short of a proper lifetime is greatly contaminated from incorrectly matched charged particles coming from the target. The final cut, cut 14, requires both child particles to have energy loss within 15% of the expected Bethe-Bloch decay for the selected dominant decay mode. Table 8.3 shows the target-in cut flow the neutral hadron analysis.

Cut	K_S^0	Λ	$\bar{\Lambda}$
00 No Cuts	15,197k	15,498k	10,294k
01 S4	15,128k	15,430k	10,252k
02 Offtime Beam Particle	11,507k	11,736k	7,796k
03 BPD Track	10,893k	11,111k	7,386k
04 Vertex Z	4,877k	4,984k	3,367k
05 Total Clusters	4,572k	4,676k	3,213k
06 VTPC Clusters	4,175k	4,234k	2,906k
07 Impact Parameter	3,747k	3,804k	2,656k
08 Decay Length	2,355k	2,399k	1,717k
09 Low p_T	2,196k	2,241k	1,645k
10 cos(θ)	1,514k	860k	513k
11 Max p_T	NA	NA	NA
12 Invariant Mass	716k	370k	193k
13 Proper Lifetime	406k	194k	81k
14 Child Energy Loss	263k	67k	9k

Table 8.3: The track-level cut flow for the target-in neutral analysis.

Figures 8.4, 8.5, and 8.6, show the binned phase space for K_S^0, Λ, and $\bar{\Lambda}$ before and after cuts, respectively. Figures 8.7, 8.8, and 8.9, show the invariant mass distributions for all kinematic bins, and Figure 8.10 shows the Armenteros-Podlanski distributions.

8.2 Invariant Mass Fits

Once the cuts have been applied and the invariant mass distributions are available for every kinematic bin, the next step is to perform the invariant mass fit and count the number of each neutral species. This determines the signal and removes the background. Five different signal

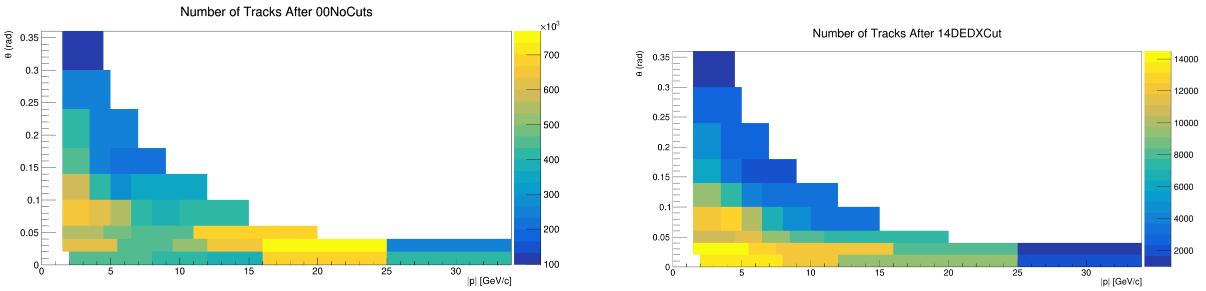

(a) (b)

Figure 8.4: Left: The phase space of neutral tracks in the K_S^0 analysis before applying any cuts. Right: After all cuts.

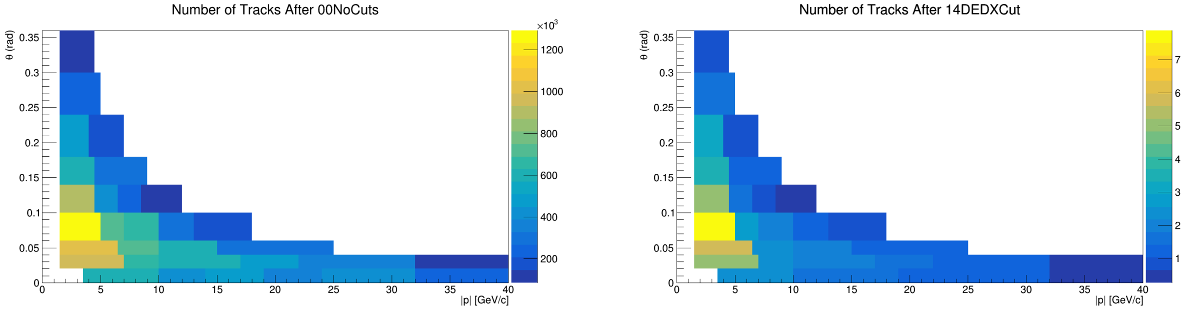

(a) (b)

Figure 8.5: Left: The phase space of neutral tracks in the Λ analysis before applying any cuts. Right: After all cuts.

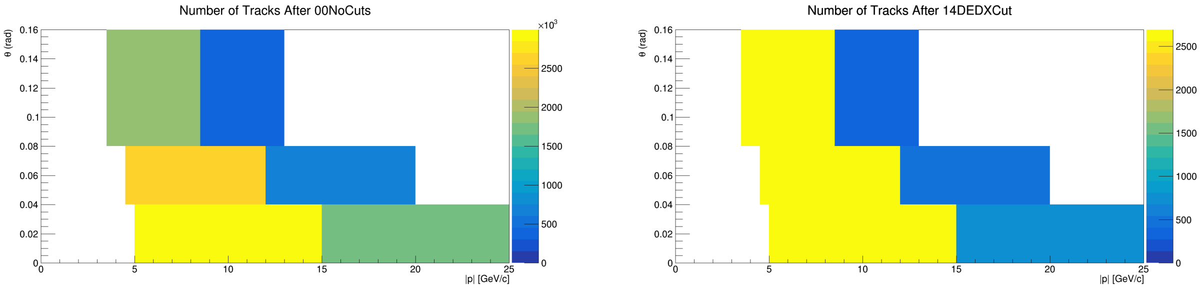

(a) (b)

Figure 8.6: Left: The phase space of neutral tracks in the $\bar{\Lambda}$ analysis before applying any cuts. Right: After all cuts.

models were considered: Cauchy, asymmetric Gaussian, Gaussian plus asymmetric Gaussian, two Gaussians, and MC templates. The Cauchy distribution, also known as a Lorentzian, was found to

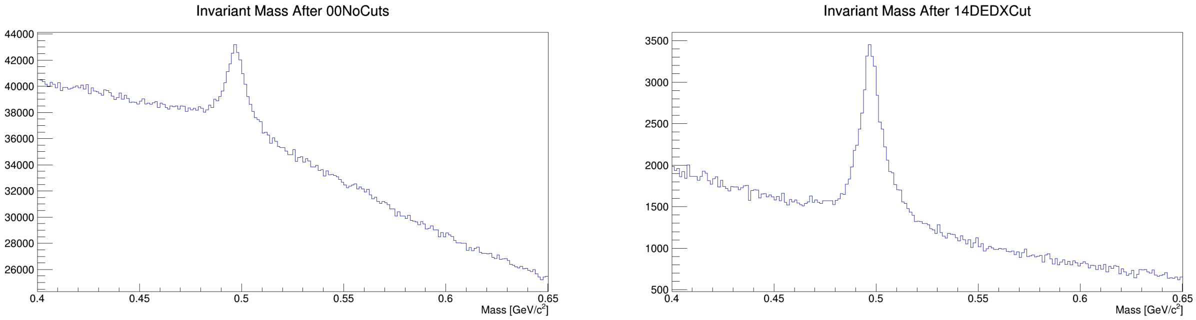

(a) (b)

Figure 8.7: Left: The reconstructed invariant mass of neutral tracks in the K_S^0 analysis before applying any cuts. Right: After all cuts.

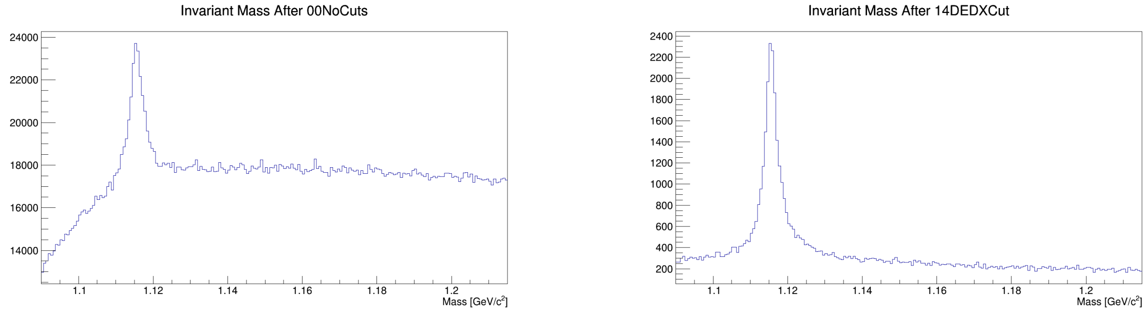

(a) (b)

Figure 8.8: Left: The reconstructed invariant mass of neutral tracks in the Λ analysis before applying any cuts. Right: After all cuts.

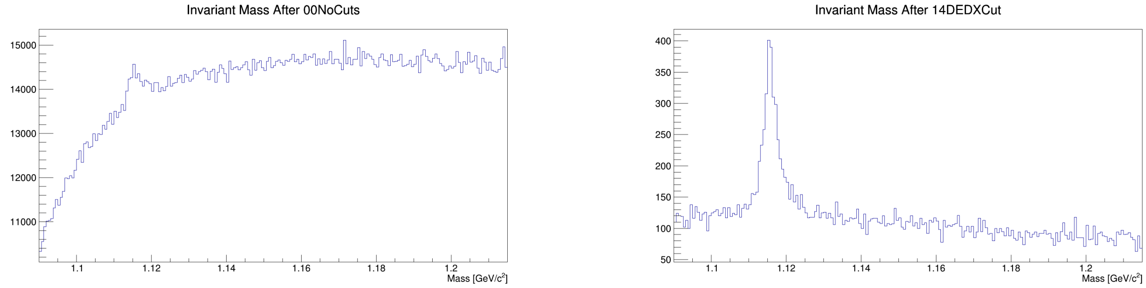

(a) (b)

Figure 8.9: Left: The reconstructed invariant mass of neutral tracks in the $\bar{\Lambda}$ analysis before applying any cuts. Right: After all cuts.

best describe the signal shapes, and is given by

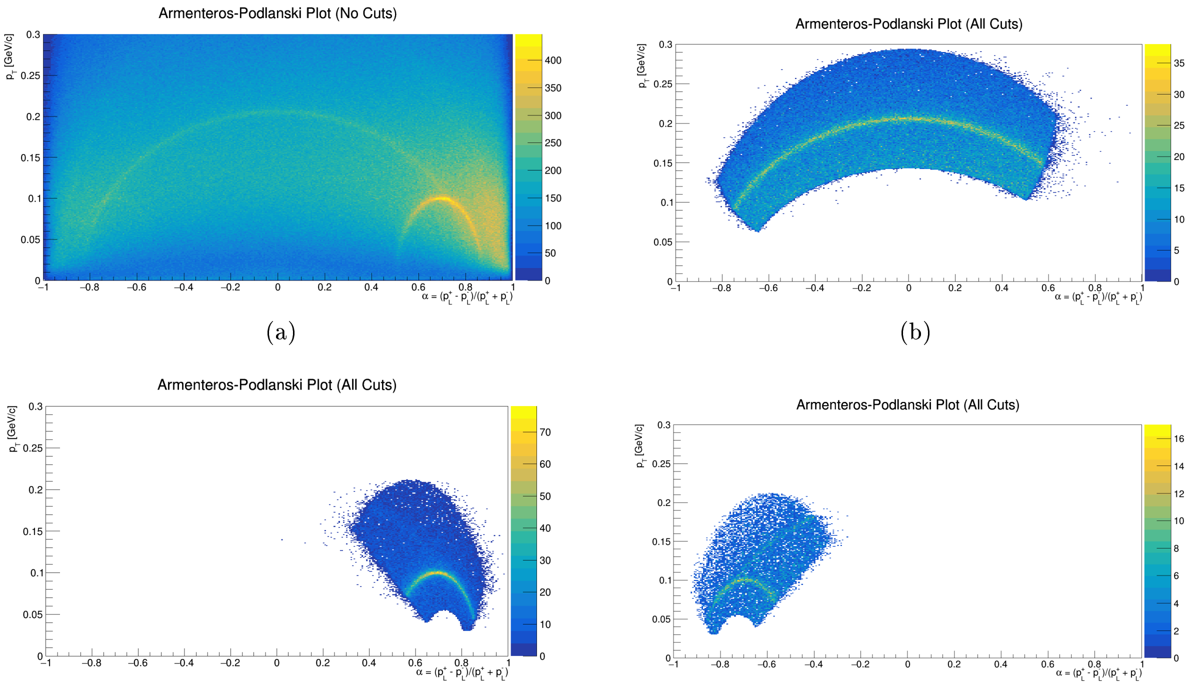

(a) (b)

(c) (d)

Figure 8.10: Top Left: Armenteros-Podlanski distribution before applying any cuts. Top Right: After applying all cuts in the K_S^0 analysis. Bottom Left: Λ. Bottom Right: $\bar{\Lambda}$.

$$f(m; m_0, \gamma) = \frac{1}{\pi\gamma}\left[\frac{1}{(m - m_{PDG} - m_0)^2 + \gamma^2}\right]. \tag{8.4}$$

The amplitude of the Cauchy distribution is given by $\frac{1}{\pi\gamma}$, m_{PDG} is the PDG mass, and m_0 is a mass offset, as the fit mass is allowed to float. A second-degree polynomial, f_{bg}, is used to fit to the background.

During the fitting procedure, a continuous log-likelihood function is constructed with the parameter c_s controlling the ratio of signal to background.

$$\ln(L) = \sum_{\text{All V0 Tracks}} \ln[c_s f_s(m; m_0, \gamma) + (1 - c_s) f_{\text{bg}}], \tag{8.5}$$

and the minimization function is constructed by

$$\text{Minimization Function} = -2\ln(L) + \text{constraints}. \tag{8.6}$$

The constraints are used to prevent run away parameters in the background distribution, and are

$$\text{constraints} = \left(\frac{c_1}{10^6}\right)^2 + \left(\frac{c_2}{10^6}\right)^2 + \left(\frac{c_3}{10^6}\right)^2. \tag{8.7}$$

The fits were performed with the ROOT class TMinuit, and the raw signal yield from each fit is $y^{\text{raw}} = c_s N_{\text{V0 Candidates}}$. Figures 8.11, 8.12, and 8.13 show a sample mass fit for each particle species.

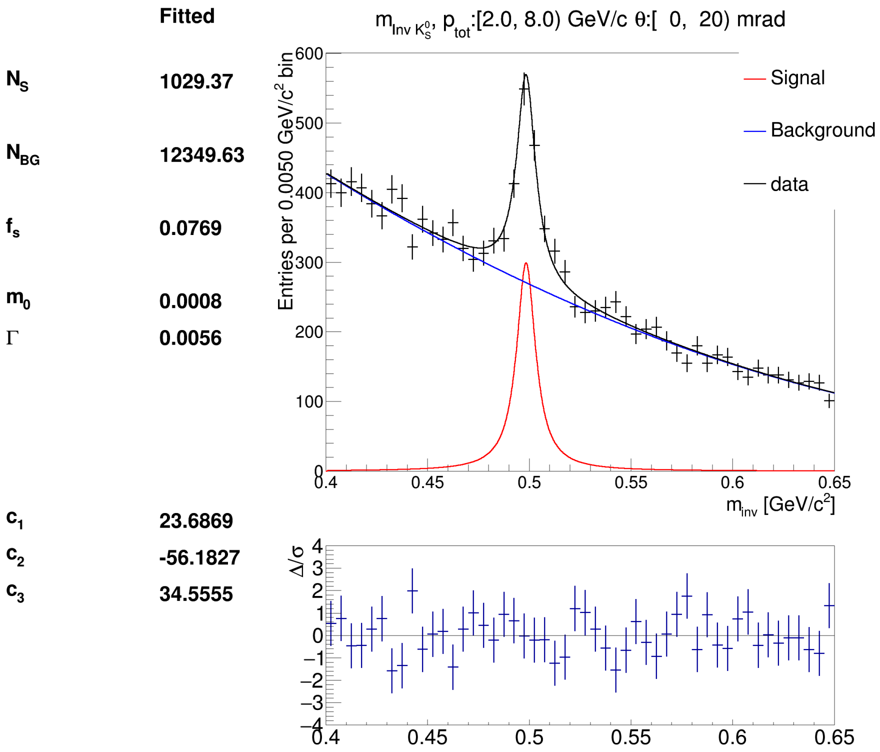

	Fitted
N_S	1029.37
N_{BG}	12349.63
f_s	0.0769
m_0	0.0008
Γ	0.0056
c_1	23.6869
c_2	-56.1827
c_3	34.5555

Figure 8.11: A sample K_S^0 invariant mass fit. The best fit values are given on the left, and the bottom plot is showing the fit residual divided by the total number of data points for each bin. The fit residual is the fit result minus the number of data points.

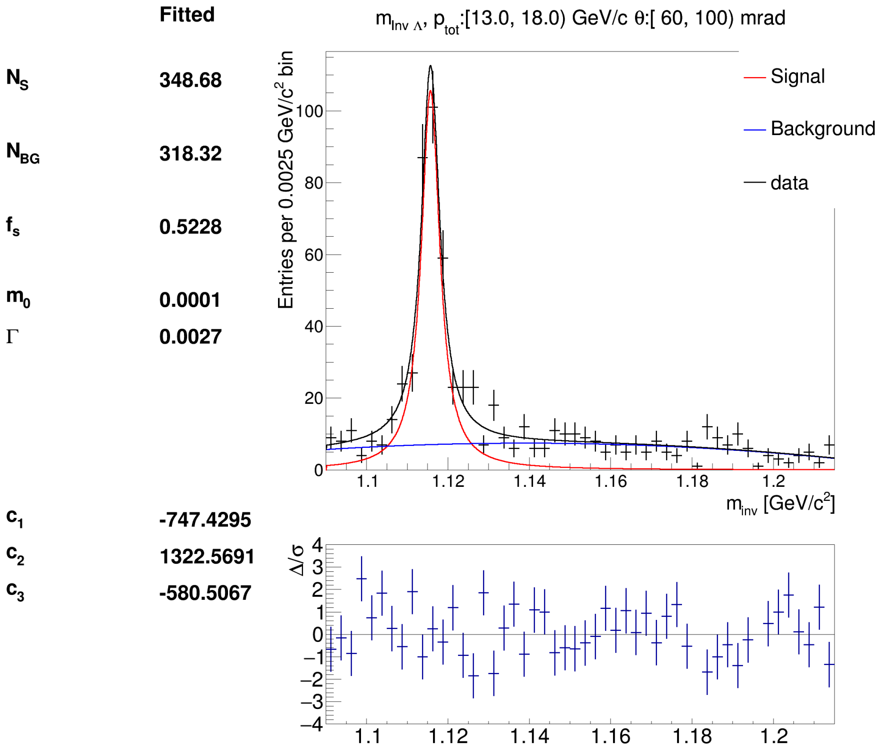

Figure 8.12: A sample Λ invariant mass fit.

8.3 MC Corrections

The raw yields obtained via the invariant mass fits need to be corrected for a variety of systematic effects, in order to properly count the number of produced particles coming from the initial proton-carbon nucleus interaction. First, the NA61/SHINE detector does not offer perfect 4π coverage, and only particles in specific regions of phase space can be reconstructed. Any particles outside the coverage area need to accounted for with a detector acceptance correction. While applying the cuts, they mainly remove the background, but inevitably some of the signal will be cut as well. A selection efficiency correction corrects for any tracks removed by the analysis cuts. On top of this, any experimental data reconstruction can never be perfect, so a reconstruction efficiency correction needs to be applied. In addition, the cuts cannot exclude all of the neutral particles resulting from decays occurring outside the target, and NA61/SHINE wants to measure particles originating inside the target; a feed-down correction needs to be applied to correct for this. (There

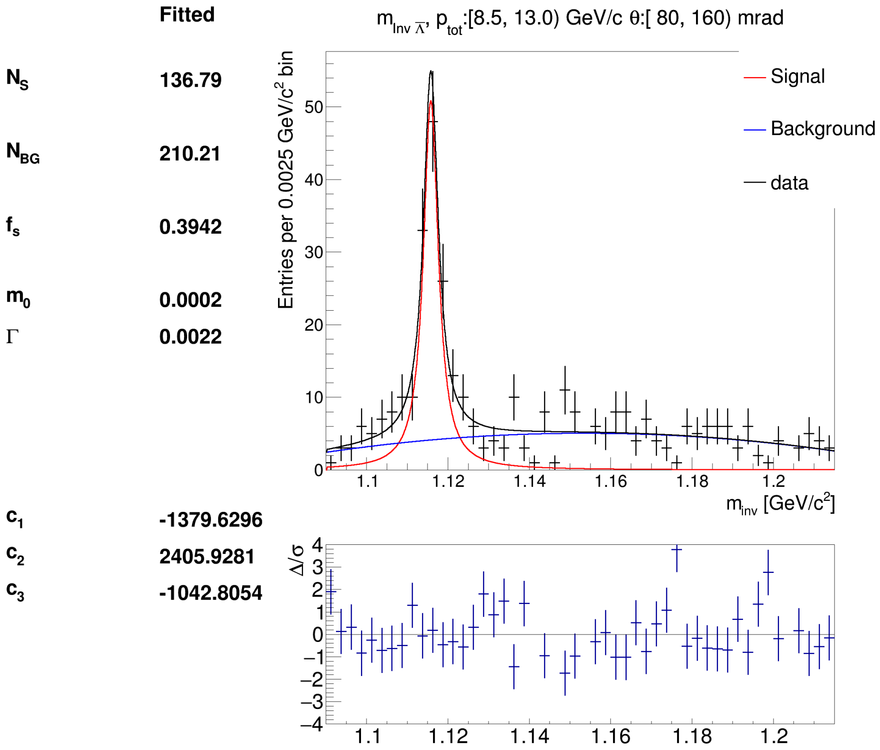

Figure 8.13: A sample $\bar{\Lambda}$ invariant mass fit.

are most likely many strong decays occurring inside the target, but it is only important to measure what comes out from the target. The feed-down correction corrects for Λ and $\bar{\Lambda}$ that originate from weak decays occurring outside the target volume. Any decays occurring inside the target contribute to the measured particle multiplicity.) Lastly, only the dominant branching ratio for each neutral particle is selected (see Table 8.1), and the missing decay pathways need to be corrected for. All of these corrections factors are grouped into a single factor for each kinematic bin i. Using K^0_S as an example, the total correction factor is

$$c_i = \frac{\text{Number of simulated K0S}}{\text{Number of reconstructed K0S}} = c_{\text{BR}} + c_{\text{acc.}} + c_{\text{fd.}} + c_{\text{rec. eff.}} + c_{\text{sel. eff.}}. \tag{8.8}$$

The correction factors are obtained through a GEANT4 MC simulation with physics list FTFP_BERT. Once the MC sample has been created, it is subject to the exact same reconstruction, cut, and fitting procedure as the dataset. As shown in Equation 8.8, the differences in the number of simulated particles and reconstructed particles gives the correction factors. Figure 8.14 shows the total correction factor for each neutral species, excluding the feed-down corrections. Figure 8.15 shows the feed-down corrections for Λ and $\bar{\Lambda}$; K^0_S does not get a feed-down correction, as there are no predicted decays to K^0_S occurring outside the target.

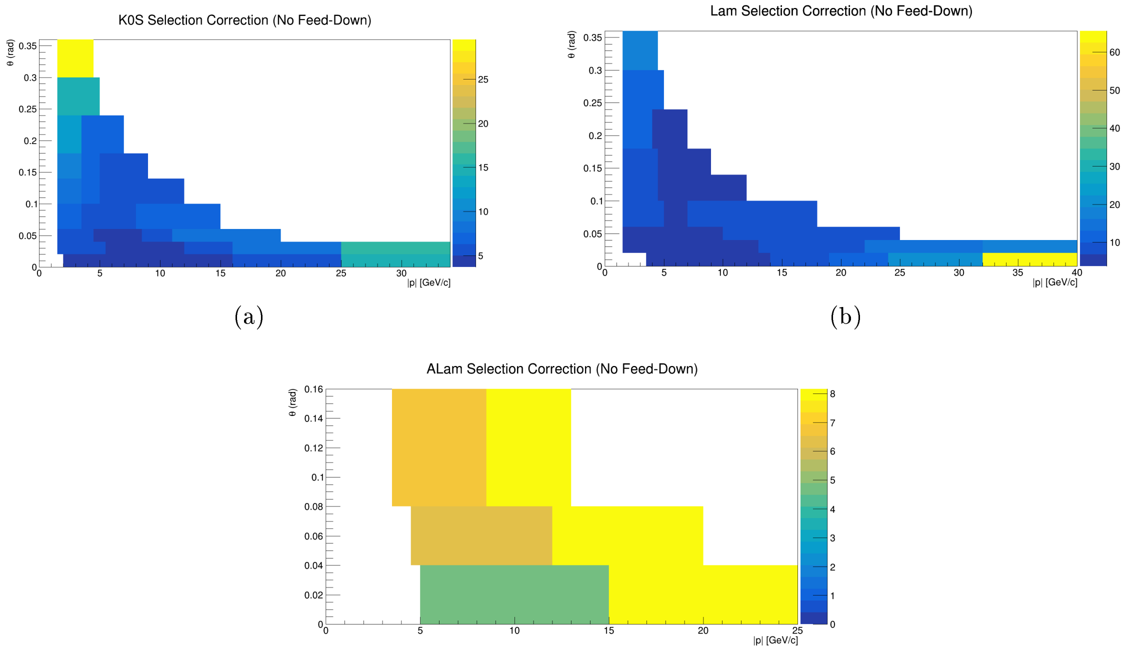

(a)

(b)

(c)

Figure 8.14: Top Left: The MC correction factors for each kinematic bin in the K^0_S analysis. The feed-down corrections are excluded. Top Right: Λ. Bottom: $\bar{\Lambda}$.

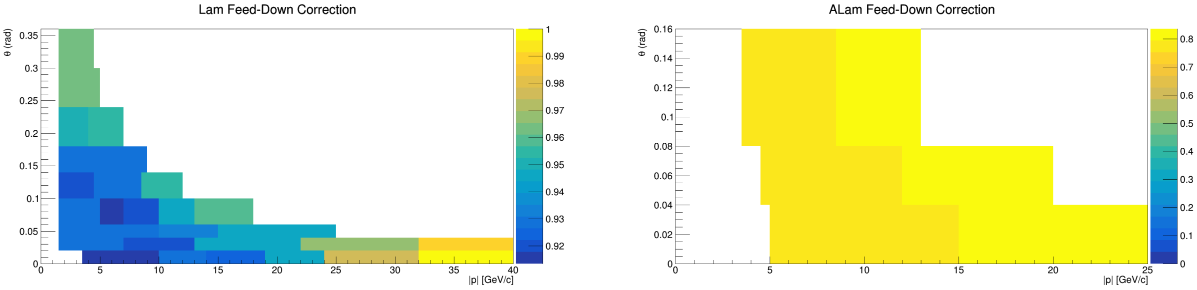

(a)

(b)

Figure 8.15: Left: The MC feed-down correction factors for each kinematic bin in the Λ analysis. Right: $\bar{\Lambda}$.

8.4 Target-Out Correction and Multiplicity Calculation

The differential multiplicity, the average number of particles produced per production event, of each species for each kinematic bin i, is given by

$$\frac{d^2 n_i}{dp d\theta} = \frac{y_i}{N_{\text{prod}} \Delta p \Delta\theta}. \tag{8.9}$$

Here $\Delta p \Delta\theta$ is the size of bin i and normalizes the result, $y_i = c_i y_i^{\text{raw}}$ is the total yield for bin i (c_i is the MC correction factor from Equation 8.8), and N_{prod} is the total number of production events. As NA61/SHINE actually measures the number of triggering events (T2), this needs to be rewritten in terms of the number of triggering events. Using

$$\frac{N_{\text{prod}}}{N_{\text{trig}}} = \frac{f_{\text{prod}} \sigma_{\text{prod}}}{\sigma_{\text{trig}}}, \tag{8.10}$$

and the fact that the fraction of production events scattered out of the S4, f_{prod}, is accounted for by the MC correction factor c_i, Equation 8.9 can be rewritten as

$$\frac{d^2 n_i}{dp d\theta} = \frac{\sigma_{\text{trig}}}{\sigma_{\text{prod}} N_{\text{trig}}} \frac{c_i y_i^{\text{raw}}}{\Delta p \Delta\theta}. \tag{8.11}$$

To correct for interactions occurring outside the target, the target subtraction is performed. Mentioned earlier, NA61/SHINE records data with the target removed during each data taking run. The target-out dataset is then analyzed in the exact same manner as the target-in dataset, and the contributions from interactions occurring outside the target are corrected for by the target-out subtraction:

$$\frac{y_i^{\text{raw}}}{N_{\text{trig}}} = \frac{1}{1-\epsilon} \left(\frac{y_i^{\text{raw, in}}}{N_{\text{trig}}^{\text{in}}} - \frac{\epsilon y_i^{\text{raw, out}}}{N_{\text{trig}}^{\text{out}}} \right). \tag{8.12}$$

$\epsilon = \frac{p_{\text{trig}}^{\text{out}}}{p_{\text{trig}}^{\text{in}}}$, the ratio between the target-in and target-out trigger probabilities. $N_{\text{trig}}^{\text{in}}$ is the total number of target-in triggering events.

Combining Equations 8.11 and 8.12 gives

$$\frac{d^2 n_i}{dp d\theta} = \frac{\sigma_{\text{trig}} c_i}{\sigma_{\text{prod}} \Delta p \Delta\theta (1-\epsilon)} \left(\frac{y_i^{\text{raw, in}}}{N_{\text{trig}}^{\text{in}}} - \frac{\epsilon y_i^{\text{raw, out}}}{N_{\text{trig}}^{\text{out}}} \right). \tag{8.13}$$

The differential multiplicity calculated from Equation 8.13 is measured for each kinematic bin i, and requires a measurement of the total number of target-in and target-out triggers, the target-in and target-out trigger probabilities, the target-in and target-out raw yields, the MC correction factor for the bin i, and the trigger and production cross sections. This value (and its uncertainty) is the desired measurement for a NA61/SHINE neutrino analysis.

8.5 Results

The following figures show the multiplicity spectra calculated for K_S^0, Λ, and $\bar{\Lambda}$. The horizontal bars show the covered total momentum region for each measurement, and the vertical bars show the total uncertainty on the multiplicity measurement; the details of the uncertainty calculations will be discussed in Section 8.7. The numerical values are presented in Appendix A.

8.6 Lifetime Cross Check

One of the most thorough checks NA61/SHINE can perform on the veracity of the reconstruction, MC corrections, and invariant mass fits is the lifetime cross check. This procedure bins the neutral hadrons in their proper lifetime, instead of angle and total momentum; each proper lifetime bin will be an aggregate of all of the angle and total momentum bins. A plot of the total number of reconstructed V0s versus the ratio of the measured proper lifetime over the PDG proper lifetime should follow an exponential distribution exactly. Any deviations from the expected distribution would indicate a problem with the analysis; for a problem to hide under this check would require it to exponentially affect each proper lifetime bin, a very unlikely possibility. Figures 8.19 through 8.21 show the results of the lifetime cross check; the fits of the slopes all being near 1.0 is an indication of a healthy analysis. (Two fits are performed for each species. The first fit excludes the

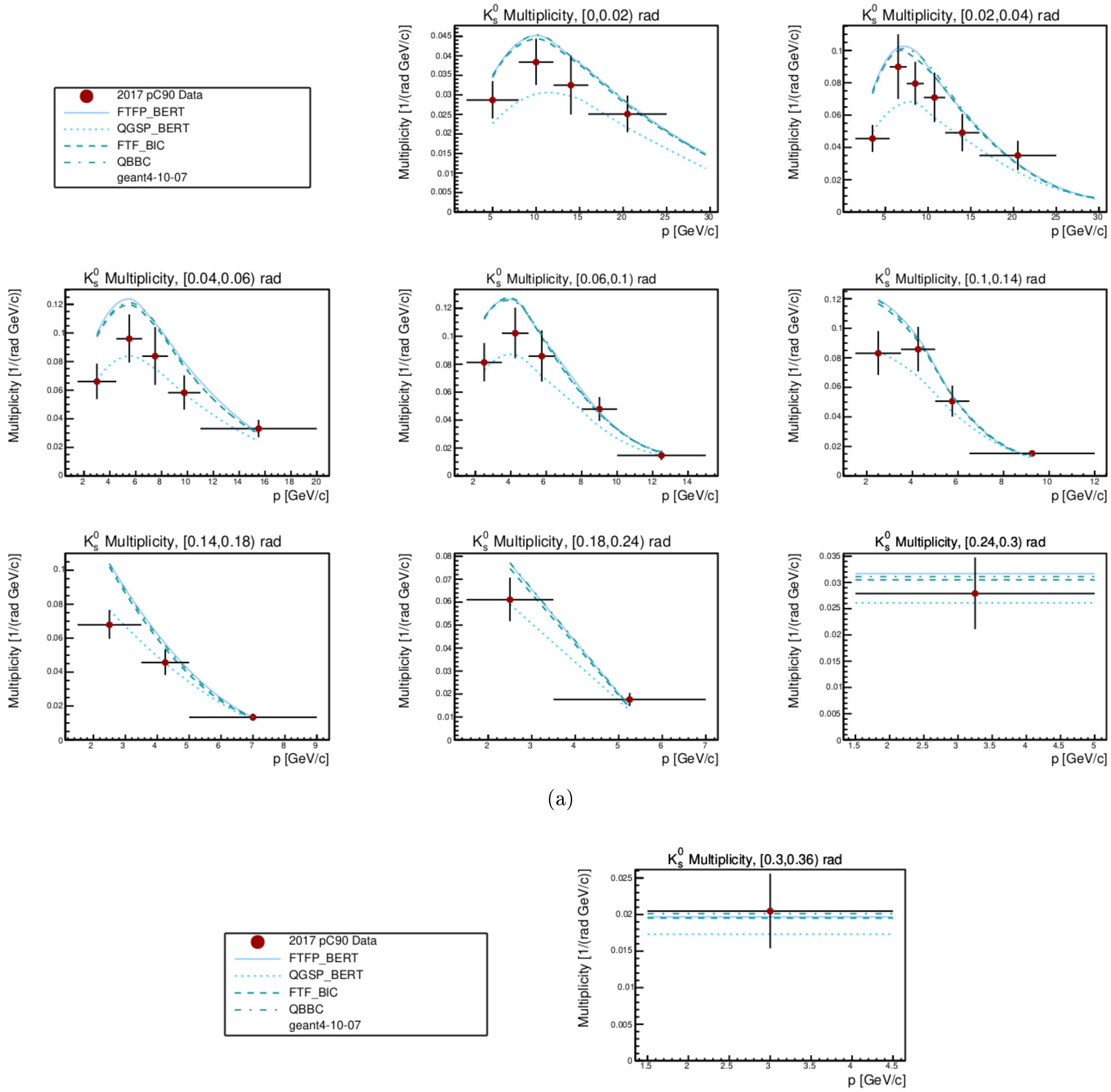

(a)

(b)

Figure 8.16: K_S^0 differential multiplicity results.

points that begin to vary due to lack of statistics, and the second fit encompasses the entire proper lifetime phase space.) This analysis is subject to the same cuts performed for the analysis in total momentum and angle bins; cut 13, the proper lifetime cut, excludes tracks with a proper lifetime less than 0.25 of the mean proper lifetime for that species.

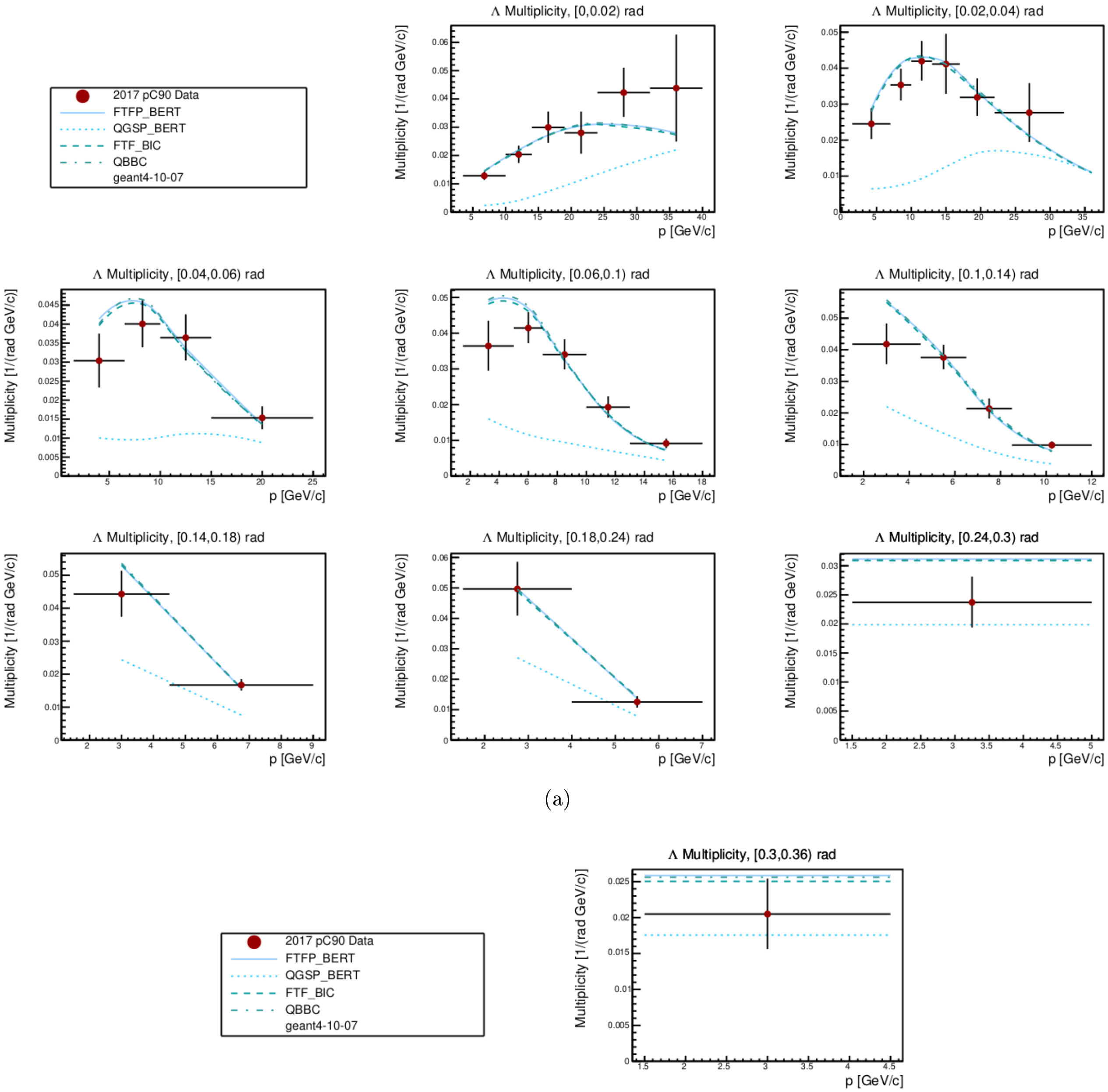

(a)

(b)

Figure 8.17: Λ differential multiplicity results.

8.7 Uncertainties

There are a number of uncertainties that need to be considered. These uncertainties include the fit, decay product dE/dx selection, selection, feed-down, production cross section, physics model, reconstruction, momentum, and statistical uncertainties. Each of these uncertainties will now be

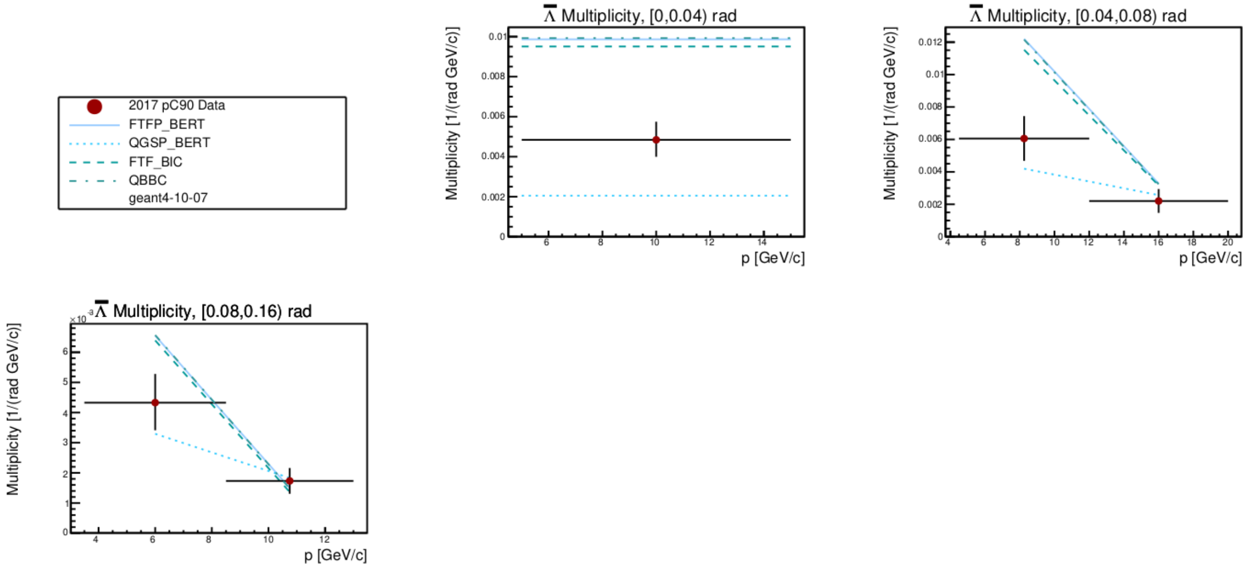

(a)

Figure 8.18: $\bar{\Lambda}$ differential multiplicity results.

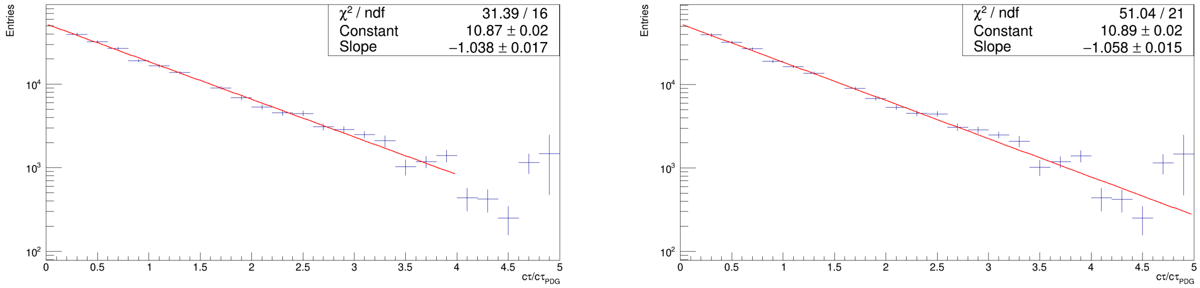

(a) (b)

Figure 8.19: K_S^0 lifetime cross check. Left: The fit range is 0.25 to 4.0 on the x-axis. Right: The fit range is 0.25 to 5.0 on the x-axis.

described.

The first uncertainty, the fit bias uncertainty, was estimated using the four GEANT4 physics lists. For each kinematic bin, the fractional differences between the number of fit signal tracks and true signal tracks was averaged and taken as a systematic uncertainty. (While the errors on the data fit parameters could be used as a different method of calculating the fit bias uncertainty, this method is more conservative.)

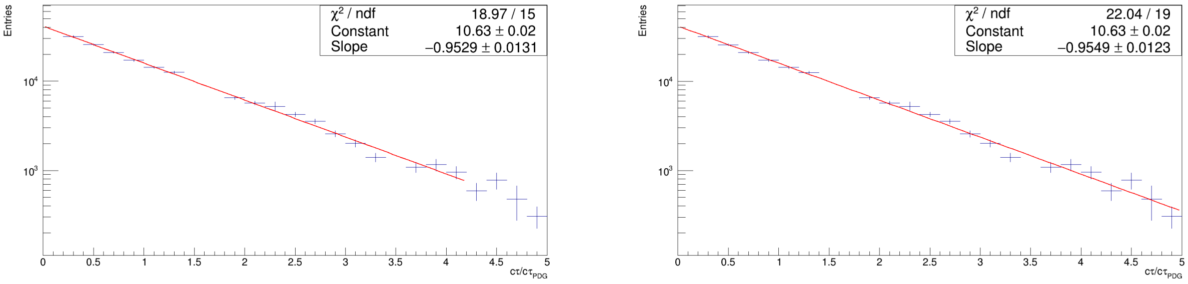

(a) (b)

Figure 8.20: Λ lifetime cross check. Left: The fit range is 0.25 to 4.25 on the x-axis. Right: The fit range is 0.25 to 5.0 on the x-axis.

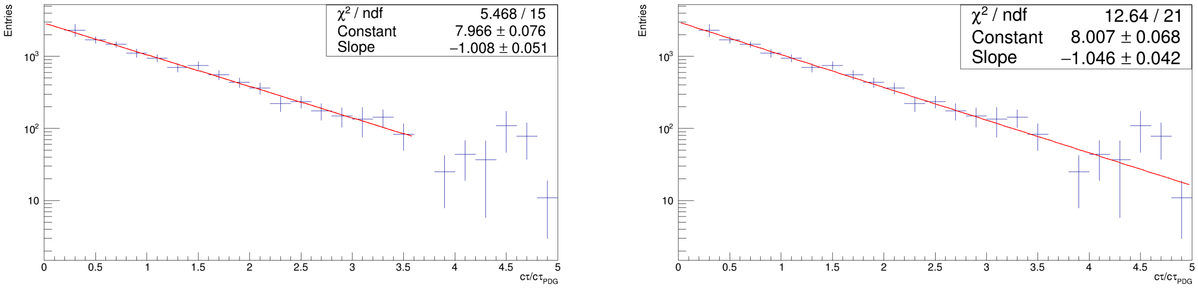

(a) (b)

Figure 8.21: $\bar{\Lambda}$ lifetime cross check. Left: The fit range is 0.25 to 3.5 on the x-axis. Right: The fit range is 0.25 to 5.0 on the x-axis.

For the decay product dE/dx selection uncertainty, the decay product Bethe-Bloch cut was relaxed by 5%, and the data and MC samples were reprocessed. The differences between the resulting multiplicities and the central multiplicities were taken as a systematic uncertainty.

When comparing data and simulated tracks, the simulated tracks have on average 5-10% more clusters than data tracks, most likely resulting from unsimulated faulty FEEs and periodic detector noise; these two effects can often lead to cluster loss. To accomodate for this, the number of clusters in data was artificially reduced by a conservative 15%. After recalculating the multiplicities, the differences between the altered data and the central values were taken as a systematic uncertainty.

As there is a lack of data on the production of Ξ and Ω baryons (which can decay to Λ and $\bar{\Lambda}$) in proton-carbon interactions, the feed-down corrections for Λ and $\bar{\Lambda}$ rely on MC estimates. However, production rates of these baryons vary up to 50% in MC models. To estimate the uncertainty from these weak decays, the number of feed-down tracks in each bin was varied by 50% in each kinematic bin, and the resulting multiplicity differences were taken as a systematic uncertainty. To constrain this uncertainty — as is done in the charged analysis — would require data on the production of Ξ and Ω baryons in 90 GeV/c proton-carbon interactions.

Since the production cross section appears in Equation 8.13, the uncertainty on the cross section was propagated through the analysis, and the result is a uniform, asymmetric uncertainty.

For the MC corrections, the GEANT4 physics list FTFP_BERT is used. The end multiplicity results should not be dependent on the physics list used, but the four physics lists, FTFP_BERT, FTF_BIC, QBBC, and QGSP_BERT predict slightly different momentum distributions. As the bin sizes used in the analysis are finite, each kinematic bin has a different calculated MC correction for each physics list. The differences in the calculated multiplicities between FTFP_BERT, FTF_BIC, and QBBC are taken as a systematic uncertainty.

The final uncertainty is the reconstruction uncertainty. During the TPC-alignment calibration procedure the track-track residuals distribution gives the VTPC alignment a standard deviation of approximately 200 µm in x. Any shifts in the x direction will significantly impact momentum and track reconstruction, as this is the bending plane of the magnetic fields. In the data reconstruction, VTPC1 and VTPC2 are shifted by +200 µm and −200 µm, and vice versa, and the resulting multiplicity differences are taken as a systematic uncertainty.

An uncertainty associated with the momentum reconstruction was also considered, but was excluded as it is negligible. To calculate any possible momentum uncertainty, the aggregate mass samples for all of the K^0_S, Λ, and $\bar{\Lambda}$ kinematic bins were given to the invariant mass fitter. Any difference between the fit mass and the PDG mass would most likely arise from a momentum reconstruction uncertainty. The calculated mass shift for K^0_S was 0.033 MeV/c^2 (0.0067%), for Λ it was 0.064 MeV/c^2 (0.0057%), and for $\bar{\Lambda}$ it was 0.18 MeV/c^2 (0.016%).

Figues 8.22, 8.23, and 8.24, show the upper and lower uncertainties for each specific uncertainty for K^0_S, Λ, and $\bar{\Lambda}$, respectively.

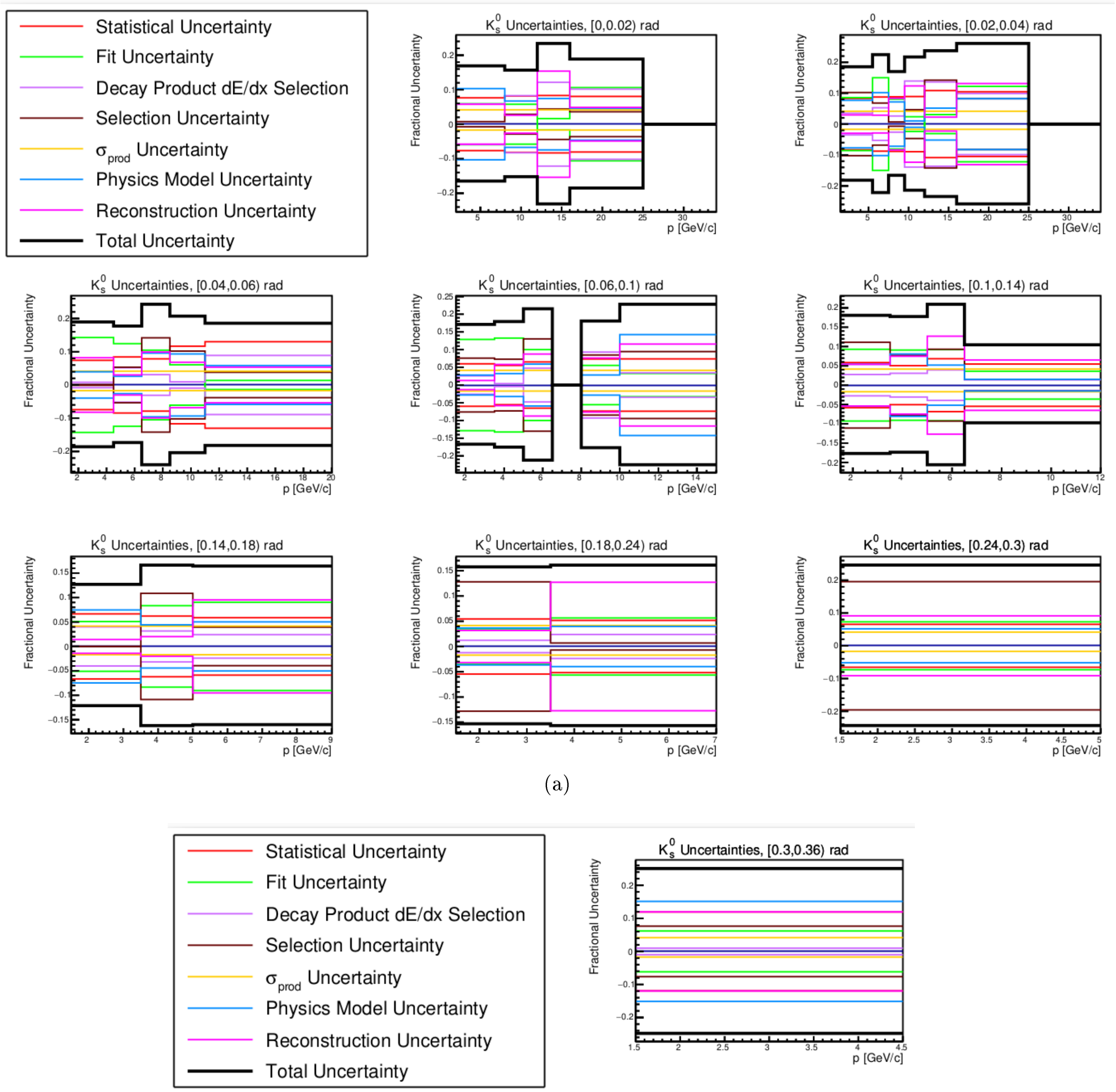

(a)

(b)

Figure 8.22: K_S^0 differential multiplicity uncertainties.

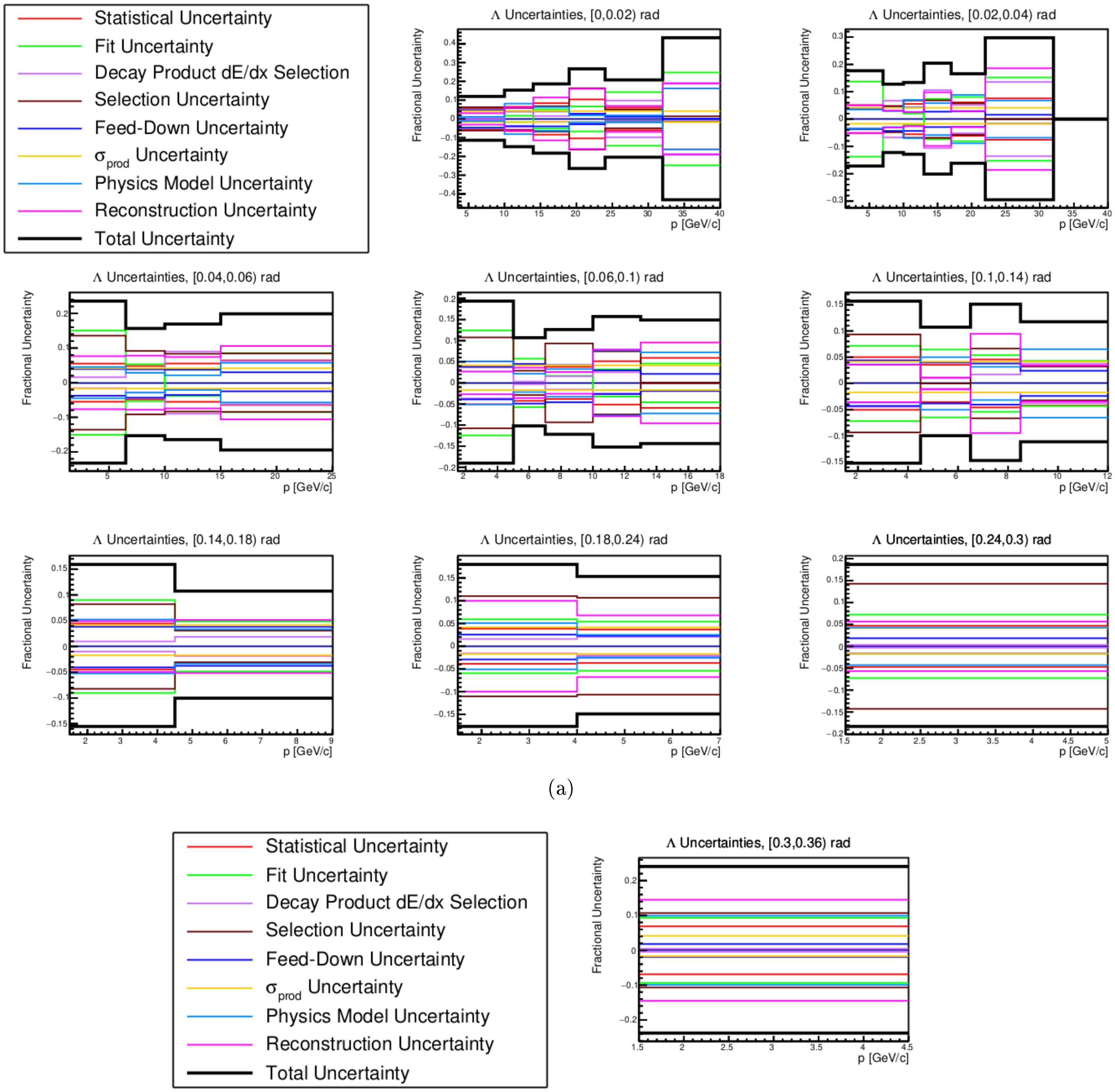

(a)

(b)

Figure 8.23: Λ differential multiplicity uncertainties.

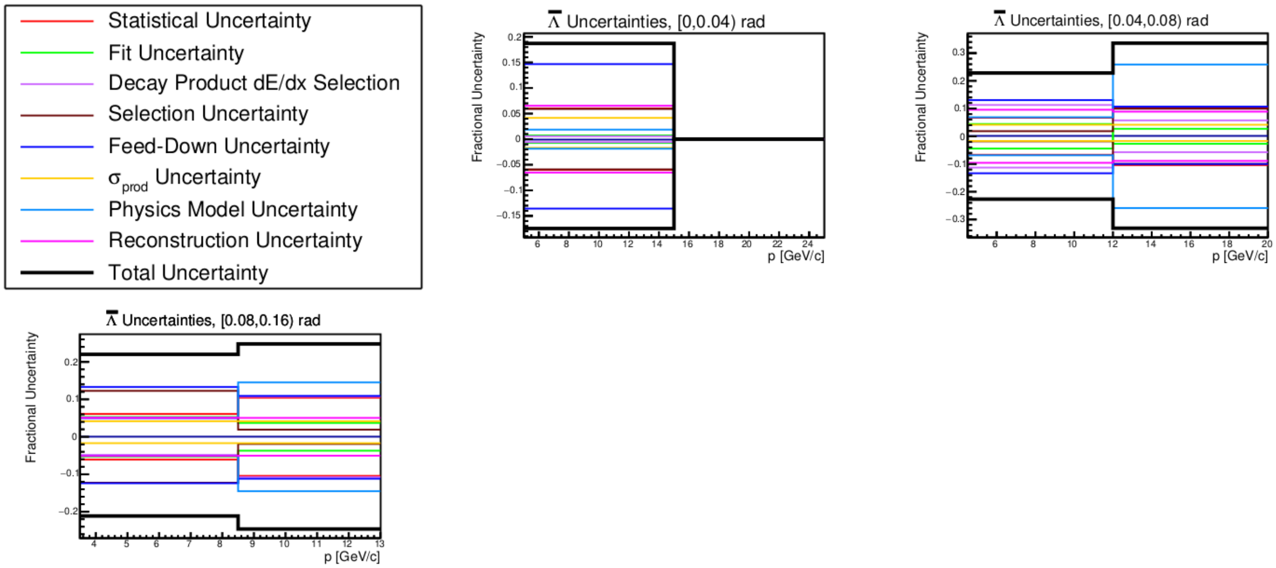

(a)

Figure 8.24: $\bar{\Lambda}$ differential multiplicity uncertainties.

Chapter 9

Charged Hadron Analysis

NA61/SHINE measures the multiplicity of the charged $\pi^{\pm}$, $K^{\pm}$, p, and $\bar{p}$ hadrons. This section will first discuss the analysis process to identify and measure the multiplicities of these particles before presenting results.

9.1 Particle Identification Via dE/dx

In order to distinguish particle types for each kinematic bin, a maximum likelihood dE/dx fit is performed. There are a total of 22 fit parameters involved, and the fit species are $e^{\pm}$, $\pi^{\pm}$, $K^{\pm}$, $p/\bar{p}$, and $D/\bar{D}$. (D stands for a deuteron, not a D meson.)

The fit model is constructed through ten asymmetric Gaussians (five each for the positive and negative particles), which describes the energy loss of each particle species through the use of the truncated mean discussed in Section 5.2.1.5. Each asymmetric Gaussian is given by

$$f(x,\sigma) = \frac{1}{\sqrt{2\pi}\sigma} e^{-\frac{1}{2}(\frac{x-\mu}{\delta\sigma})^2}, \quad \delta = \begin{cases} 1-d, & x \leq \mu \\ 1+d, & x > \mu \end{cases} . \tag{9.1}$$

This asymmetric Gaussian has two distinct widths, $\sigma_1 = (1-d)\sigma$ and $\sigma_2 = (1+d)\sigma$, and a mean of μ. If $d = 0$, then Equation 9.1 reverts to a symmetric Gaussian distribution. Figure 9.1 shows a sample representation of this distribution.

By convention from previous analyses, the peak of the asymmetric Gaussian, where the two pieces meet, is expressed in terms of the species' mean energy loss $\langle\epsilon\rangle$, d, and σ as

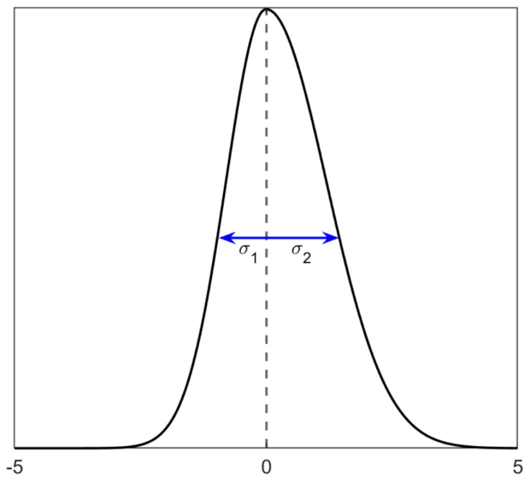

Figure 9.1: A sample asymmetric Gaussian demonstrating the two widths $\sigma_1 = (1-d)\sigma$ and $\sigma_2 = (1+d)\sigma$. For this plot $\mu = 0$, $\sigma = 1$, and $d = 0.2$ [48].

$$\mu = \langle\epsilon\rangle - \frac{4d\sigma}{\sqrt{2\pi}}. \tag{9.2}$$

For any single track i depositing energy inside the TPCs, the width σ_i of its energy loss distribution depends on the number of clusters N_{cl}, the track's energy loss ϵ, a base width σ_0, and a scaling parameter α to descibe the scaling dependance of ϵ:

$$\sigma_i = \frac{\sigma_0 \epsilon^\alpha}{N_{\mathrm{cl}}}. \tag{9.3}$$

As a result of differing TPC pad geometries and energy loss calibration, various parts of the TPCs are described by different base widths. Experimentally, NA61/SHINE needs four different base widths to accurately describe the energy loss of tracks: $\sigma_{0,\mathrm{Up}}$ for the upstream VTPC1 sectors one and four, $\sigma_{0,\mathrm{V}}$ for the rest of the VTPC sectors, $\sigma_{0,\mathrm{M}}$ for the MTPC sectors, and $\sigma_{0,\mathrm{F}}$ for the FTPC sectors. The GTPC is not included in the energy loss calibration, as it does not provide enough clusters to be of any use. VTPC1 sectors one and four get a different base width since the pad geometry in those two sectors is different than in the rest of the VTPC sectors. Putting all of these factors together, the base width for a single track can be written as

$$\sigma_i = \frac{\epsilon^{\alpha}}{\frac{N_{\text{cl, Up}}}{\sigma_{0,\text{Up}}} + \frac{N_{\text{cl, V}}}{\sigma_{0,\text{V}}} + \frac{N_{\text{cl, M}}}{\sigma_{0,\text{M}}} + \frac{N_{\text{cl, F}}}{\sigma_{0,\text{F}}}}. \tag{9.4}$$

For each kinematic bin, the fit model consists of the ten asymmetric Gaussians with widths dependent on the phase space of the constituent tracks. The likelihood function is constructed from the product of all of the positive and negative tracks in the bin. Then, taking the log to form the log-likelihood and explicity separating out positive and negative tracks, the log-likelihood is

$$LL(\text{data}; Y_e^{\pm}, Y_\pi^{\pm}, Y_K^{\pm}, Y_p^{\pm}, Y_D^{\pm}) = \sum_{i,j} \ln\left(\frac{Y_j}{\sqrt{2\pi}\sigma_i} e^{-\frac{1}{2}\left(\frac{\epsilon_i-\mu_j}{\delta\sigma_i}\right)^2}\right) + \sum_{k,l} \ln\left(\frac{Y_l}{\sqrt{2\pi}\sigma_k} e^{-\frac{1}{2}\left(\frac{\epsilon_k-\mu_l}{\delta\sigma_k}\right)^2}\right),$$

$$\begin{cases} i \in \text{positive tracks} \\ j \in e^+, \pi^+, K^+, p^+, D^+ \\ k \in \text{negative tracks} \\ l \in e^-, \pi^-, K^-, p^-, D^- \end{cases}. \tag{9.5}$$

The Y_i are the species fit yields, σ_i is the width of the energy loss distribution for a single track, ϵ_i is the single track's energy loss truncated mean, μ_j is from Equation 9.2 and corresponds to the center of each species' energy loss distribution, and δ is the asymmetry parameter, which is the same for all ten Gaussians.

To allow for variations resulting from imperfections in the calibration, six more fit parameters need to be introduced. Any misalignment to the predicted Bethe-Bloch functions for each species is given by additional X_j terms, which modify each species' mean energy loss $\langle\epsilon\rangle_j$. (Here the index j represents both the negative and positive particle species.) As the calibration is performed by selecting and fitting to regions of phase space dominated by pions, there are two $X_{\pi^\pm}$ terms to descibe each kinematic bin's shift between the fit pion peak and the predicted pion peak. Then, the other four shifts are defined as additional shifts for each particle species on top of the pion shift. Except for the pions, each species' shift is the same whether it is negative or positive. Writing it out explicity, these terms modify $\langle\epsilon\rangle_j$ in the following form:

$$\langle\epsilon\rangle_j = \begin{cases} \langle\epsilon\rangle_j + X_{\pi^\pm}, & \text{pions,} \\ \langle\epsilon\rangle_j + X_{\pi^\pm} + X_j, & \text{all other species,} \cdot \\ j \in \pi^\pm, e^\pm, K^\pm, p^\pm, D^\pm \end{cases} \tag{9.6}$$

The widths also get additional modification terms; the positive and negative track widths are allowed to vary independantly of each other, and due to the greater amount of scattering electrons undergo in comparison to the heavier particle species, the electrons are assigned a multiplicative width factor as well. Similar to how the Bethe-Bloch misalignment shifts modify each species' mean energy loss, the multiplicative width factors modify each track's σ_j by

$$\sigma_j = \begin{cases} f_\pm f_e \sigma_j, & \text{if } j = e^\pm, \\ f_\pm \sigma_j, & \text{if } j \neq e^\pm, \cdot \\ j \in e^\pm, \pi^\pm, K^\pm, p^\pm, D^\pm \end{cases} \tag{9.7}$$

To summarize, there are a total of 22 parameters for each kinematic bin's fit. As the yields are normalized to one and the contribution from negative deuterons is negligible, there are four positive yield parameters and three negative yield parameters Y_j. There are six X_j parameters to describe any shifts between each species' fit mean energy loss and the Bethe-Bloch predicted energy; two of these parameters describe the π^+ and π^- shifts, and the other four shifts are the same for the positive and negative fits for $e^\pm, K^\pm, p^\pm$, and $D^\pm$. Then, there are the four shaping parameters f_+, f_-, f_e, and d, and the four base widths $\sigma_{0,\mathrm{Up}}$, $\sigma_{0,\mathrm{V}}$, $\sigma_{0,\mathrm{M}}$, $\sigma_{0,\mathrm{F}}$. Finally, there is the scaling parameter α, which brings the total parameter count up to 22.

Parameter limits are used to prevent unphysical switching between species' peaks during the fit; for the pions the total allowed deviations from the predicted pion Bethe-Bloch were ±0.04, and the rest of the species were allowed to deviate by ±0.05. Like with the invariant mass fit in the neutral analysis, the minimization function passed to TMinuit was $-2LL$. Figure 9.2 shows a sample energy loss fit.

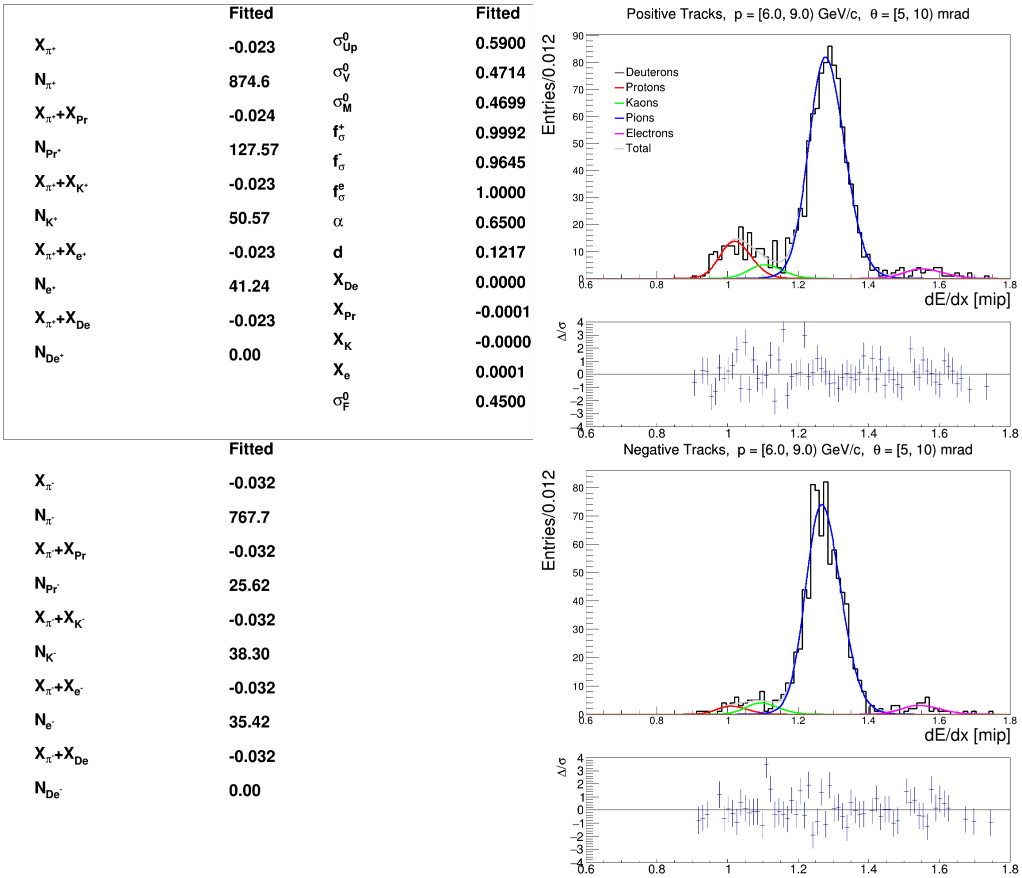

	Fitted		Fitted
X_{π^+}	-0.023	σ^0_{Up}	0.5900
N_{π^+}	874.6	σ^0_V	0.4714
$X_{\pi^+}+X_{Pr}$	-0.024	σ^0_M	0.4699
N_{Pr^+}	127.57	f^+_σ	0.9992
$X_{\pi^+}+X_{K^+}$	-0.023	f^-_σ	0.9645
N_{K^+}	50.57	f^e_σ	1.0000
$X_{\pi^+}+X_{e^+}$	-0.023	α	0.6500
N_{e^+}	41.24	d	0.1217
$X_{\pi^+}+X_{De}$	-0.023	X_{De}	0.0000
N_{De^+}	0.00	X_{Pr}	-0.0001
		X_K	-0.0000
		X_e	0.0001
		σ^0_F	0.4500

	Fitted
X_{π^-}	-0.032
N_{π^-}	767.7
$X_{\pi^-}+X_{Pr}$	-0.032
N_{Pr^-}	25.62
$X_{\pi^-}+X_{K^-}$	-0.032
N_{K^-}	38.30
$X_{\pi^-}+X_{e^-}$	-0.032
N_{e^-}	35.42
$X_{\pi^-}+X_{De}$	-0.032
N_{De^-}	0.00

Figure 9.2: A sample data energy loss fit from the charged analysis. The top plot is for positively charged particles, and the bottom plot is for negatively charged particles. A plot of the fit residual over the total number of data points for each is shown below each fit; the fit residual is the fit result minus the number of data points.

For the binning, as long as the total momentum bins are fine enough, the dE/dx will remain approximately constant in the covered phase space. When the bins were originally created for the analyses by S. Johnson [76] and B. Rumberger [48], they were created to bin the space as finely as possible while still retaining adequate statistic for each energy loss fit. This analysis uses the same binning scheme as B. Rumberger, with the removal of a handful of bins not covered by this reaction's phase space.

As shown later in Figure 9.9, there are cross-over regions in the Bethe-Bloch curves for the various particle species. When the Bethe-Bloch curves overlap, it is not possible to only use energy loss measurements to distinguish particles. The analysis for this thesis originally planned to use joint time-of-flight and energy loss measurements to cover the cross-over regions, like in the analysis by M. Pavin [78], but this plan was abandoned for two reasons. First, during the time between the dataset analyzed by M. Pavin and the 2017 90 GeV/c proton-carbon dataset, the TOFF wall configuration was reduced from 80 scintillator bars to 32 due to the addition of the FTPCs. In addition, during the 2017 dataset, the TOFF wall PMT power supply malfunctioned and set 12 PMT voltages to -3,000 V, instead of -1,600 V. The data from the six scintillator bars connected to these PMTs was rendered unusable for the entire dataset. As a result of the reduction in the phase space coverage and the malfunctioning power supply, the TOFF wall does not provide phase space coverage for the Bethe-Bloch cross-over regions for this dataset. (It is also worth mentioning part of the problem in the lack of phase space coverage results from the magnetic field configuration. The magnetic field used during the data taking of the 90 GeV/c proton-carbon dataset was four times stronger than the magnetic field in the dataset analyzed by M. Pavin; the stronger magnetic field bends the lower-momentum particles outside the coverage of the TOFF wall. A stronger magnetic field was used to be able to properly reconstruct particles with momentum up to 90 GeV/c, while the dataset analyzed by M. Pavin had a 31 GeV/c proton beam.)

9.2 Cut Flow

Typically charged analyses in NA61/SHINE differentiate between right-side tracks (RSTs) and wrong-side tracks (WSTs). RSTs are emitted from the target with momentum such that they are bent in the same direction they were produced, and WSTs are emitted where they bend in the opposite direction they were produced. This can be expressed in terms of the track's x momentum p_x and charge q as

$$\begin{cases} q \cdot p_x > 0 & \text{RST,} \\ q \cdot p_x < 0 & \text{WST} \end{cases} . \tag{9.8}$$

The reason for differentiating these two track topologies arises from the TPC pad geometry. The VTPC pads and some of the MTPC pads are angled with respect to the beamline in order for RST tracks to traverse parallel to the pads, and WST tracks will cross pads at an angle. Tracks that cross pads at an angle will produce distorted clusters, which make reconstructing the track more difficult. RST tracks are used in this analysis, and WST tracks are used as a cross-check. Figure 9.3 shows a graphical depiction of RSTs and WSTS from SHINE's eventBrowser.

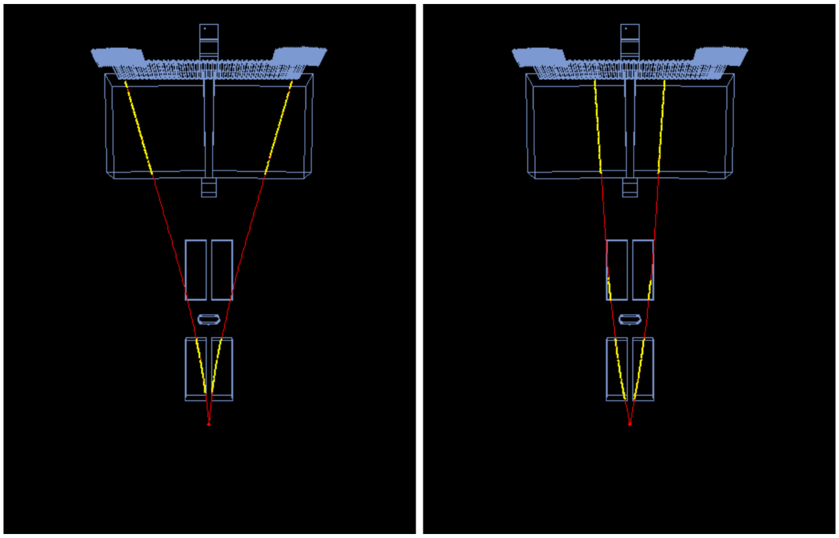

Figure 9.3: Left: RSTs curve in the same direction they were emitted from the target. Right: WSTs curve in the opposite direction [48].

After the selection of RSTs, there are 11 cuts used to remove the background and improve the signal for each kinematic bin. The first three cuts are the same event-level cuts used in the neutral analysis. The beam particle is required to extrapolate within 0.95 cm of the center of the S4, there is a 2.5 µs offtime particle cut, and the BPD track must be well-reconstructed and have a cluster in the most downstream BPD.

After these three event-level cuts, there are six cuts applied for all particle species. The first one, cut number 4, requires the main vertex of the event to be within 5 cm of the target center, to ensure the particles were produced from an interaction inside the target. Then, the impact parameter cut, (4.0, 2.0) cm in (x, y), further helps to ensure each track is coming from inside the target. After this, each track is required to have 12 total clusters for proper reconstruction; as only the VTPCs and GTPC are inside the magnetic field, cut 7 is an additional cluster topology cut that requires at least 12 VTPC clusters or 3 GTPC clusters for proper momentum reconstruction. A potential points cut looks at the ratio of measured clusters versus potential clusters from the number of pads the track crosses. The allowed potential points ratio is between 0.4 and 2.0, which removes tracks with major cluster reconstruction issues. Finally, the ninth cut requires the track's momentum to be less than 2.2 GeV/c or the track's energy loss to be less than 2.0 MIP. MIP stands for minimum ionizing particle, and the energy loss calibration places the base of the pion energy loss distribution at ~ 1.0. This ninth cut removes tracks with an unreasonable energy loss measurement.

As mentioned earlier, and shown in Figure 9.9, there are Bethe-Bloch cross-over regions where the energy loss cannot be used to distinguish particle species. These regions are removed from the analysis by the tenth cut. For pions the removed momentum region is $1.64 < |p| < 2.02$ GeV/c, for protons it is $1.64 < |p| < 4.32$ GeV/c, and for kaons it is $0.95 < |p| < 4.32$ GeV/c.

The final cut, cut number 11, selects regions of uniform phi acceptance. For each kinematic bin, a MC sample is generated, and only regions of uniform phi acceptance are used in the analysis to ensure the proper application of the MC correction factors; Figure 9.4 shows the regions of ϕ acceptance for one angular bin.

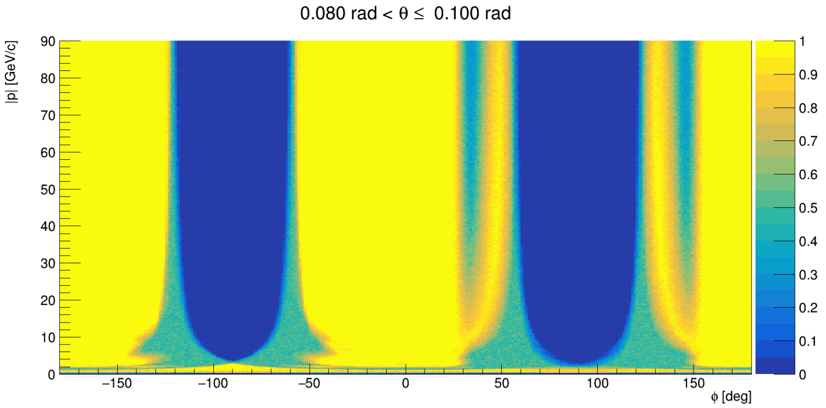

Figure 9.4: The yellow regions indicate phase space with good ϕ acceptance. Regions of poor ϕ acceptance, the blue and green regions, are excluded by the ϕ acceptance cut. This exclusion is then corrected for with the MC corrections.

The event-level cut flow is the same as shown in Table 8.2, and Table 9.1 shows the target-in track-level cut flow for the charged analysis.

Cut	π^+	π^-	K^+	K^-	p	$\bar{p}$
00 No Cuts	3,630k	2,222k	3,100k	2,072k	4,068k	2,199k
01 S4	3,584k	2,194k	3,060k	2,044k	4,013k	2,170k
02 Off-Time Beam Particle	2,753k	1,683k	2,350k	1,569k	3,035k	1,665k
03 BPD Track	2,588k	1,581k	2,208k	1,473k	2,852k	1,564k
04 Main Vertex Z	2,217k	1,346k	1,882k	1,251k	2,467k	1,332k
05 Impact Parameter	2,052k	1,245k	1,738k	1,153k	2,272k	1,232k
06 Total Clusters	2,019k	1,224k	1,712k	1,135k	2,238k	1,213k
07 Cluster Topology	1,836k	1,114k	1,584k	1,056k	2,055k	1,109k
08 Potential Points	1,818 k	1,105k	1,575k	1,049k	2,001k	1,099k
09 Reasonable Energy Loss	1,810 k	1,100k	1,567k	1,043k	1,997k	1,094k
10 Bethe-Bloch Crossing	1,716k	1,024k	931k	541k	1,467k	686k
11 Phi Acceptance	701k	424k	411k	242k	580k	295k

Table 9.1: The track-level cut flow for the target-in charged analysis.

Figure 9.5 shows the momentum distribution before applying any cuts. Figures 9.6, 9.7, and 9.8 show the binned phase space for positive RST pions, protons, and kaons, respectively, before and after applying the analysis cuts. Finally, 9.9 shows the energy loss distribution for positive pions before and after applying the analysis cuts.

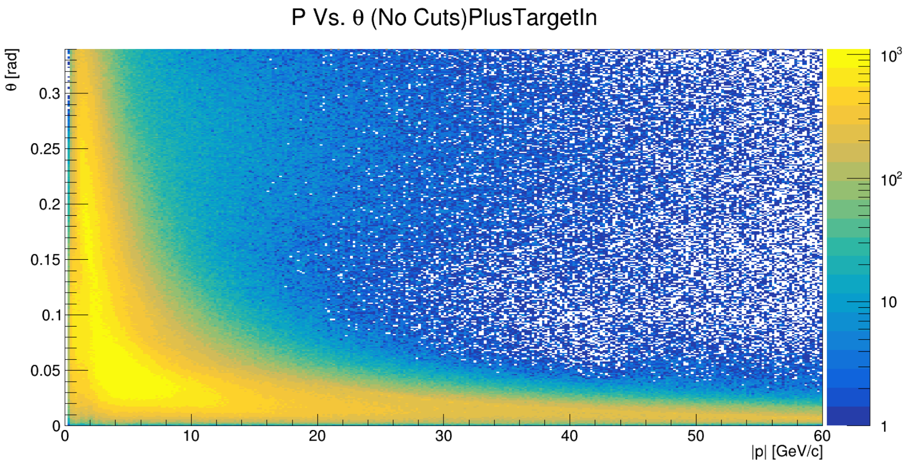

Figure 9.5: The momentum distribution for positive particles before applying any cuts.

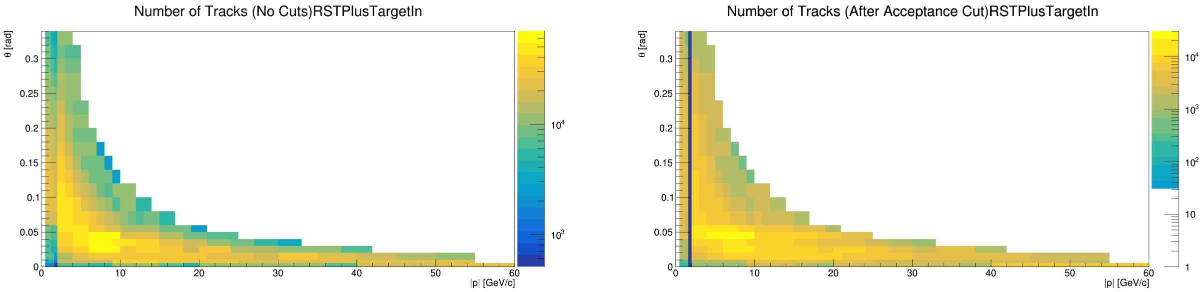

(a) (b)

Figure 9.6: Left: The binned phase space for positive pions before applying any cuts. Right: After applying all cuts in the pion analysis.

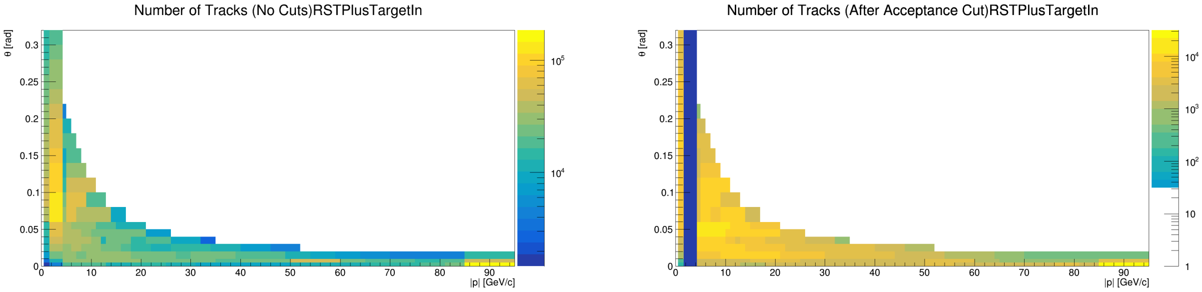

(a) (b)

Figure 9.7: Left: The binned phase space for positive protons before applying any cuts. Right: After applying all cuts in the proton analysis.

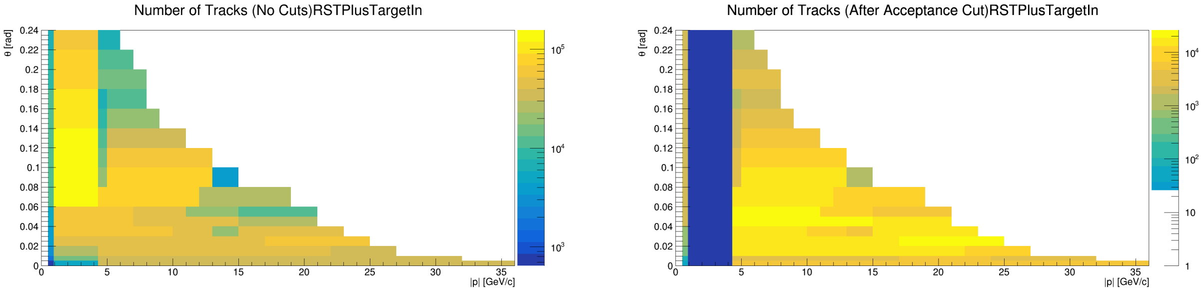

(a) (b)

Figure 9.8: Left: The binned phase space for positive kaons before applying any cuts. Right: After applying all cuts in the kaon analysis.

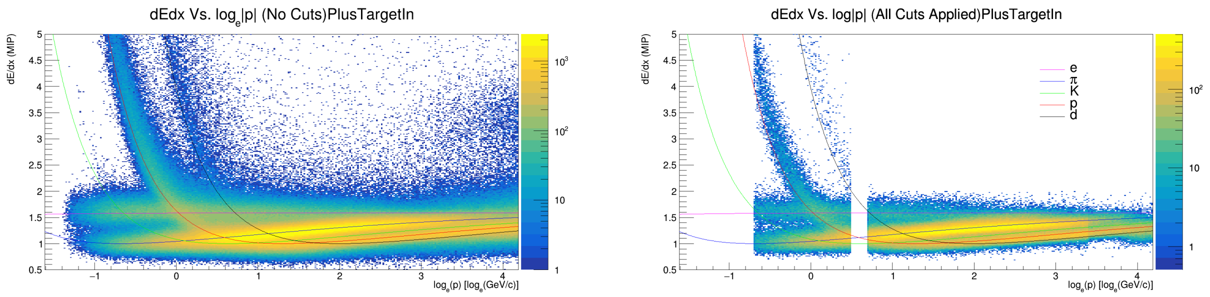

(a) (b)

Figure 9.9: Left: The energy loss distribution for positive particles before applying any cuts. Right: After applying all cuts in the pion analysis.

9.3 MC, Feed-Down, and Fit Bias Corrections

In an analagous manner to the neutral MC corrections discussed in Section 8.3, each kinematic bin in the charged analysis gets a MC correction factor; the one difference is that there is no correction for selecting a decay branching ratio. The charged analysis also gets a feed-down correction, similar to the neutral analysis. (For example, K_S^0 can decay to positively charged pions outside the target volume, and the pions from these decays need to be excluded from the multiplicity measurements.) However, with the results of the neutral analysis in hand, it is possible to reweight the charged feed-down corrections using the neutral hadron measurements, which significantly reduces the associated uncertainty. For a kinematic bin i in the charged analysis, the reweighting factor w_i is given by

$$w_i = \frac{m_i^{\text{data}}}{m_i^{\text{MC}}}, \tag{9.9}$$

where m_i^{data} is the measured multiplicity a particular neutral hadron from the neutral analysis, and m_i^{MC} is the predicted MC multiplicity. Of course, these corrections can only be applied for bins covered by the neutral analysis; if the bin is not covered, the feed-down correction has to be taken completely from MC.

Lastly, there is also a fit bias correction applied to each bin in the charged analysis. Using the data fit results for each kinematic bin, the fit parameters were varied according to their distributions, and each track's energy loss was simulated with the new fit parameters. This was done for a total of 50 trials, and the fit bias correction factor was calculated as

$$c_i^{\mathrm{fit}} = \frac{1}{N_{\mathrm{trials}}} \sum_{n=1}^{N_{\mathrm{trials}}} \left(\frac{y_n^{\mathrm{fit}} - y_n^{\mathrm{true}}}{y_n^{\mathrm{true}}} \right). \tag{9.10}$$

Here $N_{\mathrm{trials}} = 50$, and y_n^{fit} and y_n^{true} are the fit and true yields, respectively. Figure 9.10 shows the results of a sample MC energy loss fit trial.

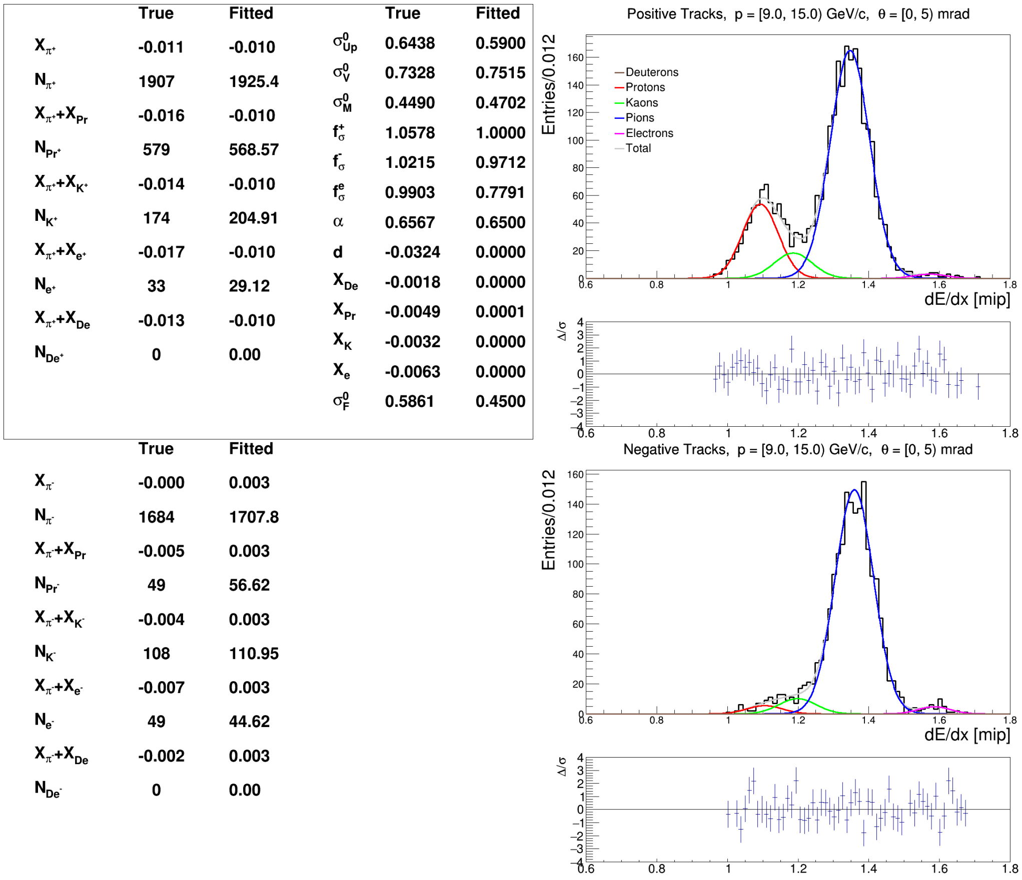

	True	Fitted
X_{π^+}	-0.011	-0.010
N_{π^+}	1907	1925.4
$X_{\pi^+}+X_{Pr}$	-0.016	-0.010
N_{Pr^+}	579	568.57
$X_{\pi^+}+X_{K^+}$	-0.014	-0.010
N_{K^+}	174	204.91
$X_{\pi^+}+X_{e^+}$	-0.017	-0.010
N_{e^+}	33	29.12
$X_{\pi^+}+X_{De}$	-0.013	-0.010
N_{De^+}	0	0.00

	True	Fitted
σ^0_{Up}	0.6438	0.5900
σ^0_{V}	0.7328	0.7515
σ^0_{M}	0.4490	0.4702
f^+_σ	1.0578	1.0000
f^-_σ	1.0215	0.9712
f^e_σ	0.9903	0.7791
α	0.6567	0.6500
d	-0.0324	0.0000
X_{De}	-0.0018	0.0000
X_{Pr}	-0.0049	0.0001
X_K	-0.0032	0.0000
X_e	-0.0063	0.0000
σ^0_F	0.5861	0.4500

	True	Fitted
X_{π^-}	-0.000	0.003
N_{π^-}	1684	1707.8
$X_{\pi^-}+X_{Pr}$	-0.005	0.003
N_{Pr^-}	49	56.62
$X_{\pi^-}+X_{K^-}$	-0.004	0.003
N_{K^-}	108	110.95
$X_{\pi^-}+X_{e^-}$	-0.007	0.003
N_{e^-}	49	44.62
$X_{\pi^-}+X_{De}$	-0.002	0.003
N_{De^-}	0	0.00

Figure 9.10: A sample MC energy loss fit trial.

Figures 9.11, 9.12, and 9.13 show the MC corrections excluding feed-down corrections, the feed-down corrections, and the fit bias corrections, respectively, for pions, protons, and kaons. The charged kaons do not get a feed-down correction.

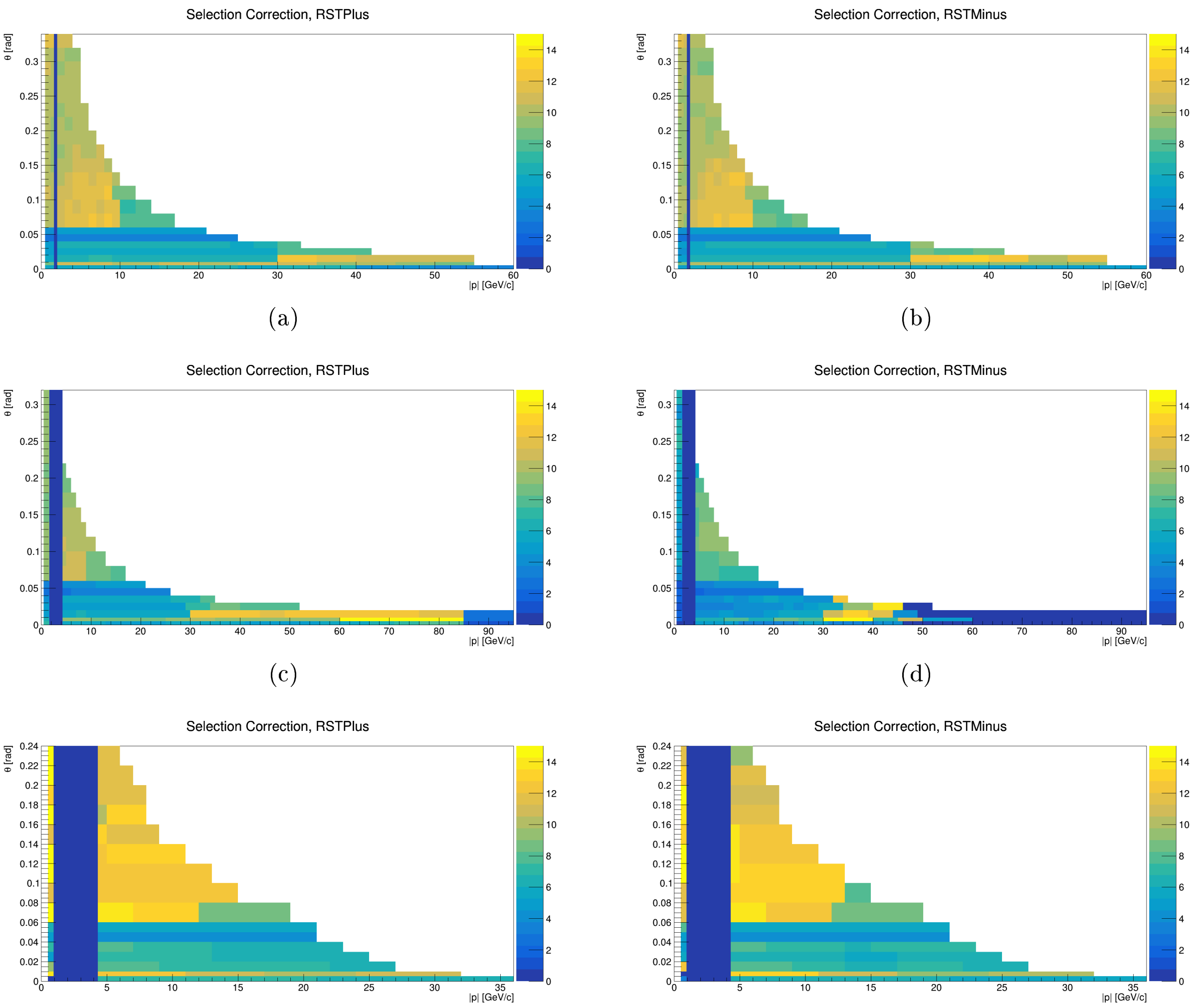

(a) (b)

(c) (d)

(e) (f)

Figure 9.11: Top Left: The MC corrections for positive pions, excluding the feed-down corrections. Top Right: Negative pions. Middle Left: Positive protons. Middle Right: Negative protons. Bottom Left: Positive kaons. Bottom Right: Negative kaons.

9.4 Results

Like with the neutral analysis, the normalized differential multiplicity is calculated for each kinematic bin using Equation 8.13. Figures 9.14-9.28 show the results of the charged analysis for $\pi^{\pm}$, $K^{\pm}$, and $p/\bar{p}$. The details of the uncertainty calculcations are presented in Section 9.5, and the numerical values are presented in Appendix A.

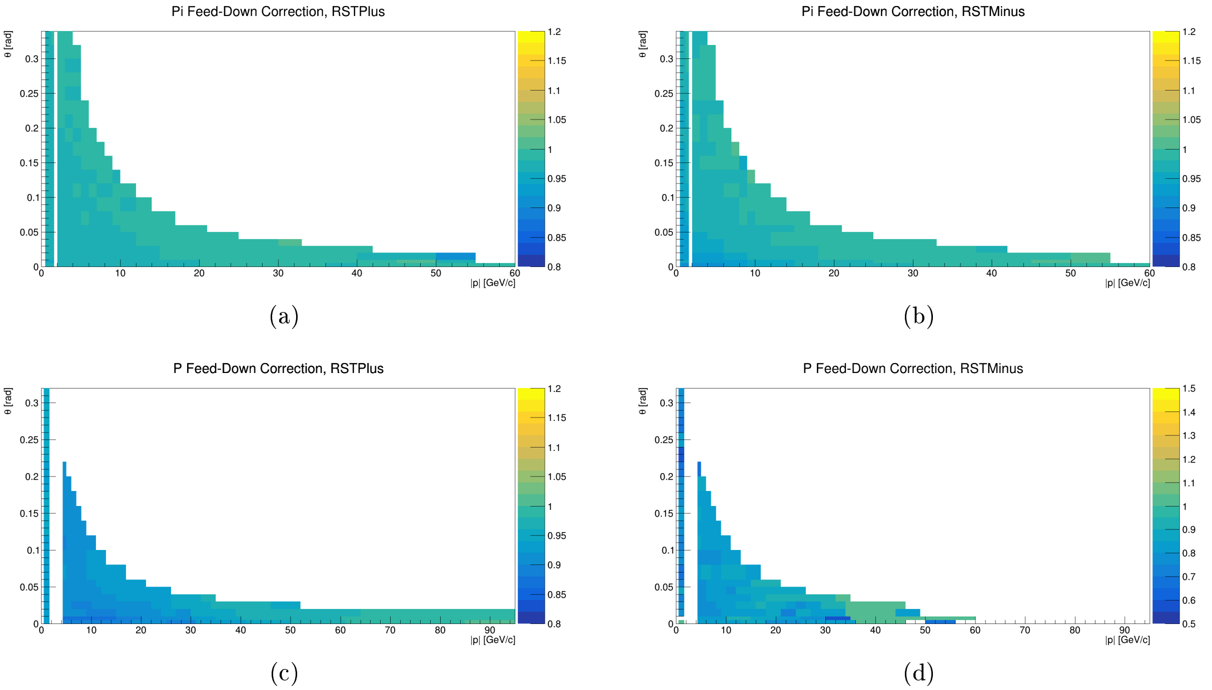

Figure 9.12: Top Left: The feed-down corrections for positive pions. Top Right: Negative pions. Bottom Left: Positive protons. Bottom Right: Negative protons.

9.5 Uncertainties

The uncertainties for the charged analysis are calculated analagously to the methods described in Section 8.7 for the neutral analysis, and the differences will be highlighted here. In the charged analysis, the fit uncertainty is calculated from the standard deviation of the 50 fit trials for each bins. For the feed-down uncertainty, if the parent particle is covered by the neutral analysis, the uncertainty is taken from the neutral multiplicity measurement; if the bin is not covered, an uncertainty of 50% is applied. Figure 9.29 shows the significant reduction in the feed-down uncertainties by reweighting with neutral data [32].

The only other difference in the calculated uncertainties comes from the reconstruction uncertainty. On top of shifting the VTPCs by 200 μm, the GTPC and FTPC1 are shifted by 100 μm in x as well. Figures 9.30-9.44 show the break down of uncertainties for each kinematic bin covered by the neutral analysis.

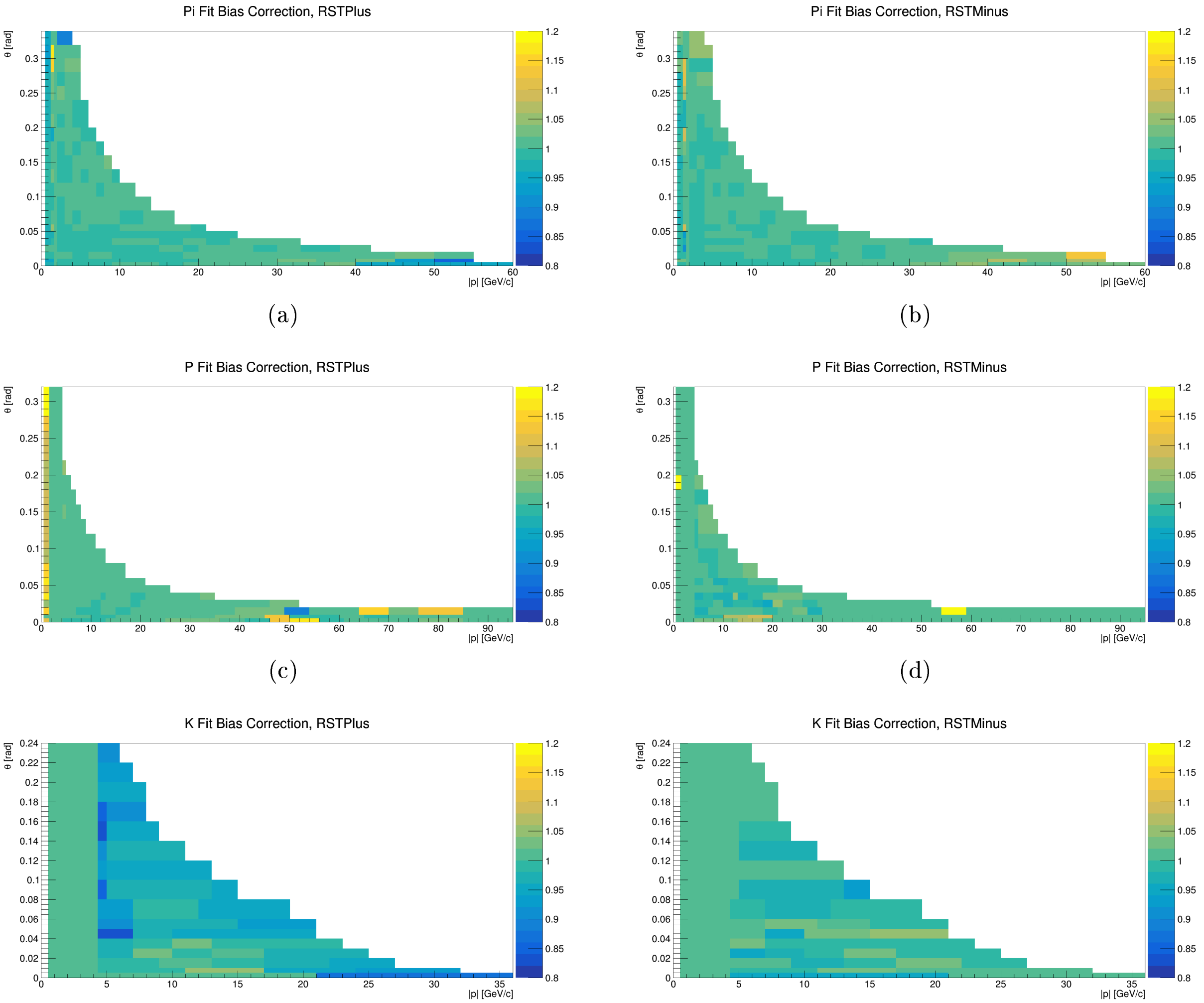

(a) (b)

(c) (d)

(e) (f)

Figure 9.13: Top Left: The fit bias corrections for positive pions. Top Right: Negative pions. Middle Left: Positive protons. Middle Right: Negative protons. Bottom Left: Positive kaons. Bottom Right: Negative kaons.

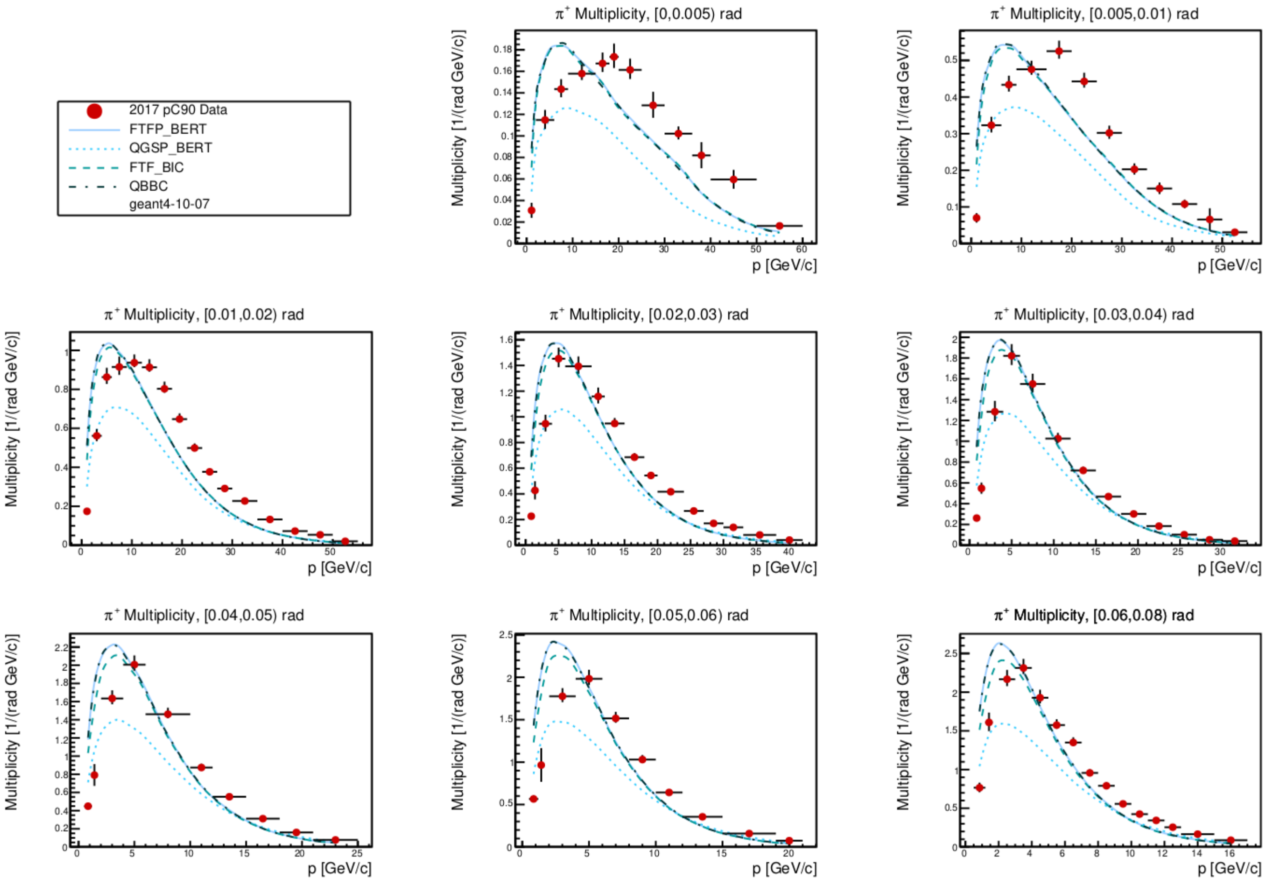

Figure 9.14: π^+ differential multiplicity results.

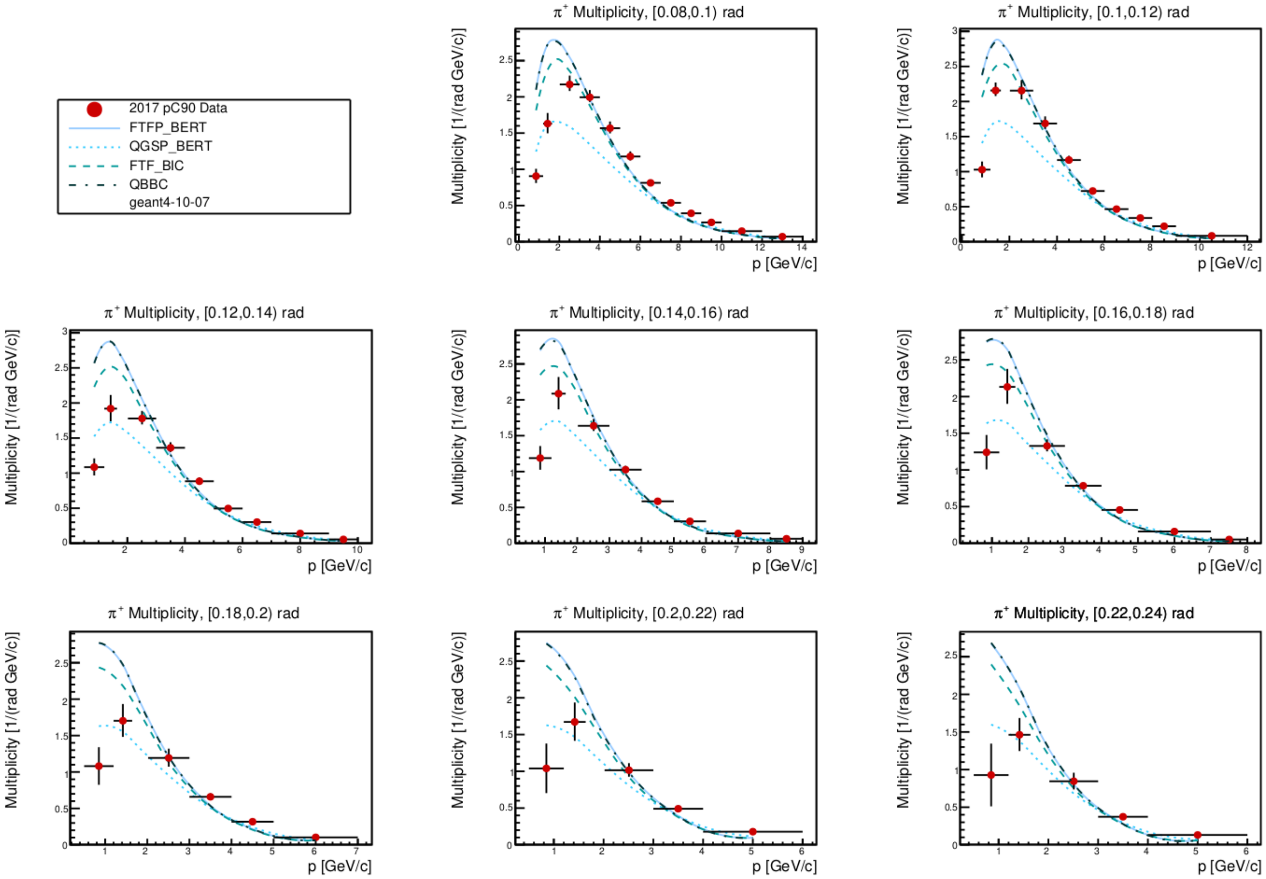

Figure 9.15: π^+ differential multiplicity results (continued).

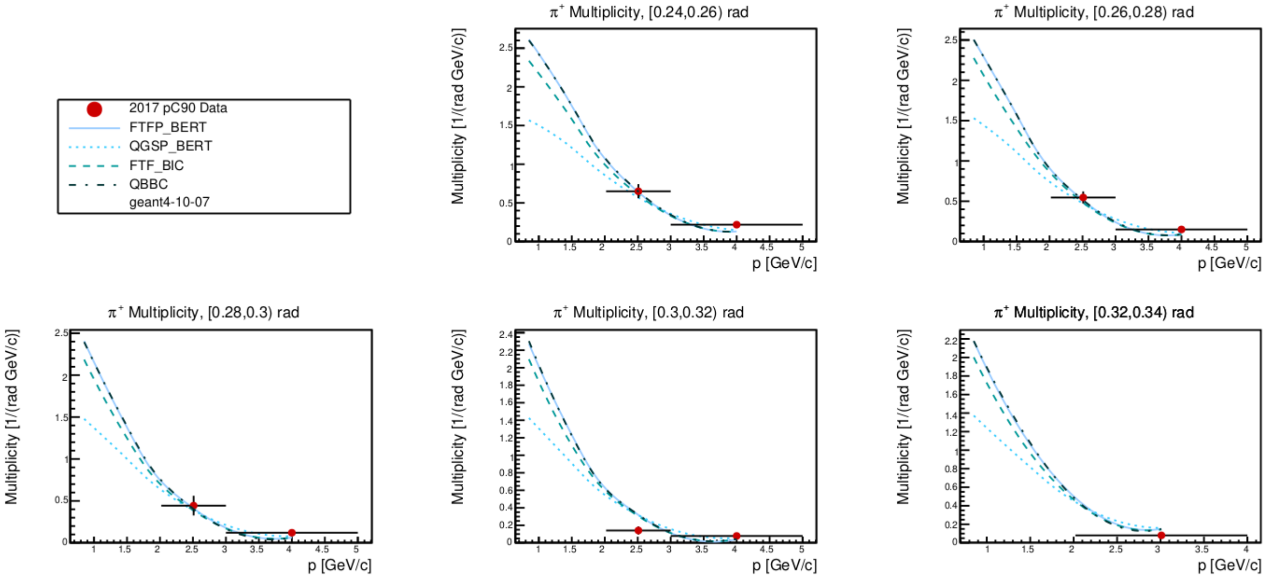

Figure 9.16: π^+ differential multiplicity results (continued).

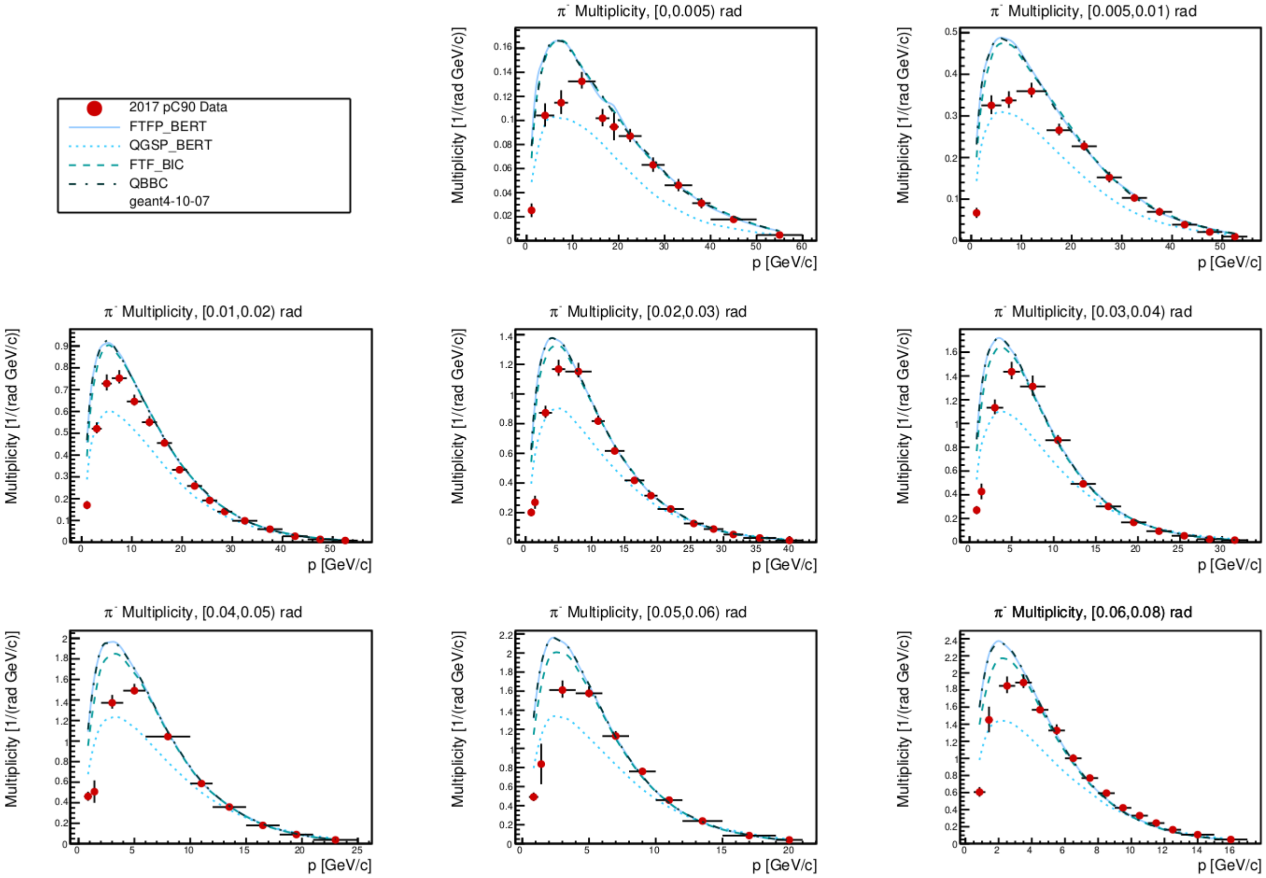

Figure 9.17: π^- differential multiplicity results.

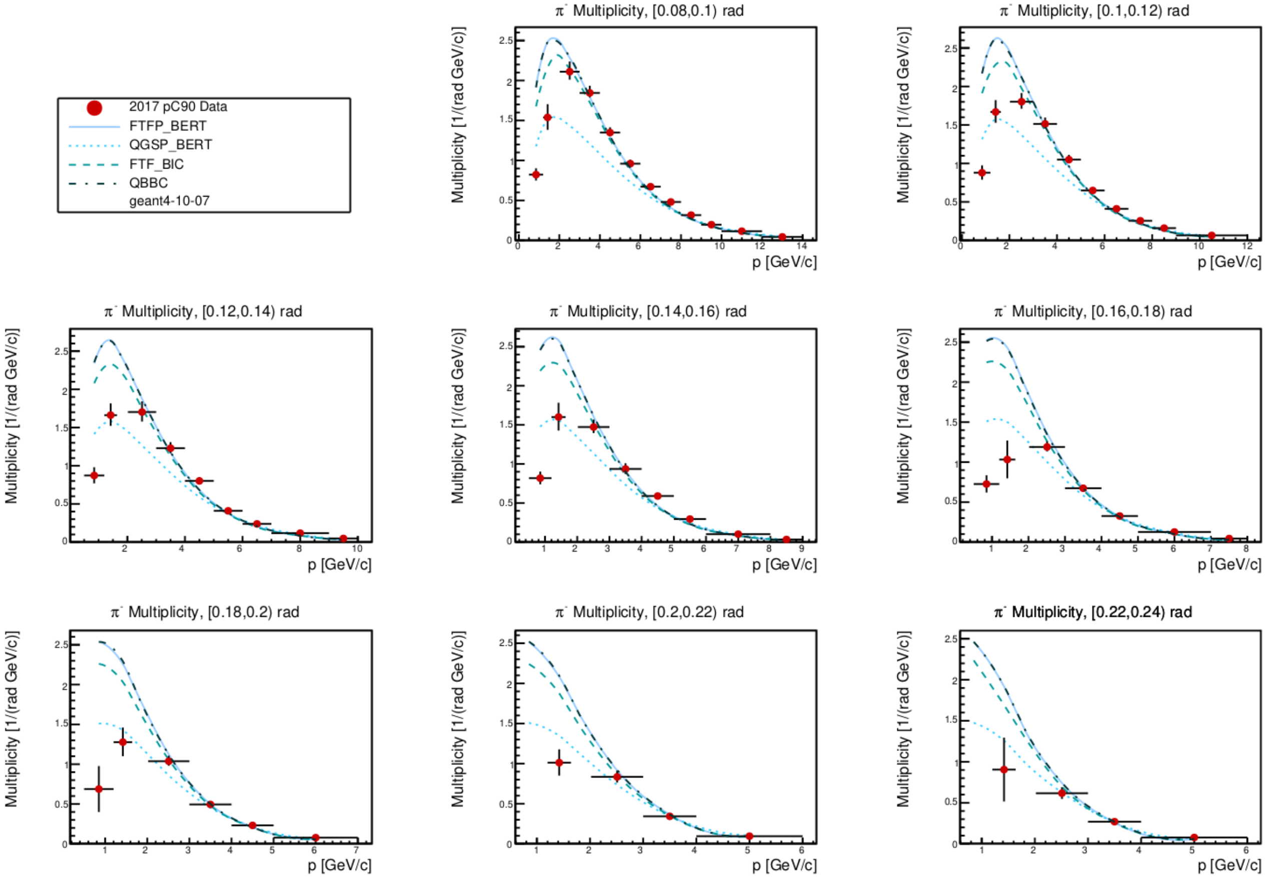

Figure 9.18: π^- differential multiplicity results (continued).

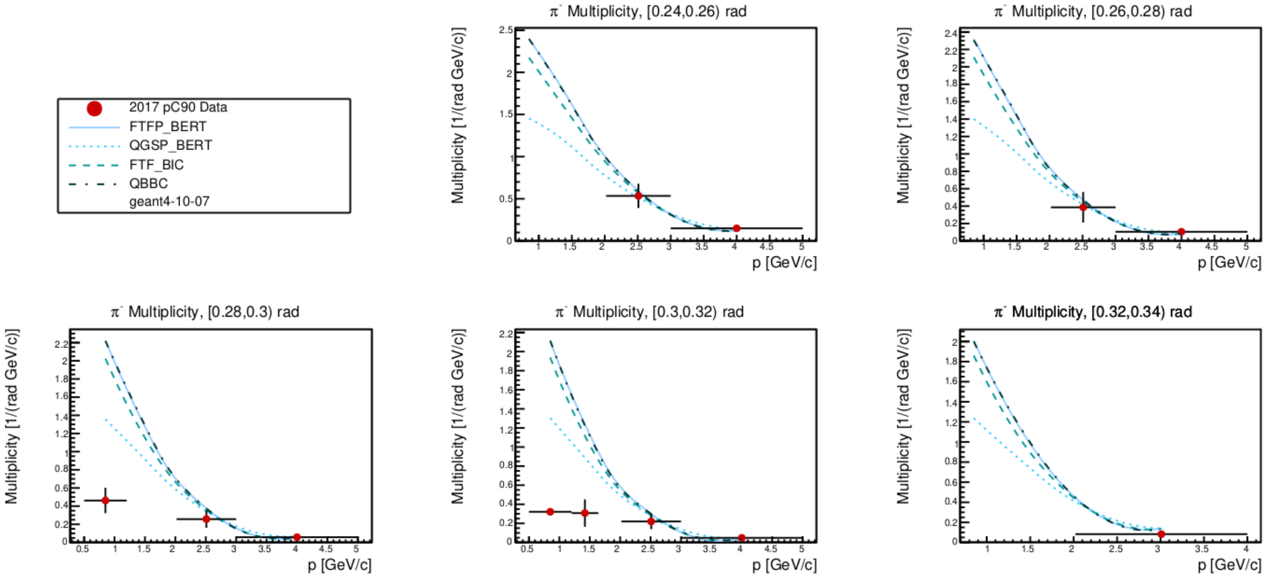

Figure 9.19: π^- differential multiplicity results (continued).

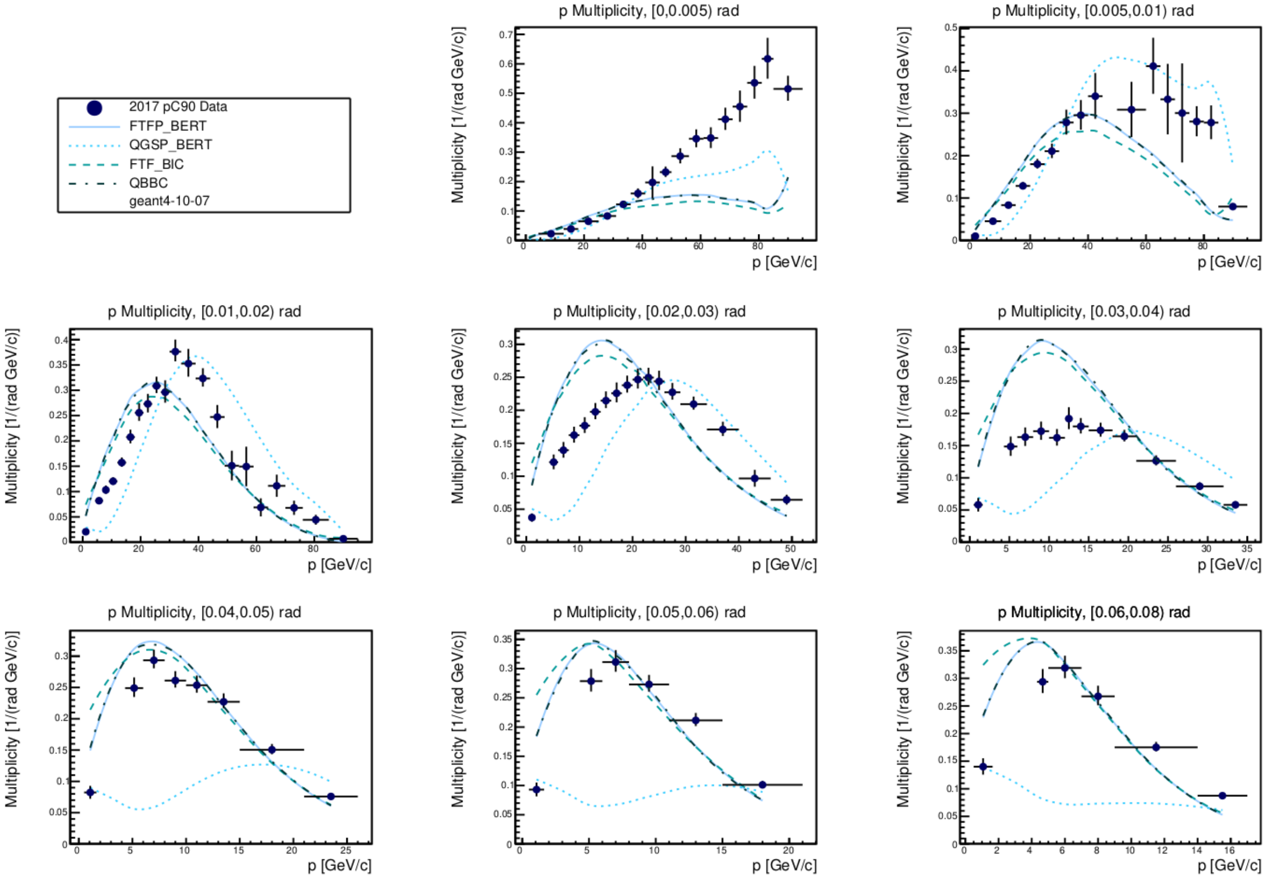

Figure 9.20: p differential multiplicity results.

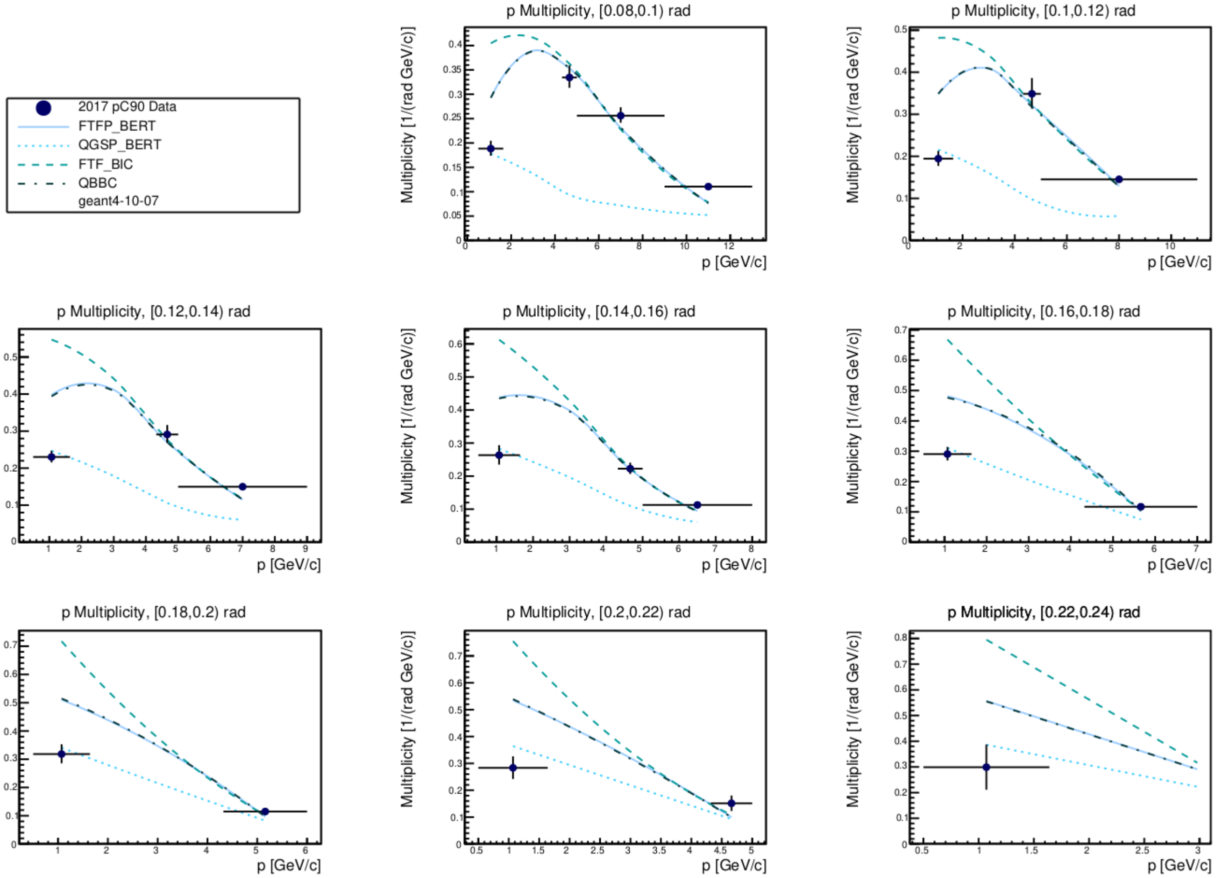

Figure 9.21: p differential multiplicity results (continued).

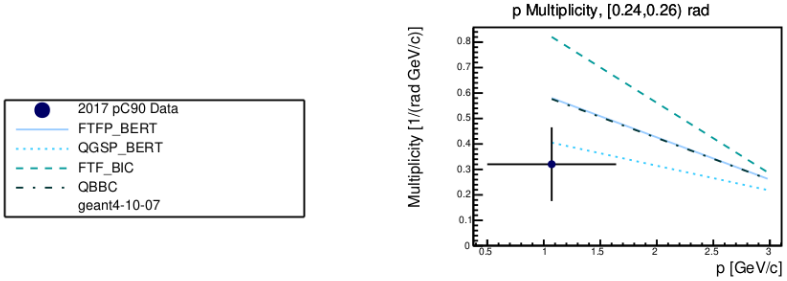

Figure 9.22: p differential multiplicity results (continued).

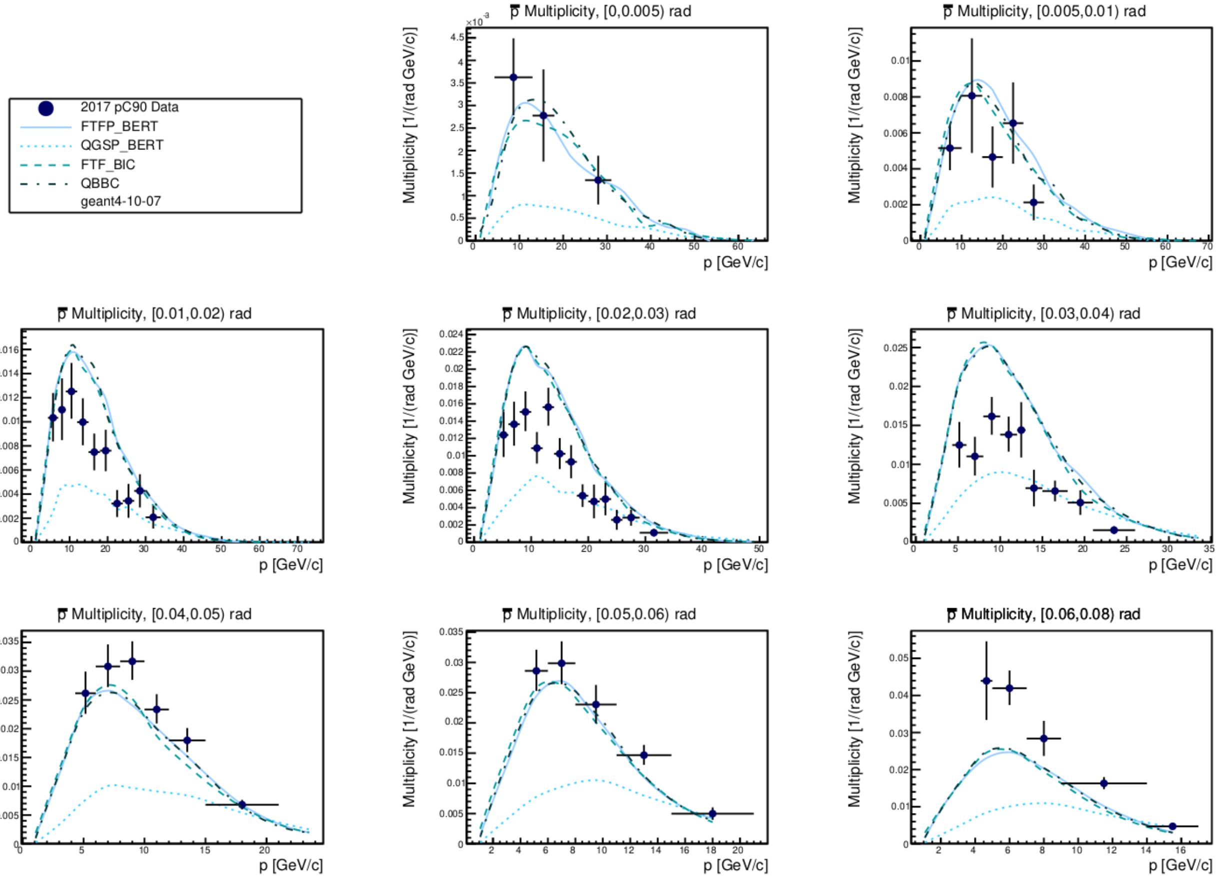

Figure 9.23: $\bar{p}$ differential multiplicity results.

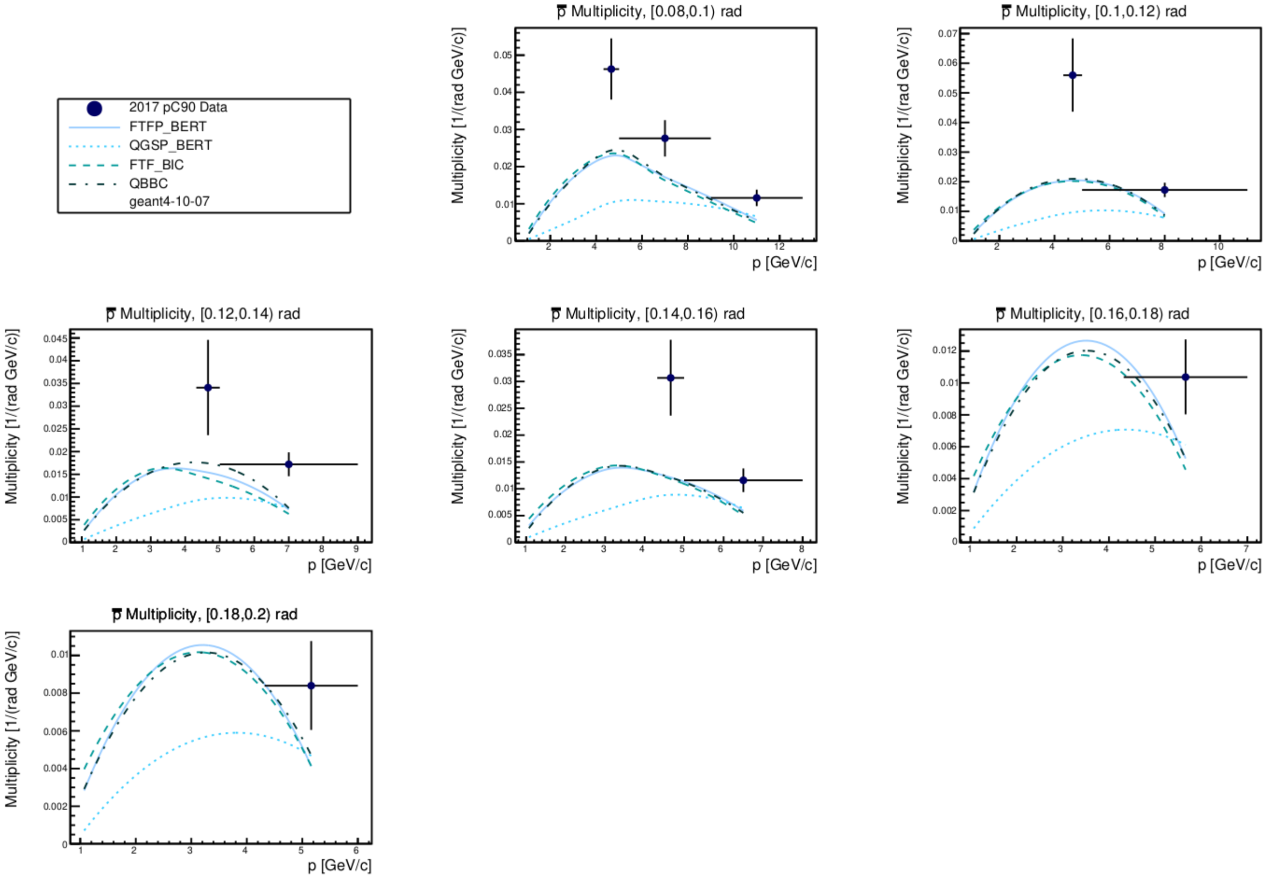

Figure 9.24: $\bar{p}$ differential multiplicity results (continued).

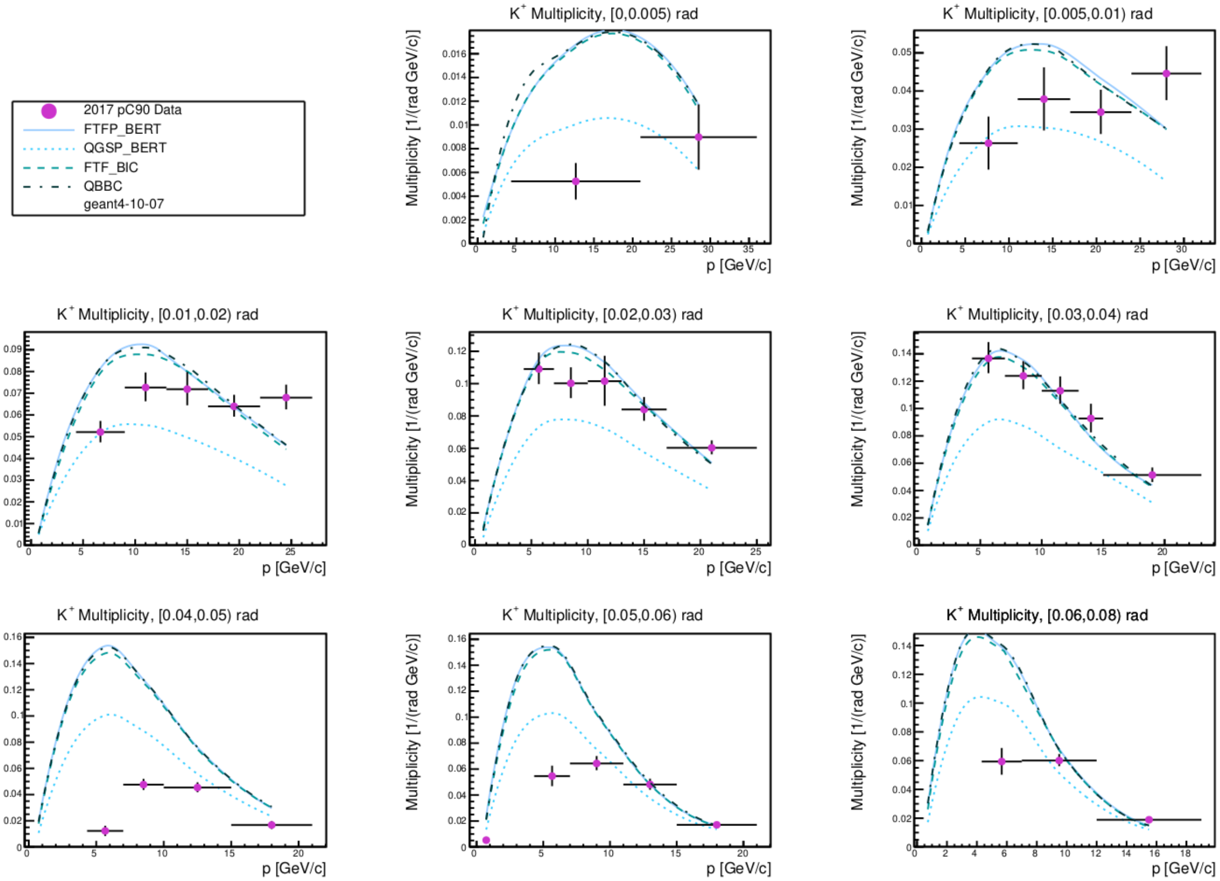

Figure 9.25: K^+ differential multiplicity results.

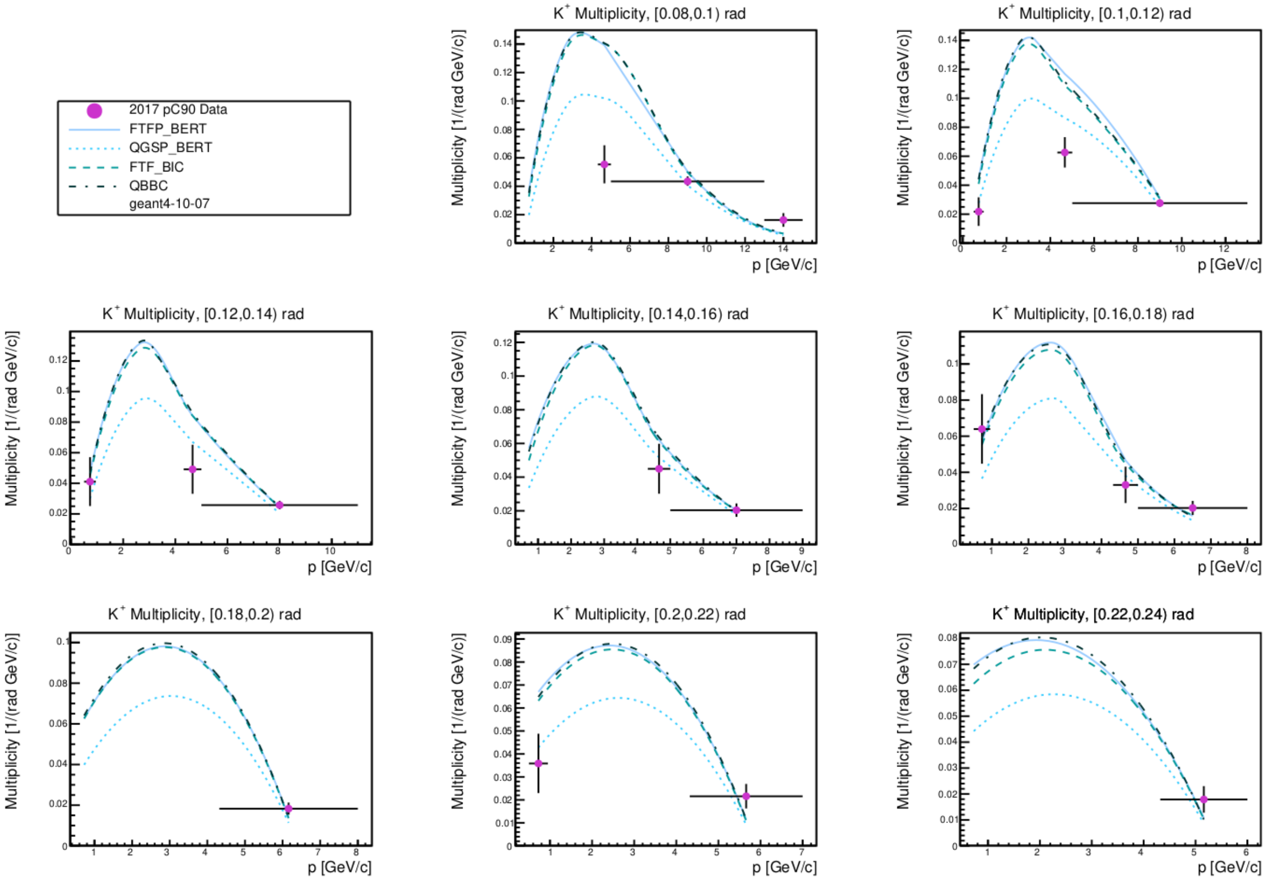

Figure 9.26: K^+ differential multiplicity results (continued).

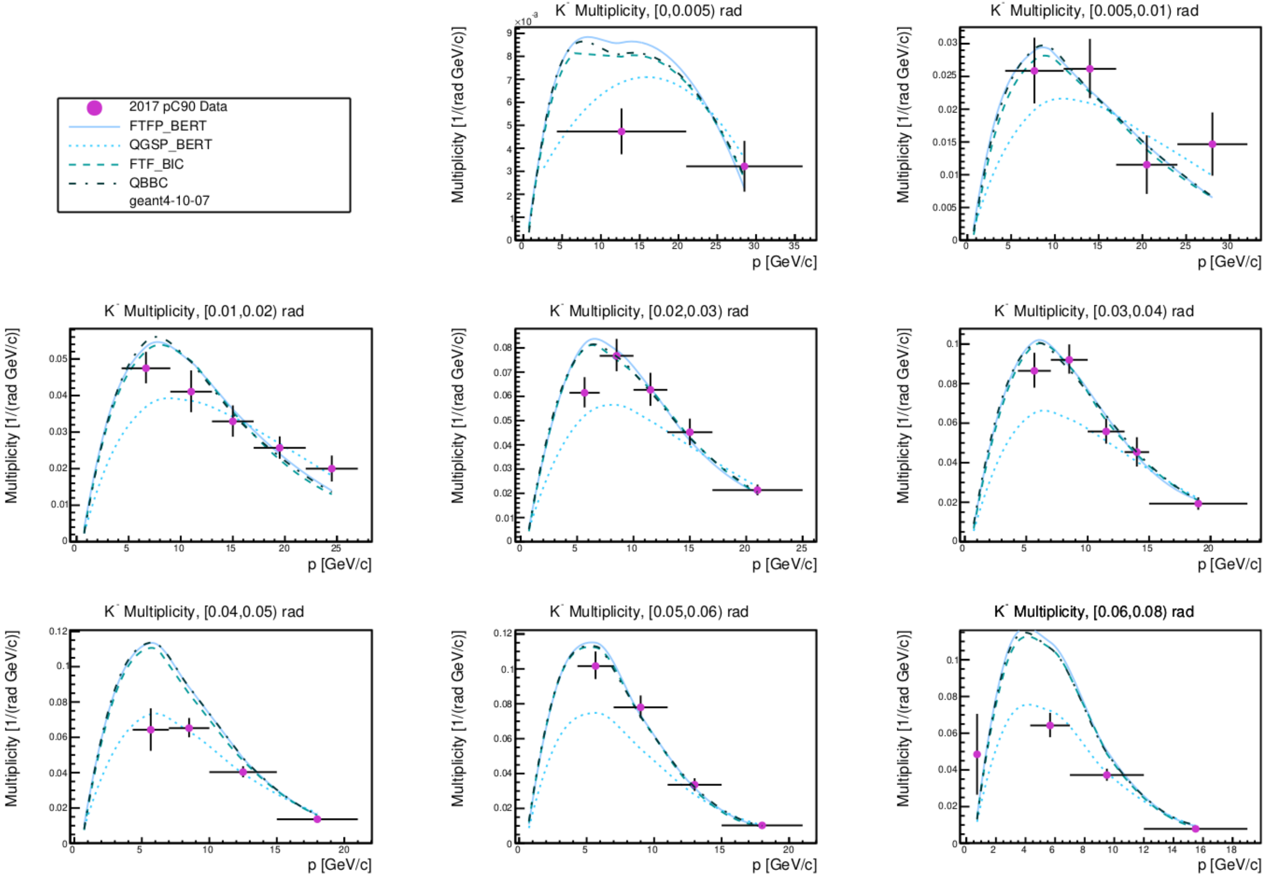

Figure 9.27: K^- differential multiplicity results.

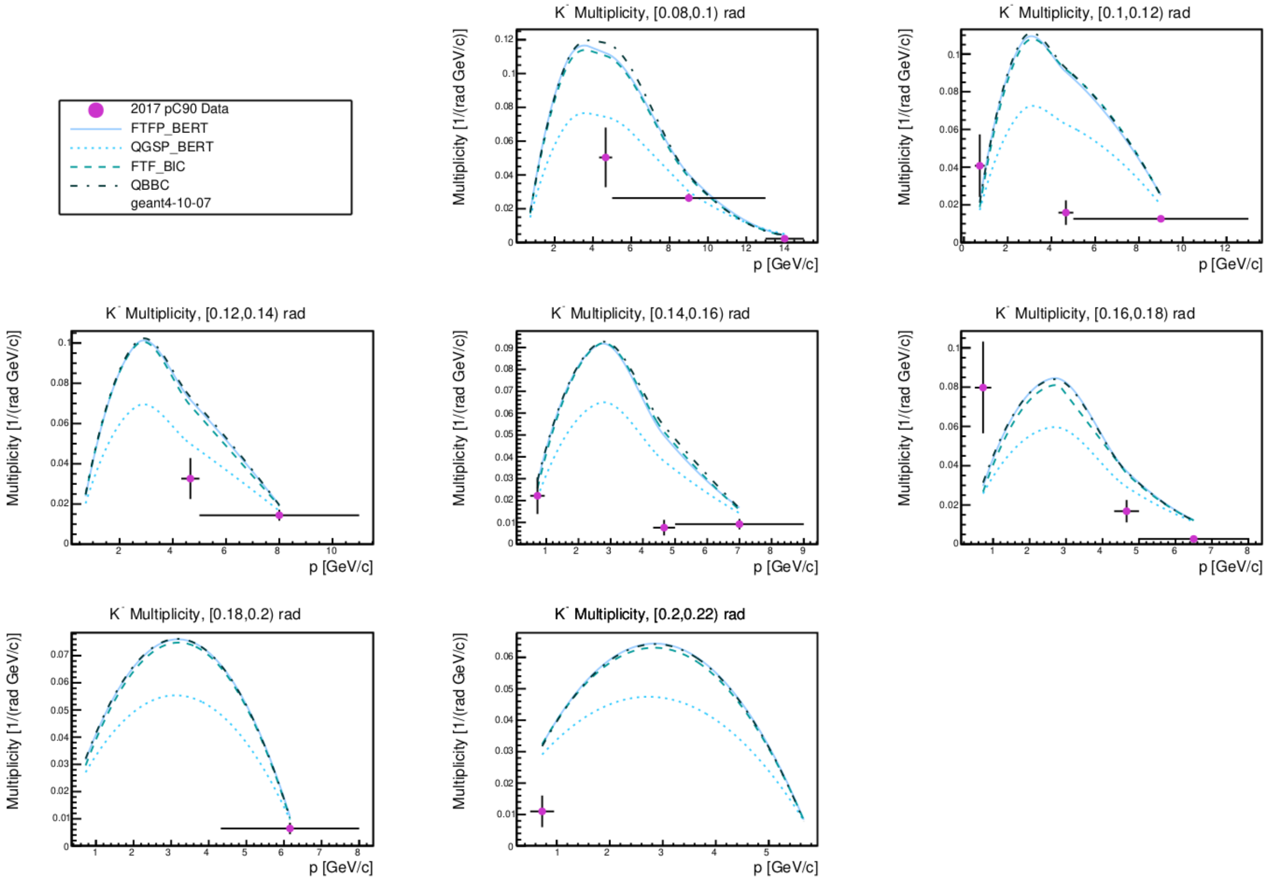

Figure 9.28: K^- differential multiplicity results (continued).

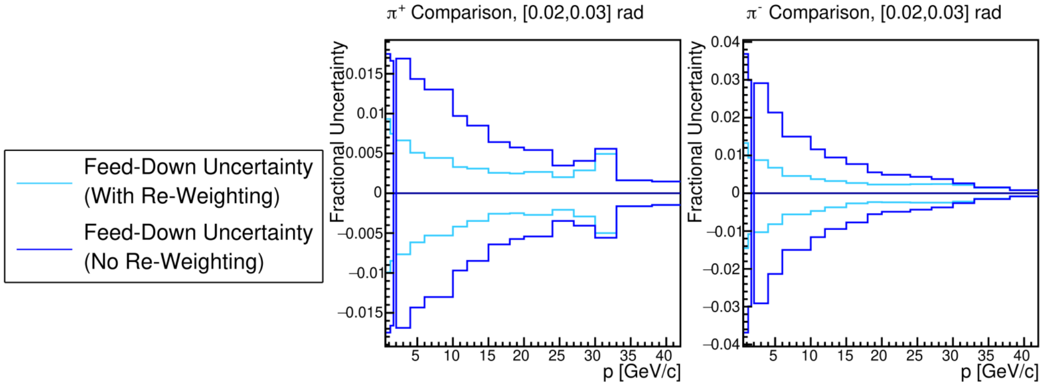

Figure 9.29: The significant reduction in the feed-down uncertainties for 120 GeV/c proton-carbon interactions by reweighting with neutral data [32].

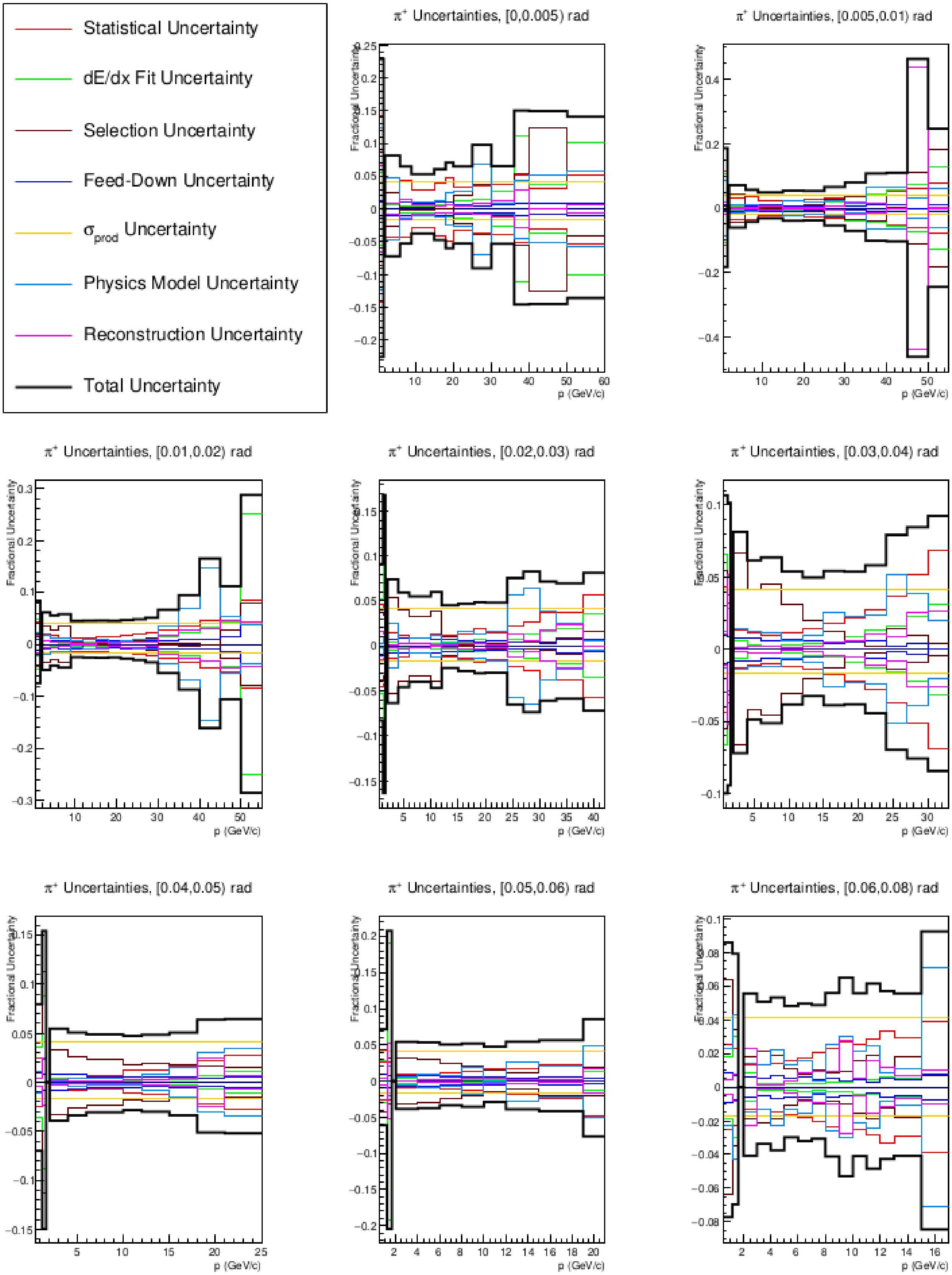

Figure 9.30: π^+ differential multiplicity uncertainties.

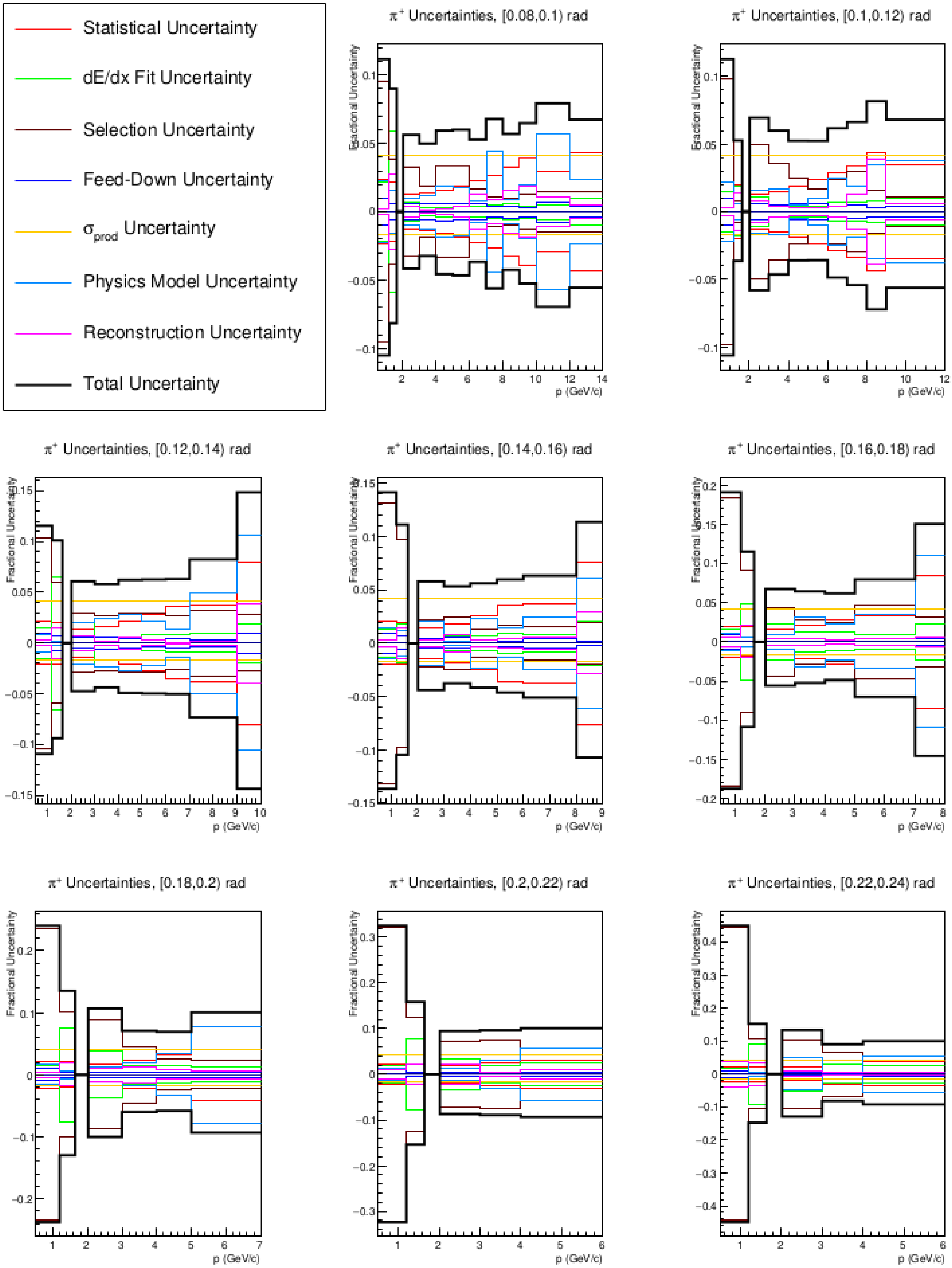

Figure 9.31: π^+ differential multiplicity uncertainties (continued).

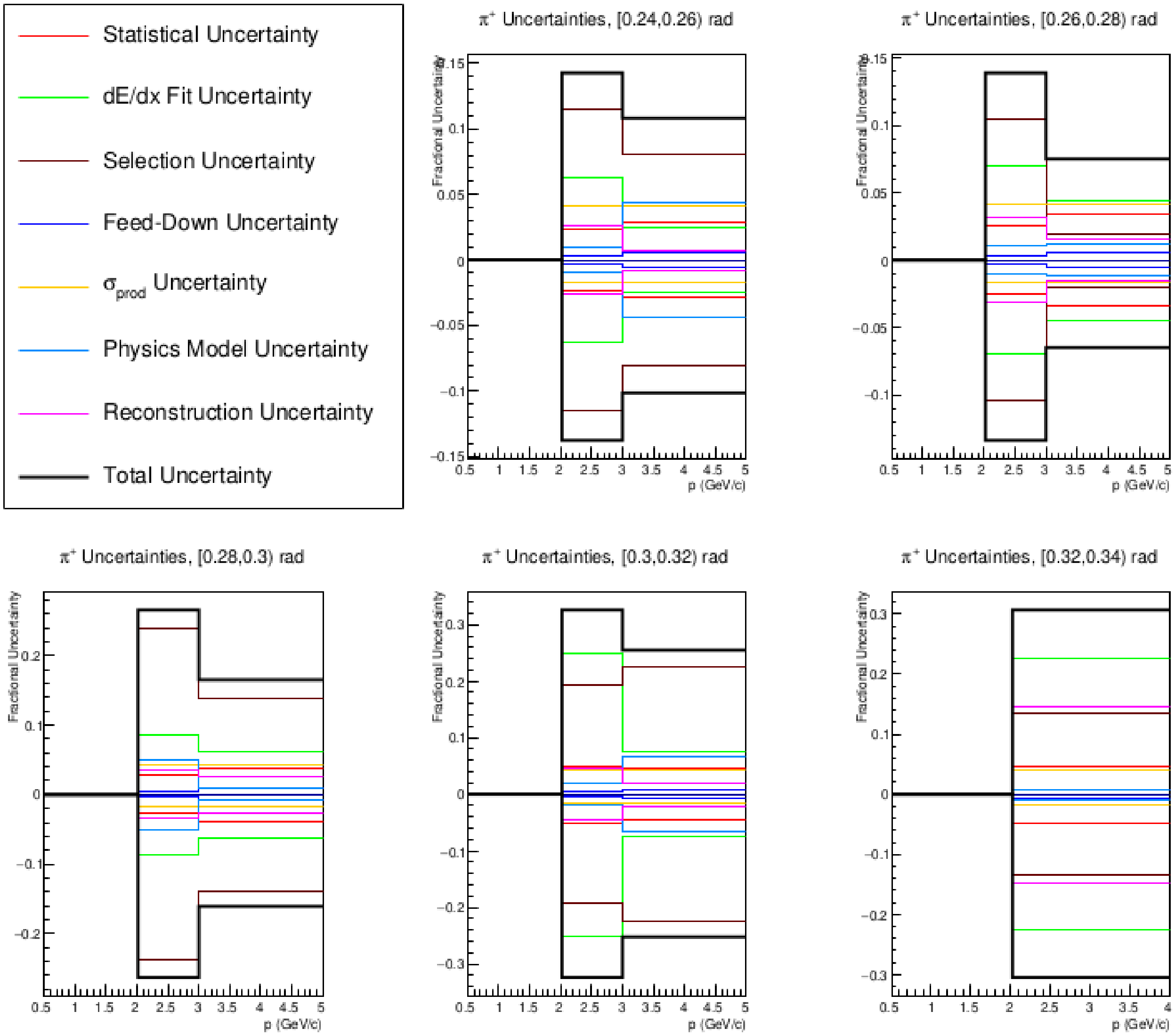

Figure 9.32: π^+ differential multiplicity uncertainties (continued).

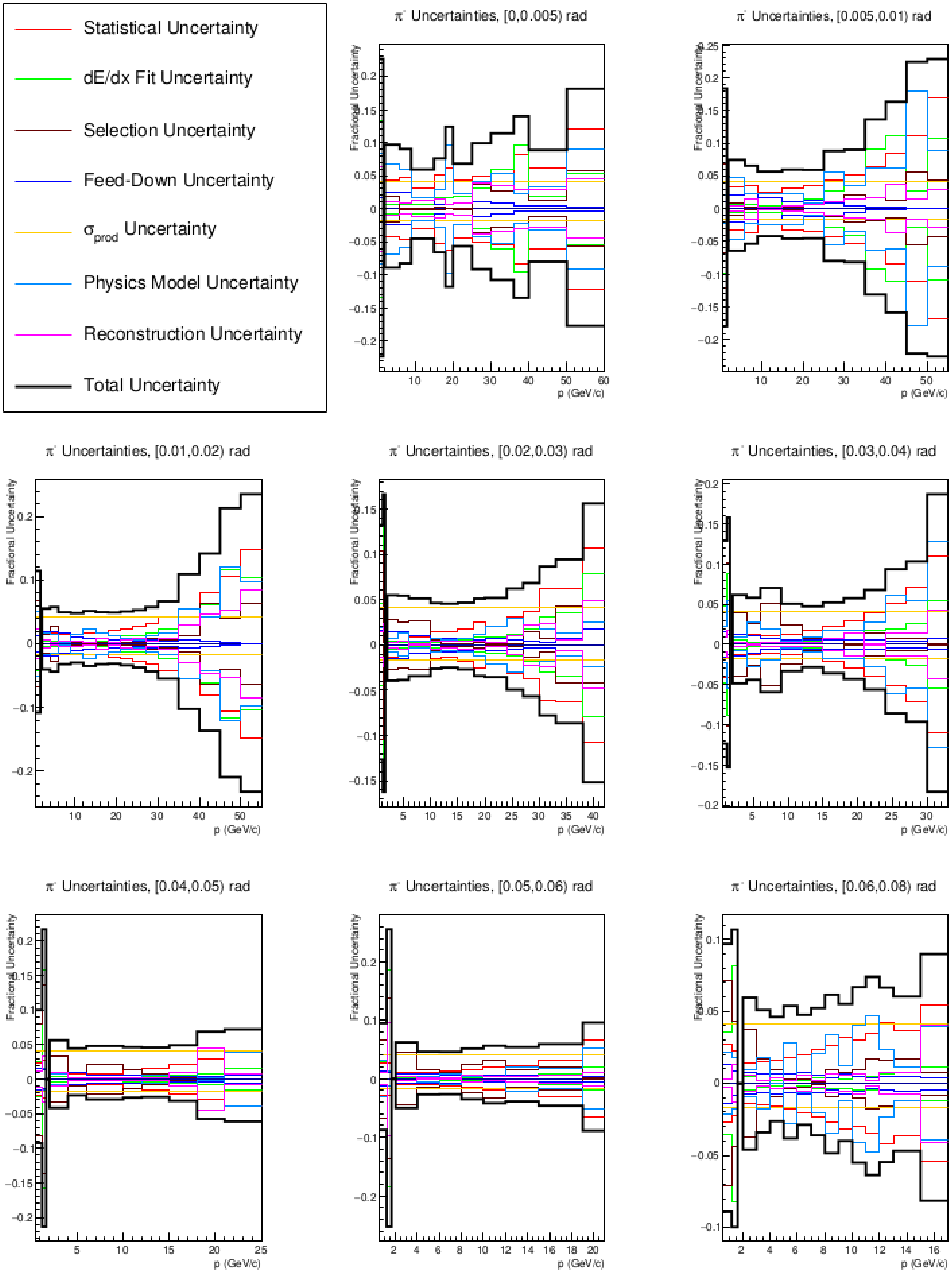

Figure 9.33: π^- differential multiplicity uncertainties.

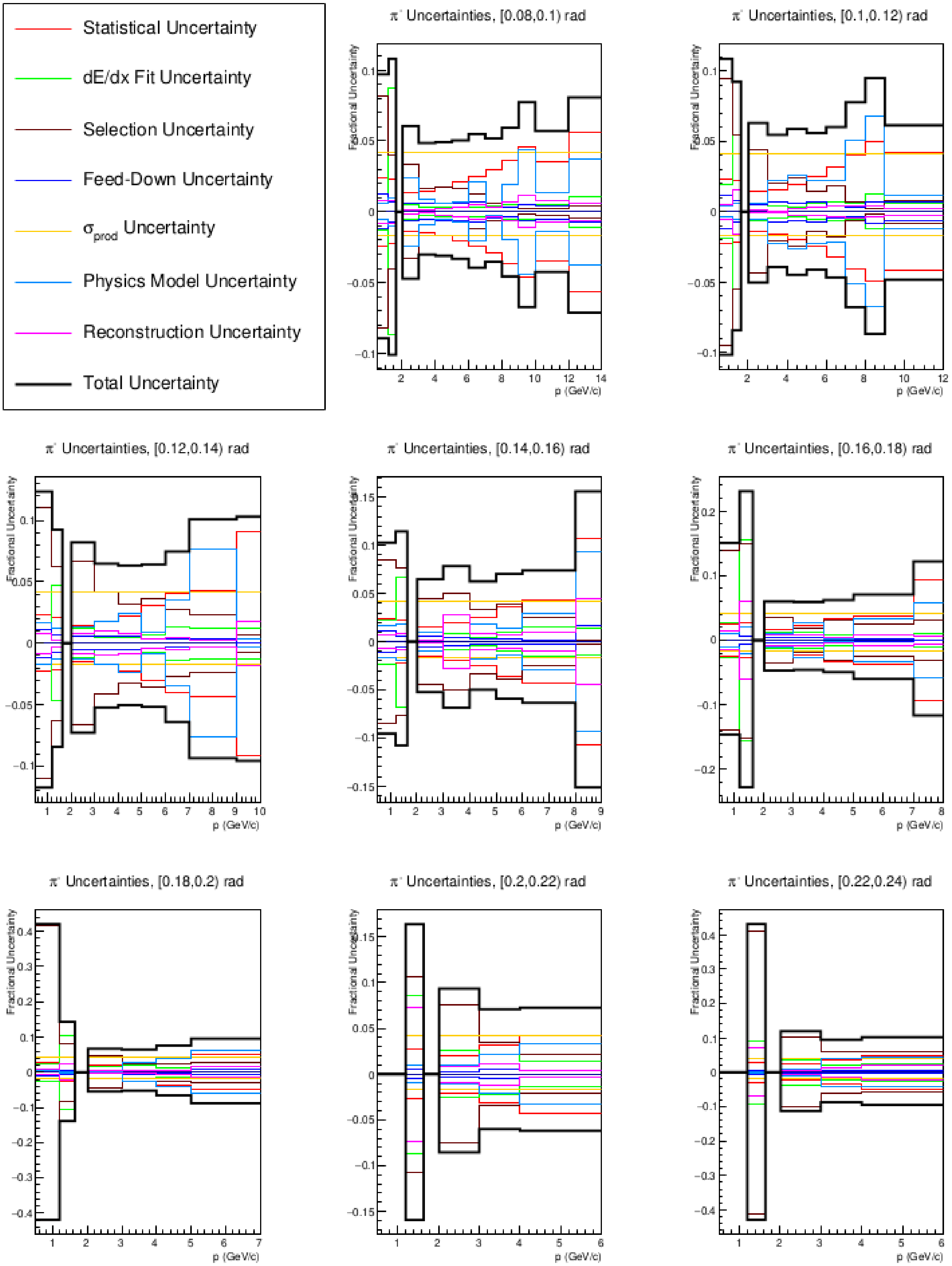

Figure 9.34: π^- differential multiplicity uncertainties (continued).

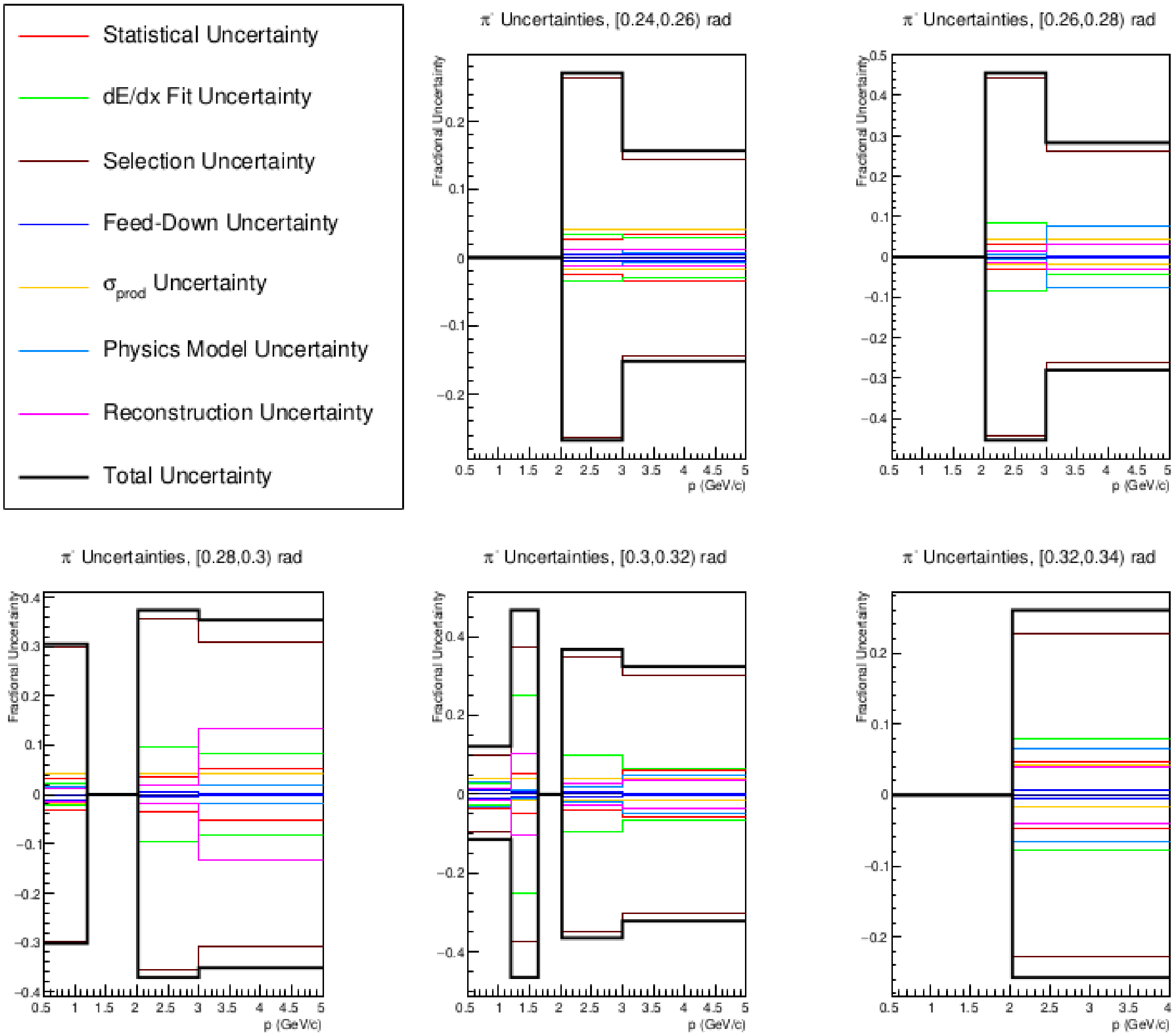

Figure 9.35: π^- differential multiplicity uncertainties (continued).

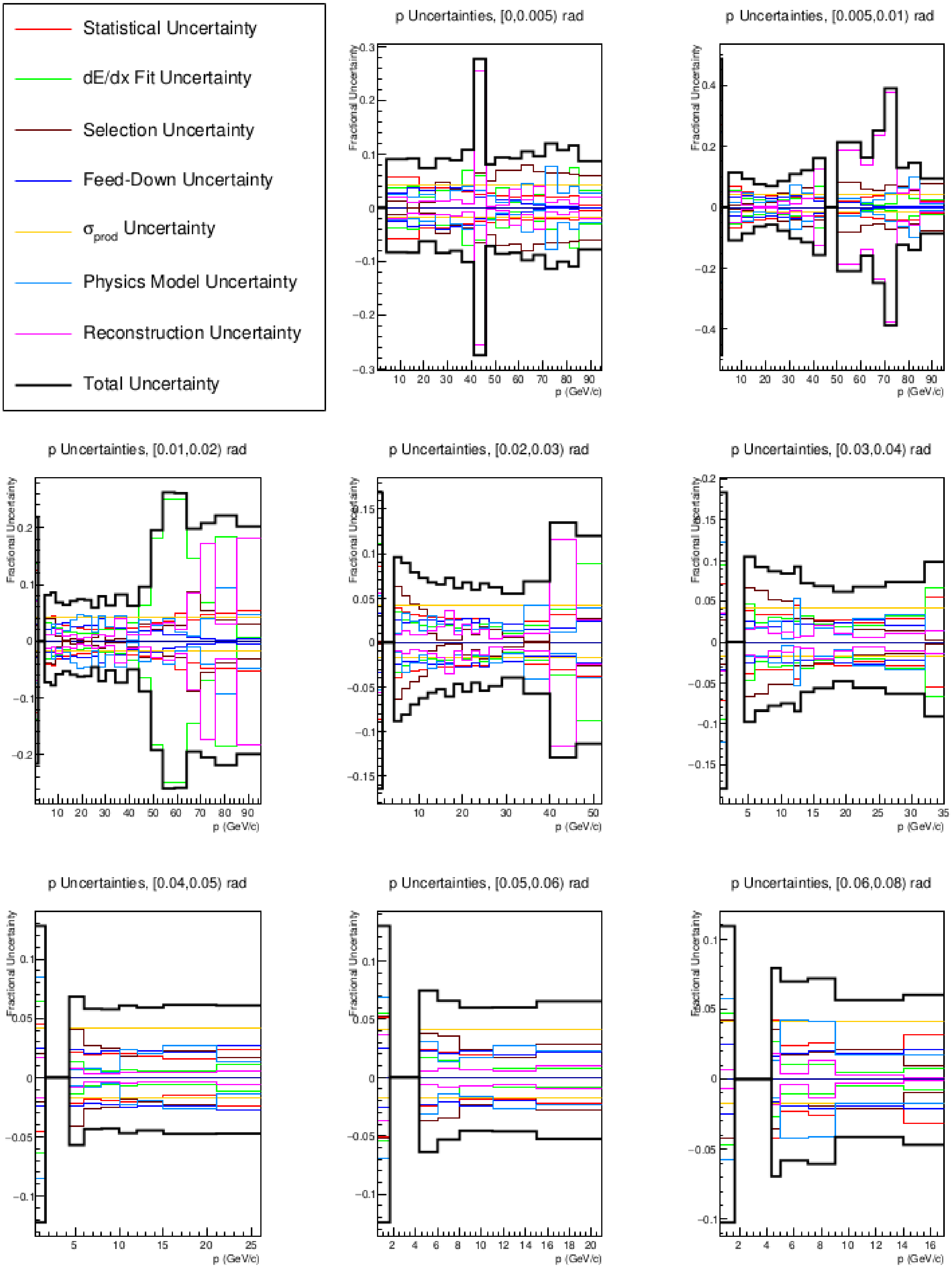

Figure 9.36: p differential multiplicity uncertainties.

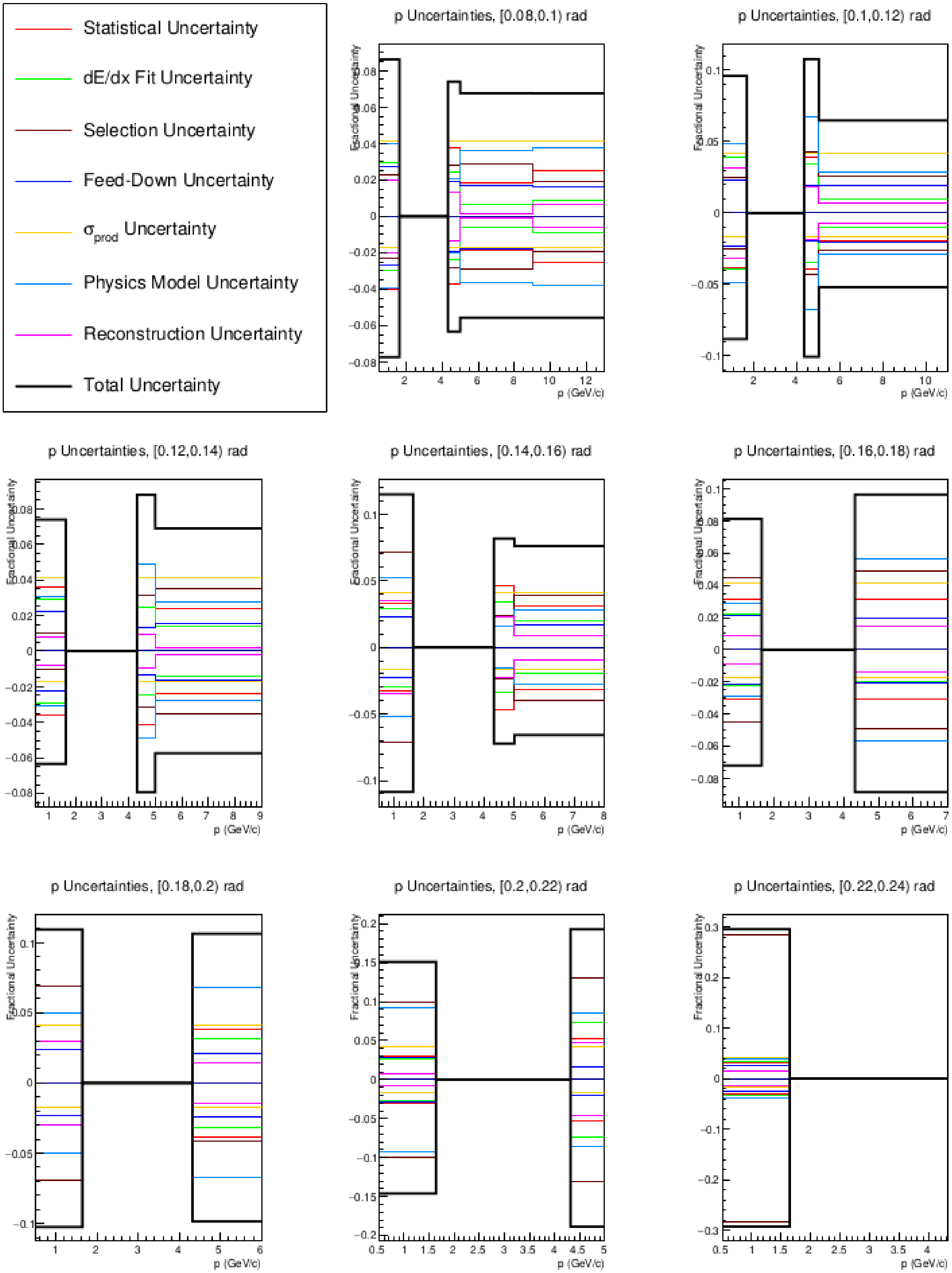

Figure 9.37: p differential multiplicity uncertainties (continued).

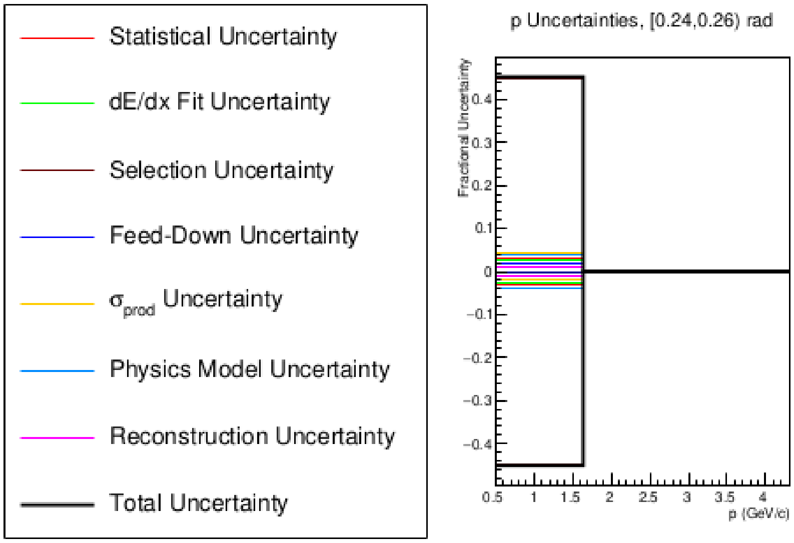

Figure 9.38: p differential multiplicity uncertainties (continued).

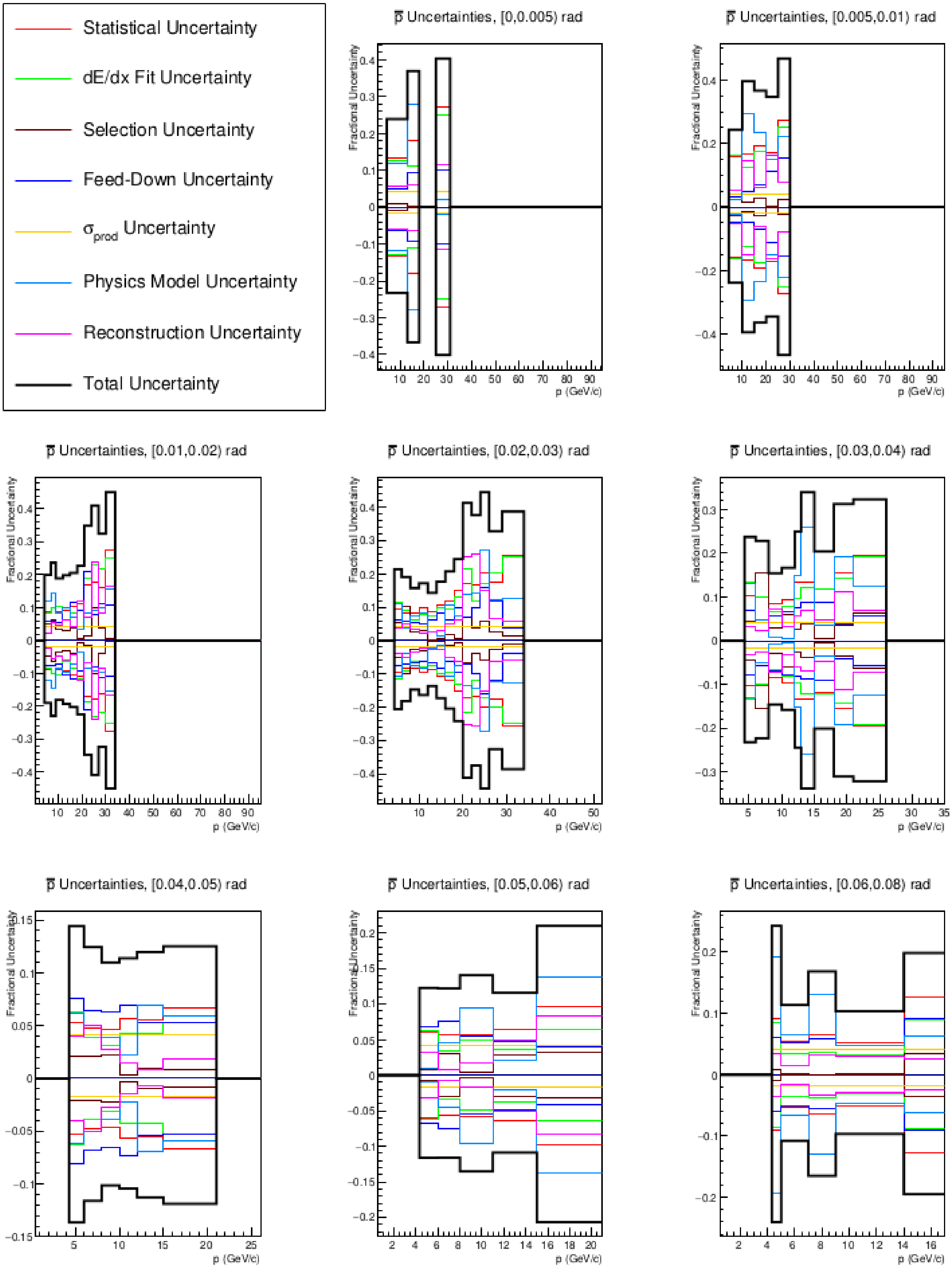

Figure 9.39: $\bar{p}$ differential multiplicity uncertainties.

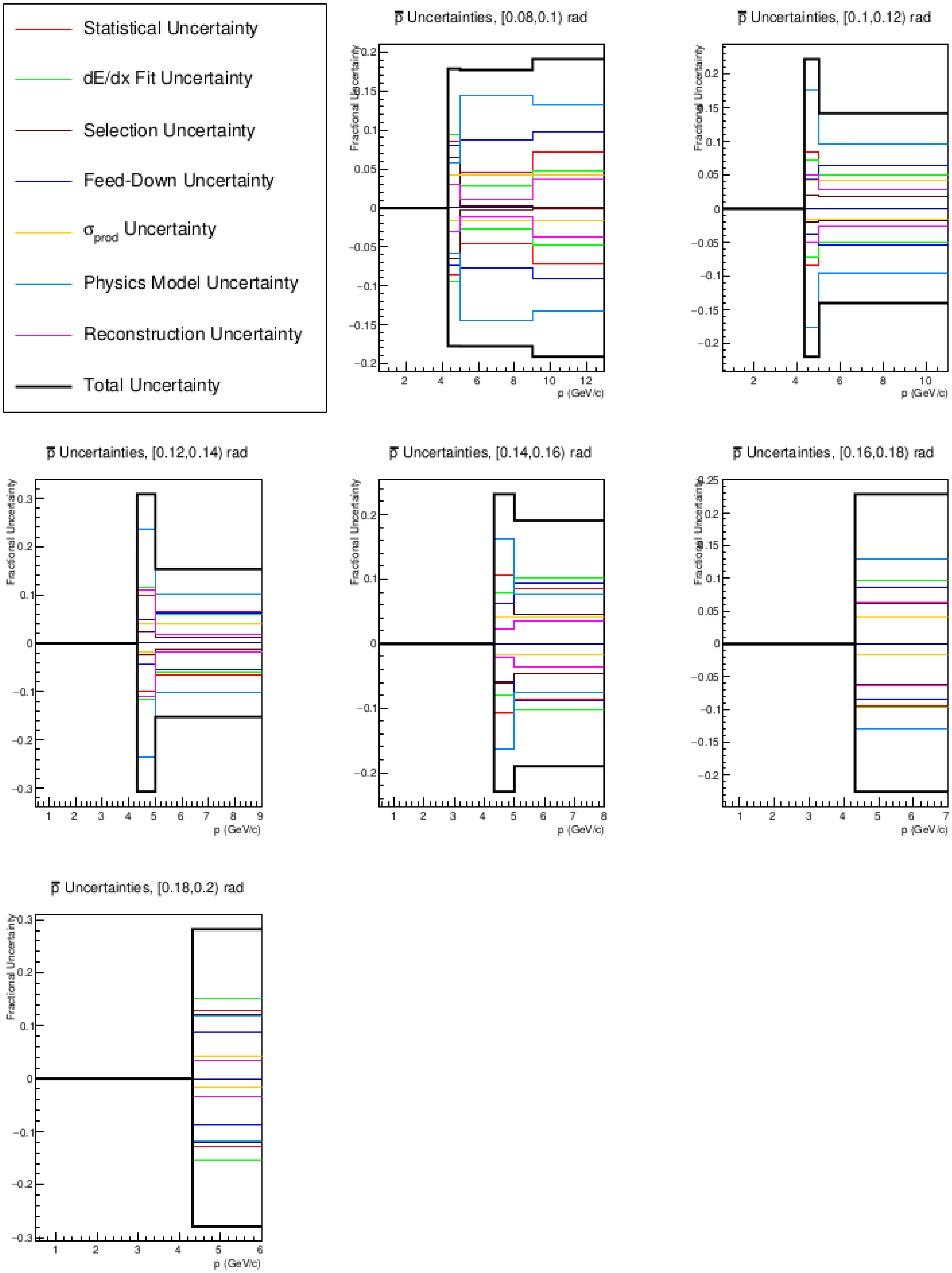

Figure 9.40: $\bar{p}$ differential multiplicity uncertainties (continued).

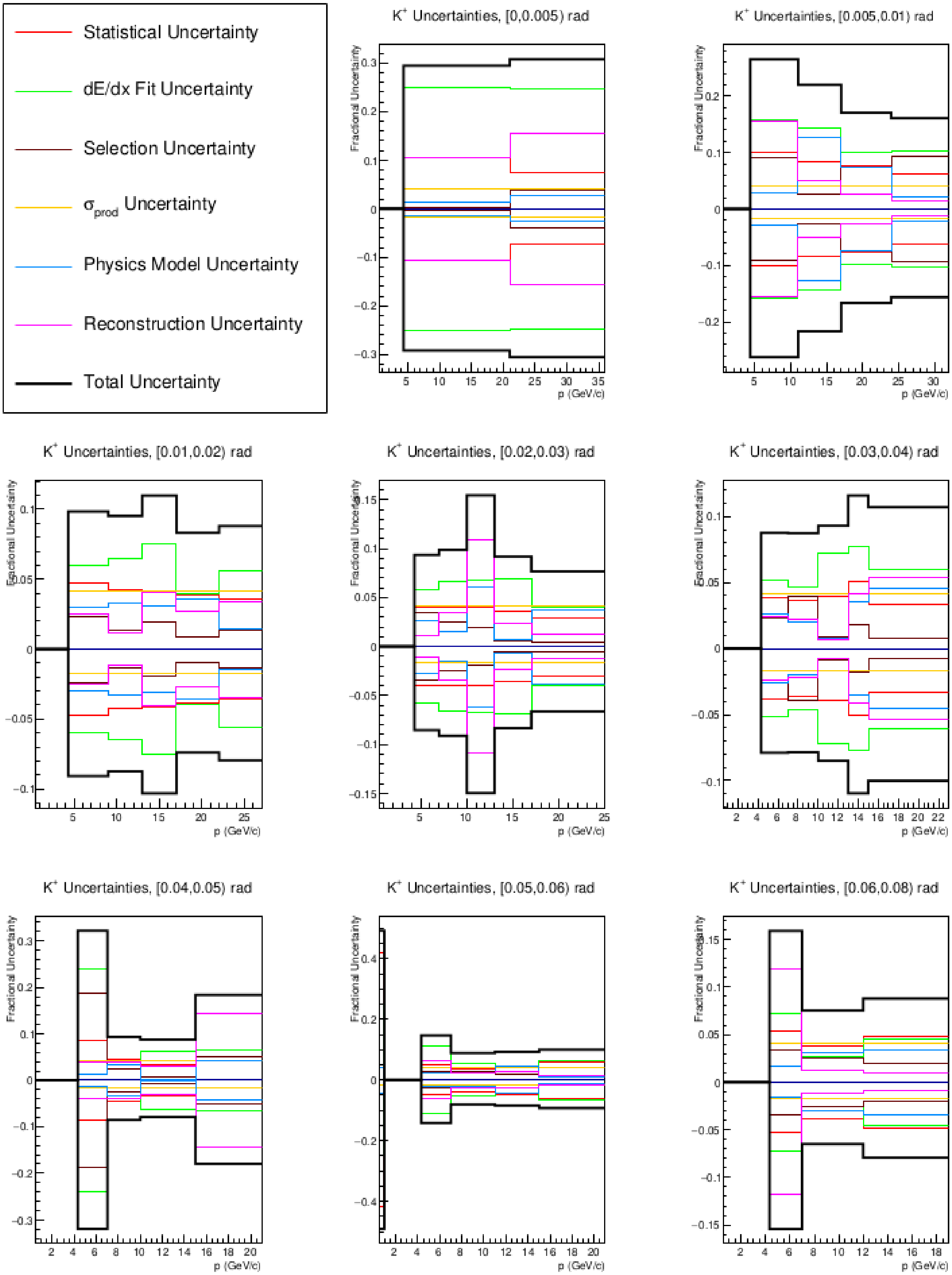

Figure 9.41: K^+ differential multiplicity uncertainties.

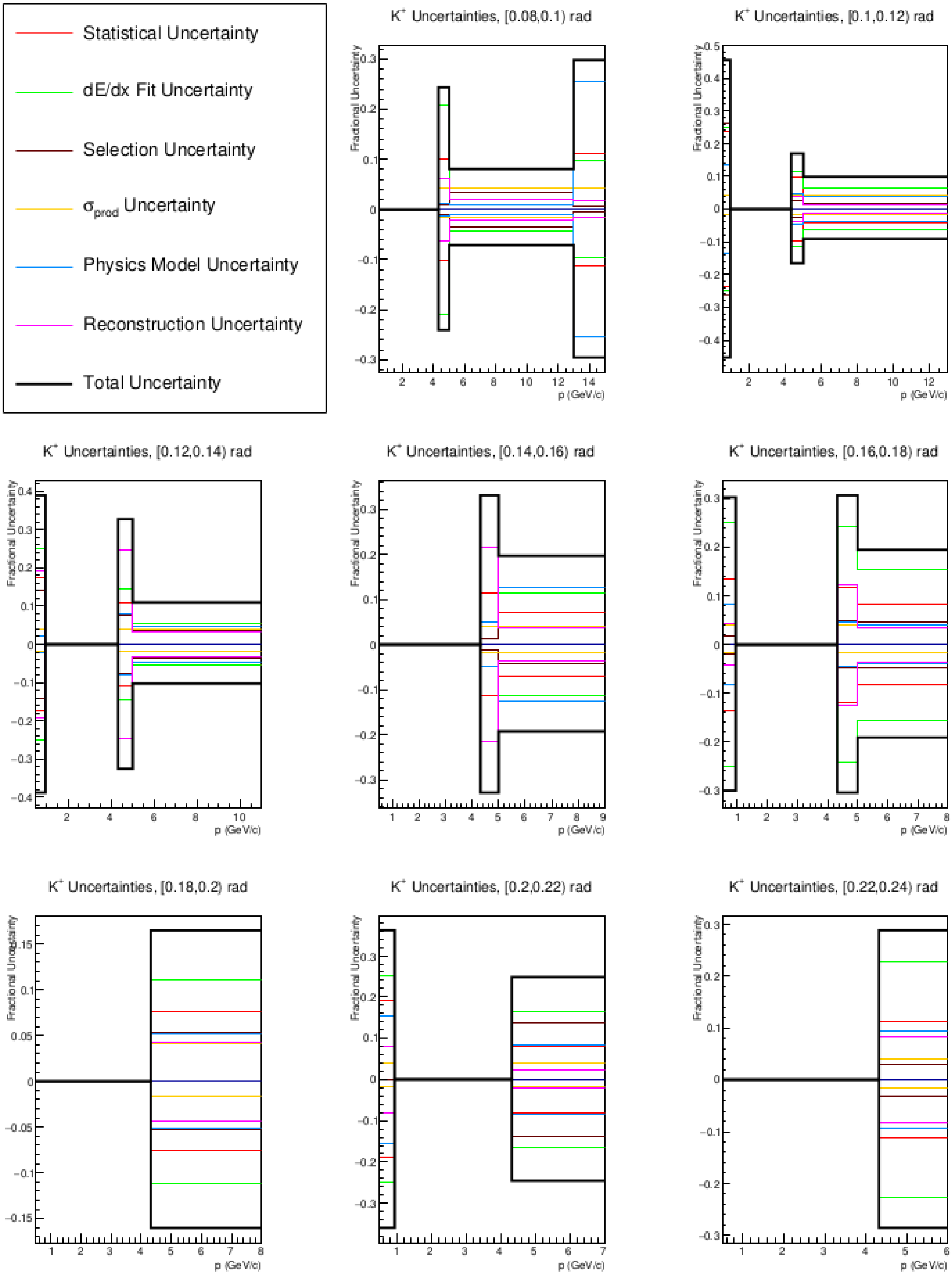

Figure 9.42: K^+ differential multiplicity uncertainties (continued).

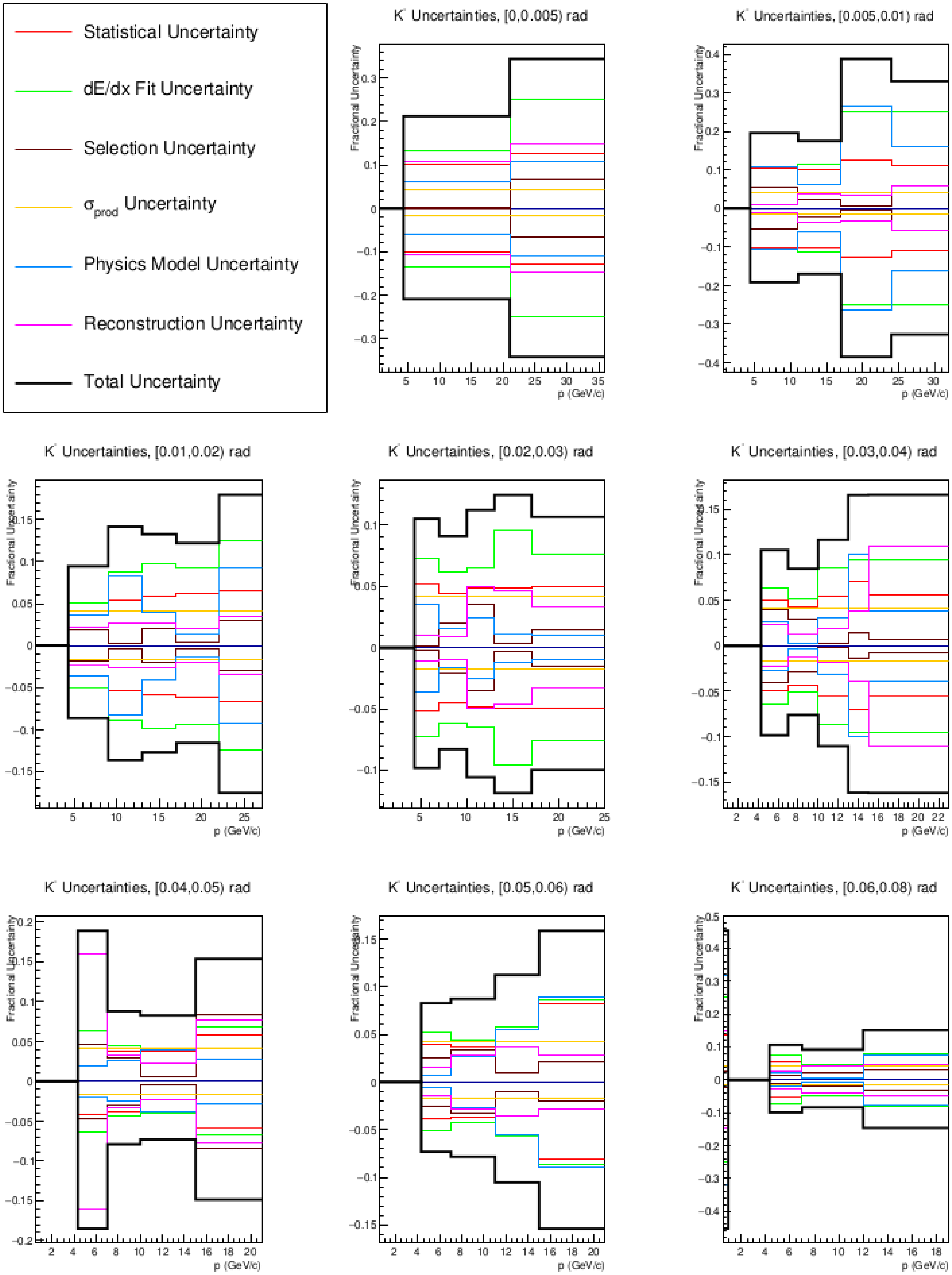

Figure 9.43: K^- differential multiplicity uncertainties.

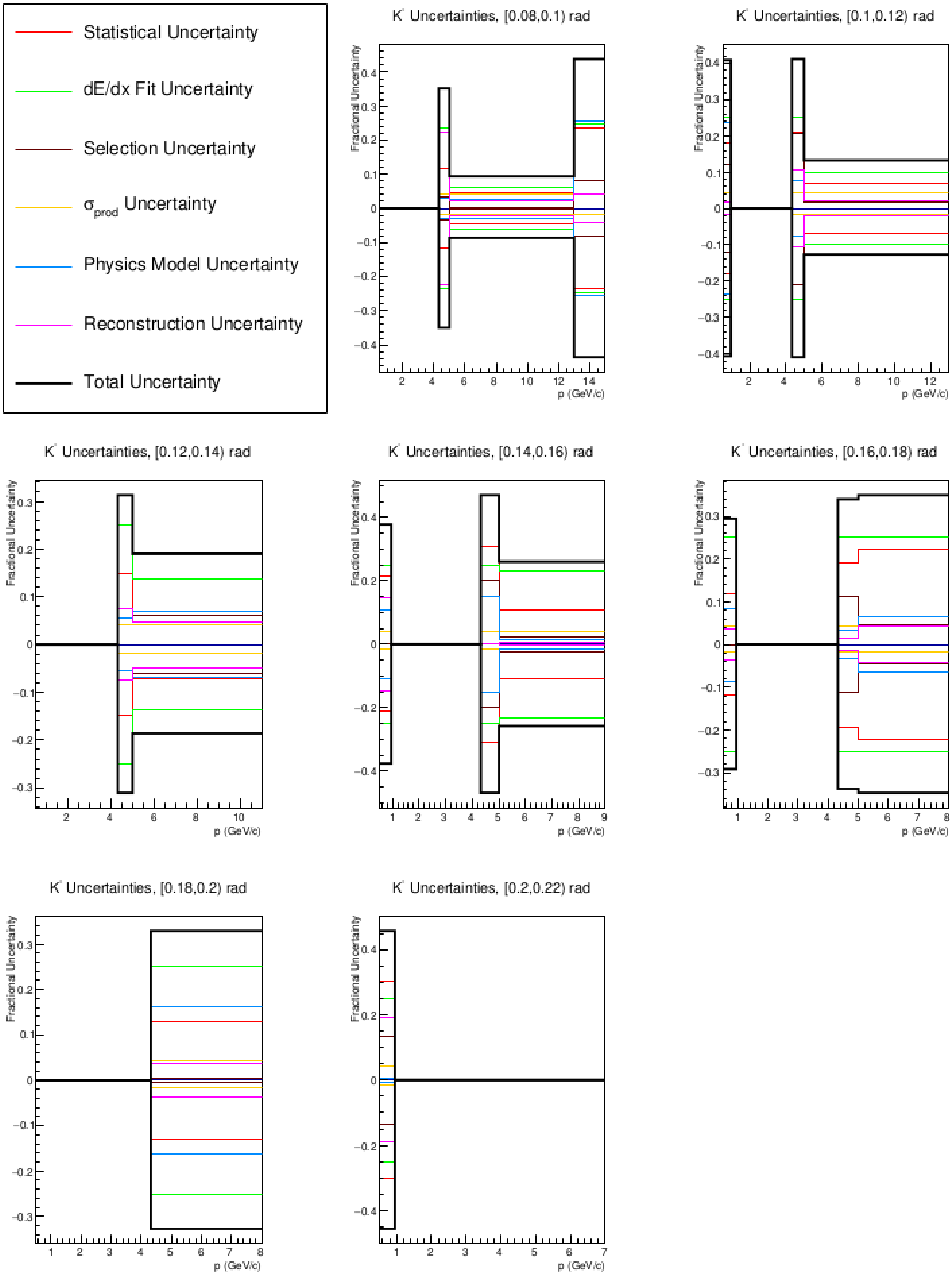

Figure 9.44: K^- differential multiplicity uncertainties (continued).

Chapter 10

Conclusion

10.1 Momentum Scaling

Existing hadron production data only covers a small range of the phase space of the hadronic interactions occurring in the production of neutrino beams for long-baseline neutrino oscillation experiments. As a result of this, these experiments rely on a combination of MC modeling and momentum scaling of existing data to describe regions not covered by existing hadron production data.

From the approximate momentum scaling behavior of invariant cross sections, there are a number of variables that appear to give reasonable predictions for scaling hadron production between different momenta [3]. This thesis will briefly compare hadron production for proton-carbon interactions at 90 GeV/c and 120 GeV/c in two parameterizations. The data at 120 GeV/c comes from the analysis performed by B. Rumberger [32].

The first parameterization is in p_T, the transverse momentum of the produced hadron, and the Feynman-x variable

$$x_F \equiv \frac{p^*_{\parallel}}{P^*_{\parallel}(max)} \approx \frac{2p^*_{\parallel}}{\sqrt{s}}. \tag{10.1}$$

All quantities are in the center of momentum (CM) frame. $p^*_{\parallel}$ is the longitudinal momentum of the produced particle, $P^*_{\parallel}$ is the max allowed longitudinal momentum of the produced particle, and s is the total energy. Following the procedure set by Aliaga and used for the NOνA experiment, the CM frame is calculated assuming a proton-proton collision [47]. This variable, x_F, was initially proposed as a method of describing particle production in a (beam) momentum invariant way.

The other parameterization is in p_T and x_R, defined as

$$x_R \equiv \frac{E^*}{E^*(max)}. \tag{10.2}$$

Here E^* is the energy of the produced particle in the CM frame, and $E^*(max)$ is the max energy available to the particle in the CM frame. Again the CM frame is calculated assuming a proton-proton interaction. This variable comes from the work performed by Bonesini *et al.*, and they found x_R to generally provide better momentum scaling than x_F [3].

Figure 10.1 shows two sample regions of the p_T, x_F scaling, and Figure 10.2 shows two samples regions of the p_T, x_R scaling for π^+. These figures help highlight the importance of covering a broad region of phase space with hadron production measurements, as neither modeling nor momentum scaling are truly accurate in describing hadron production, though x_R does appear to provide a better description than x_F. A comparison with negatively charged pions was also performed, and the results were found to be qualitatively similar.

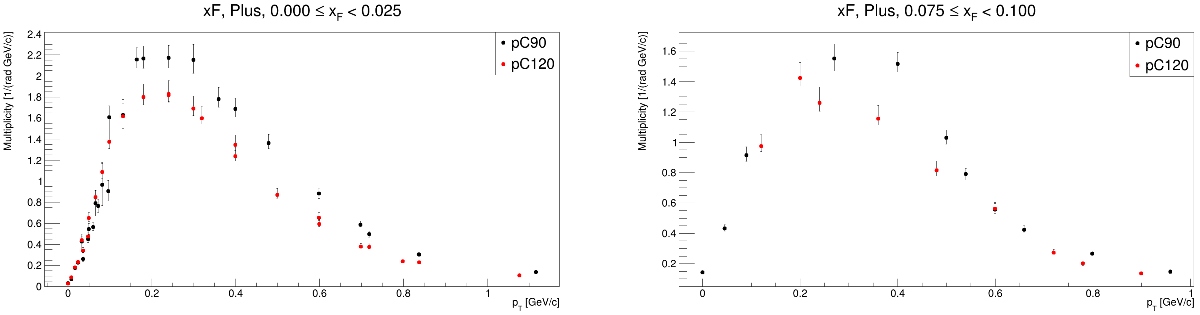

(a)

(b)

Figure 10.1: Comparison of π^+ differential multiplicities for 90 GeV/c and 120 GeV/c proton-carbon interactions parameterized in p_T and x_F. Left: $0.000 \leq x_F < 0.025$. Right: $0.075 \leq x_F < 0.100$.

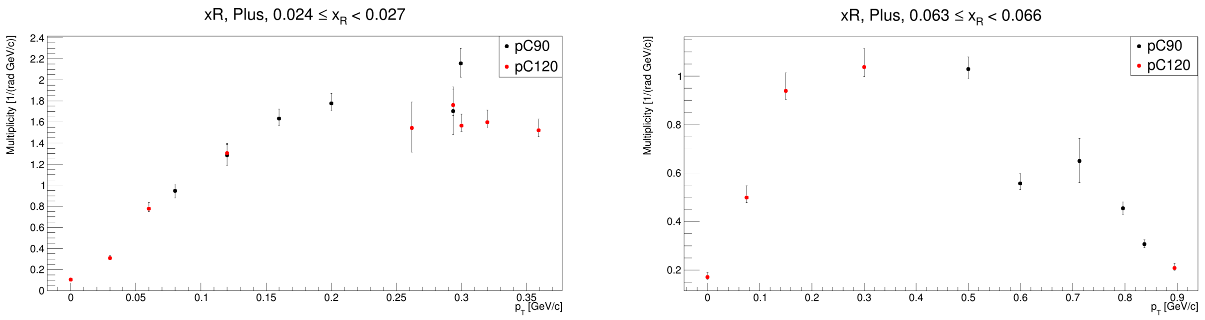

(a) (b)

Figure 10.2: Comparison of π^+ differential multiplicities for 90 GeV/c and 120 GeV/c proton-carbon interactions parameterized in p_T and x_R. Left: $0.024 \leq x_R < 0.027$. Right: $0.063 \leq x_R < 0.066$.

10.2 Discussion of Results

This thesis measured the differential multiplicity of charged ($\pi^\pm, K^\pm, p/\bar{p}$) and neutral hadrons ($K^0_S, \Lambda, \bar{\Lambda}$) produced in proton-carbon interactions with a 90 GeV/c proton beam, where energy loss was used for particle identification.

As shown in Chapters 8 and 9, in many regions of phase space, MC predictions are often inaccurate in predicting particle multiplicities in proton-carbon interactions, and this statement is not only applicable to 90 GeV/c proton-carbon interactions. Figure 10.3 shows the MC predicted and experimentally measured multiplicity of π^+ in 120 GeV/c proton-carbon interactions for two sample angle bins, and Figure 10.4 shows the measured p multiplicity; Figure 10.5 shows the multiplicity results of π^+ in 31 GeV/c proton-carbon interactions. Previously, Figure 3.8 showed the discrepancy between T2K's predicted multiplicities and NA61/SHINE's experimental data.

In a similar manner to the comparisons between data and MC shown in Chapters 8 and 9 for 90 GeV/c proton-carbon interactions, Figures 10.3, 10.4, 10.5, and 3.8 highlight the importance of experimental measurements; in some regions of phase space the MC predictions agree well with experiment, but in many regions there is a large discrepancy between the two. Notably, QGSP_BERT does not agree well with the NA61/SHINE data shown in these plots, and fails to agree with the low angle pion data shown in Figure 9.14. Making any definitive, quantitative statements about

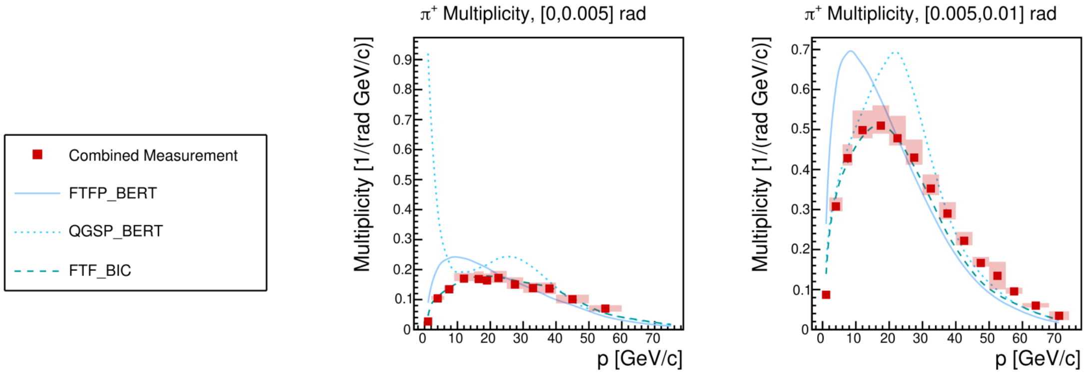

Figure 10.3: Sample differential multiplicity results of π^+ in 120 GeV/c proton-carbon interactions [32]. This plot combines two seperate datasets into one multiplicity measurement.

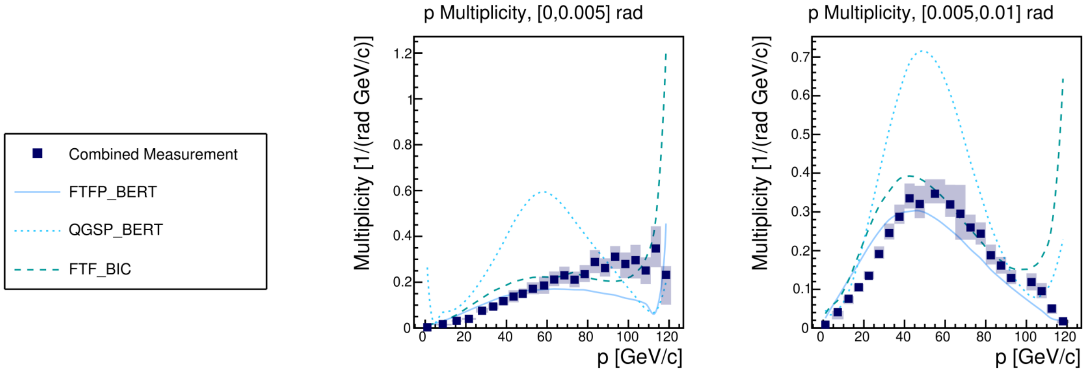

Figure 10.4: Sample differential multiplicity results of p^+ in 120 GeV/c proton-carbon interactions [32]. This plot combines two seperate datasets into one multiplicity measurement.

the agreement between MC models and experimental data is difficult; suffice it to say that no one model accurately matches NA61/SHINE's experimental data in all regions of phase space, and all models significantly incorrectly predict hadron production in certain regions of phase space.

The results of this thesis will be used to help accurately model neutrino flux for long-baseline neutrino oscillation experiments, which in turn will decrease the uncertainties on the quantities measured by the current and next generation of these neutrino oscillation experiments. The measured particle multiplicities are compared via momentum scaling to a 120 GeV/c proton-carbon dataset and to four GEANT4 physics models: FTFP_BERT, QBBC, QGSP_BERT, and FTF_BIC. Providing experimental data is vital to long-baseline neutrino oscillation experiments, as the model

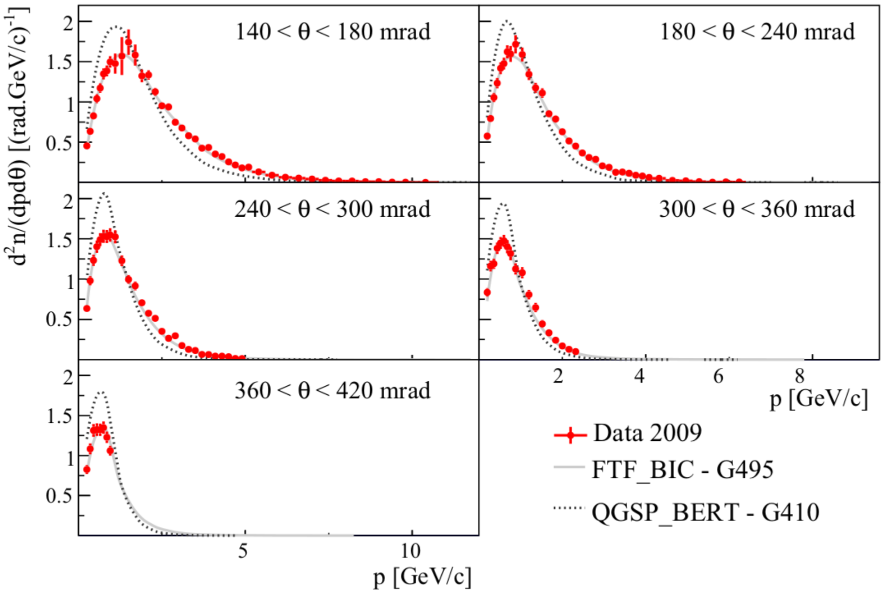

Figure 10.5: Sample differential multiplicity results of π^+ in 31 GeV/c proton-carbon interactions [49].

and momentum scaling predictions can be significantly different from the data. Future improvements could include providing time-of-flight information to fill in the Bethe-Bloch overlap regions, as well as a reduction of uncertainties on the measured multiplicities, such as the uncertainty on the production cross section.

References

[1] L. Aliaga, *et al.*, [MINERνA Collaboration], *Neutrino flux predictions for the NuMI beam*, Physical Review D **94**, 092005 (2016).

[2] K. Abe, *et al.*, [T2K Collaboration], *T2K neutrino flux prediction*, Physical Review D **87**, 012001 (2013).

[3] M. Bonesini, A. Marchionni, F. Pietropaolo, and T. Tabarelli de Fatis, *On particle production for high energy neutrino beams*, The European Physical Journal C-Particles and Fields **20**, 13 (2001).

[4] P. M. Watkins, *Discovery of the W and Z bosons*, Contemporary Physics **27**, 291 (1986).

[5] B. Gomez, *et al.*, *Observation of the top quark*, Physical Review Letters **74**, 2632 (1995).

[6] S. Chatrchyan, *et al.*, *Observation of a new boson at a mass of 125 GeV with the CMS experiment at the LHC*, Physics Letters B **716**, 30 (2012).

[7] D. Griffiths, Introduction to Elementary Particles (John Wiley & Sons, 2020).

[8] M. D. Schwartz, Quantum Field Theory and the Standard Model (Cambridge University Press, 2014).

[9] Wikipedia Contributors, *Standard model — Wikipedia, the free encyclopedia*, (2024) https://en.wikipedia.org/wiki/Mathematical_formulation_of_the_Standard_Model.

[10] A. Piepke, *et al.*, [PDG Collaboration], *Review of particle physics*: Particle Data Group*, (2008).

[11] T. Aaltonen, *et. al*, [CDF Collaboration], *Search for s-channel single top quark production in the missing energy plus jets sample using the full CDF ii data set*, arXiv preprint arXiv:1402.3756 (2014).

[12] Y. Fukuda, T. Hayakawa, E. Ichihara, K. Inoue, K. Ishihara, H. Ishino, Y. Itow, T. Kajita, J. Kameda, S. Kasuga, et al., *Evidence for oscillation of atmospheric neutrinos*, Physical review letters **81**, 1562 (1998).

[13] R. Wendell *et al.*, [Super-Kamiokande Collaboration], *Atmospheric results from Super-Kamiokande*, in AIP Conference Proceedings, Vol. 1666, 1 (AIP Publishing, 2015).

[14] K. Abe *et al.*, [T2K Collaboration], *Measurement of neutrino oscillation parameters from muon neutrino disappearance with an off-axis beam*, Physical Review Letters **111**, 211803 (2013).

[15] D. Adey *et al.* [Daya Bay Collaboration], *Measurement of the electron antineutrino oscillation with 1958 days of operation at Daya Bay*, Physical Review Letters **121**, 241805 (2018).

[16] K. Ackermann, *et. al*, [GERDA Collaboration], *The GERDA experiment for the search of 0 $\nu\beta\beta$ decay in 76 Ge*, The European Physical Journal C **73**, 1 (2013).

[17] [DUNE Collaboration], (2024) `https://lbnf-dune.fnal.gov/`.

[18] A. D. Sakharov, *Violation of cp-invariance, c-asymmetry, and baryon asymmetry of the universe*, in *Collected works on research into the essentials of theoretical physics in Russian Federal Nuclear Center* (World Scientific, 1998), pp. 84–87.

[19] I. Esteban *et al.*, *The fate of hints: updated global analysis of three-flavor neutrino oscillations*, Journal of High Energy Physics **2020**, 1 (2020).

[20] *Nufit webpage*, (2022) `www.nu-fit.org`.

[21] K. Abe, *et al.*, [T2K Collaboration], *The T2K experiment*, Nuclear Instruments and Methods in Physics Research Section A: Accelerators, Spectrometers, Detectors and Associated Equipment **659**, 106 (2011).

[22] D.S. Ayres, *et al.*, [NOvA Collaboration], *The NOvA Technical Design Report*, tech. rep. (Fermi National Accelerator Lab.(FNAL), Batavia, IL (United States), 2007).

[23] K. Abe, *et al.*, [HK Collaboration], *Hyper-Kamiokande Design Report*, arXiv preprint arXiv:1805.04163 (2018).

[24] R. Acciarri, *et al.*, [DUNE Collaboration], *Long-baseline neutrino facility (LBNF) and deep underground neutrino experiment (DUNE) conceptual design report, volume 4 the DUNE detectors at LBNF*, arXiv preprint arXiv:1601.02984 (2016).

[25] P. Adamson, *et al.*, *The NuMI Neutrino beam*, Nuclear Instruments and Methods in Physics Research Section A: Accelerators, Spectrometers, Detectors and Associated Equipment **806**, 279 (2016).

[26] K. Wood, *Measurement of neutrino oscillation parameters with T2K data corresponding to 3.6× 1021 protons on target using a Bayesian framework*, PhD thesis (State University of New York at Stony Brook, 2021).

[27] A. Abud, *et al.*, [DUNE Collaboration], *Deep underground neutrino experiment (DUNE) near detector conceptual design report*, Instruments **5**, 31 (2021).

[28] R. Acciarri, *et al.*, [DUNE Collaboration], *Long-baseline neutrino facility (LBNF) and deep underground neutrino experiment (DUNE) conceptual design report, volume 4 the DUNE detectors at LBNF*, arXiv preprint arXiv:1601.02984 (2016).

[29] S. Dolan, *Simulating neutrino interactions and their impact on oscillation experiments*, INSS, 2023.

[30] T.T. Böhlen, *et al.*, *The FLUKA code: developments and challenges for high energy and medical applications*, Nuclear data sheets **120**, 211 (2014).

[31] S. Agostinelli, *et al.*, [GEANT4 Collaboration], *GEANT4—a simulation toolkit*, Nuclear Instruments and Methods in Physics Research Section A **506**, 250 (2003).

[32] H. Adhikary, et al. [NA61/SHINE Collaboration], *Measurements of* π^+, π^-, p, $\bar{p}$, K^+ *and* K^- *production in 120 GeV/c* $p+$ *C interactions*, Physical Review D **108**, 072013 (2023).

[33] P. Lebrun, *et al.*, *On LBNE neutrino flux systematic uncertainties*, in Aip conference proceedings, Vol. 1680, 1 (AIP Publishing, 2015).

[34] B. Abi, *et al.*, [DUNE COllaboration], *Long-baseline neutrino oscillation physics potential of the dune experiment*, The European Physical Journal C **80**, 1 (2020).

[35] K. Abe, *et al.*, [T2K Collaboration], *Measurement of neutrino and antineutrino oscillations by the T2K experiment including a new additional sample of ν_e interactions at the far detector*, Physical Review D **96**, 092006 (2017).

[36] R. Acciarri, *et al.* [DUNE Collaboration], *Long-baseline neutrino facility (LBNF) and deep underground neutrino experiment (DUNE) conceptual design report volume 2: the physics program for DUNE at LBNF*, (2015).

[37] M. Catanesi, *et al.*, [HARP Collaboration], *Measurement of the production cross-section of positive pions in the collision of 8.9 GeV/c protons on beryllium*, The European Physical Journal C **52**, 29 (2007).

[38] I. Chemakin, *et al.*, *Pion production by protons on a thin beryllium target at 6.4, 12.3, and 17.5 GeV/c incident proton momenta*, Physical Review C **77**, 015209 (2008).

[39] M. Catanesi, *et al.*, [HARP Collaboration], *Measurement of the production cross-sections of* $\pi\pm$*in p–c and* $\pi\pm$*–c interactions at 12 gev/c*, Astroparticle Physics **29**, 257 (2008).

[40] M. Catanesi, *et al.*, [HARP Collaboration], *Measurement of the production cross-section of positive pions in p-al collisions at 12.9 GeV/c*, Nuclear Physics B **732**, 1 (2006).

[41] J. Allaby, *et al.*, *High-energy particle spectra from proton interactions at 19.2 GeV/c*, tech. rep. (CERN, 1970).

[42] T. Eichten, *et al.*, *Particle production in proton interactions in nuclei at 24 GeV/c*, Nuclear Physics B **44**, 333 (1972).

[43] C. Alt, *et al.*, [NA49 Collaboration], *Inclusive production of charged pions in p+c collisions at 158 GeV/c beam momentum*, The European Physical Journal C **49**, 897 (2007).

[44] R.T. Edwards, *et al.*, *Forward inclusive production spectrum of* K^0_S, Λ, $\bar{\Lambda}$, *and n in the collision of 200 GeV/c* π^-, K^-, $\bar{p}$, *and p on be*, Physical Review D **18**, 76 (1978).

[45] P. Skubic, *et al.*, *Neutral-strange-particle production by 300 GeV protons*, Physical Review D **18**, 3115 (1978).

[46] G. Ambrosini, *et al.*, [NA56/SPY Collaboration], *Measurement of charged particle production from 450 GeV/c protons on beryllium*, The European Physical Journal C-Particles and Fields **10**, 605 (1999).

[47] L. Aliaga Soplin, *Neutrino flux prediction for the NuMI beamline*, (2016).

[48] B. T. Rumberger, *Hadron production in 120 GeV/c proton-carbon interactions*, PhD thesis (University of Colorado at Boulder, 2021).

[49] N. Abgrall, *et al.*, [NA61/SHINE Collaboration], *Measurements of pi*$^\pm$, $K^\pm$, K^0_S, Λ *and proton production in proton-carbon interactions at 31 GeV/c with the NA61/SHINE spectrometer at the CERN SPS*, arXiv preprint arXiv:1510.02703 (2015).

[50] N. Abgrall, *et al.*, [NA61/SHINE Collaboration], *Measurements of* $\pi^\pm$, $K^\pm$, *and proton double differential yields from the surface of the T2K replica target for incoming 31 GeV/c protons with the NA61/SHINE spectrometer at the CERN SPS*, The European Physical Journal C **79**, 1 (2019).

[51] A. Aduszkiewicz, *et. at*, [NA61/SHINE Collaboration], *Measurements of production and inelastic cross sections for p+ C, p+ Be, and p+ Al at 60 GeV/c and p+ C and p+ Be at 120 GeV/c*, Physical Review D **100**, 112001 (2019).

[52] A. Aduszkiewicz, *et al.*, [NA61/SHINE Collaboration], *Measurements of hadron production in* $\pi^+ +$ *C and* $\pi^+ +$ *Be interactions at 60 GeV/c*, Physical Review D **100**, 112004 (2019).

[53] H. Adhikary, *et al.*, [NA61/SHINE Collaboration], *Measurements of* K_S^0*,* Λ*, and* $\bar{\Lambda}$ *production in 120 GeV/c p+ C interactions*, Physical Review D **107**, 072004 (2023).

[54] N. Abgrall, *et. al*, [NA61/SHINE Collaboration], *NA61/SHINE facility at the CERN SPS: beams and detector system*, Journal of Instrumentation **9**, P06005 (2014).

[55] Z. Fodor and S. D. Katz, *Critical point of QCD at finite T and* μ*, lattice results for physical quark masses*, Journal of High Energy Physics **2004**, 050 (2004).

[56] E. Andronov, [NA61/SHINE Collaboration], *Search for the critical point by the NA61/SHINE experiment*, Nuclear Physics A **982**, 835 (2019).

[57] A. Aduszkiewicz, *et. al*, [NA61/SHINE Collaboration], *Measurement of meson resonance production in* $\pi^\pm + C$ *interactions at SPS energies*, The European Physical Journal C **77**, 1 (2017).

[58] M. Aguilar, *et. al*, [AMS Collaboration], *Observation of new properties of secondary cosmic rays lithium, beryllium, and boron by the alpha magnetic spectrometer on the international space station*, Physical review letters **120**, 021101 (2018).

[59] C. Hailey, *An indirect search for dark matter using antideuterons: the GAPS experiment*, New Journal of Physics **11**, 105022 (2009).

[60] C. Bovet, R. Maleyran, L. Piemontese, A. Placci, and M. Placidi, *The CEDAR counters for particle identification in the SPS secondary beams: a description and an operation manual*, tech. rep. (European Organization for Nuclear Research, 1982).

[61] H. J. Hilke, *Time projection chambers*, Reports on Progress in Physics **73**, 116201 (2010).

[62] N. Abgrall, *et. al*, [NA61/SHINE Collaboration], *Measurements of* $\pi^\pm$*,* $K^\pm$*,* K_S^0*,* Λ *and proton production in proton-carbon interactions at 31 GeV/c with the NA61/SHINE spectrometer at the CERN SPS*, arXiv preprint arXiv:1510.02703 (2015).

[63] B. Maksiak, *DRS summary*, September NA61/SHINE Collaboration Meeting, 2022.

[64] A. László, *et. al*, *Design and performance of the data acquisition system for the NA61/SHINE experiment at CERN*, Nuclear Instruments and Methods in Physics Research Section A: Accelerators, Spectrometers, Detectors and Associated Equipment **798**, 1 (2015).

[65] A. László, *Software tail cancellation filter*, May NA61/SHINE Collaboration Meeting, 2022.

[66] A. Lebedev, *et. al*, [CBM Collaboration], *Track reconstruction algorithms for the CBM experiment at FAIR*, in Journal of physics: conference series, Vol. 219, 3 (IOP Publishing, 2010), p. 032048.

[67] W. Blum, W. Riegler, and L. Rolandi, Particle detection with drift chambers (Springer Science & Business Media, 2008).

[68] J. Allison, *et al.*, *Recent developments in GEANT4*, Nuclear instruments and methods in physics research section A: Accelerators, Spectrometers, Detectors and Associated Equipment **835**, 186 (2016).

[69] [GEANT4 Collaboration], *Geant4 reference physics lists*, (2023) `https://geant4-userdoc.web.cern.ch/UsersGuides/PhysicsListGuide/html/reference_PL/index.html`.

[70] M. P. Lewicki, *Pulser calibration of time projection chambers in the NA61/SHINE experiment*, PhD thesis (Wroclaw U., 2015).

[71] M. Naskret, *Krypton calibration of time projection chambers of the NA61/SHINE experiment*, PhD thesis (Wroclaw U., 2015).

[72] D. Stricker-Shaver, S. Ritt, and B. J. Pichler, *Novel calibration method for switched capacitor arrays enables time measurements with sub-picosecond resolution*, IEEE Transactions on Nuclear Science **61**, 3607 (2014).

[73] A. Carroll *et. al*, *Absorption cross sections of* $\pi^{\pm}$, $K^{\pm}$, *p and anti p on nuclei between 60 and 280 GeV/c*, Phys. Lett., B **80**, 319 (1979).

[74] S. Denisov, *et. al*, *Absorption cross sections for pions, kaons, protons and antiprotons on complex nuclei in the 6 to 60 GeV/c momentum range*, Nuclear Physics B **61**, 62 (1973).

[75] M. Pavin, *et. al*, [EMPHATIC Collaboration], *Measurement of proton-carbon forward scattering in a proof-of-principle test of the EMPHATIC spectrometer*, Physical Review D **106**, 112008 (2022).

[76] S. Johnson, *Measurements of hadron production in pion+nucleus collisions for neutrino oscillation experiments*, PhD thesis (University of Colorado at Boulder, 2019).

[77] J. Podolanski and R. Armenteros, *Iii. analysis of V-events*, The London, Edinburgh, and Dublin Philosophical Magazine and Journal of Science **45**, 13 (1954).

[78] M. Pavin, *Measurements of hadron yields from the T2K replica target in the NA61/SHINE experiment for neutrino flux prediction in T2K*, PhD thesis (Université Pierre et Marie Curie-Paris VI, 2017).

Appendix A

Tables of Multiplicity Measurements

The differential multiplicity results for $\pi^{\pm}$, $K^{\pm}$, p, $\bar{p}$, K^0_S, Λ, and $\bar{\Lambda}$ are presented in this appendix. See Chapters 8 and 9 for a in-depth description of these results.

p [GeV/c]	θ [rad]	Multiplicity $\frac{1}{\text{GeV/c rad}}$	Total Unc. [%]
$[2, 8]$	$[0, 0.02]$	0.029	$^{+13.4}_{-19.5}$
$[8, 12]$	$[0, 0.02]$	0.038	$^{+14.3}_{-16.5}$
$[12, 16]$	$[0, 0.02]$	0.032	$^{+24.6}_{-21.9}$
$[16, 25]$	$[0, 0.02]$	0.025	$^{+19.4}_{-17.9}$
$[1.5, 5.5]$	$[0.02, 0.04]$	0.045	$^{+20.1}_{-16.4}$
$[5.5, 7.5]$	$[0.02, 0.04]$	0.090	$^{+20.0}_{-24.4}$
$[7.5, 9.5]$	$[0.02, 0.04]$	0.079	$^{+15.4}_{-18.0}$
$[9.5, 12]$	$[0.02, 0.04]$	0.071	$^{+21.7}_{-21.4}$
$[12, 16]$	$[0.02, 0.04]$	0.049	$^{+23.2}_{-24.0}$
$[16, 25]$	$[0.02, 0.04]$	0.035	$^{+24.8}_{-27.1}$
$[25, 34]$	$[0.02, 0.04]$	0.007	$^{+63.8}_{-65.3}$
$[1.5, 4.5]$	$[0.04, 0.06]$	0.066	$^{+18.6}_{-19.0}$
$[4.5, 6.5]$	$[0.04, 0.06]$	0.096	$^{+17.5}_{-17.5}$
$[6.5, 8.5]$	$[0.04, 0.06]$	0.084	$^{+26.1}_{-22.0}$
$[8.5, 11]$	$[0.04, 0.06]$	0.058	$^{+18.5}_{-22.4}$
$[11, 20]$	$[0.04, 0.06]$	0.033	$^{+17.6}_{-19.1}$

p [GeV/c]	θ [rad]	Multiplicity $\frac{1}{\text{GeV/c rad}}$	Total Unc. [%]
$[1.5, 3.5]$	$[0.06, 0.1]$	0.081	$^{+16.9}_{-16.9}$
$[3.5, 5]$	$[0.06, 0.1]$	0.102	$^{+18.2}_{-17.2}$
$[5, 6.5]$	$[0.06, 0.1]$	0.086	$^{+22.3}_{-20.4}$
$[8, 10]$	$[0.06, 0.1]$	0.048	$^{+17.9}_{-17.9}$
$[10, 15]$	$[0.06, 0.1]$	0.015	$^{+26.9}_{-17.4}$
$[1.5, 3.5]$	$[0.1, 0.14]$	0.083	$^{+18.9}_{-16.8}$
$[3.5, 5]$	$[0.1, 0.14]$	0.086	$^{+15.8}_{-19.1}$
$[5, 6.5]$	$[0.1, 0.14]$	0.051	$^{+21.5}_{-20.0}$
$[6.5, 12]$	$[0.1, 0.14]$	0.015	$^{+10.6}_{-9.6}$
$[1.5, 3.5]$	$[0.14, 0.18]$	0.068	$^{+13.3}_{-11.5}$
$[3.5, 5]$	$[0.14, 0.18]$	0.046	$^{+16.5}_{-16.3}$
$[5, 9]$	$[0.14, 0.18]$	0.013	$^{+17.0}_{-15.4}$
$[1.5, 3.5]$	$[0.18, 0.24]$	0.061	$^{+16.2}_{-14.9}$
$[3.5, 7]$	$[0.18, 0.24]$	0.018	$^{+15.6}_{-16.2}$
$[1.5, 5]$	$[0.24, 0.3]$	0.028	$^{+25.2}_{-23.8}$

Table A.1: K^0_S differential multiplicity results for proton-carbon interaction at 90 GeV/c

p [GeV/c]	θ [rad]	Multiplicity $\frac{1}{\text{GeV/c rad}}$	Total Unc. [%]
$[3.5, 10]$	$[0, 0.02]$	0.013	$^{+11.9}_{-11.4}$
$[10, 14]$	$[0, 0.02]$	0.020	$^{+13.0}_{-16.9}$
$[14, 19]$	$[0, 0.02]$	0.030	$^{+17.5}_{-19.3}$
$[19, 24]$	$[0, 0.02]$	0.028	$^{+26.6}_{-26.5}$
$[24, 32]$	$[0, 0.02]$	0.042	$^{+20.8}_{-20.3}$
$[32, 40]$	$[0, 0.02]$	0.044	$^{+43.8}_{-42.5}$
$[1.5, 7]$	$[0.02, 0.04]$	0.025	$^{+17.4}_{-17.5}$
$[7, 10]$	$[0.02, 0.04]$	0.035	$^{+12.4}_{-12.6}$

p [GeV/c]	θ [rad]	Multiplicity $\frac{1}{\text{GeV/c rad}}$	Total Unc. [%]
$[10, 13]$	$[0.02, 0.04]$	0.042	$^{+11.4}_{-14.7}$
$[13, 17]$	$[0.02, 0.04]$	0.041	$^{+19.6}_{-21.0}$
$[17, 22]$	$[0.02, 0.04]$	0.032	$^{+18.8}_{-13.5}$
$[22, 32]$	$[0.02, 0.04]$	0.028	$^{+30.5}_{-28.7}$
$[32, 40]$	$[0.02, 0.04]$	0.008	$^{+84.6}_{-39.4}$
$[1.5, 6.5]$	$[0.04, 0.06]$	0.030	$^{+23.1}_{-23.7}$
$[6.5, 10]$	$[0.04, 0.06]$	0.040	$^{+15.8}_{-15.1}$
$[10, 15]$	$[0.04, 0.06]$	0.036	$^{+16.8}_{-16.6}$
$[15, 25]$	$[0.04, 0.06]$	0.015	$^{+20.7}_{-18.6}$
$[1.5, 5]$	$[0.06, 0.1]$	0.036	$^{+18.7}_{-19.7}$
$[5, 7]$	$[0.06, 0.1]$	0.041	$^{+10.9}_{-10.0}$
$[7, 10]$	$[0.06, 0.1]$	0.034	$^{+12.9}_{-11.8}$
$[10, 13]$	$[0.06, 0.1]$	0.019	$^{+17.1}_{-13.6}$
$[13, 18]$	$[0.06, 0.1]$	0.009	$^{+13.3}_{-15.9}$
$[1.5, 4.5]$	$[0.1, 0.14]$	0.042	$^{+15.3}_{-15.6}$
$[4.5, 6.5]$	$[0.1, 0.14]$	0.038	$^{+10.4}_{-10.2}$
$[6.5, 8.5]$	$[0.1, 0.14]$	0.021	$^{+15.3}_{-14.5}$
$[8.5, 12]$	$[0.1, 0.14]$	0.010	$^{+13.4}_{-9.0}$
$[1.5, 4.5]$	$[0.14, 0.18]$	0.044	$^{+15.0}_{-16.4}$
$[4.5, 9]$	$[0.14, 0.18]$	0.017	$^{+10.2}_{-10.6}$
$[1.5, 4]$	$[0.18, 0.24]$	0.050	$^{+17.3}_{-18.4}$
$[4, 7]$	$[0.18, 0.24]$	0.013	$^{+15.5}_{-14.7}$
$[1.5, 5]$	$[0.24, 0.3]$	0.024	$^{+19.2}_{-17.8}$

Table A.2: Λ differential multiplicity results for proton-carbon interaction at 90 GeV/c

p [GeV/c]	θ [rad]	Multiplicity $\frac{1}{\text{GeV/c rad}}$	Total Unc. [%]
$[5, 15]$	$[0, 0.04]$	0.005	$^{+18.6}_{-17.6}$
$[15, 25]$	$[0, 0.04]$	0.002	$^{+60.9}_{-60.7}$
$[4.5, 12]$	$[0.04, 0.08]$	0.006	$^{+21.8}_{-23.7}$
$[12, 20]$	$[0.04, 0.08]$	0.002	$^{+42.4}_{-20.7}$
$[3.5, 8.5]$	$[0.08, 0.16]$	0.004	$^{+22.6}_{-20.5}$

Table A.3: $\bar{\Lambda}$ differential multiplicity results for proton-carbon interaction at 90 GeV/c

p [GeV/c]	θ [rad]	Multiplicity $\frac{1}{\text{GeV/c rad}}$	Total Unc. [%]
$[0.5, 1.64]$	$[0, 0.005]$	0.031	$^{+22.9}_{-22.6}$
$[2.02, 6]$	$[0, 0.005]$	0.115	$^{+8.1}_{-7.2}$
$[6, 9]$	$[0, 0.005]$	0.143	$^{+6.5}_{-5.3}$
$[9, 15]$	$[0, 0.005]$	0.158	$^{+5.3}_{-3.7}$
$[15, 18]$	$[0, 0.005]$	0.167	$^{+6.1}_{-4.7}$
$[18, 20]$	$[0, 0.005]$	0.173	$^{+7.1}_{-6.0}$
$[20, 25]$	$[0, 0.005]$	0.161	$^{+6.5}_{-5.3}$
$[25, 30]$	$[0, 0.005]$	0.128	$^{+9.8}_{-9.0}$
$[30, 36]$	$[0, 0.005]$	0.102	$^{+6.5}_{-5.3}$
$[36, 40]$	$[0, 0.005]$	0.082	$^{+15.0}_{-14.5}$
$[40, 50]$	$[0, 0.005]$	0.060	$^{+15.0}_{-14.5}$
$[50, 60]$	$[0, 0.005]$	0.016	$^{+14.1}_{-13.6}$
$[0.5, 1.64]$	$[0.005, 0.01]$	0.070	$^{+18.7}_{-18.3}$
$[2.02, 6]$	$[0.005, 0.01]$	0.323	$^{+7.2}_{-6.1}$
$[6, 9]$	$[0.005, 0.01]$	0.433	$^{+5.7}_{-4.3}$
$[9, 15]$	$[0.005, 0.01]$	0.476	$^{+4.9}_{-3.1}$
$[15, 20]$	$[0.005, 0.01]$	0.525	$^{+5.4}_{-3.9}$
$[20, 25]$	$[0.005, 0.01]$	0.443	$^{+5.4}_{-3.8}$

p [GeV/c]	θ [rad]	Multiplicity $\frac{1}{\text{GeV/c rad}}$	Total Unc. [%]
$[25, 30]$	$[0.005, 0.01]$	0.302	$^{+6.6}_{-5.4}$
$[30, 35]$	$[0.005, 0.01]$	0.203	$^{+8.0}_{-7.1}$
$[35, 40]$	$[0.005, 0.01]$	0.150	$^{+10.8}_{-10.1}$
$[40, 45]$	$[0.005, 0.01]$	0.108	$^{+11.0}_{-10.3}$
$[45, 50]$	$[0.005, 0.01]$	0.066	$^{+15.8}_{-15.3}$
$[50, 55]$	$[0.005, 0.01]$	0.031	$^{+24.8}_{-24.5}$
$[0.5, 1.64]$	$[0.01, 0.02]$	0.174	$^{+8.4}_{-7.4}$
$[2.02, 4]$	$[0.01, 0.02]$	0.561	$^{+6.2}_{-4.9}$
$[4, 6]$	$[0.01, 0.02]$	0.863	$^{+5.6}_{-4.1}$
$[6, 9]$	$[0.01, 0.02]$	0.915	$^{+5.8}_{-4.4}$
$[9, 12]$	$[0.01, 0.02]$	0.937	$^{+4.5}_{-2.4}$
$[12, 15]$	$[0.01, 0.02]$	0.913	$^{+4.6}_{-2.5}$
$[15, 18]$	$[0.01, 0.02]$	0.803	$^{+4.6}_{-2.6}$
$[18, 21]$	$[0.01, 0.02]$	0.647	$^{+4.5}_{-2.5}$
$[21, 24]$	$[0.01, 0.02]$	0.499	$^{+4.7}_{-2.7}$
$[24, 27]$	$[0.01, 0.02]$	0.377	$^{+4.8}_{-3.0}$
$[27, 30]$	$[0.01, 0.02]$	0.291	$^{+5.1}_{-3.4}$
$[30, 35]$	$[0.01, 0.02]$	0.227	$^{+6.7}_{-5.5}$
$[35, 40]$	$[0.01, 0.02]$	0.132	$^{+9.5}_{-8.7}$
$[40, 45]$	$[0.01, 0.02]$	0.073	$^{+16.5}_{-16.1}$
$[45, 50]$	$[0.01, 0.02]$	0.054	$^{+11.2}_{-10.5}$
$[50, 55]$	$[0.01, 0.02]$	0.020	$^{+28.8}_{-28.5}$
$[0.5, 1.2]$	$[0.02, 0.03]$	0.226	$^{+9.1}_{-8.3}$
$[1.2, 1.64]$	$[0.02, 0.03]$	0.427	$^{+16.8}_{-16.3}$
$[2.02, 4]$	$[0.02, 0.03]$	0.946	$^{+7.4}_{-6.4}$
$[4, 6]$	$[0.02, 0.03]$	1.453	$^{+5.9}_{-4.6}$
$[6, 10]$	$[0.02, 0.03]$	1.393	$^{+5.5}_{-4.0}$

p [GeV/c]	θ [rad]	Multiplicity $\frac{1}{\text{GeV/c rad}}$	Total Unc. [%]
$[10, 12]$	$[0.02, 0.03]$	1.158	$^{+6.0}_{-4.7}$
$[12, 15]$	$[0.02, 0.03]$	0.948	$^{+4.5}_{-2.4}$
$[15, 18]$	$[0.02, 0.03]$	0.685	$^{+4.7}_{-2.8}$
$[18, 20]$	$[0.02, 0.03]$	0.543	$^{+4.9}_{-3.0}$
$[20, 24]$	$[0.02, 0.03]$	0.417	$^{+4.8}_{-3.0}$
$[24, 27]$	$[0.02, 0.03]$	0.267	$^{+7.5}_{-6.5}$
$[27, 30]$	$[0.02, 0.03]$	0.170	$^{+8.3}_{-7.4}$
$[30, 33]$	$[0.02, 0.03]$	0.140	$^{+7.2}_{-6.1}$
$[33, 38]$	$[0.02, 0.03]$	0.080	$^{+7.0}_{-5.9}$
$[38, 42]$	$[0.02, 0.03]$	0.041	$^{+8.1}_{-7.2}$
$[0.5, 1.2]$	$[0.03, 0.04]$	0.261	$^{+10.7}_{-10.0}$
$[1.2, 1.64]$	$[0.03, 0.04]$	0.547	$^{+10.2}_{-9.4}$
$[2.02, 4]$	$[0.03, 0.04]$	1.284	$^{+8.1}_{-7.2}$
$[4, 6]$	$[0.03, 0.04]$	1.821	$^{+6.2}_{-4.9}$
$[6, 9]$	$[0.03, 0.04]$	1.551	$^{+6.4}_{-5.1}$
$[9, 12]$	$[0.03, 0.04]$	1.026	$^{+5.4}_{-3.8}$
$[12, 15]$	$[0.03, 0.04]$	0.719	$^{+5.0}_{-3.2}$
$[15, 18]$	$[0.03, 0.04]$	0.468	$^{+5.4}_{-3.9}$
$[18, 21]$	$[0.03, 0.04]$	0.301	$^{+5.4}_{-3.8}$
$[21, 24]$	$[0.03, 0.04]$	0.184	$^{+5.8}_{-4.4}$
$[24, 27]$	$[0.03, 0.04]$	0.102	$^{+7.9}_{-7.0}$
$[27, 30]$	$[0.03, 0.04]$	0.053	$^{+8.5}_{-7.6}$
$[30, 33]$	$[0.03, 0.04]$	0.040	$^{+9.2}_{-8.4}$
$[0.5, 1.2]$	$[0.04, 0.05]$	0.448	$^{+7.9}_{-7.0}$
$[1.2, 1.64]$	$[0.04, 0.05]$	0.791	$^{+15.4}_{-15.0}$
$[2.02, 4]$	$[0.04, 0.05]$	1.634	$^{+5.5}_{-3.9}$
$[4, 6]$	$[0.04, 0.05]$	2.006	$^{+5.1}_{-3.4}$

p [GeV/c]	θ [rad]	Multiplicity $\frac{1}{\text{GeV/c rad}}$	Total Unc. [%]
$[6, 10]$	$[0.04, 0.05]$	1.461	$^{+4.9}_{-3.1}$
$[10, 12]$	$[0.04, 0.05]$	0.874	$^{+4.7}_{-2.8}$
$[12, 15]$	$[0.04, 0.05]$	0.553	$^{+4.8}_{-3.0}$
$[15, 18]$	$[0.04, 0.05]$	0.311	$^{+5.1}_{-3.4}$
$[18, 21]$	$[0.04, 0.05]$	0.160	$^{+6.4}_{-5.1}$
$[21, 25]$	$[0.04, 0.05]$	0.077	$^{+6.4}_{-5.2}$
$[0.5, 1.2]$	$[0.05, 0.06]$	0.566	$^{+7.2}_{-6.1}$
$[1.2, 1.64]$	$[0.05, 0.06]$	0.965	$^{+20.8}_{-20.4}$
$[2.02, 4]$	$[0.05, 0.06]$	1.776	$^{+5.4}_{-3.9}$
$[4, 6]$	$[0.05, 0.06]$	1.982	$^{+5.3}_{-3.8}$
$[6, 8]$	$[0.05, 0.06]$	1.515	$^{+5.1}_{-3.3}$
$[8, 10]$	$[0.05, 0.06]$	1.030	$^{+5.2}_{-3.6}$
$[10, 12]$	$[0.05, 0.06]$	0.642	$^{+4.8}_{-2.9}$
$[12, 15]$	$[0.05, 0.06]$	0.356	$^{+5.4}_{-3.9}$
$[15, 19]$	$[0.05, 0.06]$	0.158	$^{+5.7}_{-4.2}$
$[19, 21]$	$[0.05, 0.06]$	0.074	$^{+8.6}_{-7.7}$
$[0.5, 1.2]$	$[0.06, 0.08]$	0.766	$^{+8.6}_{-7.7}$
$[1.2, 1.64]$	$[0.06, 0.08]$	1.609	$^{+7.9}_{-7.0}$
$[2.02, 3]$	$[0.06, 0.08]$	2.166	$^{+5.6}_{-4.1}$
$[3, 4]$	$[0.06, 0.08]$	2.312	$^{+5.1}_{-3.4}$
$[4, 5]$	$[0.06, 0.08]$	1.928	$^{+5.3}_{-3.7}$
$[5, 6]$	$[0.06, 0.08]$	1.574	$^{+4.8}_{-3.0}$
$[6, 7]$	$[0.06, 0.08]$	1.349	$^{+5.0}_{-3.2}$
$[7, 8]$	$[0.06, 0.08]$	0.957	$^{+4.9}_{-3.1}$
$[8, 9]$	$[0.06, 0.08]$	0.790	$^{+5.6}_{-4.1}$
$[9, 10]$	$[0.06, 0.08]$	0.557	$^{+6.5}_{-5.3}$
$[10, 11]$	$[0.06, 0.08]$	0.424	$^{+5.6}_{-4.1}$

p [GeV/c]	θ [rad]	Multiplicity $\frac{1}{\text{GeV/c rad}}$	Total Unc. [%]
$[11, 12]$	$[0.06, 0.08]$	0.343	$^{+6.2}_{-4.8}$
$[12, 13]$	$[0.06, 0.08]$	0.255	$^{+5.7}_{-4.3}$
$[13, 15]$	$[0.06, 0.08]$	0.166	$^{+5.6}_{-4.1}$
$[15, 17]$	$[0.06, 0.08]$	0.087	$^{+9.3}_{-8.4}$
$[0.5, 1.2]$	$[0.08, 0.1]$	0.906	$^{+11.2}_{-10.5}$
$[1.2, 1.64]$	$[0.08, 0.1]$	1.630	$^{+9.0}_{-8.2}$
$[2.02, 3]$	$[0.08, 0.1]$	2.171	$^{+5.6}_{-4.2}$
$[3, 4]$	$[0.08, 0.1]$	1.995	$^{+5.0}_{-3.2}$
$[4, 5]$	$[0.08, 0.1]$	1.567	$^{+5.9}_{-4.6}$
$[5, 6]$	$[0.08, 0.1]$	1.177	$^{+6.0}_{-4.7}$
$[6, 7]$	$[0.08, 0.1]$	0.813	$^{+5.3}_{-3.7}$
$[7, 8]$	$[0.08, 0.1]$	0.538	$^{+6.8}_{-5.6}$
$[8, 9]$	$[0.08, 0.1]$	0.393	$^{+5.7}_{-4.2}$
$[9, 10]$	$[0.08, 0.1]$	0.267	$^{+6.5}_{-5.2}$
$[10, 12]$	$[0.08, 0.1]$	0.147	$^{+7.9}_{-7.0}$
$[12, 14]$	$[0.08, 0.1]$	0.070	$^{+6.7}_{-5.6}$
$[0.5, 1.2]$	$[0.1, 0.12]$	1.028	$^{+11.3}_{-10.6}$
$[1.2, 1.64]$	$[0.1, 0.12]$	2.157	$^{+5.3}_{-3.6}$
$[2.02, 3]$	$[0.1, 0.12]$	2.155	$^{+6.9}_{-5.8}$
$[3, 4]$	$[0.1, 0.12]$	1.686	$^{+6.0}_{-4.6}$
$[4, 5]$	$[0.1, 0.12]$	1.165	$^{+5.2}_{-3.6}$
$[5, 6]$	$[0.1, 0.12]$	0.724	$^{+5.2}_{-3.6}$
$[6, 7]$	$[0.1, 0.12]$	0.465	$^{+6.2}_{-4.9}$
$[7, 8]$	$[0.1, 0.12]$	0.339	$^{+6.6}_{-5.4}$
$[8, 9]$	$[0.1, 0.12]$	0.221	$^{+8.2}_{-7.2}$
$[9, 12]$	$[0.1, 0.12]$	0.085	$^{+6.8}_{-5.6}$
$[0.5, 1.2]$	$[0.12, 0.14]$	1.085	$^{+11.6}_{-10.9}$

p [GeV/c]	θ [rad]	Multiplicity $\frac{1}{\text{GeV/c rad}}$	Total Unc. [%]
$[1.2, 1.64]$	$[0.12, 0.14]$	1.919	$^{+10.1}_{-9.4}$
$[2.02, 3]$	$[0.12, 0.14]$	1.779	$^{+6.1}_{-4.8}$
$[3, 4]$	$[0.12, 0.14]$	1.361	$^{+5.8}_{-4.4}$
$[4, 5]$	$[0.12, 0.14]$	0.884	$^{+6.2}_{-4.9}$
$[5, 6]$	$[0.12, 0.14]$	0.496	$^{+6.3}_{-5.0}$
$[6, 7]$	$[0.12, 0.14]$	0.303	$^{+6.3}_{-5.0}$
$[7, 9]$	$[0.12, 0.14]$	0.140	$^{+8.3}_{-7.3}$
$[9, 10]$	$[0.12, 0.14]$	0.055	$^{+14.9}_{-14.4}$
$[0.5, 1.2]$	$[0.14, 0.16]$	1.188	$^{+14.2}_{-13.7}$
$[1.2, 1.64]$	$[0.14, 0.16]$	2.086	$^{+11.1}_{-10.5}$
$[2.02, 3]$	$[0.14, 0.16]$	1.638	$^{+5.8}_{-4.4}$
$[3, 4]$	$[0.14, 0.16]$	1.026	$^{+5.3}_{-3.8}$
$[4, 5]$	$[0.14, 0.16]$	0.585	$^{+5.6}_{-4.2}$
$[5, 6]$	$[0.14, 0.16]$	0.306	$^{+6.0}_{-4.6}$
$[6, 8]$	$[0.14, 0.16]$	0.138	$^{+6.4}_{-5.1}$
$[8, 9]$	$[0.14, 0.16]$	0.063	$^{+11.4}_{-10.7}$
$[0.5, 1.2]$	$[0.16, 0.18]$	1.239	$^{+19.1}_{-18.7}$
$[1.2, 1.64]$	$[0.16, 0.18]$	2.132	$^{+11.5}_{-10.8}$
$[2.02, 3]$	$[0.16, 0.18]$	1.327	$^{+6.7}_{-5.6}$
$[3, 4]$	$[0.16, 0.18]$	0.784	$^{+6.5}_{-5.2}$
$[4, 5]$	$[0.16, 0.18]$	0.455	$^{+6.2}_{-4.9}$
$[5, 7]$	$[0.16, 0.18]$	0.160	$^{+8.0}_{-7.0}$
$[7, 8]$	$[0.16, 0.18]$	0.052	$^{+15.0}_{-14.6}$
$[0.5, 1.2]$	$[0.18, 0.2]$	1.081	$^{+24.1}_{-23.8}$
$[1.2, 1.64]$	$[0.18, 0.2]$	1.703	$^{+13.5}_{-13.0}$
$[2.02, 3]$	$[0.18, 0.2]$	1.193	$^{+10.7}_{-10.0}$
$[3, 4]$	$[0.18, 0.2]$	0.659	$^{+7.1}_{-6.0}$

p [GeV/c]	θ [rad]	Multiplicity $\frac{1}{\text{GeV/c rad}}$	Total Unc. [%]
$[4, 5]$	$[0.18, 0.2]$	0.317	$^{+6.9}_{-5.8}$
$[5, 7]$	$[0.18, 0.2]$	0.103	$^{+10.1}_{-9.3}$
$[0.5, 1.2]$	$[0.2, 0.22]$	1.039	$^{+32.5}_{-32.3}$
$[1.2, 1.64]$	$[0.2, 0.22]$	1.672	$^{+15.8}_{-15.3}$
$[2.02, 3]$	$[0.2, 0.22]$	1.015	$^{+9.5}_{-8.7}$
$[3, 4]$	$[0.2, 0.22]$	0.491	$^{+9.7}_{-8.9}$
$[4, 6]$	$[0.2, 0.22]$	0.179	$^{+10.1}_{-9.3}$
$[0.5, 1.2]$	$[0.22, 0.24]$	0.927	$^{+45.0}_{-44.9}$
$[1.2, 1.64]$	$[0.22, 0.24]$	1.463	$^{+15.2}_{-14.8}$
$[2.02, 3]$	$[0.22, 0.24]$	0.845	$^{+13.4}_{-12.9}$
$[3, 4]$	$[0.22, 0.24]$	0.373	$^{+9.0}_{-8.1}$
$[4, 6]$	$[0.22, 0.24]$	0.131	$^{+10.0}_{-9.2}$
$[1.2, 1.64]$	$[0.24, 0.26]$	1.058	$^{+17.6}_{-17.1}$
$[2.02, 3]$	$[0.24, 0.26]$	0.650	$^{+14.3}_{-13.7}$
$[3, 5]$	$[0.24, 0.26]$	0.218	$^{+10.8}_{-10.1}$
$[1.2, 1.64]$	$[0.26, 0.28]$	0.931	$^{+28.0}_{-27.8}$
$[2.02, 3]$	$[0.26, 0.28]$	0.546	$^{+13.9}_{-13.4}$
$[3, 5]$	$[0.26, 0.28]$	0.150	$^{+7.5}_{-6.5}$
$[2.02, 3]$	$[0.28, 0.3]$	0.443	$^{+26.6}_{-26.3}$
$[3, 5]$	$[0.28, 0.3]$	0.120	$^{+16.5}_{-16.1}$
$[2.02, 3]$	$[0.3, 0.32]$	0.141	$^{+32.6}_{-32.4}$
$[3, 5]$	$[0.3, 0.32]$	0.078	$^{+25.5}_{-25.2}$

Table A.4: π^+ differential multiplicity results for proton-carbon interaction at 90 GeV/c

p [GeV/c]	θ [rad]	Multiplicity $\frac{1}{\text{GeV/c rad}}$	Total Unc. [%]
$[0.5, 1.64]$	$[0, 0.005]$	0.025	$^{+22.6}_{-22.3}$
$[2.02, 6]$	$[0, 0.005]$	0.104	$^{+9.7}_{-8.9}$
$[6, 9]$	$[0, 0.005]$	0.115	$^{+9.0}_{-8.2}$
$[9, 15]$	$[0, 0.005]$	0.132	$^{+5.9}_{-4.5}$
$[15, 18]$	$[0, 0.005]$	0.102	$^{+7.6}_{-6.6}$
$[18, 20]$	$[0, 0.005]$	0.095	$^{+12.4}_{-11.8}$
$[20, 25]$	$[0, 0.005]$	0.087	$^{+6.8}_{-5.7}$
$[25, 30]$	$[0, 0.005]$	0.063	$^{+9.9}_{-9.1}$
$[30, 36]$	$[0, 0.005]$	0.046	$^{+11.4}_{-10.7}$
$[36, 40]$	$[0, 0.005]$	0.031	$^{+14.0}_{-13.5}$
$[40, 50]$	$[0, 0.005]$	0.018	$^{+8.9}_{-8.0}$
$[50, 60]$	$[0, 0.005]$	0.005	$^{+18.1}_{-17.7}$
$[0.5, 1.64]$	$[0.005, 0.01]$	0.067	$^{+18.4}_{-18.0}$
$[2.02, 6]$	$[0.005, 0.01]$	0.325	$^{+7.5}_{-6.4}$
$[6, 9]$	$[0.005, 0.01]$	0.337	$^{+6.5}_{-5.4}$
$[9, 15]$	$[0.005, 0.01]$	0.359	$^{+5.7}_{-4.2}$
$[15, 20]$	$[0.005, 0.01]$	0.266	$^{+6.0}_{-4.6}$
$[20, 25]$	$[0.005, 0.01]$	0.227	$^{+5.9}_{-4.5}$
$[25, 30]$	$[0.005, 0.01]$	0.152	$^{+8.8}_{-8.0}$
$[30, 35]$	$[0.005, 0.01]$	0.103	$^{+9.0}_{-8.1}$
$[35, 40]$	$[0.005, 0.01]$	0.069	$^{+13.6}_{-13.1}$
$[40, 45]$	$[0.005, 0.01]$	0.039	$^{+16.3}_{-15.9}$
$[45, 50]$	$[0.005, 0.01]$	0.021	$^{+22.4}_{-22.1}$
$[50, 55]$	$[0.005, 0.01]$	0.010	$^{+22.9}_{-22.5}$
$[0.5, 1.64]$	$[0.01, 0.02]$	0.170	$^{+11.4}_{-10.8}$
$[2.02, 4]$	$[0.01, 0.02]$	0.521	$^{+5.5}_{-4.0}$
$[4, 6]$	$[0.01, 0.02]$	0.728	$^{+5.8}_{-4.4}$

p [GeV/c]	θ [rad]	Multiplicity $\frac{1}{\text{GeV/c rad}}$	Total Unc. [%]
$[6, 9]$	$[0.01, 0.02]$	0.753	$^{+5.0}_{-3.2}$
$[9, 12]$	$[0.01, 0.02]$	0.646	$^{+4.8}_{-3.0}$
$[12, 15]$	$[0.01, 0.02]$	0.551	$^{+5.2}_{-3.5}$
$[15, 18]$	$[0.01, 0.02]$	0.455	$^{+5.0}_{-3.2}$
$[18, 21]$	$[0.01, 0.02]$	0.332	$^{+4.9}_{-3.1}$
$[21, 24]$	$[0.01, 0.02]$	0.258	$^{+5.1}_{-3.4}$
$[24, 27]$	$[0.01, 0.02]$	0.192	$^{+5.3}_{-3.7}$
$[27, 30]$	$[0.01, 0.02]$	0.141	$^{+5.8}_{-4.3}$
$[30, 35]$	$[0.01, 0.02]$	0.099	$^{+6.7}_{-5.5}$
$[35, 40]$	$[0.01, 0.02]$	0.060	$^{+10.9}_{-10.2}$
$[40, 45]$	$[0.01, 0.02]$	0.028	$^{+14.2}_{-13.7}$
$[45, 50]$	$[0.01, 0.02]$	0.013	$^{+21.3}_{-21.0}$
$[50, 55]$	$[0.01, 0.02]$	0.008	$^{+23.5}_{-23.2}$
$[0.5, 1.2]$	$[0.02, 0.03]$	0.201	$^{+13.2}_{-12.6}$
$[1.2, 1.64]$	$[0.02, 0.03]$	0.269	$^{+16.6}_{-16.2}$
$[2.02, 4]$	$[0.02, 0.03]$	0.873	$^{+5.5}_{-4.0}$
$[4, 6]$	$[0.02, 0.03]$	1.168	$^{+5.4}_{-3.9}$
$[6, 10]$	$[0.02, 0.03]$	1.151	$^{+5.1}_{-3.4}$
$[10, 12]$	$[0.02, 0.03]$	0.817	$^{+4.6}_{-2.6}$
$[12, 15]$	$[0.02, 0.03]$	0.616	$^{+4.5}_{-2.5}$
$[15, 18]$	$[0.02, 0.03]$	0.417	$^{+4.7}_{-2.7}$
$[18, 20]$	$[0.02, 0.03]$	0.315	$^{+5.1}_{-3.4}$
$[20, 24]$	$[0.02, 0.03]$	0.225	$^{+5.2}_{-3.5}$
$[24, 27]$	$[0.02, 0.03]$	0.127	$^{+6.2}_{-4.9}$
$[27, 30]$	$[0.02, 0.03]$	0.089	$^{+6.8}_{-5.7}$
$[30, 33]$	$[0.02, 0.03]$	0.053	$^{+8.7}_{-7.8}$
$[33, 38]$	$[0.02, 0.03]$	0.029	$^{+9.4}_{-8.6}$

p [GeV/c]	θ [rad]	Multiplicity $\frac{1}{\text{GeV/c rad}}$	Total Unc. [%]
$[38, 42]$	$[0.02, 0.03]$	0.013	$^{+15.6}_{-15.1}$
$[0.5, 1.2]$	$[0.03, 0.04]$	0.270	$^{+12.9}_{-12.3}$
$[1.2, 1.64]$	$[0.03, 0.04]$	0.427	$^{+15.7}_{-15.3}$
$[2.02, 4]$	$[0.03, 0.04]$	1.133	$^{+6.2}_{-4.8}$
$[4, 6]$	$[0.03, 0.04]$	1.436	$^{+5.8}_{-4.4}$
$[6, 9]$	$[0.03, 0.04]$	1.312	$^{+7.0}_{-5.9}$
$[9, 12]$	$[0.03, 0.04]$	0.859	$^{+5.0}_{-3.3}$
$[12, 15]$	$[0.03, 0.04]$	0.492	$^{+4.7}_{-2.8}$
$[15, 18]$	$[0.03, 0.04]$	0.302	$^{+5.2}_{-3.6}$
$[18, 21]$	$[0.03, 0.04]$	0.168	$^{+5.7}_{-4.3}$
$[21, 24]$	$[0.03, 0.04]$	0.094	$^{+6.8}_{-5.6}$
$[24, 27]$	$[0.03, 0.04]$	0.055	$^{+9.3}_{-8.5}$
$[27, 30]$	$[0.03, 0.04]$	0.026	$^{+10.3}_{-9.6}$
$[30, 33]$	$[0.03, 0.04]$	0.018	$^{+18.7}_{-18.3}$
$[0.5, 1.2]$	$[0.04, 0.05]$	0.462	$^{+10.0}_{-9.3}$
$[1.2, 1.64]$	$[0.04, 0.05]$	0.508	$^{+21.7}_{-21.4}$
$[2.02, 4]$	$[0.04, 0.05]$	1.372	$^{+5.6}_{-4.1}$
$[4, 6]$	$[0.04, 0.05]$	1.491	$^{+4.5}_{-2.3}$
$[6, 10]$	$[0.04, 0.05]$	1.044	$^{+4.8}_{-2.9}$
$[10, 12]$	$[0.04, 0.05]$	0.587	$^{+4.6}_{-2.7}$
$[12, 15]$	$[0.04, 0.05]$	0.358	$^{+4.6}_{-2.6}$
$[15, 18]$	$[0.04, 0.05]$	0.180	$^{+4.9}_{-3.1}$
$[18, 21]$	$[0.04, 0.05]$	0.090	$^{+6.9}_{-5.8}$
$[21, 25]$	$[0.04, 0.05]$	0.038	$^{+7.2}_{-6.1}$
$[0.5, 1.2]$	$[0.05, 0.06]$	0.491	$^{+9.5}_{-8.7}$
$[1.2, 1.64]$	$[0.05, 0.06]$	0.836	$^{+25.6}_{-25.3}$
$[2.02, 4]$	$[0.05, 0.06]$	1.611	$^{+6.3}_{-5.0}$

p [GeV/c]	θ [rad]	Multiplicity $\frac{1}{\text{GeV/c rad}}$	Total Unc. [%]
$[4, 6]$	$[0.05, 0.06]$	1.578	$^{+4.6}_{-2.7}$
$[6, 8]$	$[0.05, 0.06]$	1.129	$^{+4.6}_{-2.6}$
$[8, 10]$	$[0.05, 0.06]$	0.759	$^{+5.2}_{-3.5}$
$[10, 12]$	$[0.05, 0.06]$	0.458	$^{+5.6}_{-4.2}$
$[12, 15]$	$[0.05, 0.06]$	0.239	$^{+5.4}_{-3.9}$
$[15, 19]$	$[0.05, 0.06]$	0.086	$^{+6.0}_{-4.6}$
$[19, 21]$	$[0.05, 0.06]$	0.041	$^{+9.6}_{-8.8}$
$[0.5, 1.2]$	$[0.06, 0.08]$	0.606	$^{+9.7}_{-8.9}$
$[1.2, 1.64]$	$[0.06, 0.08]$	1.451	$^{+10.7}_{-10.0}$
$[2.02, 3]$	$[0.06, 0.08]$	1.849	$^{+6.0}_{-4.6}$
$[3, 4]$	$[0.06, 0.08]$	1.887	$^{+5.1}_{-3.4}$
$[4, 5]$	$[0.06, 0.08]$	1.568	$^{+4.6}_{-2.6}$
$[5, 6]$	$[0.06, 0.08]$	1.327	$^{+5.4}_{-3.8}$
$[6, 7]$	$[0.06, 0.08]$	1.001	$^{+4.8}_{-2.9}$
$[7, 8]$	$[0.06, 0.08]$	0.770	$^{+5.2}_{-3.6}$
$[8, 9]$	$[0.06, 0.08]$	0.593	$^{+6.2}_{-4.8}$
$[9, 10]$	$[0.06, 0.08]$	0.421	$^{+5.5}_{-4.0}$
$[10, 11]$	$[0.06, 0.08]$	0.330	$^{+6.7}_{-5.5}$
$[11, 12]$	$[0.06, 0.08]$	0.243	$^{+7.4}_{-6.4}$
$[12, 13]$	$[0.06, 0.08]$	0.165	$^{+6.7}_{-5.5}$
$[13, 15]$	$[0.06, 0.08]$	0.107	$^{+6.0}_{-4.7}$
$[15, 17]$	$[0.06, 0.08]$	0.050	$^{+9.0}_{-8.2}$
$[0.5, 1.2]$	$[0.08, 0.1]$	0.822	$^{+9.7}_{-8.9}$
$[1.2, 1.64]$	$[0.08, 0.1]$	1.538	$^{+10.8}_{-10.1}$
$[2.02, 3]$	$[0.08, 0.1]$	2.110	$^{+6.0}_{-4.7}$
$[3, 4]$	$[0.08, 0.1]$	1.845	$^{+4.8}_{-3.0}$
$[4, 5]$	$[0.08, 0.1]$	1.349	$^{+4.9}_{-3.1}$

p [GeV/c]	θ [rad]	Multiplicity $\frac{1}{\text{GeV/c rad}}$	Total Unc. [%]
$[5, 6]$	$[0.08, 0.1]$	0.960	$^{+5.0}_{-3.3}$
$[6, 7]$	$[0.08, 0.1]$	0.672	$^{+5.5}_{-3.9}$
$[7, 8]$	$[0.08, 0.1]$	0.481	$^{+5.2}_{-3.5}$
$[8, 9]$	$[0.08, 0.1]$	0.316	$^{+5.9}_{-4.6}$
$[9, 10]$	$[0.08, 0.1]$	0.197	$^{+7.7}_{-6.7}$
$[10, 12]$	$[0.08, 0.1]$	0.115	$^{+5.7}_{-4.2}$
$[12, 14]$	$[0.08, 0.1]$	0.044	$^{+8.1}_{-7.1}$
$[0.5, 1.2]$	$[0.1, 0.12]$	0.879	$^{+10.8}_{-10.2}$
$[1.2, 1.64]$	$[0.1, 0.12]$	1.669	$^{+9.2}_{-8.4}$
$[2.02, 3]$	$[0.1, 0.12]$	1.802	$^{+6.3}_{-5.0}$
$[3, 4]$	$[0.1, 0.12]$	1.513	$^{+5.5}_{-3.9}$
$[4, 5]$	$[0.1, 0.12]$	1.049	$^{+5.9}_{-4.5}$
$[5, 6]$	$[0.1, 0.12]$	0.648	$^{+5.6}_{-4.1}$
$[6, 7]$	$[0.1, 0.12]$	0.411	$^{+6.0}_{-4.7}$
$[7, 8]$	$[0.1, 0.12]$	0.255	$^{+7.8}_{-6.8}$
$[8, 9]$	$[0.1, 0.12]$	0.160	$^{+9.5}_{-8.7}$
$[9, 12]$	$[0.1, 0.12]$	0.065	$^{+6.1}_{-4.8}$
$[0.5, 1.2]$	$[0.12, 0.14]$	0.872	$^{+12.3}_{-11.7}$
$[1.2, 1.64]$	$[0.12, 0.14]$	1.662	$^{+9.3}_{-8.4}$
$[2.02, 3]$	$[0.12, 0.14]$	1.703	$^{+8.2}_{-7.3}$
$[3, 4]$	$[0.12, 0.14]$	1.229	$^{+6.5}_{-5.2}$
$[4, 5]$	$[0.12, 0.14]$	0.801	$^{+6.3}_{-5.1}$
$[5, 6]$	$[0.12, 0.14]$	0.409	$^{+6.4}_{-5.2}$
$[6, 7]$	$[0.12, 0.14]$	0.238	$^{+7.5}_{-6.4}$
$[7, 9]$	$[0.12, 0.14]$	0.117	$^{+10.1}_{-9.4}$
$[9, 10]$	$[0.12, 0.14]$	0.048	$^{+10.3}_{-9.6}$
$[0.5, 1.2]$	$[0.14, 0.16]$	0.818	$^{+10.3}_{-9.6}$

p [GeV/c]	θ [rad]	Multiplicity $\frac{1}{\text{GeV/c rad}}$	Total Unc. [%]
$[1.2, 1.64]$	$[0.14, 0.16]$	1.600	$^{+11.4}_{-10.8}$
$[2.02, 3]$	$[0.14, 0.16]$	1.472	$^{+6.5}_{-5.2}$
$[3, 4]$	$[0.14, 0.16]$	0.936	$^{+7.8}_{-6.9}$
$[4, 5]$	$[0.14, 0.16]$	0.589	$^{+6.3}_{-5.0}$
$[5, 6]$	$[0.14, 0.16]$	0.295	$^{+7.0}_{-5.9}$
$[6, 8]$	$[0.14, 0.16]$	0.102	$^{+7.4}_{-6.4}$
$[8, 9]$	$[0.14, 0.16]$	0.034	$^{+15.6}_{-15.1}$
$[0.5, 1.2]$	$[0.16, 0.18]$	0.726	$^{+15.1}_{-14.6}$
$[1.2, 1.64]$	$[0.16, 0.18]$	1.032	$^{+23.1}_{-22.7}$
$[2.02, 3]$	$[0.16, 0.18]$	1.189	$^{+6.0}_{-4.7}$
$[3, 4]$	$[0.16, 0.18]$	0.673	$^{+5.9}_{-4.6}$
$[4, 5]$	$[0.16, 0.18]$	0.326	$^{+6.2}_{-4.9}$
$[5, 7]$	$[0.16, 0.18]$	0.127	$^{+7.1}_{-6.0}$
$[7, 8]$	$[0.16, 0.18]$	0.044	$^{+12.2}_{-11.6}$
$[0.5, 1.2]$	$[0.18, 0.2]$	0.687	$^{+42.1}_{-41.9}$
$[1.2, 1.64]$	$[0.18, 0.2]$	1.277	$^{+14.4}_{-13.8}$
$[2.02, 3]$	$[0.18, 0.2]$	1.037	$^{+6.7}_{-5.5}$
$[3, 4]$	$[0.18, 0.2]$	0.494	$^{+6.5}_{-5.2}$
$[4, 5]$	$[0.18, 0.2]$	0.232	$^{+7.6}_{-6.5}$
$[5, 7]$	$[0.18, 0.2]$	0.077	$^{+9.6}_{-8.8}$
$[1.2, 1.64]$	$[0.2, 0.22]$	1.012	$^{+16.4}_{-15.9}$
$[2.02, 3]$	$[0.2, 0.22]$	0.835	$^{+9.3}_{-8.5}$
$[3, 4]$	$[0.2, 0.22]$	0.342	$^{+7.1}_{-6.0}$
$[4, 6]$	$[0.2, 0.22]$	0.095	$^{+7.3}_{-6.2}$
$[1.2, 1.64]$	$[0.22, 0.24]$	0.905	$^{+43.1}_{-42.9}$
$[2.02, 3]$	$[0.22, 0.24]$	0.617	$^{+11.9}_{-11.3}$
$[3, 4]$	$[0.22, 0.24]$	0.269	$^{+9.5}_{-8.7}$

p [GeV/c]	θ [rad]	Multiplicity $\frac{1}{\mathrm{GeV/c\ rad}}$	Total Unc. [%]
$[4, 6]$	$[0.22, 0.24]$	0.077	$^{+10.2}_{-9.5}$
$[2.02, 3]$	$[0.24, 0.26]$	0.534	$^{+27.0}_{-26.8}$
$[3, 5]$	$[0.24, 0.26]$	0.149	$^{+15.7}_{-15.2}$
$[2.02, 3]$	$[0.26, 0.28]$	0.386	$^{+45.5}_{-45.4}$
$[3, 5]$	$[0.26, 0.28]$	0.105	$^{+28.3}_{-28.0}$
$[0.5, 1.2]$	$[0.28, 0.3]$	0.462	$^{+30.4}_{-30.2}$
$[2.02, 3]$	$[0.28, 0.3]$	0.257	$^{+37.3}_{-37.1}$
$[3, 5]$	$[0.28, 0.3]$	0.058	$^{+35.3}_{-35.1}$
$[0.5, 1.2]$	$[0.3, 0.32]$	0.322	$^{+12.1}_{-11.5}$
$[1.2, 1.64]$	$[0.3, 0.32]$	0.308	$^{+46.7}_{-46.5}$
$[2.02, 3]$	$[0.3, 0.32]$	0.220	$^{+36.7}_{-36.5}$
$[3, 5]$	$[0.3, 0.32]$	0.049	$^{+32.4}_{-32.2}$
$[1.2, 1.64]$	$[0.32, 0.34]$	0.192	$^{+47.9}_{-47.8}$

Table A.5: π^- differential multiplicity results for proton-carbon interaction at 90 GeV/c

p [GeV/c]	θ [rad]	Multiplicity $\frac{1}{\mathrm{GeV/c\ rad}}$	Total Unc. [%]
$[4.32, 13]$	$[0, 0.005]$	0.023	$^{+9.0}_{-8.3}$
$[13, 18]$	$[0, 0.005]$	0.039	$^{+9.2}_{-8.3}$
$[18, 25]$	$[0, 0.005]$	0.065	$^{+7.4}_{-6.2}$
$[25, 31]$	$[0, 0.005]$	0.083	$^{+9.2}_{-8.4}$
$[31, 36]$	$[0, 0.005]$	0.123	$^{+8.8}_{-8.0}$
$[36, 41]$	$[0, 0.005]$	0.160	$^{+10.8}_{-10.1}$
$[41, 46]$	$[0, 0.005]$	0.197	$^{+11.3}_{-10.6}$
$[46, 50]$	$[0, 0.005]$	0.232	$^{+8.1}_{-7.1}$
$[50, 56]$	$[0, 0.005]$	0.286	$^{+9.4}_{-8.6}$
$[56, 61]$	$[0, 0.005]$	0.346	$^{+9.2}_{-8.4}$

p [GeV/c]	θ [rad]	Multiplicity $\frac{1}{\text{GeV/c rad}}$	Total Unc. [%]
$[61, 66]$	$[0, 0.005]$	0.348	$^{+10.5}_{-9.8}$
$[66, 71]$	$[0, 0.005]$	0.412	$^{+9.6}_{-8.8}$
$[71, 76]$	$[0, 0.005]$	0.455	$^{+12.0}_{-11.4}$
$[76, 81]$	$[0, 0.005]$	0.536	$^{+10.7}_{-10.1}$
$[81, 85]$	$[0, 0.005]$	0.617	$^{+11.6}_{-10.9}$
$[85, 95]$	$[0, 0.005]$	0.515	$^{+8.7}_{-7.8}$
$[0.5, 1.64]$	$[0.005, 0.01]$	0.010	$^{+48.7}_{-48.5}$
$[4.32, 10]$	$[0.005, 0.01]$	0.045	$^{+11.4}_{-10.9}$
$[10, 15]$	$[0.005, 0.01]$	0.083	$^{+9.3}_{-8.6}$
$[15, 20]$	$[0.005, 0.01]$	0.129	$^{+7.5}_{-6.4}$
$[20, 25]$	$[0.005, 0.01]$	0.180	$^{+6.9}_{-5.8}$
$[25, 30]$	$[0.005, 0.01]$	0.211	$^{+8.6}_{-7.7}$
$[30, 35]$	$[0.005, 0.01]$	0.278	$^{+10.9}_{-10.3}$
$[35, 40]$	$[0.005, 0.01]$	0.295	$^{+12.1}_{-11.5}$
$[40, 45]$	$[0.005, 0.01]$	0.340	$^{+16.1}_{-15.7}$
$[45, 50]$	$[0.005, 0.01]$	0.336	$^{+8.5}_{-7.6}$
$[50, 60]$	$[0.005, 0.01]$	0.308	$^{+21.3}_{-21.0}$
$[60, 65]$	$[0.005, 0.01]$	0.411	$^{+16.3}_{-15.9}$
$[65, 70]$	$[0.005, 0.01]$	0.333	$^{+25.1}_{-24.8}$
$[70, 75]$	$[0.005, 0.01]$	0.300	$^{+12.9}_{-12.3}$
$[75, 80]$	$[0.005, 0.01]$	0.280	$^{+12.9}_{-12.4}$
$[80, 85]$	$[0.005, 0.01]$	0.278	$^{+14.6}_{-14.1}$
$[85, 95]$	$[0.005, 0.01]$	0.080	$^{+9.4}_{-8.6}$
$[0.5, 1.64]$	$[0.01, 0.02]$	0.021	$^{+21.9}_{-21.6}$
$[4.32, 7]$	$[0.01, 0.02]$	0.082	$^{+8.2}_{-7.3}$
$[7, 9]$	$[0.01, 0.02]$	0.103	$^{+8.6}_{-7.8}$
$[9, 12]$	$[0.01, 0.02]$	0.120	$^{+6.8}_{-5.8}$

p [GeV/c]	θ [rad]	Multiplicity $\frac{1}{\text{GeV/c rad}}$	Total Unc. [%]
$[12, 15]$	$[0.01, 0.02]$	0.157	$^{+6.4}_{-5.3}$
$[15, 18]$	$[0.01, 0.02]$	0.208	$^{+7.1}_{-5.9}$
$[18, 21]$	$[0.01, 0.02]$	0.256	$^{+7.4}_{-6.2}$
$[21, 24]$	$[0.01, 0.02]$	0.273	$^{+7.3}_{-6.1}$
$[24, 27]$	$[0.01, 0.02]$	0.309	$^{+5.9}_{-4.6}$
$[27, 30]$	$[0.01, 0.02]$	0.296	$^{+7.9}_{-7.0}$
$[30, 34]$	$[0.01, 0.02]$	0.376	$^{+6.3}_{-5.1}$
$[34, 39]$	$[0.01, 0.02]$	0.353	$^{+8.2}_{-7.3}$
$[39, 44]$	$[0.01, 0.02]$	0.323	$^{+6.2}_{-5.0}$
$[44, 49]$	$[0.01, 0.02]$	0.247	$^{+9.6}_{-8.8}$
$[49, 54]$	$[0.01, 0.02]$	0.151	$^{+19.6}_{-19.2}$
$[54, 59]$	$[0.01, 0.02]$	0.149	$^{+26.3}_{-26.0}$
$[59, 64]$	$[0.01, 0.02]$	0.069	$^{+26.1}_{-25.9}$
$[64, 70]$	$[0.01, 0.02]$	0.111	$^{+19.8}_{-19.5}$
$[70, 76]$	$[0.01, 0.02]$	0.068	$^{+20.8}_{-20.5}$
$[76, 85]$	$[0.01, 0.02]$	0.044	$^{+22.2}_{-21.9}$
$[85, 95]$	$[0.01, 0.02]$	0.007	$^{+20.3}_{-19.9}$
$[0.5, 1.64]$	$[0.02, 0.03]$	0.037	$^{+16.9}_{-16.5}$
$[4.32, 6]$	$[0.02, 0.03]$	0.121	$^{+9.6}_{-8.8}$
$[6, 8]$	$[0.02, 0.03]$	0.139	$^{+8.9}_{-8.1}$
$[8, 10]$	$[0.02, 0.03]$	0.162	$^{+7.9}_{-7.0}$
$[10, 12]$	$[0.02, 0.03]$	0.177	$^{+7.3}_{-6.3}$
$[12, 14]$	$[0.02, 0.03]$	0.198	$^{+6.8}_{-5.6}$
$[14, 16]$	$[0.02, 0.03]$	0.215	$^{+6.5}_{-5.3}$
$[16, 18]$	$[0.02, 0.03]$	0.226	$^{+7.3}_{-6.1}$
$[18, 20]$	$[0.02, 0.03]$	0.238	$^{+6.1}_{-4.7}$
$[20, 22]$	$[0.02, 0.03]$	0.247	$^{+6.8}_{-5.5}$

p [GeV/c]	θ [rad]	Multiplicity $\frac{1}{\text{GeV/c rad}}$	Total Unc. [%]
$[22, 24]$	$[0.02, 0.03]$	0.250	$^{+5.9}_{-4.5}$
$[24, 26]$	$[0.02, 0.03]$	0.244	$^{+6.6}_{-5.4}$
$[26, 29]$	$[0.02, 0.03]$	0.227	$^{+6.2}_{-4.9}$
$[29, 34]$	$[0.02, 0.03]$	0.209	$^{+5.5}_{-4.0}$
$[34, 40]$	$[0.02, 0.03]$	0.171	$^{+6.9}_{-5.8}$
$[40, 46]$	$[0.02, 0.03]$	0.097	$^{+13.5}_{-12.9}$
$[46, 52]$	$[0.02, 0.03]$	0.064	$^{+12.0}_{-11.4}$
$[0.5, 1.64]$	$[0.03, 0.04]$	0.058	$^{+18.3}_{-17.9}$
$[4.32, 6]$	$[0.03, 0.04]$	0.149	$^{+10.5}_{-9.8}$
$[6, 8]$	$[0.03, 0.04]$	0.163	$^{+9.2}_{-8.4}$
$[8, 10]$	$[0.03, 0.04]$	0.172	$^{+8.7}_{-7.8}$
$[10, 12]$	$[0.03, 0.04]$	0.162	$^{+8.4}_{-7.5}$
$[12, 13]$	$[0.03, 0.04]$	0.192	$^{+9.3}_{-8.5}$
$[13, 15]$	$[0.03, 0.04]$	0.180	$^{+7.2}_{-6.1}$
$[15, 18]$	$[0.03, 0.04]$	0.174	$^{+6.9}_{-5.6}$
$[18, 21]$	$[0.03, 0.04]$	0.164	$^{+6.2}_{-4.8}$
$[21, 26]$	$[0.03, 0.04]$	0.126	$^{+6.8}_{-5.6}$
$[26, 32]$	$[0.03, 0.04]$	0.087	$^{+7.4}_{-6.3}$
$[32, 35]$	$[0.03, 0.04]$	0.058	$^{+9.9}_{-9.1}$
$[0.5, 1.64]$	$[0.04, 0.05]$	0.082	$^{+12.8}_{-12.2}$
$[4.32, 6]$	$[0.04, 0.05]$	0.249	$^{+6.8}_{-5.7}$
$[6, 8]$	$[0.04, 0.05]$	0.293	$^{+5.8}_{-4.3}$
$[8, 10]$	$[0.04, 0.05]$	0.261	$^{+5.8}_{-4.3}$
$[10, 12]$	$[0.04, 0.05]$	0.254	$^{+6.1}_{-4.7}$
$[12, 15]$	$[0.04, 0.05]$	0.227	$^{+5.9}_{-4.5}$
$[15, 21]$	$[0.04, 0.05]$	0.151	$^{+6.1}_{-4.7}$
$[21, 26]$	$[0.04, 0.05]$	0.076	$^{+6.1}_{-4.7}$

p [GeV/c]	θ [rad]	Multiplicity $\frac{1}{\text{GeV/c rad}}$	Total Unc. [%]
$[0.5, 1.64]$	$[0.05, 0.06]$	0.093	$^{+13.0}_{-12.4}$
$[4.32, 6]$	$[0.05, 0.06]$	0.279	$^{+7.4}_{-6.4}$
$[6, 8]$	$[0.05, 0.06]$	0.311	$^{+6.6}_{-5.3}$
$[8, 11]$	$[0.05, 0.06]$	0.273	$^{+6.0}_{-4.6}$
$[11, 15]$	$[0.05, 0.06]$	0.211	$^{+6.0}_{-4.6}$
$[15, 21]$	$[0.05, 0.06]$	0.101	$^{+6.5}_{-5.3}$
$[0.5, 1.64]$	$[0.06, 0.08]$	0.140	$^{+10.9}_{-10.2}$
$[4.32, 5]$	$[0.06, 0.08]$	0.294	$^{+7.9}_{-6.9}$
$[5, 7]$	$[0.06, 0.08]$	0.319	$^{+7.0}_{-5.8}$
$[7, 9]$	$[0.06, 0.08]$	0.267	$^{+7.2}_{-6.1}$
$[9, 14]$	$[0.06, 0.08]$	0.175	$^{+5.6}_{-4.1}$
$[14, 17]$	$[0.06, 0.08]$	0.087	$^{+6.0}_{-4.7}$
$[0.5, 1.64]$	$[0.08, 0.1]$	0.188	$^{+8.6}_{-7.7}$
$[4.32, 5]$	$[0.08, 0.1]$	0.334	$^{+7.4}_{-6.3}$
$[5, 9]$	$[0.08, 0.1]$	0.256	$^{+6.8}_{-5.6}$
$[9, 13]$	$[0.08, 0.1]$	0.111	$^{+6.8}_{-5.6}$
$[0.5, 1.64]$	$[0.1, 0.12]$	0.194	$^{+9.6}_{-8.8}$
$[4.32, 5]$	$[0.1, 0.12]$	0.349	$^{+10.8}_{-10.1}$
$[5, 11]$	$[0.1, 0.12]$	0.145	$^{+6.5}_{-5.2}$
$[0.5, 1.64]$	$[0.12, 0.14]$	0.230	$^{+7.4}_{-6.3}$
$[4.32, 5]$	$[0.12, 0.14]$	0.291	$^{+8.8}_{-7.9}$
$[5, 9]$	$[0.12, 0.14]$	0.150	$^{+6.9}_{-5.7}$
$[0.5, 1.64]$	$[0.14, 0.16]$	0.263	$^{+11.5}_{-10.8}$
$[4.32, 5]$	$[0.14, 0.16]$	0.223	$^{+8.2}_{-7.2}$
$[5, 8]$	$[0.14, 0.16]$	0.113	$^{+7.6}_{-6.6}$
$[0.5, 1.64]$	$[0.16, 0.18]$	0.290	$^{+8.1}_{-7.2}$
$[4.32, 7]$	$[0.16, 0.18]$	0.117	$^{+9.7}_{-8.9}$

p [GeV/c]	θ [rad]	Multiplicity $\frac{1}{\text{GeV/c rad}}$	Total Unc. [%]
$[0.5, 1.64]$	$[0.18, 0.2]$	0.318	$^{+10.9}_{-10.2}$
$[4.32, 6]$	$[0.18, 0.2]$	0.115	$^{+10.6}_{-9.8}$
$[0.5, 1.64]$	$[0.2, 0.22]$	0.283	$^{+15.1}_{-14.6}$
$[4.32, 5]$	$[0.2, 0.22]$	0.151	$^{+19.3}_{-18.9}$
$[0.5, 1.64]$	$[0.22, 0.24]$	0.299	$^{+29.6}_{-29.3}$
$[0.5, 1.64]$	$[0.24, 0.26]$	0.320	$^{+45.3}_{-45.1}$

Table A.6: p differential multiplicity results for proton-carbon interaction at 90 GeV/c

p [GeV/c]	θ [rad]	Multiplicity $\frac{1}{\text{GeV/c rad}}$	Total Unc. [%]
$[4.32, 13]$	$[0, 0.005]$	0.004	$^{+23.9}_{-23.2}$
$[13, 18]$	$[0, 0.005]$	0.003	$^{+36.9}_{-36.7}$
$[25, 31]$	$[0, 0.005]$	0.001	$^{+40.3}_{-40.1}$
$[4.32, 10]$	$[0.005, 0.01]$	0.005	$^{+24.3}_{-23.8}$
$[10, 15]$	$[0.005, 0.01]$	0.008	$^{+39.6}_{-39.4}$
$[15, 20]$	$[0.005, 0.01]$	0.005	$^{+36.6}_{-36.4}$
$[20, 25]$	$[0.005, 0.01]$	0.007	$^{+34.7}_{-34.5}$
$[25, 30]$	$[0.005, 0.01]$	0.002	$^{+46.7}_{-46.6}$
$[4.32, 7]$	$[0.01, 0.02]$	0.010	$^{+19.9}_{-19.0}$
$[7, 9]$	$[0.01, 0.02]$	0.011	$^{+23.7}_{-22.9}$
$[9, 12]$	$[0.01, 0.02]$	0.013	$^{+18.9}_{-18.1}$
$[12, 15]$	$[0.01, 0.02]$	0.010	$^{+19.8}_{-19.2}$
$[15, 18]$	$[0.01, 0.02]$	0.007	$^{+20.6}_{-20.2}$
$[18, 21]$	$[0.01, 0.02]$	0.008	$^{+22.8}_{-22.5}$
$[21, 24]$	$[0.01, 0.02]$	0.003	$^{+34.9}_{-34.7}$
$[24, 27]$	$[0.01, 0.02]$	0.003	$^{+41.0}_{-40.8}$
$[27, 30]$	$[0.01, 0.02]$	0.004	$^{+32.5}_{-32.3}$

p [GeV/c]	θ [rad]	Multiplicity $\frac{1}{\mathrm{GeV/c\ rad}}$	Total Unc. [%]
$[30, 34]$	$[0.01, 0.02]$	0.002	$^{+45.1}_{-45.0}$
$[4.32, 6]$	$[0.02, 0.03]$	0.012	$^{+21.4}_{-20.6}$
$[6, 8]$	$[0.02, 0.03]$	0.014	$^{+19.1}_{-18.2}$
$[8, 10]$	$[0.02, 0.03]$	0.015	$^{+15.8}_{-14.7}$
$[10, 12]$	$[0.02, 0.03]$	0.011	$^{+17.2}_{-16.4}$
$[12, 14]$	$[0.02, 0.03]$	0.016	$^{+14.3}_{-13.7}$
$[14, 16]$	$[0.02, 0.03]$	0.010	$^{+17.7}_{-17.3}$
$[16, 18]$	$[0.02, 0.03]$	0.009	$^{+20.8}_{-20.5}$
$[18, 20]$	$[0.02, 0.03]$	0.005	$^{+24.5}_{-24.2}$
$[20, 22]$	$[0.02, 0.03]$	0.005	$^{+41.4}_{-41.2}$
$[22, 24]$	$[0.02, 0.03]$	0.005	$^{+37.7}_{-37.5}$
$[24, 26]$	$[0.02, 0.03]$	0.003	$^{+44.6}_{-44.5}$
$[26, 29]$	$[0.02, 0.03]$	0.003	$^{+32.8}_{-32.6}$
$[29, 34]$	$[0.02, 0.03]$	0.001	$^{+38.8}_{-38.6}$
$[4.32, 6]$	$[0.03, 0.04]$	0.012	$^{+23.7}_{-23.2}$
$[6, 8]$	$[0.03, 0.04]$	0.011	$^{+22.8}_{-22.3}$
$[8, 10]$	$[0.03, 0.04]$	0.016	$^{+15.4}_{-14.6}$
$[10, 12]$	$[0.03, 0.04]$	0.014	$^{+16.7}_{-15.8}$
$[12, 13]$	$[0.03, 0.04]$	0.014	$^{+24.9}_{-24.4}$
$[13, 15]$	$[0.03, 0.04]$	0.007	$^{+34.0}_{-33.7}$
$[15, 18]$	$[0.03, 0.04]$	0.007	$^{+20.4}_{-20.1}$
$[18, 21]$	$[0.03, 0.04]$	0.005	$^{+31.2}_{-31.0}$
$[21, 26]$	$[0.03, 0.04]$	0.002	$^{+32.3}_{-32.1}$
$[4.32, 6]$	$[0.04, 0.05]$	0.026	$^{+14.4}_{-13.6}$
$[6, 8]$	$[0.04, 0.05]$	0.031	$^{+12.4}_{-11.6}$
$[8, 10]$	$[0.04, 0.05]$	0.032	$^{+11.0}_{-10.1}$
$[10, 12]$	$[0.04, 0.05]$	0.023	$^{+11.4}_{-10.4}$

p [GeV/c]	θ [rad]	Multiplicity $\frac{1}{\text{GeV/c rad}}$	Total Unc. [%]
$[12, 15]$	$[0.04, 0.05]$	0.018	$^{+12.0}_{-11.3}$
$[15, 21]$	$[0.04, 0.05]$	0.007	$^{+12.5}_{-11.9}$
$[4.32, 6]$	$[0.05, 0.06]$	0.029	$^{+12.2}_{-11.6}$
$[6, 8]$	$[0.05, 0.06]$	0.030	$^{+12.2}_{-11.6}$
$[8, 11]$	$[0.05, 0.06]$	0.023	$^{+14.0}_{-13.5}$
$[11, 15]$	$[0.05, 0.06]$	0.015	$^{+11.6}_{-10.9}$
$[15, 21]$	$[0.05, 0.06]$	0.005	$^{+21.0}_{-20.6}$
$[4.32, 5]$	$[0.06, 0.08]$	0.044	$^{+24.3}_{-24.0}$
$[5, 7]$	$[0.06, 0.08]$	0.042	$^{+11.4}_{-10.8}$
$[7, 9]$	$[0.06, 0.08]$	0.028	$^{+16.8}_{-16.5}$
$[9, 14]$	$[0.06, 0.08]$	0.016	$^{+10.3}_{-9.6}$
$[14, 17]$	$[0.06, 0.08]$	0.005	$^{+19.8}_{-19.5}$
$[4.32, 5]$	$[0.08, 0.1]$	0.046	$^{+17.9}_{-17.7}$
$[5, 9]$	$[0.08, 0.1]$	0.028	$^{+17.7}_{-17.8}$
$[9, 13]$	$[0.08, 0.1]$	0.012	$^{+19.1}_{-19.1}$
$[4.32, 5]$	$[0.1, 0.12]$	0.056	$^{+22.2}_{-22.0}$
$[5, 11]$	$[0.1, 0.12]$	0.017	$^{+14.2}_{-14.0}$
$[4.32, 5]$	$[0.12, 0.14]$	0.034	$^{+30.9}_{-30.7}$
$[5, 9]$	$[0.12, 0.14]$	0.017	$^{+15.4}_{-15.2}$
$[4.32, 5]$	$[0.14, 0.16]$	0.031	$^{+23.2}_{-22.9}$
$[5, 8]$	$[0.14, 0.16]$	0.012	$^{+19.1}_{-19.0}$
$[4.32, 7]$	$[0.16, 0.18]$	0.010	$^{+22.8}_{-22.5}$
$[0.5, 1.64]$	$[0.18, 0.2]$	0.010	$^{+38.4}_{-38.2}$
$[4.32, 6]$	$[0.18, 0.2]$	0.008	$^{+28.2}_{-27.9}$

Table A.7: $\bar{p}$ differential multiplicity results for proton-carbon interaction at 90 GeV/c

p [GeV/c]	θ [rad]	Multiplicity $\frac{1}{\text{GeV/c rad}}$	Total Unc. [%]
$[4.32, 21]$	$[0, 0.005]$	0.005	$^{+29.5}_{-29.2}$
$[21, 36]$	$[0, 0.005]$	0.009	$^{+30.8}_{-30.6}$
$[4.32, 11]$	$[0.005, 0.01]$	0.026	$^{+26.6}_{-26.3}$
$[11, 17]$	$[0.005, 0.01]$	0.038	$^{+22.0}_{-21.7}$
$[17, 24]$	$[0.005, 0.01]$	0.034	$^{+17.1}_{-16.6}$
$[24, 32]$	$[0.005, 0.01]$	0.045	$^{+16.1}_{-15.6}$
$[4.32, 9]$	$[0.01, 0.02]$	0.052	$^{+9.8}_{-9.1}$
$[9, 13]$	$[0.01, 0.02]$	0.073	$^{+9.5}_{-8.7}$
$[13, 17]$	$[0.01, 0.02]$	0.072	$^{+11.0}_{-10.3}$
$[17, 22]$	$[0.01, 0.02]$	0.064	$^{+8.3}_{-7.4}$
$[22, 27]$	$[0.01, 0.02]$	0.068	$^{+8.8}_{-7.9}$
$[4.32, 7]$	$[0.02, 0.03]$	0.109	$^{+9.4}_{-8.6}$
$[7, 10]$	$[0.02, 0.03]$	0.100	$^{+9.9}_{-9.1}$
$[10, 13]$	$[0.02, 0.03]$	0.102	$^{+15.5}_{-15.0}$
$[13, 17]$	$[0.02, 0.03]$	0.084	$^{+9.2}_{-8.3}$
$[17, 25]$	$[0.02, 0.03]$	0.060	$^{+7.7}_{-6.7}$
$[4.32, 7]$	$[0.03, 0.04]$	0.137	$^{+8.8}_{-7.9}$
$[7, 10]$	$[0.03, 0.04]$	0.124	$^{+8.7}_{-7.9}$
$[10, 13]$	$[0.03, 0.04]$	0.113	$^{+9.3}_{-8.5}$
$[13, 15]$	$[0.03, 0.04]$	0.093	$^{+11.6}_{-11.0}$
$[15, 23]$	$[0.03, 0.04]$	0.051	$^{+10.7}_{-10.0}$
$[4.32, 7]$	$[0.04, 0.05]$	0.012	$^{+32.2}_{-31.9}$
$[7, 10]$	$[0.04, 0.05]$	0.048	$^{+9.3}_{-8.5}$
$[10, 15]$	$[0.04, 0.05]$	0.045	$^{+8.7}_{-7.9}$
$[15, 21]$	$[0.04, 0.05]$	0.017	$^{+18.4}_{-18.0}$
$[0.5, 0.95]$	$[0.05, 0.06]$	0.005	$^{+49.1}_{-49.0}$
$[4.32, 7]$	$[0.05, 0.06]$	0.055	$^{+14.7}_{-14.2}$

p [GeV/c]	θ [rad]	Multiplicity $\frac{1}{\text{GeV/c rad}}$	Total Unc. [%]
$[7, 11]$	$[0.05, 0.06]$	0.064	$^{+8.9}_{-8.0}$
$[11, 15]$	$[0.05, 0.06]$	0.048	$^{+9.3}_{-8.4}$
$[15, 21]$	$[0.05, 0.06]$	0.017	$^{+10.0}_{-9.2}$
$[4.32, 7]$	$[0.06, 0.08]$	0.059	$^{+15.9}_{-15.4}$
$[7, 12]$	$[0.06, 0.08]$	0.060	$^{+7.5}_{-6.5}$
$[12, 19]$	$[0.06, 0.08]$	0.019	$^{+8.8}_{-7.9}$
$[4.32, 5]$	$[0.08, 0.1]$	0.055	$^{+24.3}_{-24.0}$
$[5, 13]$	$[0.08, 0.1]$	0.043	$^{+8.1}_{-7.1}$
$[13, 15]$	$[0.08, 0.1]$	0.016	$^{+29.8}_{-29.5}$
$[0.5, 0.95]$	$[0.1, 0.12]$	0.022	$^{+45.5}_{-45.3}$
$[4.32, 5]$	$[0.1, 0.12]$	0.063	$^{+17.0}_{-16.5}$
$[5, 13]$	$[0.1, 0.12]$	0.028	$^{+9.9}_{-9.1}$
$[0.5, 0.95]$	$[0.12, 0.14]$	0.041	$^{+39.0}_{-38.8}$
$[4.32, 5]$	$[0.12, 0.14]$	0.049	$^{+32.8}_{-32.5}$
$[5, 11]$	$[0.12, 0.14]$	0.026	$^{+10.9}_{-10.3}$
$[4.32, 5]$	$[0.14, 0.16]$	0.045	$^{+33.1}_{-32.9}$
$[5, 9]$	$[0.14, 0.16]$	0.020	$^{+19.6}_{-19.3}$
$[0.5, 0.95]$	$[0.16, 0.18]$	0.064	$^{+30.3}_{-30.0}$
$[4.32, 5]$	$[0.16, 0.18]$	0.033	$^{+30.7}_{-30.4}$
$[5, 8]$	$[0.16, 0.18]$	0.020	$^{+19.5}_{-19.1}$
$[4.32, 8]$	$[0.18, 0.2]$	0.018	$^{+16.5}_{-16.0}$
$[0.5, 0.95]$	$[0.2, 0.22]$	0.036	$^{+36.1}_{-35.9}$
$[4.32, 7]$	$[0.2, 0.22]$	0.022	$^{+24.8}_{-24.5}$

Table A.8: K^+ differential multiplicity results for proton-carbon interaction at 90 GeV/c

p [GeV/c]	θ [rad]	Multiplicity $\frac{1}{\mathrm{GeV/c\ rad}}$	Total Unc. [%]
$[4.32, 21]$	$[0, 0.005]$	0.005	$^{+21.3}_{-20.9}$
$[21, 36]$	$[0, 0.005]$	0.003	$^{+34.4}_{-34.2}$
$[4.32, 11]$	$[0.005, 0.01]$	0.026	$^{+19.6}_{-19.2}$
$[11, 17]$	$[0.005, 0.01]$	0.026	$^{+17.5}_{-17.1}$
$[17, 24]$	$[0.005, 0.01]$	0.012	$^{+38.8}_{-38.6}$
$[24, 32]$	$[0.005, 0.01]$	0.015	$^{+33.0}_{-32.8}$
$[4.32, 9]$	$[0.01, 0.02]$	0.047	$^{+9.4}_{-8.7}$
$[9, 13]$	$[0.01, 0.02]$	0.041	$^{+14.2}_{-13.7}$
$[13, 17]$	$[0.01, 0.02]$	0.033	$^{+13.3}_{-12.7}$
$[17, 22]$	$[0.01, 0.02]$	0.026	$^{+12.2}_{-11.6}$
$[22, 27]$	$[0.01, 0.02]$	0.020	$^{+18.0}_{-17.6}$
$[4.32, 7]$	$[0.02, 0.03]$	0.061	$^{+10.5}_{-9.8}$
$[7, 10]$	$[0.02, 0.03]$	0.077	$^{+9.1}_{-8.3}$
$[10, 13]$	$[0.02, 0.03]$	0.063	$^{+11.2}_{-10.6}$
$[13, 17]$	$[0.02, 0.03]$	0.045	$^{+12.4}_{-11.8}$
$[17, 25]$	$[0.02, 0.03]$	0.021	$^{+10.7}_{-10.0}$
$[4.32, 7]$	$[0.03, 0.04]$	0.086	$^{+10.6}_{-9.8}$
$[7, 10]$	$[0.03, 0.04]$	0.092	$^{+8.5}_{-7.6}$
$[10, 13]$	$[0.03, 0.04]$	0.056	$^{+11.7}_{-11.0}$
$[13, 15]$	$[0.03, 0.04]$	0.045	$^{+16.6}_{-16.1}$
$[15, 23]$	$[0.03, 0.04]$	0.019	$^{+16.6}_{-16.2}$
$[4.32, 7]$	$[0.04, 0.05]$	0.064	$^{+18.9}_{-18.5}$
$[7, 10]$	$[0.04, 0.05]$	0.065	$^{+8.8}_{-7.9}$
$[10, 15]$	$[0.04, 0.05]$	0.040	$^{+8.2}_{-7.3}$
$[15, 21]$	$[0.04, 0.05]$	0.014	$^{+15.4}_{-14.9}$
$[4.32, 7]$	$[0.05, 0.06]$	0.102	$^{+8.3}_{-7.3}$
$[7, 11]$	$[0.05, 0.06]$	0.078	$^{+8.7}_{-7.8}$

p [GeV/c]	θ [rad]	Multiplicity $\frac{1}{\text{GeV/c rad}}$	Total Unc. [%]
$[11, 15]$	$[0.05, 0.06]$	0.034	$^{+11.2}_{-10.5}$
$[15, 21]$	$[0.05, 0.06]$	0.010	$^{+15.9}_{-15.4}$
$[0.5, 0.95]$	$[0.06, 0.08]$	0.048	$^{+45.5}_{-45.3}$
$[4.32, 7]$	$[0.06, 0.08]$	0.064	$^{+10.6}_{-9.9}$
$[7, 12]$	$[0.06, 0.08]$	0.037	$^{+9.2}_{-8.4}$
$[12, 19]$	$[0.06, 0.08]$	0.008	$^{+15.2}_{-14.7}$
$[4.32, 5]$	$[0.08, 0.1]$	0.050	$^{+35.2}_{-35.0}$
$[5, 13]$	$[0.08, 0.1]$	0.026	$^{+9.4}_{-8.6}$
$[13, 15]$	$[0.08, 0.1]$	0.002	$^{+43.8}_{-43.6}$
$[0.5, 0.95]$	$[0.1, 0.12]$	0.041	$^{+40.8}_{-40.7}$
$[4.32, 5]$	$[0.1, 0.12]$	0.016	$^{+41.1}_{-41.0}$
$[5, 13]$	$[0.1, 0.12]$	0.013	$^{+13.2}_{-12.7}$
$[4.32, 5]$	$[0.12, 0.14]$	0.033	$^{+31.3}_{-31.1}$
$[5, 11]$	$[0.12, 0.14]$	0.014	$^{+19.0}_{-18.6}$
$[0.5, 0.95]$	$[0.14, 0.16]$	0.022	$^{+37.8}_{-37.6}$
$[4.32, 5]$	$[0.14, 0.16]$	0.008	$^{+47.1}_{-46.9}$
$[5, 9]$	$[0.14, 0.16]$	0.009	$^{+26.1}_{-25.8}$
$[0.5, 0.95]$	$[0.16, 0.18]$	0.080	$^{+29.4}_{-29.2}$
$[4.32, 5]$	$[0.16, 0.18]$	0.017	$^{+34.0}_{-33.8}$
$[5, 8]$	$[0.16, 0.18]$	0.003	$^{+34.9}_{-34.7}$
$[4.32, 8]$	$[0.18, 0.2]$	0.006	$^{+32.9}_{-32.7}$
$[0.5, 0.95]$	$[0.2, 0.22]$	0.011	$^{+45.8}_{-45.6}$

Table A.9: K^- differential multiplicity results for proton-carbon interaction at 90 GeV/c